Universitá degli Studi di Padova

SCUOLA DI SCIENZE
DIPARTIMENTO DI FISICA ED ASTRONOMIA
"GALILEO GALILEI"

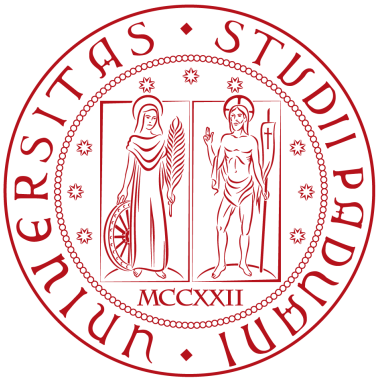

LAUREA MAGISTRALE IN ASTRONOMIA

Constraining the physical properties of high-redshift star-forming galaxies with MUSE and ALMA

Relatore: Chiar.mo Prof. Alberto Franceschini
Correlatore: Dott.ssa Giulia Rodighiero
Correlatore: Dott.ssa Lucía Rodríguez-Muñoz
Correlatore: Dott.ssa Chiara Mancini

Laureando: EDOARDO IANI

A.A. 2015 - 2016

To my grandmother
Giovanna

"[...]; e chi sedea
A libar latte o a raccontar sue pene
Ai cari estinti, una fragranza intorno
Sentia qual d'aura de' beati Elisi." [U. Foscolo]

Abstract

The main purpose of this Master Degree Thesis has been the measurement of physical parameters, i.e. the stellar mass content ($M_\star$), the Star Formation Rate (SFR) and the extinction (A_V), for a sample of distant dusty galaxies selected with ALMA, i.e. the Atacama Large Millimeter/submillimeter Array, in the Hubble Ultra Deep Field (HUDF, Beckwith et al. 2003). The sources were chosen among the galaxies presented in a recent paper by Dunlop et al. (2016) and their physical parameters, subjects of our study, were retrieved by means of an advanced modeling analysis which combines the high-resolution spectroscopy from MUSE instrument (i.e. the Multi-Unit Spectroscopic Explorer) and a multi-wavelength photometry. To this aim, we referred to the photometric catalog presented by Santini et al. (2009), an updated version of the multicolour GOODS-MUSIC catalog (i.e. GOODS MUlitcolour Southern Infrared Catalog, Grazian et al. 2006). The software adopted for this task has been the spectro-photometric fitting code SINOPSIS by Fritz et al. (2007).
Concurrently to the study on the ALMA-detected sources, we performed a statistical analysis on a comparison sample of unobscured star-forming galaxies selected from the *HST* catalog by Coe et al. (2006), on the basis of well-defined criteria. We limited the comparison sample to galaxies within the deepest pointing of the MUSE HUDF survey (Program ID 094.A-0289, P.I. Bacon; paper in prep.), in the photometric redshift range $0.5 < z < 0.8$, where MUSE optical spectra provide a direct measure of [OII] emission lines, and to sources with a detection in the H band. This last demand allowed to restrict our analysis to a well controlled sample, where the near-IR detection guarantees the measurements of secure stellar masses.
To compare the results obtained by means of SINOPSIS to what is attainable with a classical photometric SED-fitting approach, we resort to *HyperZmass* (Pozzetti et al., 2007). This procedure gave us the opportunity to investigate the potential improvements in the measurements of the physical parametrs of distant galaxies due to the inclusion of high-resolution spectral information (in particular emission lines) in SED fitting procedures. In fact, even if looking at the larger comparison sample of normal star-forming galaxies, we found that the two codes provide consistent results, within the range of allowed parameters (in particular the SF histories). Our results show that a spectro-photometric code (SINOPSIS), accounting for the presence of emission lines and combined to broad-band optical/near-IR photometry, returns very high extinctions for the dusty sources selected in the millimeter continuum. Indeed, the ALMA sources resulted

to be the most obscured and star-forming objects of the sample. Such level of obscuration is not recovered by a standard SED fitting approach (e.g. *HyperZmass*), neglecting the presence of emission lines. The A_V derived from SINOPSIS for this starbursting source also exceeds the A_{IRX} computed including *Herschel* photometry, but the large formal uncertainties on this parameter for this source do not provide a conclusive result.
Concluding, our work highlighted how the combination of ALMA and MUSE, two state-of-the-art instruments working in completely different spectral ranges (millimeter and optical), provides an important test on the potential scientific exploitation of the large data-sets that are becoming publicly available to the community (through the respective data archives).

Contents

List of Figures

List of Tables

Acknowledgements

Firstly, I would like to thank my parents since they have always been supportive to me both psychologically and economically. The achievements reached in this Thesis were not possible without their efforts, support and unconditional love during all my life. I am really grateful to them, because they made me the man I am.
Nonetheless, this work could not have seen the light without the essential help of Giulia Rodighiero, my assistant supervisor, who has been always patient and friendly towards me, devoting most of her time in the last weeks overseeing my work and correcting my typos. I wish to thank Lucía Rodríguez-Muñoz, who has been always truly helpful, giving me precious advices and suggestions to improve this work along with fun and amusement, and Chiara Mancini, who helped me with the use of the *HyperZmass* software and has been always ready to give her contribution. I am also grateful to Jacopo Fritz, who has been always available to help me solving the difficulties found in running SINOPSIS and giving important and enriching suggestions to this work.
Finally, I would like to thank my supervisor, Prof. Alberto Franceschini, who gave me the opportunity to dive into an unexpected but fascinating field of the modern observational Cosmology.

Introduction

The general context of this Master Degree Thesis lies within the field of galaxy evolution in the distant Universe (i.e. at redshifts $z > 0.5$).
In the last decades, thanks to the advent of new generation telescopes, either from ground (VLT, ALMA, etc...) or space (*HST*, Spitzer, *Herschel*, etc...), the possibility to conduct deep extragalactic surveys in the whole e.m. spectrum opened up to astronomers, thus probing the Universe back to the first Myr after the Big-Bang. Since the first Hubble Deep Field project (Williams et al., 1996) many deep survey projects revolutionized our view of the Universe, leaving to astronomers the hard task to observe and interpret the evolutionary history of galaxies. As a matter of fact, thanks to the detection of thousand of galaxies at high-z, it has been possible to reconstruct the main characteristics of galaxy evolution during the last 13 Gyr.

Star Formation in distant galaxies is the central aspect of this Thesis. Currently, we know that stars were not formed yet in the very early stages of the Universe, i.e. at a cosmic time before at least 100 Myr from the Big Bang. Nonetheless, at the time when the first stars formed and ignited ($z \simeq 15 - 30$, Bromm et al. 2009), intense events of star formation rapidly became common, supported by the favorable conditions of the denser early Universe (Bouwens et al., 2011). Therefore, during the first Gyr of the Universe, this evolution led to a rapid stellar mass build up and chemical enrichment. This scenario has been proved by the *Herschel* detection of a starburst high-redshift galaxy ($z = 6.34$; Riechers 2013), the detection of multiple Active Galactic Nuclei (AGN) at $z \geq 6.5$ with galactic black hole masses of the order of 10^9 $M_\odot$ (Venemans et al., 2015), along with the proto-cluster[1] source at $z \simeq 5.3$ observed by Capak et al. (2011). These sources are believed to be the progenitors of today's most massive elliptical galaxies lying at the center of galaxy clusters, the biggest gravitationally bound structures in the Universe. Even though in the Local Universe such galaxies rarely show signs of ongoing star formation, their stellar populations are very old, according to the fact that they built up most of their mass very early on.
The first deep surveys (e.g. Lilly et al. 1996, Madau et al. 1996, among others) provided the ultraviolet Luminosity Function (LF), i.e. the number of galaxies per luminosity bin in a given space volume, across various redshifts thus characterizing the evolution of the luminosity density with cosmic time. From these UV luminosities it is possible to

[1]The proto-clusters are early overdensities of galaxies that are expected to undergo merging to form gravitationally bound clusters, as we observe them in the present Universe.

Figure 1: Evolution of the cosmic SFR density (ψ, **top panel**) and stellar mass density ($\rho_\star$, **bottom panel**) as functions of the redshift and time. The orange, red and dark red markers correspond to data from restframe IR observations. The remaining data correspond restframe UV observations. Figure from Fig. 9 and Fig. 11 in Madau and Dickinson (2014).

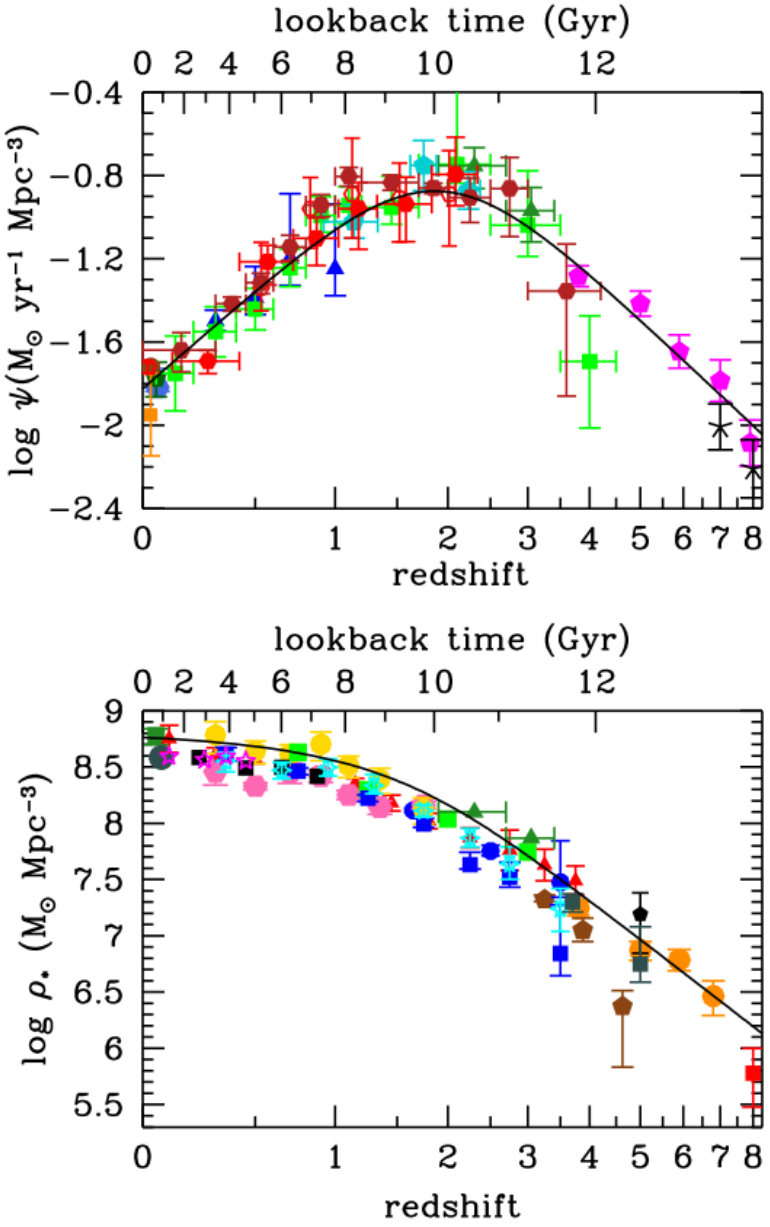

derive the Star Formation Rate (SFR) of the galaxies by means of simple calibrations (e.g. Kennicutt 1998, Talia et al. 2015), hence relating directly the luminosity density to the SFR density ($\rho_{\rm SFR}$). This relation has enabled the astronomers to reconstruct the Cosmic Star Formation History (CSFH), a fundamental result of modern observational Cosmology. At this regard, in Fig. 1 we present the current picture of the CFSH (from Madau and Dickinson 2014), in terms of the evolution of the global SFR density (ψ, *top panel*) and stellar mass density ($\rho_\star$, *bottom panel*) as functions of the redshift and time. Fig. 1 clearly shows that the Universe went through a phase of rapid increase in the star formation during the firsts Gyr of its existence, reaching a peak at $z \sim 2$ and has been gradually declining after. Currently, this decrease of the SF is mainly attributed to the expansion and slow depletion of gas in the Local Universe galaxies (Tacconi et al. 2010; Combes et al. 2013; Santini et al. 2014).

Nonetheless, to answer to question such as how galaxies grow their stellar mass with time and what explains the diversity in size, content and evolutionary stages we witness in the Local Universe, the astronomers had to focus their work on the Star Formation Histories (SFHs)[2] of galaxies, trying to identify the high-z progenitors of various type of galaxies at $z = 0$, to understand the process which drive and inhibit the star formation and the role of gas in this (inflows, outflows).

Star Forming Galaxies (SFG) emit light almost across the whole e.m. spectrum with stars dominating the emission from the UV to the NIR (i.e. stellar emission), while the emissions due to the Interstellar Medium (ISM) prevail in the IR domain. The ISM starts to dominate in proximity of restframe 8 μm where broad absorption and emission features set on due to the interaction between photons and the Polycyclic Aromatic Hydrocarbons (PAH). At higher wavelength, from the Mid-Infrared (MIR) on, the thermal emission from dust grains dominates completely the galaxy spectra. Dust, one of the by-products of stellar evolution created after evolved stars explode and enrich the ISM with heavy elements, formed as a result of the thermonuclear fusion processes, is heated by stars and cools off by re-emitting thermal radiation in the form of a modified Planck's law, i.e. a blackbody-like radiation. The blackbody-like radiation is a direct consequence of the different temperatures dust can reach when heated. The dust grains are wavelength-selective since they display a preference in absorbing photons with increasingly higher energy, i.e. shorter wavelength. Therefore, because dust attenuates blue and UV light more than the red or NIR, the effect it causes is defined as *reddening*. In particular, the relation bounding the relative reddening with the wavelength at which occurs is commonly defined as the *extinction* or *attenuation law*. Even though evidences suggest that there is no a unique attenuation law (e.g. Cardelli et al. 1989, Calzetti et al. 1994, among others) due to dust grain geometry, the different gas-to-dust ratios and the star-forming intensity of the environment, all the relations can be divided into two main categories on the basis of the stepness of the law in the UV and the presence/absence of the so-called *2175 Å bump* (see Fig. 2). In the context of characterizing SFGs and their physical properties via their SED, the Calzetti law (Calzetti et al., 1994) is favored (see Appendix B, Sec. B.4.2).

[2]The SFH of a galaxy describes the evolution of the galaxy SFR with time.

Figure 2: Examples of commonly considered extinction laws. Figure from Bolzonella et al. (2000).

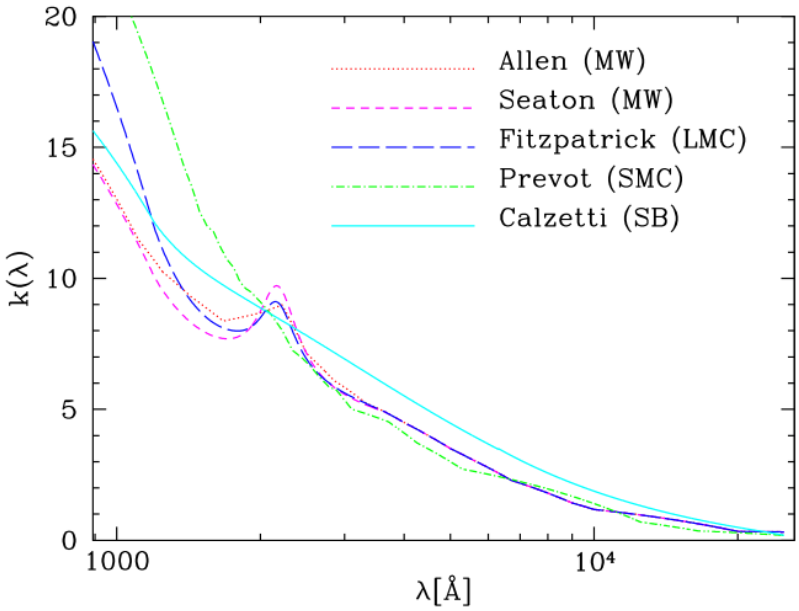

Dust emission decreases with increasing wavelength from the FIR to the millimetric wavelengths, and entering the radio domain the emission beacomes dominated by the free-free emission (i.e. *Bremsstrahlung emission*) coming from the HII regions and the synchrotron radiation from relativistic electrons.
On the contrary, at the high-energies, X-ray radiation as well as γ photons result from phenomena taking place in proximity of evolved compact objects (i.e. neutron stars, stellar black holes, etc...) or the galactic black hole.
By means of SED-fitting techniques, our principle aim has been to characterize ALMA-detected high-z galaxies, in terms of their stellar populations and dust properties.
One of the most important and characterizing property in the study of galaxies is the stellar mass ($M_\star$), a well-constrained parameter by the multi-wavelength photometry of the sources, specifically from the restframe NIR photometry in the range from 1 to 2 μm. To this regard, the restframe NIR stellar emission of galaxies is essential to retrieve estimates on the total stellar mass of the galaxies since the low mass stars ($M_\star \leq 1\ M_\odot$), emitting at redder wavelengths than massive stars ($M_\star > 2\ M_\odot$) due to their lower effective temperatures, represent the largest fraction of the stars in a galaxy, even if greatly outshined by the massive ones. In particular, the mass distribution of a Single Stellar Population (SSP), i.e. its Initial Mass Function (IMF), follows a negative powerlaw with mass whatever the parametrization adopted (e.g. Salpeter 1955, Kroupa 2001, Chabrier 2003).[3]

[3]The differences in the parametrizations lie essentially in the low mass end of the IMF, for stars with masses below 1 $M_\odot$.

The other important quantity that must be evaluated as best as possible to properly assess the evolutionary state of a galaxy, is its SFR, i.e. the amount of gas converted into stars per unit time, a quantity generally measured in $M_\odot$ yr^{-1} unit. This parameter is not as straightforward to derive as the stellar mass. In fact, the observables which help to evaluate the SFR (Kennicutt, 1998) are the luminosities retrieved in the UV and IR regimes of the galaxy spectra.
The UV emission is generally a direct tell-tale sign of star formation activity since the very massive young stars (i.e. OB-type stars), which contribute the most to the total UV emission,[4] have short lifespans (≤ 10 Myr), thus limiting the age of the stellar population if UV light is observing the spectra. Indeed, if star formations stops, the UV emission drastically decreases over a few tens of Myr. Due to this fact, over the years it has been possible to calibrate an estimation of the SFR to the observed UV light, by selecting fluxes in the range from 1500 to 2800 Å (e.g. Kennicutt 1998, Talia et al. 2015). Nevertheless, according to what we have previously described, the UV emission suffers dust attenuation. Not correcting for its effect naturally provides an understimated value for the SFR, i.e. the *unobscured SFR* (SFR_{UV}). In the majority of galaxies correcting for dust attenuation allows to obtain a good estimate of the total SFR, even if Calzetti (2001) argumented that in the case of extremely dust-obscured star-forming regions, the UV emission can be suppressed to such a level that it would not affect the UV spectrum, which would be dominated by the UV emission originating from the less obscured star-forming regions. From this scenario, it descends clearly the fundamental role fulfilled by the IR emission to constrain the *dust-obscured SFR* (SFR_{IR}). Similarly to the UV case, the SFR can be obtained from the IR luminosity by means of well-calibrated relations (Kennicutt, 1998) but with only one disadvantage: star formation is not the only source of dust heating since older stars in the diffuse Intersellar Medium (ISM) and unoscured AGNs contribute to the IR emission. Nonetheless, at high-z the contribution of older stars is expected to be very small, whereas for the presence of AGNs various diagnostics exist (e.g. line emission ratios, NIR-MIR colors, properties of the X-ray emission) that allow to exclude them when studying SFGs. On the basis of what we have described, the SFR_{IR} result to be an accurate estimation of the total SFR in highly dust obscured sources.
The large galaxy samples yielded from the last decade deep surveys have pointed out the existence of a tight correlation between the stellar mass $M_\star$ and the SFR as inferred by the UV and IR luminosities. This relation, first shown in H_α and UV-MIR studies (e.g. Brinchmann et al. (2004), Daddi et al. (2007)) and further constrained by *Herschel*'s contribution in the FIR (e.g. Rodighiero et al. 2010, Rodighiero et al. 2011, Renzini and Peng 2015), was defined as the *main sequence of str-forming galaxies* (MS) by Noeske et al. (2007), since at any given z the SFR of SFGs is observed to closely depend on $M_\star$ in a quasi-linear way at relatively low masses ($M_\star \leq 10^{10}$ $M_\odot$) while at larger masses the relation flattens (Schreiber et al., 2015). When compared at different redshifts, the MS scales up with increasing z with the obvious meaning that, fixed the stellar mass, a

[4]Young massive stars are not the oly sources of UV photons. Old populations always have some persisting UV emission, including contribution from planetary nebulæ, hot giants from the horizontal branch and white dwarfs.

Figure 3: The Main Sequence of star-forming galaxies (Schreiber et al., 2015) for redshifts spanning the range from $z \sim 0$ to $z \sim 4$. The relation is shown in four different colours for likewise values of z, according to the colorbar. The dots indicates the masses and $\mathrm{SFR}_{\mathrm{UV+IR}}$ for sources in all the GOODS-*Herschel* catalogs. Figure from Sklias (2016).

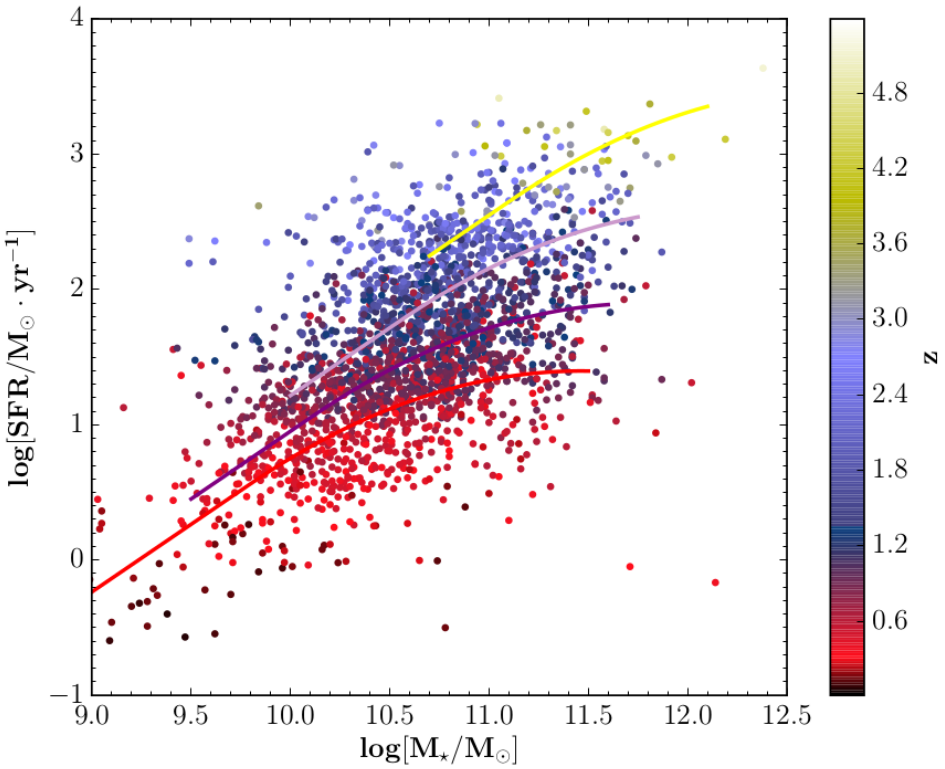

MS galaxy observed at a high redshift has a SFR higher than one at low-z (see Fig. 3). Implying that most SF galaxies are in a quasi-steady SF regime, the existence of the MS has several important ramifications. According to Rodighiero et al. (2014), the MS existence dictates a very rapid stellar mass growth of galaxies at early times, paralleled by a secular growth of their SFR itself (e.g. Renzini 2009; Peng et al. 2010), quite at odds with the widespread assumption of exponentially declining SFRs. Even more importantly, the slope of the MS controls the relative growth of high-mass versus low-mass galaxies, thus directly impinging on the evolution of the galaxy stellar mass function (Peng et al. 2013). While the existence of the MS is generally undisputed, its slope and width may differ significantly from one observational study to another, depending on the sample selection and the adopted SFR and stellar mass diagnostics. The MS adopted in this Thesis has been obtained from the relation presented in Renzini and Peng (2015), conveniently rescaled to the median z of our sample of sources.
In this Thesis we investigate how the synergy of ALMA and MUSE, two state-of-the-art instruments working in completely different spectral ranges (millimeter and optical), can constrain the physical parameters that regulate galaxies growth through cosmic times, parametrized for example through an accurate determination of the Main Sequence.

In Chapter 1, we will present a description of both the cosmological field subject of this Thesis, i.e. the Hubble Ultra Deep Field (HUDF), and the spatial facility used for its first observations: the Hubble Space Telescope (*HST*). In Chapter 2, we will describe the recent observations in the HUDF by means of MUSE (Program ID 094.A-0289, P.I. Bacon; paper in prep.) and ALMA (Dunlop et al. 2016, Walter et al. 2016) along with concise descriptions of the two instruments. In Chapter 3, we will present our spectroscopic investigation of ALMA-detected sources (presented in recent papers by Dunlop et al. (2016) and Walter et al. (2016) on the MUSE data cubes in the HUDF. We will also report on the analysis of a comparison sample selected from the photometric catalog presented by Coe et al. (2006), requiring an H-band detection to ensure a reliable stellar mass measurement. In Chapter 4, we will present a complete analysis, by means of SINOPSIS (Fritz et al., 2007) and *HyperZmass* (Pozzetti et al., 2007), of the physical properties of the sources presented in Chapter 3, derived from the combination of MUSE spectra and their broad-band photometry. In Appendix A, we will present a brief description of the EZ software (see Garilli et al. 2010), a tool we extensively used to measure the spectroscopic redshifts for all the sources presented in our work, along with the results obtained from our first training on a sample of sources in HFF MACS J0416.1-2403. In Appendix B, we will describe SINOPSIS (Fritz et al., 2007), the spectro-photometric fitting code used to derive stellar masses, SFRs and extinctions for all the galaxy in our sample. We will also present SINOPSIS working principles besides the main adjustments to adapt the code to our requirements. Finally, in Appendix C we will report the fundamental data and multiwavelength postage-stamp images for each galaxy studied in this work.
In this work, we adopted a flat Λ-CDM cosmology with $\Omega = 0.3$, $\Lambda = 0.7$ and $H_0 = 70$ km s^{-1} Mpc^{-1}.

Chapter 1

The Hubble Ultra Deep Field

In this chapter we will briefly describe the characteristics of the cosmological field studied in this Thesis: the Hubble Ultra Deep Field (HUDF, Beckwith et al. 2003). To this aim, a detailed description of the observed field and its characteristics will be presented in Sec. 1.3.
In Sec. 1.2 we will present a characterization of the Hubble Deep Field (HDF, Williams et al. 1996). The HDF description is essential to well-understand the context in which the idea of such a deep imaging of the Universe (i.e. the HUDF field) was born.
Since the HDF and HUDF fields are named after the *Hubble Space Telescope* (*HST*), the spatial facility used for the observations of these two astronomical fields, a concise description of the observatory will be presented as well (see Sec. 1.1).

1.1 The Hubble Space Telescope

Named after the American astronomer Edwin Hubble (1889-1953), the *Hubble Space Telescope* (*HST*) is one of the NASA's Great Observatories[1], launched from the Kennedy Space Center (Cape Canaveral, Florida) into a low Earth orbit[2] (LEO) on April 24^{th}, 1990 (12:33:51 UTC) with the shuttle mission STS-31.[3]
The *HST* was built during the period from the late 70s to 1986 by the USA National Aeronautics and Space Administration (NASA) department with contributions from the European Space Agency (ESA).
The Space Telescope is a Cassegrain reflector of Ritchey-Chrétien design (i.e. with two hyperbolic mirrors), with a 2.4 m primary mirror and a collecting area of 4.5 m^2. Since the *HST* was specified to be diffraction limited and used for observations from the visible through the UV, the mirrors were polished to an accuracy of 10 nm.
At the time of the launch, the telescope was equipped with five scientific instruments: the

[1] Along with the Compton Gamma-Ray Observatory (CGRO), the Chandra X-ray Observatory (CXO) and the Spitzer Space Telescope (SST).

[2] The semi-major axis of the orbit is equal to 6918.88 km, with a perigee altitude of 538.79 km (and apogee at 542.70 km) and with a period of 95.47 minutes, thus a velocity of 7.59 km s^{-1}.

[3] The mission used the Space Shuttle *Discovery*.

Wide Field and Planetary Camera (WF/PC), the Goddard High Resolution Spectrograph (GHRS), the High Speed Photometer (HSP), the Faint Object Camera (FOC) and the Faint Object Spectrograph (FOS). Nonetheless, over the course of time all the initial instruments were replaced during five subsequently servicing missions of which the first[4] took place in December 1993 and the last in May 2009. Currently, the *HST* carries the Wide Field Camera 3 (WFC3), the Near Infrared Camera and Multi-Object Spectrometer (NICMOS)[5], the Cosmic Origins Spectrograph (COS), the Advanced Camera for Surveys (ACS) and the Space Telescope Imaging Spectrograph (STIS).
Among all the instruments described-above, for the HUDF observations the ACS instrument and the WFC3 were fundamental. The ACS was installed in the *HST* on March 7^{th}, 2002[6], replacing the FOC device and thus becoming the primary imaging instrument aboard *HST*. The Advanced Camera for Surveys features three independent, high resolution channels optimized for specific scientific tasks: the Wide Field Channel (WFC), the High-Resolution Channel (HRC)[7] and the Solar Blind Channel (SBC). Each channel covers a different portion of the e.m. spectrum: from 350 to 1100 nm for the WFC, from 170 to 1100 nm for the HRC and from 115 to 170 nm for the SBH. ACS offers a wide selection of filters and grisms along with two sets of polarizers (one optimized for near-UV/blue wavelengths whereas the other for visible/red wavelengths), a coronograph and two different types of detectors, CCDs and MAMA (i.e. the Multi-Anode Microchannel Array), depending on the observing wavelength range, i.e. the channel used. The effective dimensions of the ACS field of view depend on the channel to which reference is made: 202×202 arcsec for the WFC, 26×29 arcsec for HRC and, finally, 25×25 arcsec for the SBH.
Installed as a replacement for the WFPC-2 on May 14^{th}, 2009[8]; the WFC3 features a pair of CCDs, each 2048×4096 pixels, to record images from 200 nm to 1000 nm; and a separete near infrared detector array of 1024×1024 pixels, covering the wavelength

[4]The *HST* first servicing mission (SM1), flown aboard the *Endeavour* Shuttle in December 1993, passed into the annals of history. As a matter of fact, the first returned images of *HST* indicated a serious problem with the optical system since the Space Telescope failed to achieve a sharp focus thus retrieving a quality image drastically lower than expected. Instead of having a PSF within a $0.1''$ diameter circle, the images of point sources spread out over a radius of more than $1''$. This effect on the images was due to a wrong shaping of the primary mirror at the perimeter thus introducing severe spherical aberrations. The only possible solution to correct the mirror flaw was to design two different sets of correctors to be applied at the *HST* at the first servicing mission: the Corrective Optics Space Telescope Axial Replacement (COSTAR) and the Wide Field and Planetary Camera 2 (WFPC-2). While the COSTAR system was designed to correct the spherical aberration for light at the FOC, FOS and GHRS due to the replacement of the HSP, the WFPC-2 was projected to replace the WF/PC. The solar arrays and their drive electronics were also replaced, as well as four gyroscopes in the telescope pointing system, two electrical control units and other electrical components, and two magnetometers. The onboard computers were upgraded with added coprocessors, and Hubble's orbit was boosted. On January 13, 1994, NASA declared the mission (one of the most complex at the time) a complete success and showed the first sharper images.

[5]On June 18^{th}, 2010, it was announced NICMOS would not be available for science during the latest proposal Cycle 18.

[6]During the shuttle mission STS-109.

[7]Currently, the HRC channel is disabled due to electrical faults.

[8]During the shuttle mission STS-125.

range from 800 nm to 1700 nm. Both these two independent light paths are equipped with a variety of broad-band and narrow-band filters (i.e. 63 in the UVIS channel, 17 in the IR channel)[9] along with prisms and grisms. While the UVIS channel has a total field of view of 162×162 arcsec with $0.04''$ pixels, the IR channel covers a 123×136 arcsec sky-region with a $0.13''$ pixels.
Even though the telescope is orbiting since more than 25 years, the use of the *HST* is thought to be possible until 2030-2040 when the Space Telescope, due to the orbital decay originated from the atmospheric drag and the solar activity, will undergo the atmospheric reentry (if not re-boosted).

1.2 The Hubble Deep Fields

Born as an outgrowth of previous *HST* imaging projects (e.g. the Medium Deep Survey, MDS see Driver et al. 1995) intended to uncover the evolution of galaxies at high redshift, the Hubble Deep Field North (HDF-N, originally HDF, see Williams et al. 1996) was a Director's Discretionary program on the *HST* during Cycle 5. The project aim was the imaging of a high Galactic latitude field in four passbands of the Wide-Field Planetary Camera 2 (WFPC-2).
The field was chosen inside the *HST* continuous viewing zones (CVZ) beacuse of the significantly higher observing efficiency if compared with other locations on the sky. In particular, Williams et al. (1996) constrained the HDF-N location in a narrow declination range centered at about $\delta_{\rm J2000.0} = +62^\circ$, i.e. in the northern CVZ. The sky-region chosen, satisfied fundamental constraint such as a low optical extinction (E(B-V)< 0.01 mag), a low HI column density ($N_{\rm HI} < 2.5 \times 10^{20}$ atoms cm^{-2}) and a low Far-InfraRed (FIR) cirrus emission. In addition, all the areas presenting nearby galaxy clusters ($z < 0.3$) where excluded. As a matter of fact, the absence of bright sources in the X-ray, UV, optical, IR and radio passbands was essential to allow multi-wavelength studies on faint objects. To this aim, after the inspection of the *IRAS* maps and VLA snapshots at 3.6 and 21 cm (Kellermann et al., 1995), the choice of the region to image reduced to two candidate fields. The final decision between the two remaining fields was based on the possible presence of an independent pair of back-up guide stars. It was on the basis of the above mentioned criteria that Williams et al. (1996) ended up chosing the region centered in $\alpha_{\rm J2000.0} = 12^h\ 36^m\ 49.4^s$, $\delta_{\rm J2000.0} = +62^\circ\ 12'\ 58''$ (WFPC-2 "WFALL FIX" position).
The HDF-N observations took place in 1995, from December 18^{th} to 30^{th}, through the use of the combined F300W, F450W, F606W and F814W filters efficiently covering the optical portion of the WFPC-2 bandpass. The combination of deeper images and new cameras with sensitivity at redder wavelengths pushed the redshift limits of the observations well into the reionization epoch, i.e. in the first Gyr of the Universe.
To minimize the effects due to the Cosmic Variance, using a large fraction of Cycle 7 Director's Discretionary Time (October 1998), a second HDF campaign was undertaken

[9]The actual transmission data for all the filters can be found at `ftp://ftp.stsci.edu/cdbs/comp/wfc3/` .

by the *HST* in the southern empisphere: the Hubble Deep Field South (HDF-S) campaign (Williams et al., 2000)).
Similar in character to the HDF-N but with the added benefits of a QSO in the field (i.e. QSO J2233-606, $z = 2.24$) and parallel observations by the then-new *HST* instruments STIS and NICMOS[10], the HDF-S observations consist of WFPC-2 images in the broadband filters F300W, F450W, F606W and F814W; a deep STIS image of the field surrounding the QSO; spectroscopy of the QSO with STIS from 1150 to 3560 Å and a deep imaging of the adjacent field with NICMOS camera 3 at 1.1, 1.6 and 2.2 μm (filters F110W, F160W and F222W). The WFPC-2 main-field observations were centered around $\alpha_{\rm J2000.0} = 22^h\ 32^m\ 56.22^s$, $\delta_{\rm J2000.0} = -60^\circ\ 33'\ 02.69''$, about $5'$ west of the QSO on which the STIS observations were centered.

1.3 The Hubble Ultra Deep Field

The Hubble Ultra Deep Field (HUDF, see Beckwith et al. 2003) is a one million second exposure of an 11 arcmin^2 region in the southern sky (see Fig. 1.1). The HUDF was observed by Beckwith et al. with the then-new *HST*-ACS, using the Director's Discretionary Time and dividing the exposure time among four filters, F435W (B_{435}), F606W (V_{606}), F775W (i_{775}), and F850LP (z_{850}), to give approximately uniform limiting magnitudes $m_{AB} \approx 29$ for point sources.
The choice of the observing region was made attempting to meet some fundamental requirements: to minimize the celestial foreground radiation, maximize the overlap with extant or planned deep observations at X-ray, IR and radio wavelengths and maximize the observing efficiency of the Hubble Space Telescope. Therefore, unlike the HDF, the HUDF field region was chose outside the *HST* CVZ due to the bright background light in the part of the *HST* orbit grazing the Earth limb.[11] Conditions on the sky-coordinates of the field due to Zodiacal dust[12] and on the field accesibility to ground astronomical observatories (e.g. ALMA, the Mauna Kea observatories, etc...), reduced the choice to regions inside the Chandra Deep Field South (CDF-S, Giacconi et al. 2000). The CDF-S is a large field, $15' \times 15'$, located in the direction $\alpha_{\rm J2000.0} = 03^h\ 30^m$, $\delta_{\rm J2000.0} = -28^\circ$ and characterized by very low Galactic cirrus emission and atomic hydrogen column density (Schlegel et al., 1998) along with substantial investment in deep X-ray (*Chandra* and *XMM-Newton*) and IR (Spitzer Space Telescope) observations. Nonetheless, since the CDF-S is larger than a single ACS field, several additional criteria guided the exact

[10]The Space Telescope Imaging Spectrograph (STIS) and the Near Infrared Camera and Multi-Object Spectrometer (NICMOS) were installed during the second *HST* servicing mission, in 1997.

[11]The HDF overcame this limitation by taking images in the UV filter F300W during the bright periods, because WFPC-2 images in this filter are detector-noise-limited and relatively unaffected by increased background. On the contrary, the ACS-WFC is not sensitive at ultraviolet wavelengths, and the enhanced background of the bright CVZ orbits would seriously limit their usefulness (from Beckwith et al. 2003).

[12]At this regard, Beckwith et al. (2003) decided to locate the HUDF as far as possible from the ecliptic since the Zodiacal dust within approximately 30° of the ecliptic plane is bright for *HST*.

Figure 1.1: An *HST* colour image of the HUDF (Beckwith et al., 2003). Credits: NASA and the European Space Agency.

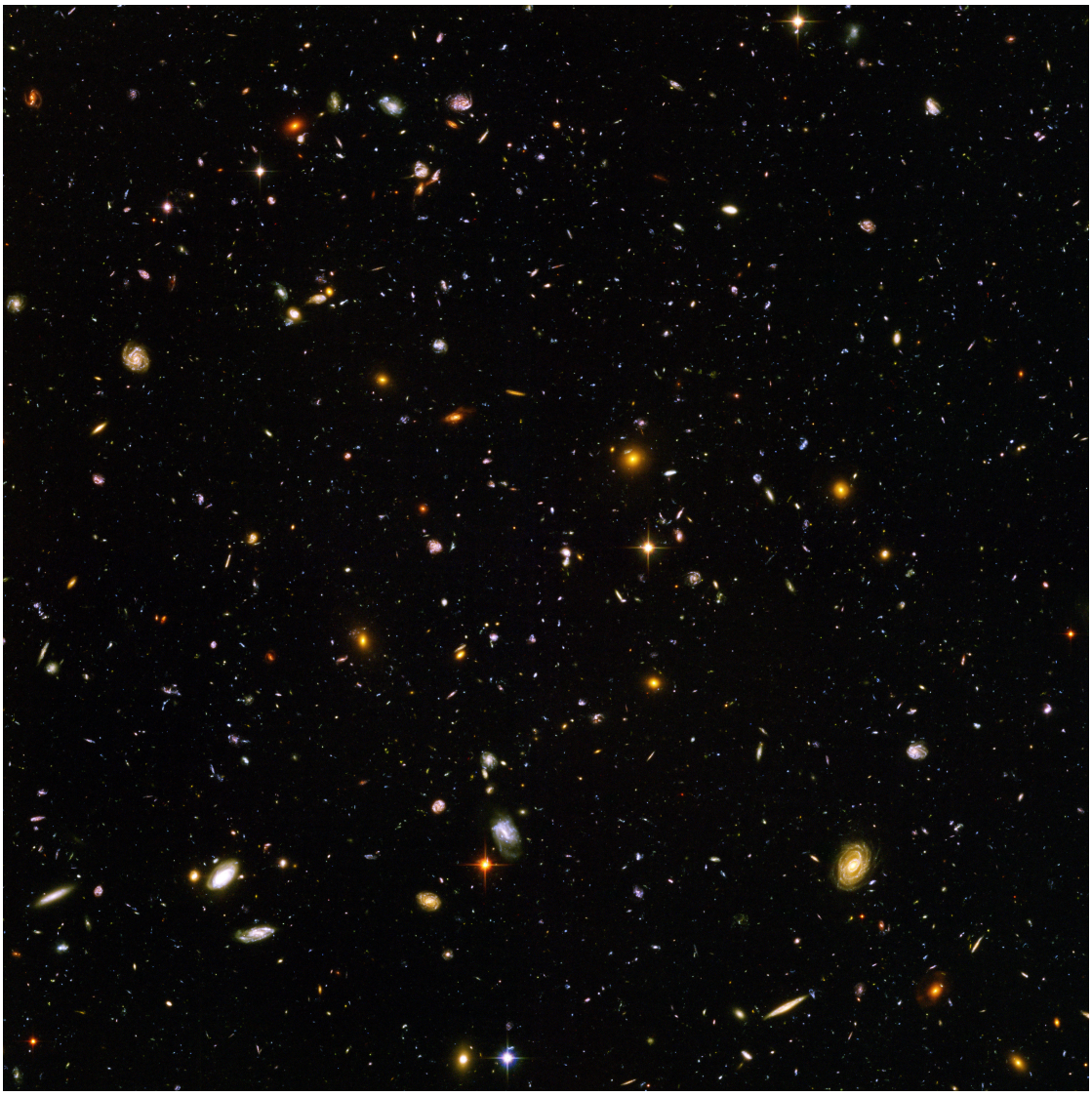

choice of the pointing: the *Chandra* X-ray sensitivity[13] and the presence of interesting objects identified through GOODS (Giavalisco et al., 2004). Therefore, the field chosen was centered on $\alpha_{\rm J2000.0} = 03^h\ 32^m\ 39^s$, $\delta_{\rm J2000.0} = -27^\circ\ 47'\ 29.1''$ with a field of view of $200'' \times 200''$, a E(B − V) = 0.008 and a HI column density $N_{\rm HI} = 7.9 \times 10^{19}$ cm^{-2}.
Compared to the HDF, the ACS provided over an order of magnitude gain in discovery efficiency (Illingworth et al., 2013) over the WFPC-2 and thanks to the redder filter (F850LP) the HUDF opened up the Universe at $z \simeq 5 - 6$, revealing a large number of galaxies just at the end of the reionization epoch. The image obtained by Beckwith et al. (2003) contains at least 10000 objects, the vast majority of which are galaxies. Visual inspection of the images shows few if any galaxies at redshifts greater than ≈ 4 that resemble present day spiral or elliptical galaxies. The image reinforces the conclusion from the original Hubble Deep Field that galaxies evolved strongly during the first few billion years of the Universe.
Since the initial observations on the HUDF in 2003, numerous surveys and programs, including supernova followup, HUDF09 (PI: Illingworth; e.g. Bouwens et al. 2011), CANDELS (PI: Faber/Ferguson; Grogin et al. 2011; Koekemoer et al. 2011), and HUDF12 have contributed additional imaging data across the region. Nonetheless it was with the eXtreme Deep Field (XDF, Illingworth et al. 2013) that data from ten years of observations with the *HST*-ACS and the WFC3/IR were combined, resulting in the deepest imaging ever taken ranging from 29.1to 30.3 AB-mag in 9 filters[14]. The SExtractor catalog obtained by the XDF program revealed about 14140 sources in the full field, of which 7121 galaxies in the deepest part of the image.

[13]The X-ray sensitivity with Chandra varies across the field. For this reason, the HUDF region was chose to coincide with a region of good X-ray sensitivity.
[14]The filters used were, F435W, F606W, F775W, F814W, F850LP, F105W, F125W, F140W and F160W.

Chapter 2

MUSE and ALMA, new horizons for the HUDF

In this chapter we will discuss about the recent observations in the HUDF by means of MUSE (i.e. the Multi-Unit Spectroscopic Explorer) and ALMA (i.e. the Atacama Large Millimeter/submillimeter Array).
In Sec. 2.1 we will present a concise description of the MUSE instrument and an overview on its most recent results obtained from the HUDF imaging (Program ID 094.A-0289, P.I. Bacon; paper in prep.). On the contrary, in Sec. 2.2 we will briefly describe ALMA, giving way to a more detailed characterization of the two HUDF ALMA surveys discussed in this Thesis, i.e. the papers by Dunlop et al. (2016) and Walter et al. (2016).

2.1 The integral field spectroscopy in the HUDF: MUSE

2.1.1 MUSE: the instrument

Designed for the ESO Very Large Telescope (VLT[1]), the Multi-Unit Spectroscopic Explorer (MUSE, see Bacon et al. 2010 and Bacon et al. 2012) is a panoramic integral-field spectrograph located in the Nasmyth B focus of the 8.2 m telescope UT4 (Yepun).
MUSE instrument has been designed and realized by a consortium of 7 major european research institutes: the Centre de Recherche Astrophysique de Lyon (CRAL, France) which is the leading institute guided by the PI Roland Bacon, the European Southern Observatory (ESO), the Leiden Observatory (Sterrewacht Leiden, Netherlands), the Laboratoire d'Astrophysique de Tarbes-Toulouse (LATT, France), the Göttingen Astrophysics Institute (AIG, Germany), the Astrophysics department of the Zurich Polytechnic Institute of Technology (ETH, Switzerland) and the Potsdam Astrophysikalisches Institut (AIP, Germany).
MUSE project started on January 18^{th}, 2005 with the final design reviewed in March 2009. The instrument passed its final acceptance in Europe on September 10^{th}, 2013 and

[1]The VLT telescope facility is located on Cerro Paranal, Atacama Desert, Chile (24° 37′ 38″ S; 70° 24′ 15″ W).

had first light on the VLT on January 31^{th}, 2014.
MUSE has been optimised for studies in the most different fields of astrophysics starting from the formation of galaxies (high redshift Lyman alpha emitters, flouorescent emission and the cosmic web, reionisation, feedback processes and galaxy formation, ultra-deep surveys using strong gravitational lensing, resolved spectroscopy at intermediate redshifts, Sunyaev-Zeldovich effect, late forming population III objects) to studies of nearby galaxies (supermassive black holes, kinematics and stellar populations, interacting galaxies, star formation), stars and resolved stellar populations (early stages of stellar evolution and massive spectroscopy of stellar fields such as the Milky Way, the Magellanic Clouds, the Local Group and beyond), solar system (Galilean satellites, surface heterogeneities of small bodies, temporal changes in the gas of giant planets) and serendipity.
Spectrally MUSE covers the visible range of the electromagnetic spectrum, having a nominal wavelength range from 480 to 930 nm (subsequently extended 465-930 nm) with a mean resolution of 3000. Spatially the instrument samples the sky with $0.2''$ spaxels in the WFM-noAO (Wide Field Mode with natural seeing). MUSE is composed by 24 identical IFU modules that make possible the sampling of a near-contiguos 1 arcmin^2 Field-of-View (FoV).
Technically MUSE can be divided into Fore-Optics (FO) instrumentation, the Split and relay Optics (SRO) and the Integral Field Units (IFUs).
The Fore-Optics reshapes the VLT focus image to adapt it for the SRO subsystem which in turn splits the $60''\times60''$ MUSE FoV (in WFM) in 24 channels ($2.5''\times60''$). The main moving functions implemented in the Fore Optics are the derotation of the Nasmyth Field of view, the selection of the instrumental mode (Wide Field Mode or Narrow Field Mode) by means of the Mode Switching Unit (MSU), the NFM dispersion adjustment thanks to the Atmospheric Dispersion Corrector, and the selection of one of the filter positions from the filter wheel. In addition, an Anamorphoser magnifies the beam in the vertical direction while a NACE CCD is used to implement the Slow Guiding System which aims is to correct for small residual displacement between the telescope and the MUSE focal plane. The Exposure Shutter is located in the Fore Optics as well.
As already mentioned, the SRO system splits the MUSE field-of-view into 24 channels and redirects the light of each channel towards the entrance of an IFU. To this purpose, the SRO is composed of a field-splitter, a field separator, which divides the beams, and 24 relay optics, which correct for the variations in the optical path from one channel to another.
In each one of the 24 IFU units, the $2.5''\times60''$ channel is sliced into 48 mini slits ($0.2''\times15''$) in turn rearranged in a long slit at the entrance of the spectrograph. All the above-described procedure are reproduced by means of an image dissector array, which separates each one of the 24 beam in the 48 slices, a focusing mirror array, which rearranges and aligns the 48 mini slits, and a pupils/slits mask, which reduces scatter light and ghost images before entering the spectrograph. Therefore, the light coming from the 48 mini slits is guided into a spectrograph composed by a collimator, a Volume Phase Holographic Grating (VPHG) and a camera onto which spectra are recorded. The VPH grating achieves a spectral resolution of 1750 at 465 nm to 3750 at 930 nm. The light exiting

Figure 2.1: Footprints of the ten MUSE pointings (Bacon et al., paper in prep.) overlaid onto an *HST* colour image (V_{606}+i_{775}+z_{850}) of the HUDF (Beckwith et al., 2003). The green squares show the 3×3 array (i.e. the UDF01, UDF02, UDF03, UDF04, UDF05, UDF06, UDF07, UDF08 and UDF09 pointings) whereas the magenta one identify the UDF10 pointing, the deepest image of the field (19.5 h of exposure time).

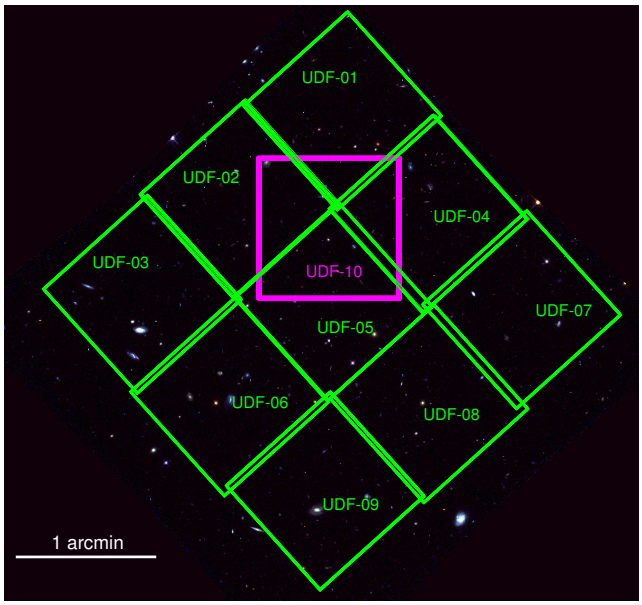

each of the 24 spectrographs is sent onto a $4k \times 4k$, 15 μm pixel CCD, operating at 163 K.

2.1.2 MUSE observations of the HUDF

The HUDF (Beckwith et al., 2003), as previously imaged by the *HST* Advanced Camera for Surveys (ACS), has been the subject of a series of MUSE observations (Program ID 094.A-0289, P.I. Bacon; paper in prep.) which took place between October and December 2014 as part of the facility guaranteed-time program. The HUDF region observed with MUSE has been covered with 10 different pointings: a 3×3 pointing mosaic (UDF01, UDF02, UDF03, UDF04, UDF05, UDF06, UDF07, UDF08 and UDF09) of ≈ 18.2 ks integrations plus a single deep exposure (UDF10) in the center of the field. The footprints of the ten MUSE pointings are shown in Fig. 2.1 (the green squares for the 3×3 array and the magenta one for UDF10), overlaid onto an *HST* colour image (V_{606}+i_{775}+z_{850}) of the HUDF.

According to the MUSE IFU characteristics, the pointings covered the spectral range from 4750 to 9350 Å with a contiguous field of view of $60'' \times 60''$, a spatial sampling of 0.2 arcsec/pixel and a spectral resolution of R=3000 at $\lambda = 7000$ Å.

At the time of our work, not all the 10 MUSE pointings were publicly-availablein the ESO archive but the UDF01, UDF02, UDF05, UDF06 and UDF10 pointings with exposure

time of 6.7h for UDF01; 5.8h for UDF02, UDF05 and UDF06; and finally 19.5h for UDF10.
Even if the starting point of our work were the HUDF ALMA-detections (see Sec. 2.2), these MUSE observations represent the major set of spectroscopic data analyzed and discussed in this Thesis (see Chap. 3, Sec. 3.2).

2.2 The ALMA dusty view of the HUDF

2.2.1 ALMA: the instrument

The Atacama Large Millimeter/submillimeter Array (ALMA), located in the astronomical site of Llano de Chajnantor[2], has been realized by a consortium of international research institutes: the European Southern Observatory (ESO), the US National Science Foundation (NSF), the Japanese National Institutes of Natural Science (NINS), the National Research Council of Canada, the Academia Sinica Insitute of Astronomy & Astrophysics (ASIAA, Taiwan), the Korea Astronomy and Space Science Institute (KASI) in partnership with the Republic of Chile.
Based on the projects of the American Millimiter Array (MMA), the European Large Southern Array (LSA) and the Japanese Large Millimeter Array (LMA), ALMA is composed by 66 antennas operating in the wavelength range from 0.3 to 9.6 mm. Out of the 66 antennas, 54 have the reflector dish with a 12 m diameter while the remaining 12 have a 7 m diameter. Thanks to the large number of antenna dishes, which can be moved across the desert plateau over distances from 150 m to 16 km, ALMA achieves a high sensitivity thanks to interferometric procedures.

2.2.2 Dunlop et al. (2016) observations of the HUDF

In a recent paper, Dunlop et al. (2016) presented the results of one of the first, deep ALMA imaging at $\lambda = 1.3$ mm, covering the full $\simeq 4.5$ arcmin^2 of the HUDF as previously imaged with the WFC3/IR instrument on the *HST*.
The ALMA observations of the HUDF were taken during two separated observing seasons; the first nine Execution Blocks (EBs) were obtained from July to September 2014 while the remaining four in May 2015.[3] Therefore, the HUDF was observed using a 45-pointing mosaic, with each pointing separated by 0.8 times the antenna beamsize.
Using the 45 ALMA pointings mosaic[4], Dunlop et al. obtained an homogeneous image of the HUDF, achieving an rms sensitivity of $\sigma_{1.3\mathrm{mm}} \simeq 35$ μJy at a resolution of $\simeq 0.7''$.
After a rigourous analysis of an initial list of $\simeq 50 > 3.5\sigma_{1.3\mathrm{mm}}$ peaks (i.e. source candidates), 16 objects with flux densities $S_{1.3\mathrm{mm}} > 120$ μJy were confirmed (see Fig. 2.2). All

[2]Atacama desert, Chile (23° 01′ 09″S; 67° 45′ 12″ W) at $\sim$ 5058 m above the sea level.
[3]The amplitude and bandpass calibrator for each EB was the unresolved quasar J0334-401. This quasar was used also as a phase calibrator during the second observing season while in the first EBs was emploied the J0348-2749 quasar.
[4]All data reduction was carried out using the CASA (the Common Astronomy Software Applications package) software (McMullin et al. 2007).

Figure 2.2: The map distribution of the 16 ALMA-detected sources (*empty red circles*) by Dunlop et al. (2016) onto an *HST* colour image (V_{606}+i_{775}+z_{850}) of the HUDF (a zoomed region of about 160 × 160 arcsec).

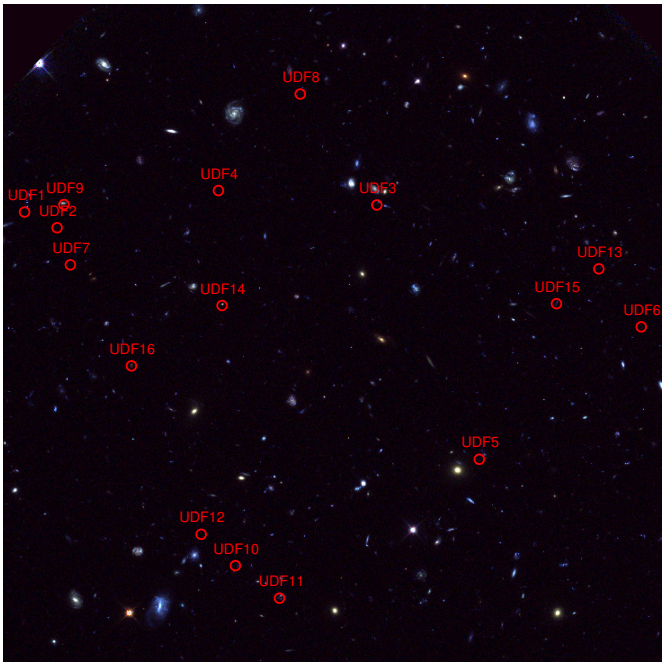

these detected sources showed a secure *HST* galaxy counterparts and 12 are also detected in a new ultra-deep JVLA[5] imaging[6] at 6 GHz. Even if 13 out of the 16 ALMA-detected galaxies had optical-NIR spectroscopic redshifts, to complete the redshift content of their sample, Dunlop et al. estimated the redshifts of the remaining three sources by means of the median value of five different evaluations of the $z_{\rm phot}$, determined on the basis of likewise SED-fitting codes[7]. For the redshift distribution of the 16 ALMA-detected galaxies see Fig. 2.3.

To derive the stellar masses of the sources, Dunlop et al. fitted to the optical-IR photometry of the galaxies the Bruzual and Charlot (2003) evolutionary synthesis models. Dunlop et al. applied the reddening assuming the dust extinction law by Calzetti et al. (2000) and Madau's IGM absorption model (Madau, 1995). It was also assumed a

[5]The Karl G. Jansky Very Large Array.

[6]The new, ultra-deep, JVLA 4-8 GHz survey (PI: Rujopakarn, see Rujopakarn et al. 2016) has been undertaken over the period March 2014 - September 2015 within GOODS-South, with a single pointing (7.2′ primary beam at 6 GHz) centred on the HUDF ($\alpha_{\rm J2000.0} = 03^h\ 32^m\ 38.6^s$, $\delta_{\rm J2000.0} = -27^\circ\ 46'\ 59.83''$). This new JVLA imaging comprises 149, 17 and 11 hours of imaging in the A, B and C configurations respectively. The image obtained has a synthesized beam of 0.31×0.61 ″ (PA= -3.6°) and a rms sensitivity at 6 GHz of $\sigma_{\rm 6GHz} \simeq 0.32$ μJy per beam at the phase centre while $\sigma_{\rm 6GHz} \simeq 0.35$ μJy per beam at the edge of the HUDF.

[7]Dunlop et al. tests of $z_{\rm phot}$ vs. $z_{\rm spec}$ also for the 13 sources with spectroscopic redshifts showed a high-degree of accuracy in the redshift determination. As a matter of fact, the three lasting photometric redshifts carry a typical rms uncertainty of $\delta z \simeq 0.1$.

Figure 2.3: Redshift distribution of the 16 ALMA-detected galaxies in the HUDF from Dunlop et al. (2016). The redshift information consists of 13 spectroscopic redshifts, and three accurate photometric redshifts (figure taken from Fig. 5 in Dunlop et al. 2016)

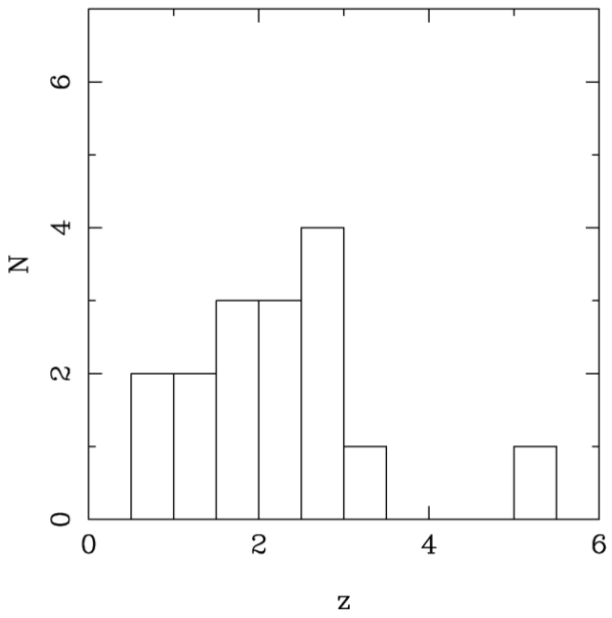

Chabrier IMF (see Chabrier 2003) thus obtaining as a result that all the stellar masses retrieved were *total*, i.e. the mass derives both from still nuclear-burning stars and stellar remnants. Thanks to the high-quality of the multi-wavelength photometry used and of the redshift informations, Dunlop et al. were able to derive various alternative estimates of the SFR for the 16 ALMA-detected galaxies. A first SFR evaluation was made through the absolute magnitude (M_{1500}) of the rest-frame UV emission ($\lambda = 1500$ Å)[8]. This procedure allowed to estimate the unobscured SFR produced by young stars not embedded in their native dusty molecular clouds.
A second SFR estimate was obtained by means of a SED fitting approach. This method allows to retrieve the measurements of the extinction-corrected SFR from the UV-NIR SED besides the corresponding best-fitting values of the dust absorption in the V-band (A_V)[9].
A third SFR measurement, for the dust-enshrouded SFR, was derived from the long-wavelength photometry by means of ALMA data, the deconfused *Herschel* photometry and testing the impact of including or excluding the use of the Spitzer 24-μm photometry. Although this approach retrieve robust dust masses estimates, the inferred SFR strongly depends on the form of the adopted FIR SED template. The best-fitting model SED,

[8]In agreement with Kennicutt and Evans (2012), the adopted calibration means than an absolute magnitude of $M_{1500} = -18.75$ mag corresponds to a SFR$= 1$ $M_\odot$ yr^{-1}.

[9]In the SED fitting process, the extinction was allowed to range up to $A_V = 6$ mag, but the best-fitting values lie in the range 0.2 to 3.1 mag.

Table 2.1: Details of the final sample of 16 ALMA-detected sources in the HUDF (table adapted from Table 2 and Table 4 in Dunlop et al. 2016). Column 1 gives source numbers, while column 2 and 3 give the positions of the ALMA sources as determined from the 1.3-mm map by Dunlop et al. (2016). In column 4 and 5 are retrieved the estimated total flux densities ($S_{1.3\mathrm{mm}}$) and S/N ratio at 1.3 mm, respectively. Column 6 gives the total H_{160} magnitude of each *HST* galaxy counterpart while column 7 lists the redshift for each source (with a dagger, †, at the end of the source name had been highlighted all the objects with a MUSE spectroscopic evaluation of the redshift in Dunlop et al. 2016). Column 8 gives the stellar mass of each galaxy while column 9 then gives the raw UV SFR (SFR_{UV}) based on the uncorrected UV absolute magnitude. Column 10 then gives the best-estimate of extinction, A_V,as derived from the optcial-infrared SED fitting. In columns 11 to 14 are presented alternative measures of SFR, namely: i) the dust-corrected SFR from the infrared-optical SED fitting (SFR_{SED}); ii) and iii) the SFRs derived from fitting the Spitzer-Herschel-ALMA photometry with different templates (SFR_{FIR1} and SFR_{FIR2}; see Dunlop et al. 2016); iiii) the SFR inferred from the radio detections (SFR_{Rad}). Finally, the ratio of the obscured/unobscured SFR in column 15 and in column 16 the estimates of specific star-formation rates. All values given assume a Chabrier (2003) IMF.

id_{Dunlop}	$\alpha_{J2000.0}$ [deg]	$\delta_{J2000.0}$ [deg]	$S_{1.3mm}$ [μJy]	S/N	H_{160} [mag_{AB}]	z	$\log_{10}(M_\star/M_\odot)$	SFR_{UV} [$M_\odot$ yr^{-1}]	A_V [mag]	SFR_{SED} [$M_\odot$ yr^{-1}]	SFR_{FIR1} [$M_\odot$ yr^{-1}]	SFR_{FIR2} [$M_\odot$ yr^{-1}]	SFR_{Rad} [$M_\odot$ yr^{-1}]	SFR_{Obs}/SFR_{UV}	sSFR [Gyr^{-1}]
UDF1	53.18348	-27.77667	924±76	18.37	24.75	3.000	10.7±0.10	0.31±0.05	3.1	399.4	326±83	364±82	439±28	1052±317	6.50±2.24
UDF2	53.18137	-27.77757	996±87	16.82	24.70	2.794	11.1±0.15	0.32±0.10	2.2	50.2	247±76	194±64	242±22	772±339	1.96±0.92
UDF3†	53.16062	-27.77627	863±84	13.99	23.41	2.541	10.3±0.15	4.70±0.30	0.9	42.0	195±69	173±1	400±17	41±15	9.77±4.88
UDF4	53.17090	-27.77544	303±46	6.63	24.85	2.430	10.5±0.15	0.43±0.20	1.6	20.0	94±4	58±5	89±17	219±102	2.97±1.05
UDF5	53.15398	-27.79087	311±49	6.33	23.30	1.759	10.4±0.15	0.20±0.05	2.4	36.1	102±7	67±25	86±6	510±132	4.06±1.46
UDF6†	53.14347	-27.78327	239±49	4.93	22.27	1.411	10.5±0.10	0.10±0.02	2.8	78.0	87±11	66±5	68±5	870±205	2.75±0.73
UDF7	53.18051	-27.77970	231±48	4.92	24.17	2.590	10.6±0.10	0.50±0.03	1.5	16.5	56±22	77±42	617±20	112±45	1.41±0.64
UDF8	53.16559	-27.76990	208±46	4.50	21.75	1.552	11.2±0.15	0.98±0.02	1.6	35.8	149±90	94±37	73±5	152±92	0.94±0.66
UDF9†	53.18092	-27.77624	198±39	4.26	21.41	0.667	10.0±0.10	0.06±0.01	0.9	0.5	23±25	5±2	5±1	383±421	2.30±2.56
UDF10	53.16981	-27.79697	184±46	4.02	23.32	2.086	10.2±0.15	1.14±0.10	1.5	37.0	45±22	34±7	<35	39±20	2.84±1.71
UDF11†	53.16695	-27.79884	186±46	4.02	21.62	1.996	10.8±0.10	6.29±0.20	1.4	162.8	162±94	232±10	172±14	26±15	2.57±1.60
UDF12	53.17203	-27.79517	154±40	3.86	27.00	5.000	9.6±0.15	1.55±0.10	0.2	2.6	37±14	21±7	<100	24±10	9.29±4.80
UDF13	53.14622	-27.77994	174±45	3.85	23.27	2.497	10.8±0.10	0.95±0.05	1.3	18.0	68±18	60±19	142±17	72±19	1.08±0.38
UDF14†	53.17067	-27.78204	160±44	3.67	22.76	0.769	9.7±0.10	0.05±0.01	1.3	1.0	44±17	3±2	<4	880±383	8.78±3.96
UDF15	53.14897	-27.78194	166±46	3.56	23.37	1.721	9.9±0.15	1.14±0.02	1.1	15.5	38±27	25±8	<20	33±24	4.78±3.79
UDF16†	53.17655	-27.78550	155±44	3.51	21.42	1.314	10.9±0.10	0.10±0.05	0.6	0.5	40±18	25±4	38±3	400±269	0.50±0.26

Figure 2.4: The map distribution of the 21 ALMA-detections (*empty yellow circles*) by Walter et al. (2016) onto an *HST* colour image (V_{606}+i_{775}+z_{850}) of the HUDF (a zoomed region of about 80×80 arcsec).

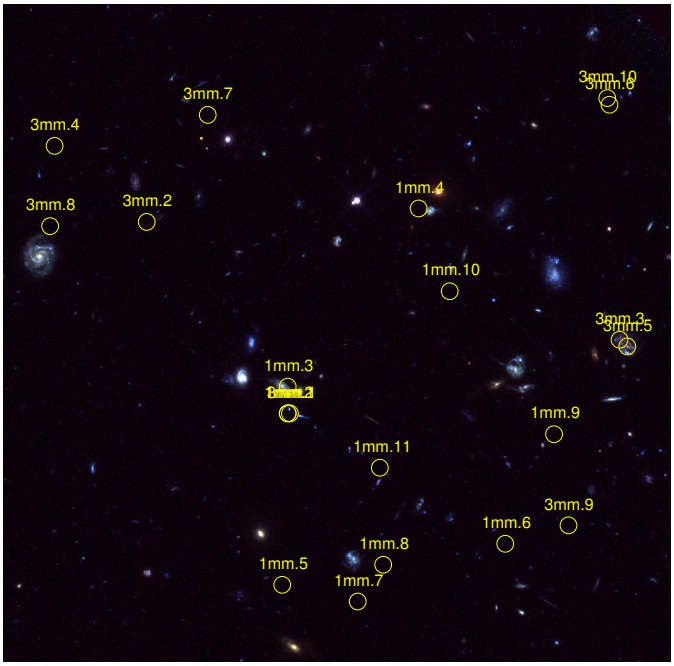

obtained by Dunlop et al. from a combined SED[10], was an AGN+star forming composite model (Kirkpatrick et al. 2015).
A fourth, and final, SFR evaluation was retrieved on the basis of the new JVLA 6 GHz photometry of the ALMA sources. Nevertheless, due to the potential AGN contamination at radio wavelengths, the uncertainty in the precise radio-SFR calibration and the need to adopt a consistent SFR estimator for all the 16 ALMA sources, this radio-based evaluation of the SFR was ignored in Dunlop et al. (2016). The values of all the different SFR mentioned retrived by Dunlop et al. as well as a comparaison with our evaluations are reported in Table 2.1.

2.2.3 Walter et al. (2016) observations of the HUDF

In a recent series of papers, Walter et al. presented a detailed description of ASPECS: The ALMA SPECtroscopic Survey in the HUDF.
ASPECS goal was obtaining an unbiased census of molecular gas and dust continuum emission in galaxies at $z > 0.5$. To this purpose, the observed region ($\sim 1'$) was chosen to overlap the deepest available *HST* imaging within the HUDF, i.e. the so-called UDF12

[10]The combined SED was obtained from the 16-sources photometry after deredshifting and normalizing at $\lambda_0 = 1.3$ mm.

(Ellis et al. 2013) or the eXtremely Deep Field (XDF, Illingworth et al. 2013). ALMA observations of this region were carried out with full frequency scans at 3 mm (band 3, i.e. 84-115 GHz) and at 1 mm (band 6, i.e. 212-272 GHz) with continuum noise levels of 3.8 μJy and 12.7 μJy per beam[11], respectively. These two ALMA bands were selected due to the continuos CO redshift coverage provided at virtually any redshift, with only a tiny gap at $0.6309 < z < 0.6950$. In addition to the CO rotational emission lines, the synergy between the observations at 1 mm and 3 mm allowed also the detection of the [CII] emission line in the redshift range $6.0 < z < 8.0$.
The $\sim 1'$ region was covered with a single pointing ($\alpha_{\rm J2000.0} = 03^h\ 32^m\ 37.90^s$, $\delta_{\rm J2000.0} = -27^\circ\ 46'\ 25.0''$) in band 3 and with a 7-pointings mosaic (centered on the same coordinates as for the 3 mm observations) in band 6. While the 3 mm observations (ALMA Projet ID: 2013.1.00146.S) were carried out between July 1^{st}, 2014 and January 6^{th}, 2015; the 1 mm scans (ALMA Projet ID: 2013.1.00718.S) took place between December 12^{th}, 2014 and April 21^{st}, 2015.

After the data reduction[12], by means of a specifically developed IRAF-based routine which operated directly on the imaged data cubes, Walter et al. searched for line emitting sources. The blind search operated resulted in[13] 10 line candidates from the 3 mm data cubes, and 11 line candidates from the 1 mm search.[14] In Table 2.2 we present the catalog of the line candidates identified by Walter et al. (2016).

[11]The compact array configurations chosen by Walter et al. for band 3 and band 6 (C34-2 and C34-1 configurations, respectively), resulted in a dimension of the beam size equal to $3.6'' \times 2.1''$ (band 3) and $1.7'' \times 0.9''$ (band 6).

[12]The data reduction was carried out using the CASA (the Common Astronomy Software Applications package) software (McMullin et al. 2007) .

[13]Well-defined fidelity constraints were adopted to discard as much as possible all fake peaks (for more details see Walter et al. 2016) besides the search for optical/NIR counterparts by matching the positions of the sources in multi-wavelength catalogs with the line candidates.

[14]For more details on the line candidates identified see the Appendix in Walter et al. 2016.

Table 2.2: Catalogue of the line candidates identified by Walter et al. (2016). In column 1 the id of the line (3mm. if the line has been detected from observations in band 3; 1mm. for detections from the ALMA band 1). In column 2 and 3 the right ascension and declination (J2000.0) for each detection, respectively. In column 4 the central frequency and uncertainty (based on Gaussian fit). Velocity integrated flux and uncertainty are presented in column 5 while in column 6 is reported the line Full Width at Half Maximum, as derived from a Gaussian fit. To conclude, in column 7 the S/N as measured by the line searching algorithm used by Walter et al. (2016).

id_{Walter}	$\alpha_{J2000.0}$ [h:m:s]	$\delta_{J2000.0}$ [deg : arcmin : arcsec]	ν [GHz]	F_ν [Jy km s^{-1}]	FWHM [km s^{-1}]	S/N
3mm.1†	03:32:38.52	-27:46:34.5	97.567±0.003	0.72±0.03	500±30	19.91
3mm.2†	03:32:39.81	-27:46:11.6	90.443±0.003	0.44±0.08	540±30	12.80
3mm.3†	03:32:35.55	-27:46:25.7	96.772±0.003	0.13±0.01	57±30	9.48
3mm.4	03:32:40.64	-27:46:02.5	91.453±0.003	0.23±0.03	73±30	5.86
3mm.5†	03:32:35.48	-27:46:26.5	110.431±0.003	0.18±0.02	82±25	5.42
3mm.6	03:32:35.64	-27:45:57.6	99.265±0.003	0.23±0.02	160±30	5.40
3mm.7	03:32:39.26	-27:45:58.8	100.699±0.003	0.08±0.01	60^{+25}_{-30}	5.40
3mm.8	03:32:40.68	-27:46:12.1	101.130±0.003	0.19±0.01	100^{+25}_{-30}	5.30
3mm.9	03:32:36.01	-27:46:47.9	98.082±0.003	0.09±0.01	64±30	5.28
3mm.10†	03:32:35.66	-27:45:56.8	102.587±0.003	0.24±0.02	120±25	5.18
1mm.1†	03:32:38.54	-27:46:34.5	227.617±0.003	0.79±0.04	463^{+80}_{-10}	18.28
1mm.2†	03:32:38.54	-27:46:34.5	$260.027^{+0.003}_{-0.059}$	1.10±0.05	478^{+11}_{-70}	16.46
1mm.3†	03:32:38.54	-27:46:31.3	225.181±0.003	0.22±0.02	101±18	5.87
1mm.4	03:32:37.36	-27:46:10.0	$258.333^{+0.016}_{-0.003}$	0.27±0.02	150±20	5.62
1mm.5	03:32:38.59	-27:46:55.0	$265.320^{+0.003}_{-0.031}$	0.72±0.03	211^{+37}_{-10}	5.47
1mm.6†	03:32:36.58	-27:46:50.1	222.553±0.003	0.56±0.02	302^{+12}_{-40}	5.45
1mm.7	03:32:37.91	-27:46:57.0	257.042±0.003	1.78±0.03	179±11	5.43
1mm.8	03:32:37.68	-27:46:52.6	$222.224^{+0.022}_{-0.003}$	0.39±0.02	210^{+30}_{-12}	5.33
1mm.9	03:32:36.14	-27:46:37.0	$249.085^{+0.016}_{-0.003}$	0.34±0.02	150±20	5.19
1mm.10	03:32:37.08	-27:46:19.9	237.133±0.003	0.49±0.04	281^{+48}_{-12}	5.18
1mm.11	03:32:37.71	-27:46:41.0	$223.067^{+0.003}_{-0.025}$	0.27±0.02	169^{+35}_{-12}	5.16

Figure 2.5: Footprints of the three HUDF surveys used in this Thesis, overlaid onto an *HST* colour image (V_{606}+i_{775}+z_{850}) of the HUDF (Beckwith et al., 2003). In green the 3×3 array (i.e. the UDF01, UDF02, UDF03, UDF04, UDF05, UDF06, UDF07, UDF08 and UDF09 pointings) from the MUSE survey (Bacon et al., paper in prep.) while the magenta square identify the UDF10 pointing, the deepest MUSE image of the field (19.5 h of exposure time). In red and yellow the ALMA surveys by Dunlop et al. (2016) and Walter et al. (2016), respectively.

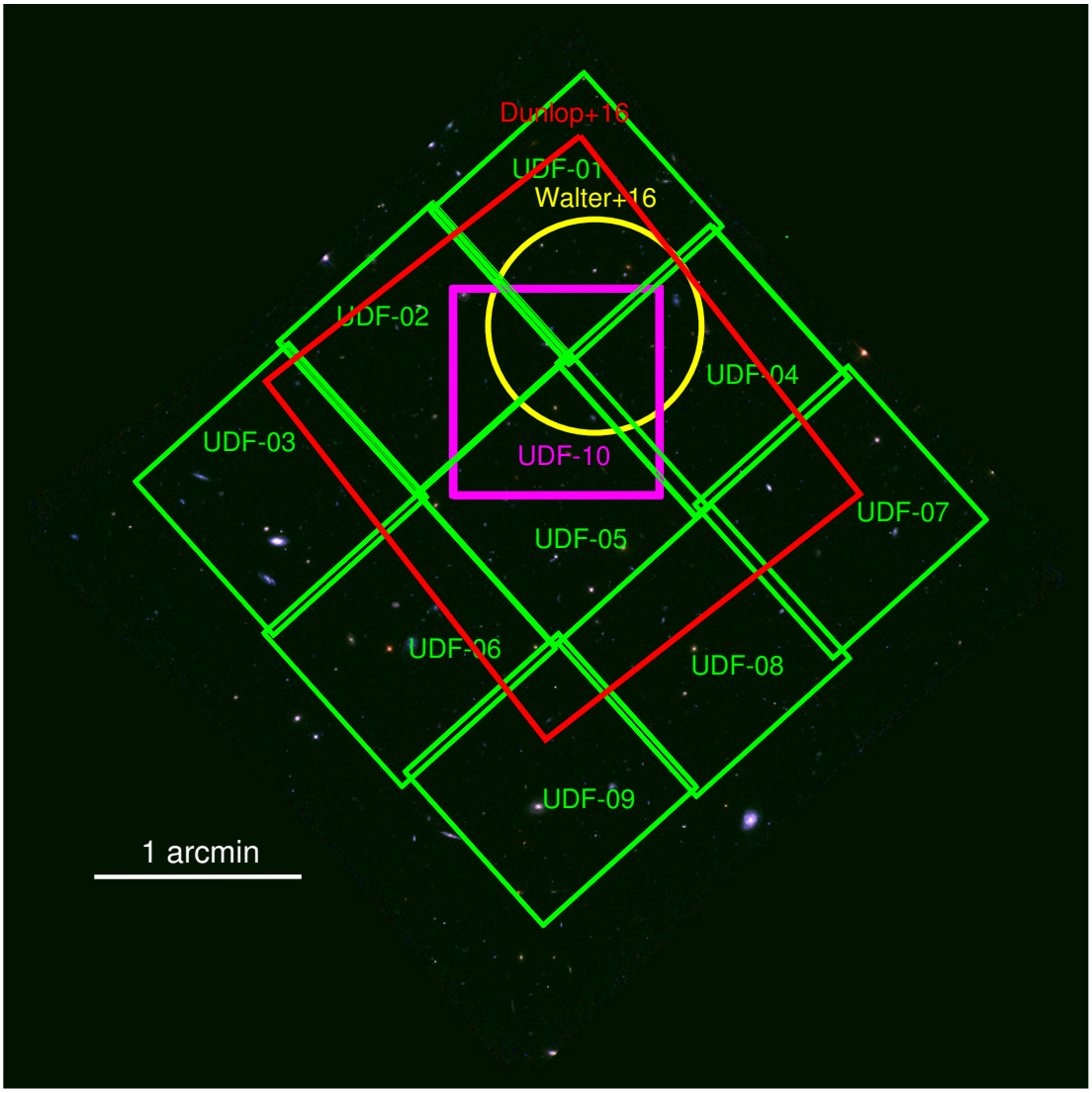

Chapter 3

MUSE optical spectra of dusty ALMA sources

In this chapter we present our spectroscopic investigation of ALMA-detected sources (presented in recent papers by Dunlop et al. (2016) and Walter et al. (2016), see Chap. 2) on the MUSE data cubes in the HUDF. We also report on the analysis of a comparison sample selected from the photometric catalog presented by Coe et al. (2006), requiring an H-band detection to ensure a reliable stellar mass measurement.
While for the extraction of the spectra from the MUSE data cubes we resorted to a Python script, the analysis of the spectral features was done by means of the EZ code (Garilli et al. 2010; for more details see Appendix A).

3.1 Analysis of the ALMA detections in the HUDF

The first step of our work has been the detection of the optical counterparts of the ALMA-detected sources (Dunlop et al. 2016 and Walter et al. 2016) from the investigation of the new HUDF MUSE survey (see Chap. 2, Sec. 2.1.2). In particular, we extracted the 1-D spectra from the MUSE data cubes at the sky-coordinates presented in Dunlop et al. (2016) and Walter et al. (2016). We had the possibility to access fully reduced MUSE data cubes through a collaboration with the University of Ferrara (in particular the group leaded by Prof. Piero Rosati), especially for the UDF01, UDF02, UDF05, UDF06 and UDF10 pointings that were already publicly available in the ESO raw data archive. To process the raw calibration and science exposures of each single night of observations and to combine the data into the final data cubes, the data reduction was carried out by means of the MUSE pipeline[1] version 1.2.1. During this process all the standard calibration procedures (bias and flat field corrections, wavelength and flux calibration, etc...) provided by the pipeline were applied. Even though different configurations of the MUSE pipeline settings were checked to improve the quality of the final cubes,

[1]Freely downloadable at `http://www.eso.org/sci/software/pipelines/` .

particularly the sky subtraction, no significant differences were recorded. The final WCS adjustment was made matching compact sources detected with SExtractor (Bertin and Arnouts, 1996) in the broad-band images of the final data-cubes with the corresponding objects in the HUDF catalog for the filter F606W. As a final post-processing step to minimize the sky residuals, the Zurich Atmosphere Purge (ZAP, Soto et al. 2016) tool was applied using SExtractor segmentation maps to define sky regions. After applying the ZAP tool, an overall improvement was achieved in the sky subtraction even though artefacts in the background at specific wavelengths still remained.
The final data cubes have a spatial pixel scale of $0.2''$, a spectral coverage from 4750 Å to 9350 Å with a dispersion of 1.25 Å/pixel and a fairly constant spectral resolution of ≈ 2.4 Å over the entire spectral range.

3.1.1 Dunlop et al. (2016) detections

The first catalog of ALMA-detected sources we analyzed was the one presented by Dunlop et al. (2016). Because of the non-availability of the UDF03, UDF04, UDF07, UDF08, UDF09 MUSE pointings, not all the objects detected by Dunlop et al. (see Table 2.1) were accessible. As a matter of fact, the UDF6 ($\alpha_{\rm J2000.0} = 53.14347°$, $\delta_{\rm J2000.0} = -27.78327°$), UDF13 ($\alpha_{\rm J2000.0} = 53.14622°$, $\delta_{\rm J2000.0} = -27.77994°$), UDF15 ($\alpha_{\rm J2000.0} = 53.14897°$, $\delta_{\rm J2000.0} = -27.78194°$) and UDF16 ($\alpha_{\rm J2000.0} = 53.17655°$, $\delta_{\rm J2000.0} = -27.78550°$) sources were out of the MUSE data cubes at our disposal. Hence our starting sample of 12 ALMA-detected objects from Dunlop et al. (2016) includes the UDF1, UDF2, UDF3, UDF4, UDF5, UDF7, UDF8, UDF9, UDF10, UDF11, UDF12 and UDF14 galaxies (see Table 2.1).
Therefore, after the definition of our starting sample, we evaluated the spectroscopic redshift for each object. Nevertheless, before the extraction of the spectra from the cubes, it was necessary to determine for each object which pointing was the most suitable. To this aim, it is worth to recall that the S/N ratio of the sources is proportional to the image exposure time. For the available data cubes the exposure time is of 6.7h for UDF01; 5.8h for UDF02, UDF05 and UDF06; and finally 19.5h for UDF10. So in principle, when the same source is present in more than one image, it is better to extract the spectra from the deepest data cube. At the same time it is also fundamental to avoid border effects. Hence, for each object, we determined the best HUDF pointing on the basis of its sky-coordinates (see Table 3.1).

After the accomplishment of an initial analysis on the image position of our sample of galaxies, we extracted the spectra from the data cubes thanks to a Python script. Giving into a single command-line the name of the data cube to adopt and a list file in which were stored the name of the sources, their celestial coordinates and the dimensions (in arcseconds) of the spaxel apertures within which to integrate the flux, the script returns for each object two files: the spectrum and its variance (σ^2). In the spectrum file, for each value of the wavelength (in Å) the script returns the corresponding measure of the flux (in 10^{-20} erg cm^{-2} s^{-1} Å^{-1} units) while in the variance file the code retrieves the mean value of the σ^2 (always in 10^{-20} erg cm^{-2} s^{-1} Å^{-1} units). Both the spectrum flux and the variance are calculated over the input spaxel aperture. In that respect, in our

Table 3.1: Selected MUSE pointings (column 4) for the extraction of the optical counterpart spectra for the 16 ALMA-detected sources by Dunlop et al. (2016) (column 1). In column 2 and 3 we report the sky-coordinates of the ALMA sources as determined from the 1.3-mm map by Dunlop et al. (2016).

id_{Dunlop}	$\alpha_{J2000.0}$ [deg]	$\delta_{J2000.0}$ [deg]	MUSE pointing
UDF1	53.18348	-27.77667	UDF02
UDF2	53.18137	-27.77757	UDF02
UDF3	53.16062	-27.77627	UDF10
UDF4	53.17090	-27.77544	UDF02
UDF5	53.15398	-27.79087	UDF05
UDF7	53.18051	-27.77970	UDF02
UDF8	53.16559	-27.76990	UDF01
UDF9	53.18092	-27.77624	UDF02
UDF10	53.16981	-27.79697	UDF06
UDF11	53.16695	-27.79884	UDF06
UDF12	53.17203	-27.79517	UDF06
UDF14	53.17067	-27.78204	UDF10

Table 3.2: Spectroscopic redshifts retrieved by Dunlop et al. (2016) (z_{Dunlop}) and this work (z_{IANI}) for the three ALMA-detected sources UDF9, UDF11, UDF14 with a clear MUSE spectroscopic counterpart in the HUDF.

id_{Dunlop}	z_{Dunlop}	z_{IANI}
UDF9	0.667	0.6675
UDF11	1.996	1.9976
UDF14	0.769	0.7666

Figure 3.1: *HST* colour (V_{606}+i_{775}+z_{850}) images of the ALMA-detected galaxies (from Dunlop et al. 2016) UDF9, UDF11 and UDF14. The red circles, centered in the sky-coordinates of the ALMA detections (Table 2 from Dunlop et al. 2016), have a 1″ radius and mark the image region within which we extracted the spectra from the MUSE datacubes.

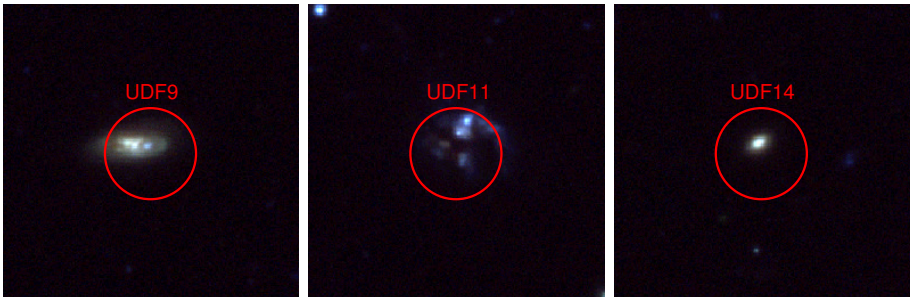

study we extracted the spectra within circular apertures having a radius of $1''$.
So, after the extraction of all the spectra from the MUSE data cubes, we started the EZ analysis.[2] At this regard, before using the EZ tool to determine the spectroscopic redshifts of the ALMA-detected sources, to acquire a good degree of expertise in the software use, we did a training on a sample of sources extracted from the Hubble Frontier Field (HFF) MACS J0416.1-2403. The spectroscopic redshifts obtained for each galaxy in the sample were compared with the measurements retrieved by Caminha et al. (2016b). For the analysis of the results obtained, we refer the reader to Appendix A, Sec. A.2.2.
Out of the 12 sources detected by Dunlop et al. (2016) and available for our study, we succeeded in obtaining a spectroscopic redshift measurement for only three sources: UDF9, UDF11 and UDF14. The RGB optical cutout (V_{606}+i_{775}+z_{850}) of UDF9, UDF11 and UDF14 are presented in Fig. 3.1 along with the $1''$ radius region, centered at the ALMA sky-coordinates of the detections, within which the Python script extracted the spectra. For these objects, in Table 3.2 are reported both the spectroscopic redshift obtained by Dunlop et al. (2016) and ours. Clearly, the differences between the z estimates are on the order of 0.003, or less, thus showing a good-agreement between these two works.
In Fig. 3.2 and Fig. 3.3 we present the MUSE spectrum, its variance and the principal observed lines for the UDF9, UDF11 and UDF14 galaxies.

3.1.2 Walter et al. (2016) detections

In addition to Dunlop et al. sources, we decided to extend our sample of ALMA detected galaxies taking into account also the data presented in a recent series of papers by Walter et al. (2016).
At this regard, in Table 2.2 we have presented the ALMA measured fluxes and S/N ratios for the 21 sources identified in Walter et al. (2016).
Fig. 2.4 shows the sky-positions of all the 21 ALMA sources retrieved by Walter et al. onto an *HST* colour image (V_{606}+i_{775}+z_{850}) of the HUDF.
Following the same analysis procedure adopted for the ALMA detections by Dunlop et al. (2016) (see Sec. 3.1.1), in Table 3.3 we have reported for each one of the galaxies detected by Walter et al. (2016) the corresponding best MUSE pointing. Also in this case, some of the sources fall into one of the not yet available MUSE pointings (i.e. UDF04) thus making impossible any analysis of their optical spectra. For this reason the total number of sources for which we were able to extract the spectrum shrinked from 21 to 17.
Also in this case, we extracted the spectra at the sources sky-coordinates (Walter et al., 2016) with a spaxel-radius aperture of $1''$. Nevertheless, after the analysis of the spectra by means of the EZ tool, we ended up with no redshift measurements. For most of the objects, this result was the direct consequence of a low MUSE S/N ratio, probably due to their high redshifts.
Therefore, even if we tried to increase our poor sample of ALMA-detected galaxies in the HUDF (i.e.UDF9, UDF11 and UDF14) by means of the detections in Walter et al.

[2]For more details on the EZ tool, see Appendix A.

Figure 3.2: MUSE spectra (top panel) and respective variance (bottom panel) for the ALMA-detected sources UDF9, UDF11 and UDF14 (Dunlop et al., 2016). In the **top panel** a smoothed MUSE spectrum (*green solid line*) is over-plotted onto the spectrum extracted from the MUSE data cubes. The smoothed spectrum has been obtained as a result of the convolution between the original spectrum and a box function. When present, the vertical orange solid lines show the position of the main absorption/emission lines in the spectrum (i.e. [OII], CaII(H), CaII(K), H_δ, H_β, O[III](db-1/3) and O[III](db-1)). The measured spectroscopic redshift of the source and an *HST* RGB (B_{435}+V_{606}+z_{850}) $10''$ image of the galaxy are reported.

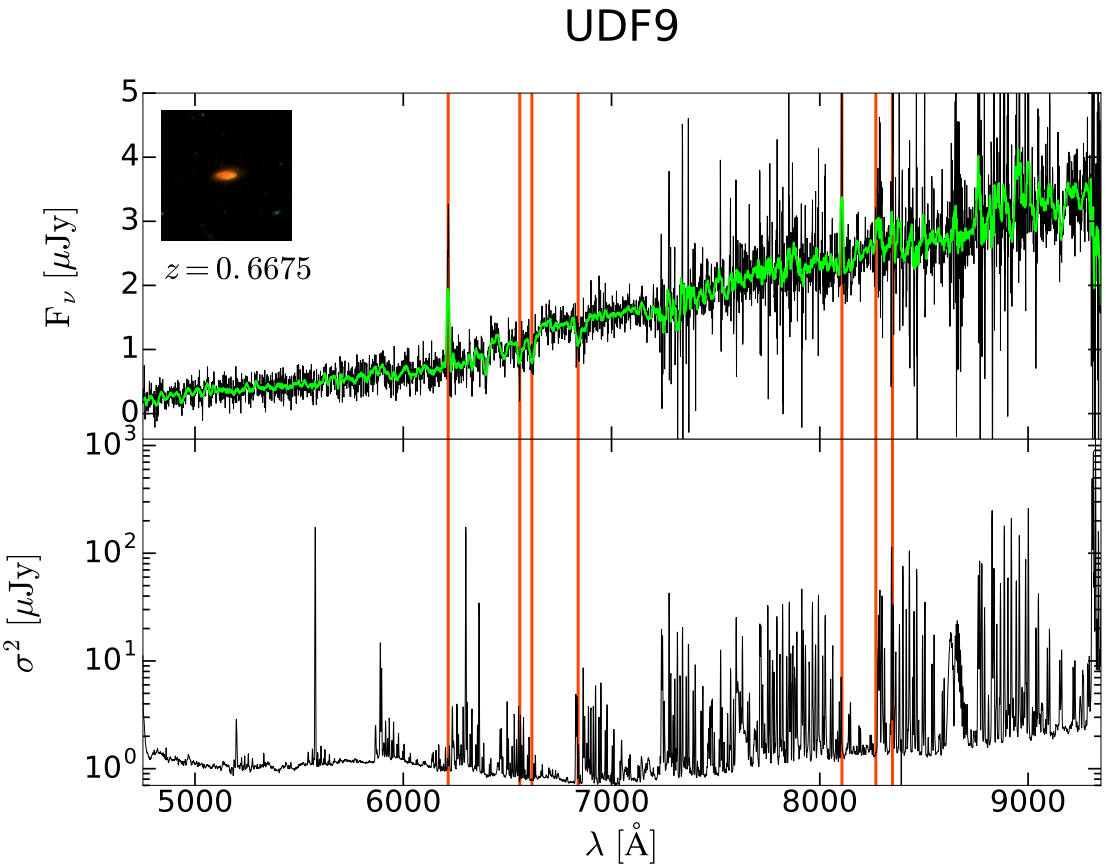

Figure 3.3: continuing Fig. 3.2

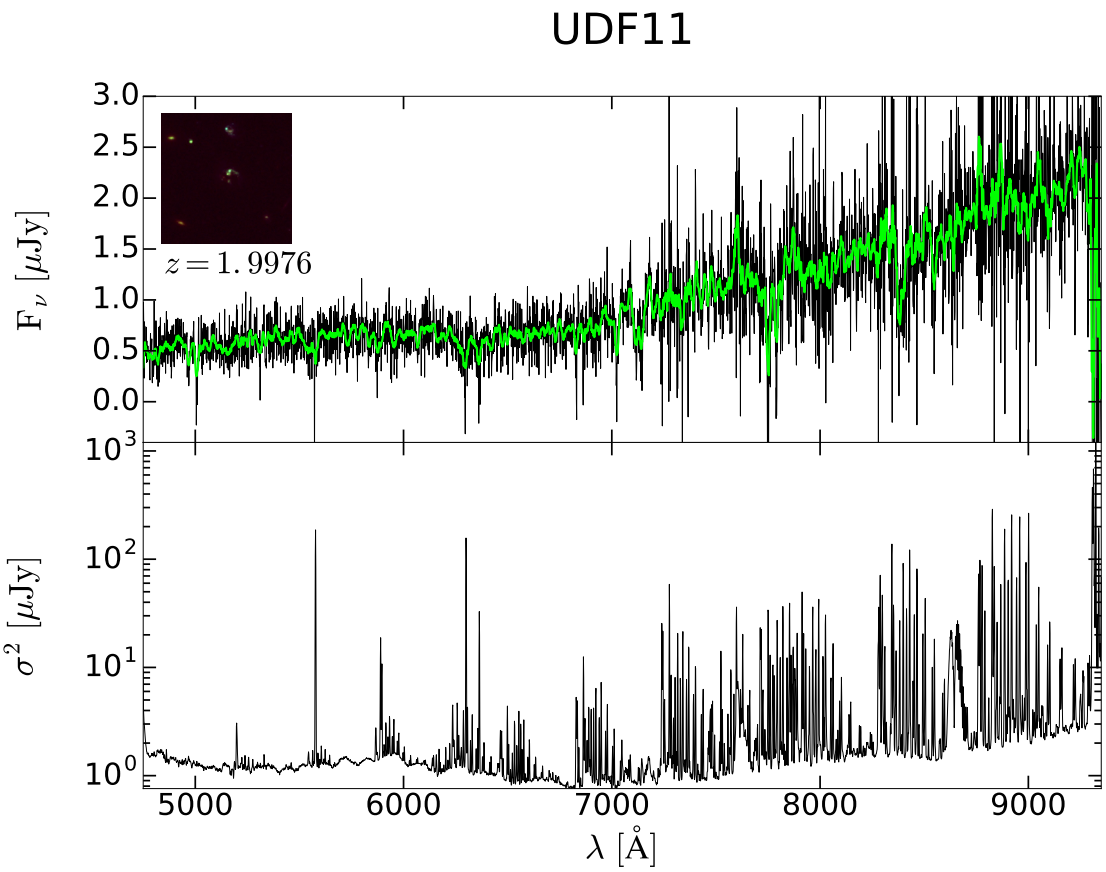

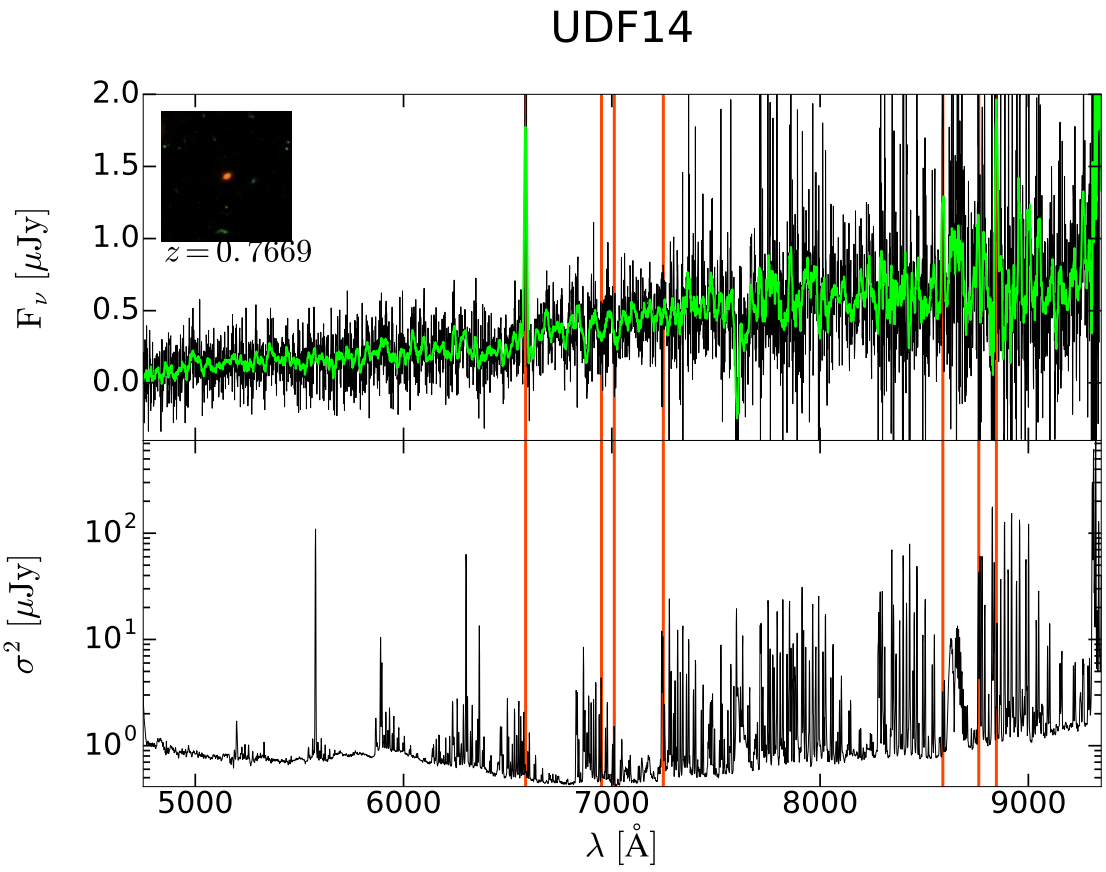

Table 3.3: Selected MUSE pointings (column 4) for the extraction of the optical counterpart spectra for the 21 ALMA line candidates sources by Walter et al. (2016) (column 1). In column 2 and 3 the sky-coordinates of the ALMA sources as determined by Walter et al. (2016).

id_{Walter}	$\alpha_{J2000.0}$ [h:m:s]	$\delta_{J2000.0}$ [deg : arcmin : arcsec]	MUSE pointing
3mm.1	03:32:38.52	-27:46:34.5	UDF10
3mm.2	03:32:39.81	-27:46:11.6	UDF01
3mm.3	03:32:35.55	-27:46:25.7	UDF04
3mm.4	03:32:40.64	-27:46:02.5	UDF01
3mm.5	03:32:35.48	-27:46:26.5	UDF04
3mm.6	03:32:35.64	-27:45:57.6	UDF01
3mm.7	03:32:39.26	-27:45:58.8	UDF01
3mm.8	03:32:40.68	-27:46:12.1	UDF02
3mm.9	03:32:36.01	-27:46:47.9	UDF04
3mm.10	03:32:35.66	-27:45:56.8	UDF01
1mm.1	03:32:38.54	-27:46:34.5	UDF10
1mm.2	03:32:38.54	-27:46:34.5	UDF10
1mm.3	03:32:38.54	-27:46:31.3	UDF10
1mm.4	03:32:37.36	-27:46:10.0	UDF01
1mm.5	03:32:38.59	-27:46:55.0	UDF10
1mm.6	03:32:36.58	-27:46:50.1	UDF10
1mm.7	03:32:37.91	-27:46:57.0	UDF10
1mm.8	03:32:37.68	-27:46:52.6	UDF10
1mm.9	03:32:36.14	-27:46:37.0	UDF04
1mm.10	03:32:37.08	-27:46:19.9	UDF10
1mm.11	03:32:37.71	-27:46:41.0	UDF10

(2016), we failed.

3.2 MUSE spectra extractions and analysis

After the spectral analysis of the sources detected with ALMA in the HUDF, we decided to study their statistical properties.
To do so, we selected a comparison sample of *HST*-detected sources from Coe et al. (2006) with redshift comparables with those of UDF9, UDF11 and UDF14. To this aim we defined two redshift ranges: the first from 0.5 to 0.8 and the second one from 1.5 to 2.5. The redshift cut was made possible since in the catalog by Coe et al. (2006)[3] the Bayesian photometric redshift[4] (z_b) of the sources is presented as well as the B, V, i′, z′, J, H photometry[5].
So, based on the sources sky-coordinates and their z_b parameter, we extracted the two different samples of galaxies (for $0.5 < z_b < 0.8$ and $1.5 < z_b < 2.5$) considering only the sources within the UDF10 MUSE pointing.[6] The total number of sources obtained was 1803.
In addition to these criteria, we decided to consider only the objects with a detection in the H band, thus reducing our sample to 220. This condition restricts our analysis to a well controlled sample, where the near-IR detection guarantees the measurements of secure stellar masses.
In Fig. 3.4 we present the photometric redshift distribution of the sources collected from Coe et al. (2006) with celestial coordinates within the UDF10 pointing (*grey solid line*). The photometric redshift distribution of the subsample with a H-band detection (*orange solid line*) is presented as well, while the green shadowed regions show the two photometric redshift cut adopted in this work.
After a further removal of the sources too close to the edges of the frame, we ended up with 197 galaxies of which 52 in the lower redshift cut (i.e. $0.5 < z_b < 0.8$) and 145 in the higher z_b-range (i.e. $1.5 < z_b < 2.5$).
In Fig. 3.5 we report the H-band magnitude distribution of all the 197 HUDF sources: the green solid line representing the galaxies in the lower z_b-cut whereas the grey solid line for the objects at higher redshifts.
Following the same procedure adopted for the analysis of the ALMA-detected sources (see Sec. 3.1.1 and Sec. 3.1.2), we used the Python script to obtain all the spectra. In this case, the spectra were extracted from the UDF10 data cube with a spaxel-radius

[3]The catalog sums up the results obtained from the ACS images by Beckwith et al. (2003) and the NIC3 image reductions and catalog by Thompson et al. (2004, unpublished).

[4]The Bayesian photometric redshifts were obtained by means of the BPZ tool (see Benítez et al. 2004). For each galaxy, the BPZ code returned an entire probability distribution $P(z)$. The value of the photometric redshift corresponding to the peak of the BPZ distribution $P(z)$ at the 95% confidence interval was defined by Coe et al. as z_b.

[5]The *HST* filters used in Coe et al. (2006) were the B(F435W), V(F606W), i′(F775W), z′(F850LP) ACS filters and the J(F110W), H(F160W) filters from NIC3.

[6] The UDF10 MUSE pointing has sky-coordinates $\alpha_{\rm J2000.0} \simeq 03^h\ 32^m\ 36.28^s \div 03^h\ 32^m\ 41.13^s$, $\delta_{\rm J2000.0} \simeq -27^\circ\ 47'\ 16.1'' \div -27^\circ\ 46'\ 11.9''$

Figure 3.4: Photometric redshift distribution of the HUDF sources presented in Coe et al. (2006) with sky-coordinates within the UDF10 MUSE pointing (Bacon et al., paper in prep.). The solid grey line shows the redshift distribution of all the sources in Coe et al. (2006) with sky-coordinates within the UDF10 MUSE pointing while the solid orange line marks the redshift distribution for the sources with also a detection in the H band (F160W filter). The two green shadowed regions highlight the photometric redshift (z_b) cut adopted in this work: $0.5 < z_b < 0.8$ and $1.5 < z_b < 2.5$.

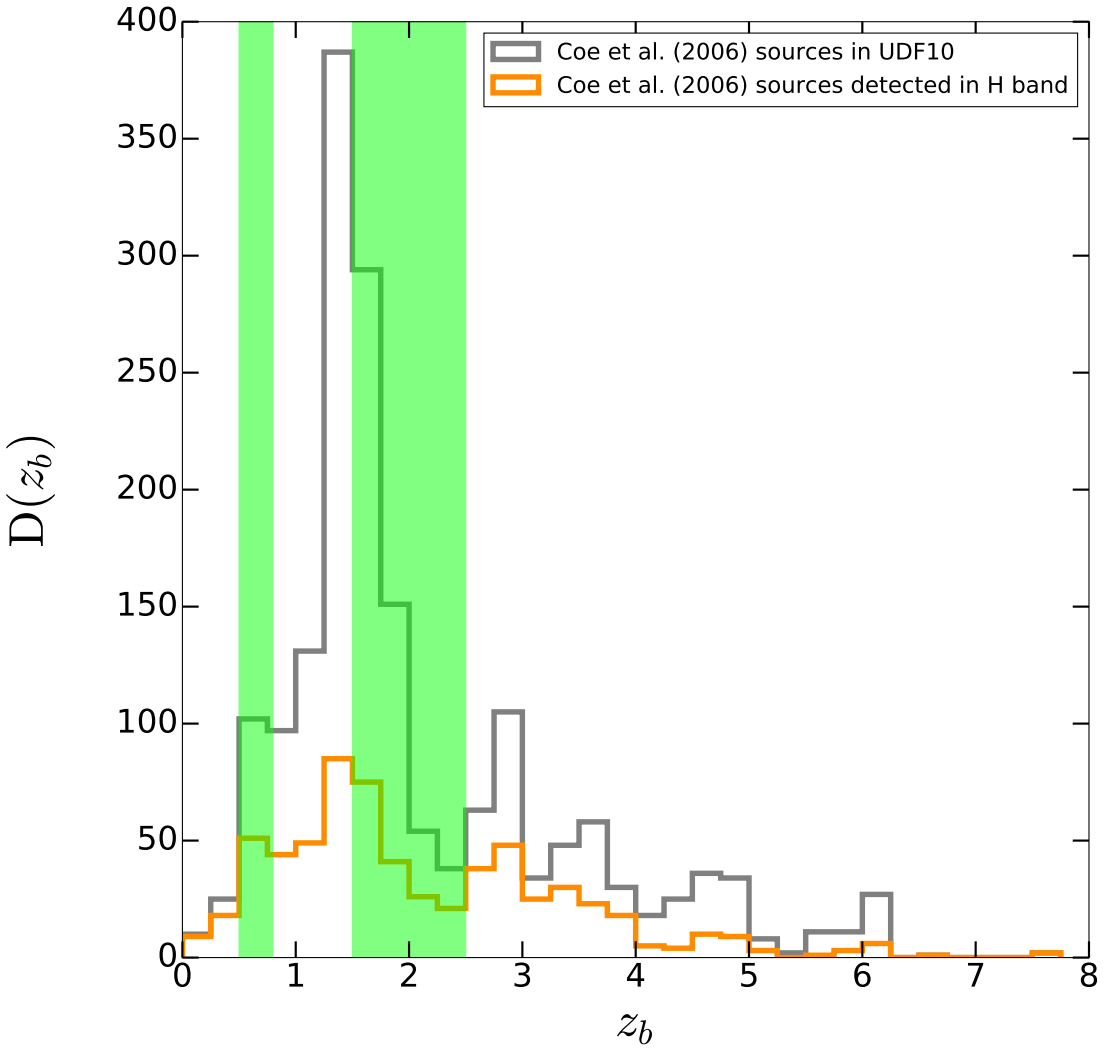

Figure 3.5: H-band magnitude (m_H) distribution of the 197 HUDF sources retrieved from Coe et al. (2006) with sky-coordinates in the UDF10 MUSE pointing. The distribution of the 52 sources with $0.5 < z_b < 0.8$ is shown with a solid green line whereas a grey solid line has been adopted to mark the distribution of the 145 galaxies with $1.5 < z_b < 2.5$.

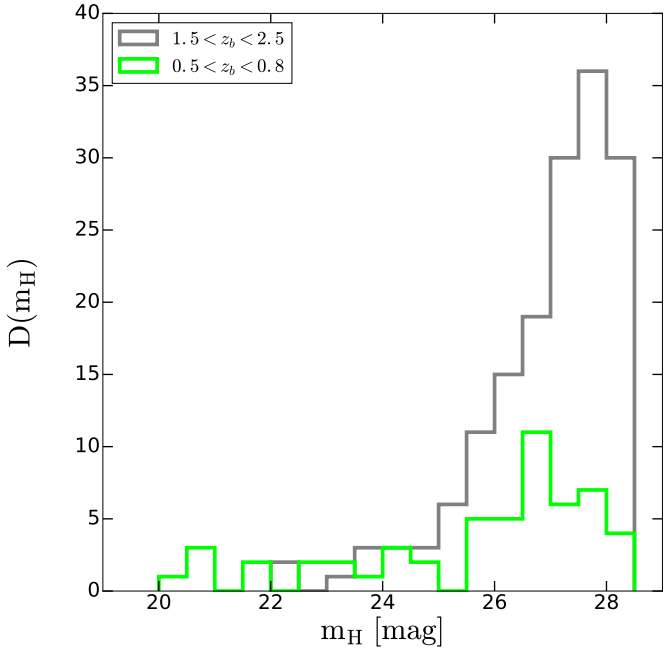

aperture of 1″ at the sky-coordinates given in Coe et al. (2006). Hence, with the EZ tool we looked into each spectrum to search for distinguishing features to estimate their spectroscopic redshift.

While for objects with $0.5 < z_b < 0.8$ we obtained the spectroscopic redshift for 21 sources out of 52, in the range $1.5 < z_b < 2.5$ we succeeded in the determination of only 3 spectroscopic redshifts out of 145. This extremely poor result is not surprising at all; as a matter of fact, in the redshift range studied, i.e. the so-called *redshift desert*, optical spectra are characterized by the complete absence of important emission lines.[7]

In addition to this fact, the low S/N ratio of the majority of the spectra explains the extremely low number of galaxies for which we were able to obtain a spectroscopic redshift.

In Table 3.4 we present the spectroscopic redshift obtained ($z_{\rm IANI}$) and their quality flag ($qf_{\rm IANI}$) for this final subsample of 24 HUDF sources. For consistency with our collaborators, for the assignement of the quality flags, we decided to adopt the scheme described in Caminha et al. (2016a) and Balestra et al. (2016), i.e. 3=secure, 2=likely, 1=not-reliable and 9=based on a single emission line.

The data presented in Table 3.4 are graphically reported in Fig. 3.6, a plot in which we

[7]Emission lines such as the Ly$_\alpha$ (λ_0 = 1215.7 Å), [OII] (λ_0 = 3272.5 Å), H$_\beta$ (λ_0 = 4861.3 Å), [OIII](db−1/3) (λ_0 = 4958.9 Å) and [OIII](db−1) (λ_0 = 5006.8 Å).

present on the y-axis our estimates of the spectroscopic redshifts while on the x-axis the values of the photometric measurements and errorbars obtained by Coe et al. (2006) (z_b). In the plot, thanks to the use of a colour code, we pointed out our quality flags, i.e. 3=green, 2=blue, 1=red and 9=yellow.
From Fig. 3.6 it appears clear that for the majority of the sources, our redshift evaluations ($z_{\rm IANI}$) are in good agreement with the photometric measurements (z_b): only 4 sources (i.e. 6433, 7382, 8084 and 8625) out of 24 show a $|\Delta z/(1+z_b)| > 0.2$ while among the remaining 20 sources, 2 have $0.05 < |\Delta z/(1+z_b)| < 0.2$ and 18 present $|\Delta z/(1+z_b)| < 0.05$.
Nonetheless, before running the softwares that allowed us to obtain the results presented in this work (see Chap. 4), from an analysis of the sky-coordinates of the sources considered, we noticed a good match between the coordinates of UDF14 (sample from Dunlop et al. 2016) and the right-ascension and declination of 7121 (sample from Coe et al. 2006). As a matter of fact, also the spectroscopic redshift were in almost a perfect agreement: while for UDF14 we obtained $z = 0.7666$ for 7121 we evaluated $z = 0.7669$. This fact allowed us to conclude that we were looking at the same source. Therefore, in the following steps of our work we did not consider anymore the 7121 source but we referred only to UDF14. In addition, considering the low number of galaxies with a spectroscopic redshift measurement in the range $1.5 < z_b < 2.5$, we decided to confine our study just to the sources with $0.5 < z_b < 0.8$.
In conclusion, we ended up with a final subsample of 22 HUDF galaxies, out of which two were the ALMA-detected sources UDF9 and UDF14 (Dunlop et al., 2016), while the remaining 20 were *HST*-detected sources from Coe et al. (2006). This sample represents the ideal set to perform an analysis of the whole Spectral Energy Distributions (SED, see Chap. 4).
At this regard, similarly to Fig. 3.2 and Fig. 3.3, in Fig. 3.7, and above, we present the MUSE spectra for all the sources in Coe et al. (2006) within our final sample.

Table 3.4: Comparison between the photometric redshifts (z_b) in Coe et al. (2006) and the spectroscopic redshifts ($z_{\rm IANI}$) measured in this work for all the 24 sources in Coe et al. (2006) of which we were able to extract the MUSE spectra thus retrieving an estimate of the redshift. Column 1 gives the source number ($\rm id_{Coe}$, from Coe et al. 2006), while column 2 and 3 give their sky-positions ($\alpha_{\rm J2000.0}$, $\delta_{\rm J2000.0}$) in Coe et al. (2006). In column 3 is reported the photometric redshift of each source (z_b) while in column 4 and 5 their spectroscopic redshift ($z_{\rm IANI}$, this work) and the quality flag of the measurement ($\rm qf_{IANI}$), respectively. The adopted quality flag scheme is described in Caminha et al. (2016a) and Balestra et al. (2016).

$\rm id_{Coe}$	$\alpha_{\rm J2000.0}$ [deg]	$\delta_{\rm J2000.0}$ [deg]	z_b	$z_{\rm IANI}$	$\rm qf_{IANI}$
6853	53.15183640	-27.78286362	0.703±0.200	0.8438	3
7071	53.15186310	-27.78195763	0.731±0.204	0.8940	2
8275	53.15205765	-27.77471733	0.705±0.201	0.7651	3
6953	53.15278625	-27.78269577	0.744±0.205	0.7655	3
7382	53.15341949	-27.78104782	1.996±0.352	3.4724	9
7664	53.15398026	-27.77099228	0.761±0.207	0.8325	3
7526	53.15450668	-27.77972603	2.226±0.379	1.8495	1
6945	53.15462494	-27.78359604	$0.623^{+3.999}_{-0.191}$	1.0011	1
7432	53.15566635	-27.77927971	1.659±0.313	1.8450	2
6038	53.15722656	-27.78526688	0.644±0.193	0.6671	3
8624	53.15746307	-27.77644920	0.780±0.209	0.8321	2
6974	53.15818787	-27.78109169	0.660±0.195	0.6198	3
8316	53.16015244	-27.77552986	0.675±0.197	0.6221	3
8257	53.16078568	-27.77544975	0.621±0.191	0.6217	3
7046	53.16096115	-27.78285217	0.558±0.183	0.6182	2
6747	53.16163254	-27.78025436	0.560±0.183	0.6211	3
7678	53.16246414	-27.77091789	0.707±0.201	1.0382	1
8265	53.16426849	-27.77409363	$0.680^{+3.793}_{-0.198}$	4.8200	9
6685	53.16578293	-27.78460884	0.668±0.196	0.7005	9
6433	53.16603851	-27.78560448	0.787±0.210	5.4700	2
6008	53.16608047	-27.78686714	0.502±0.177	0.5440	1
8084	53.16765976	-27.77315903	0.593±0.187	1.2710	2
41030	53.16839600	-27.77810669	$0.582^{+2.979}_{-0.368}$	0.6291	1
7121	53.17069244	-27.78197289	0.775±0.209	0.7669	2

Figure 3.6: Measured spectroscopic redshifts ($z_{\rm IANI}$, this work) vs. photometric redshifts (z_b, Coe et al. 2006) for the 24 galaxies (21 with $0.5 < z_b < 0.8$ and 3 with $1.5 < z_b < 2.5$) in our initial sample. The black dashed lines represents the limiting values within which there is a good correspondance between spectroscopic and photometric redshifts (i.e. $\Delta z/(1+z_b) = \pm 0.2$). The colour code adopted shows the likelihood of our measurements, with the red circles corresponding to $\rm qf_{IANI} = 1$, the blue ones to $\rm qf_{IANI} = 2$, the green ones to $\rm qf_{IANI} = 3$ and finally the yellow ones to $\rm qf_{IANI} = 9$. The quality flag scheme adopted is the one from Caminha et al. (2016a) and (Balestra et al., 2016), i.e. 3=secure, 2=likely, 1=not-reliable and 9=based on a single emission line. Histograms on the redshift distribution of the sources (for z_b and $z_{\rm IANI}$) are reported too. In grey the cumulative redshift distributions of the measurements, while in red, blue, green and yellow the sources redshift distributions according to the above-described colour code.

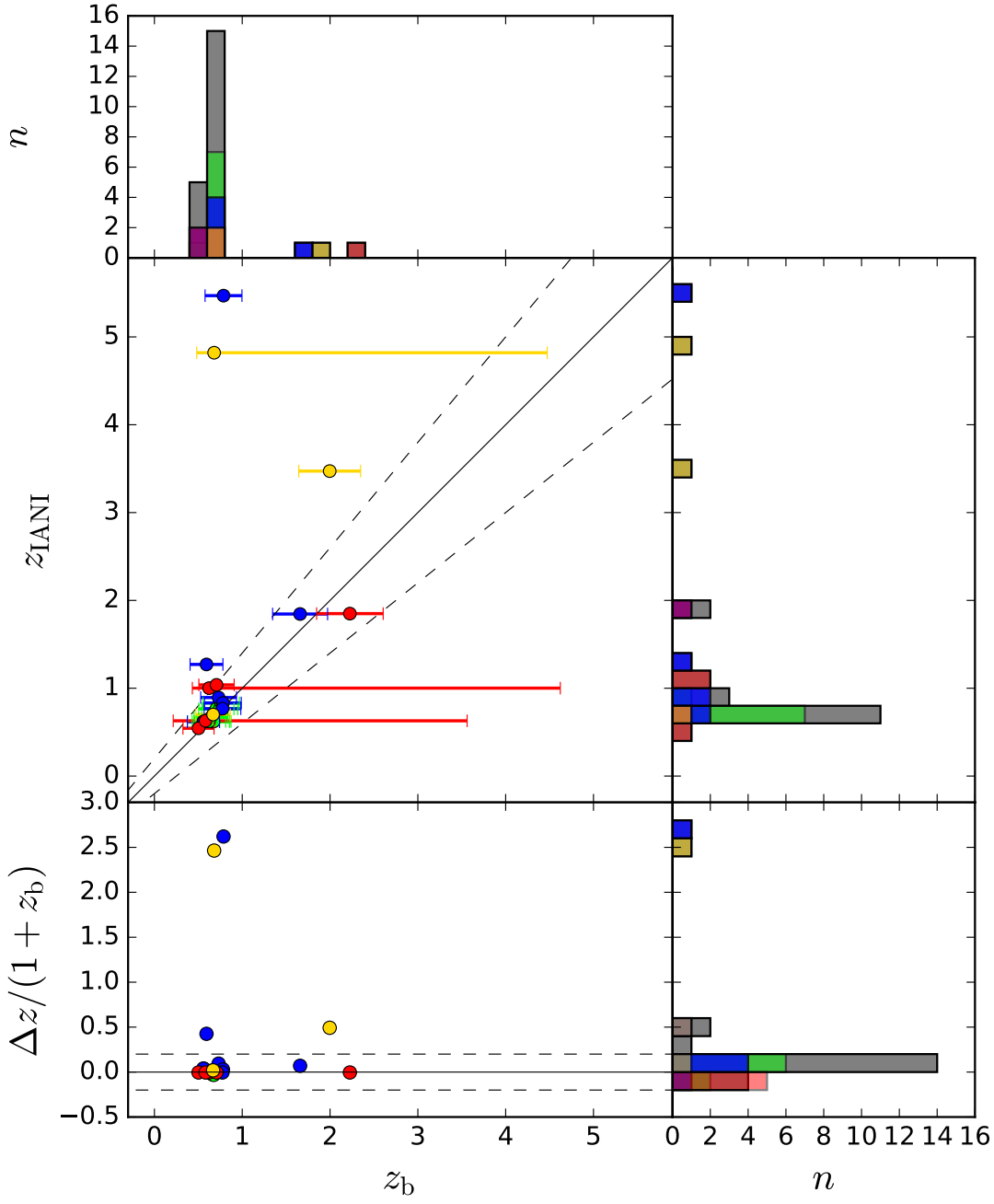

Figure 3.7: MUSE spectra (top panel) and respective variance (bottom panel) for the ALMA-detected sources extracted in the UDF10 pointing from (Coe et al., 2006) with $0.5 < z_b < 0.8$ and a detection in the H band. In the **top panel** a smoothed MUSE spectrum (*green solid line*) is over-plotted onto the spectrum extracted from the MUSE data cubes. The smoothed spectrum has been obtained as a result of the convolution between the original spectrum and a box function. The vertical orange solid lines show the position of the main absorption/emission lines in the spectrum (i.e. [OII], CaII(H), CaII(K), H_δ, H_β, O[III](db-1/3) and O[III](db-1)). The measured spectroscopic redshift of the source and an *HST* RGB (B_{435}+V_{606}+z_{850}) $10''$ image of the galaxy are reported too.

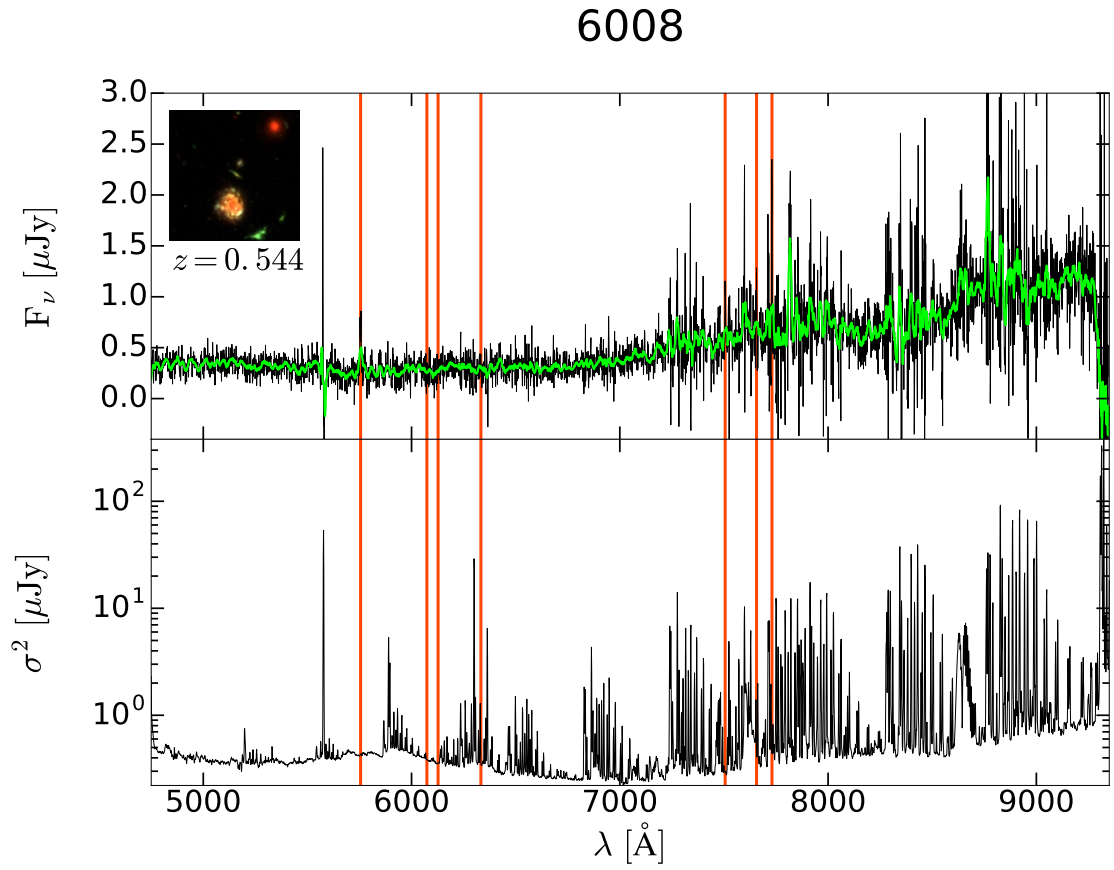

Figure 3.8: continuing Fig. 3.7

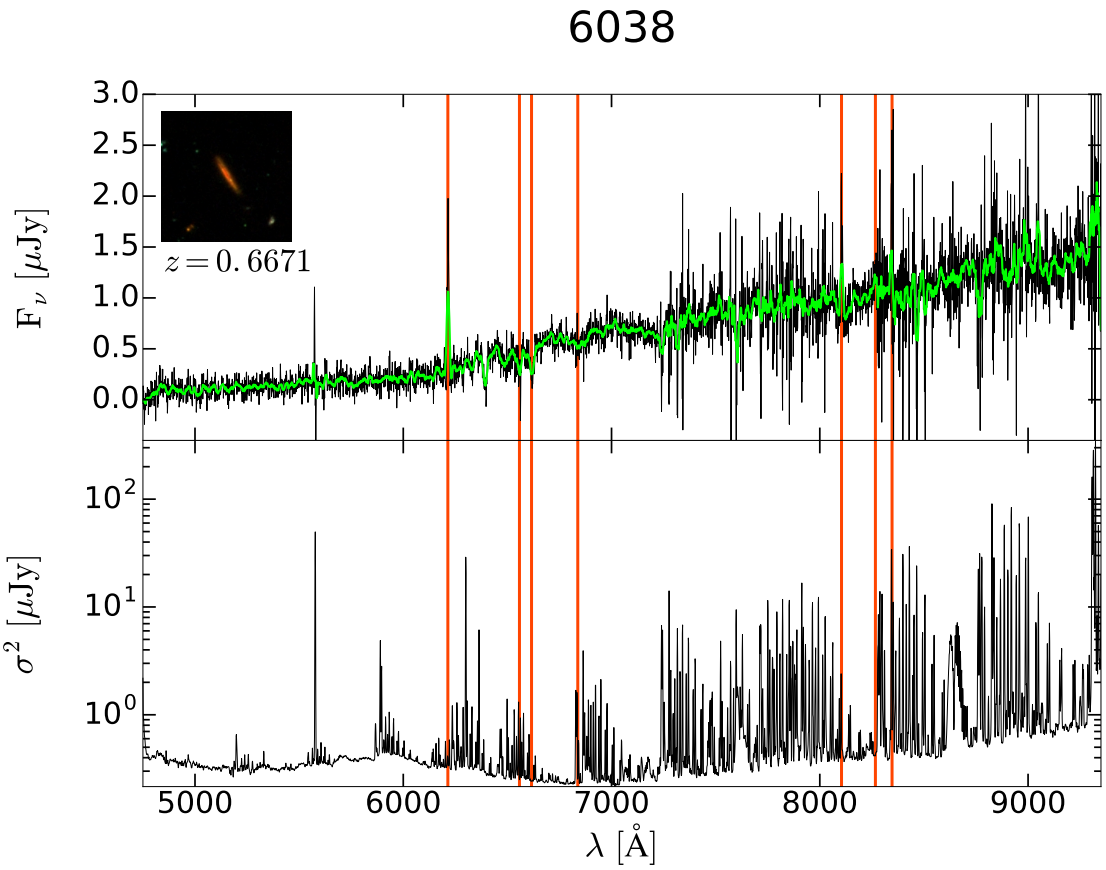

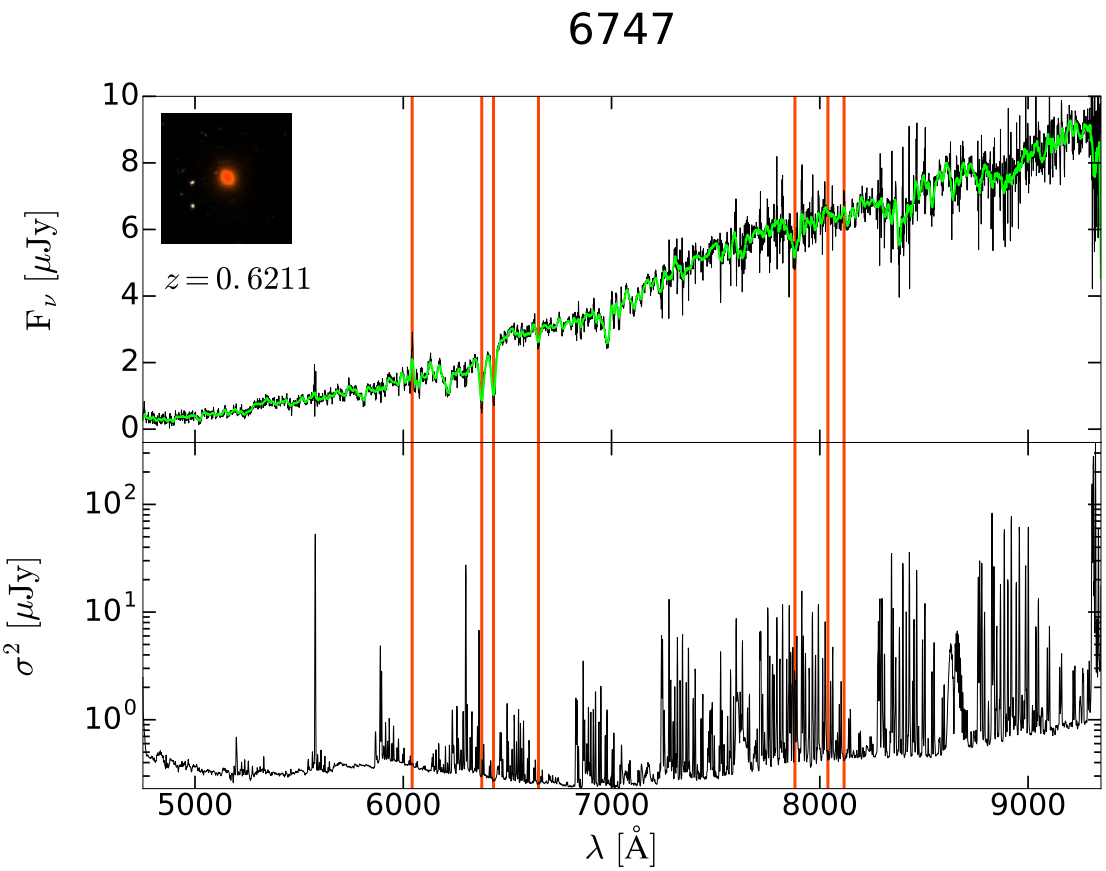

Figure 3.9: continuing Fig. 3.7

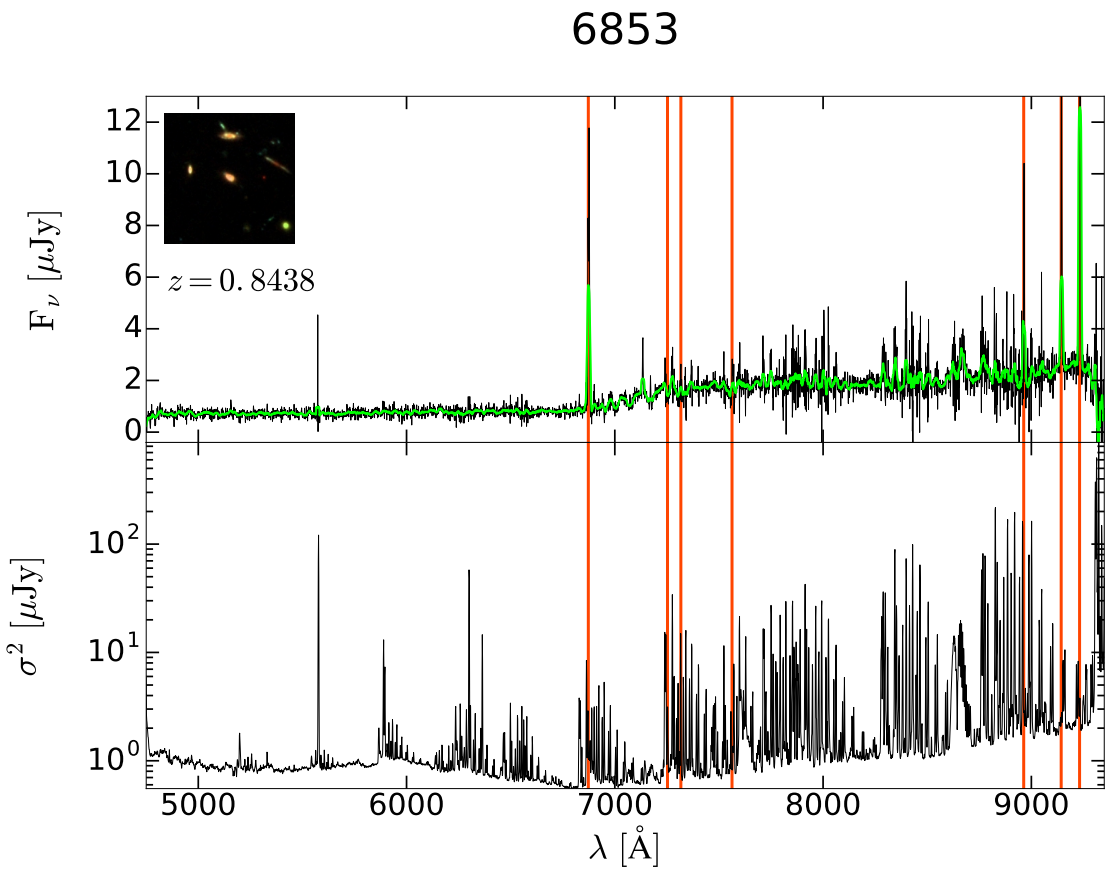

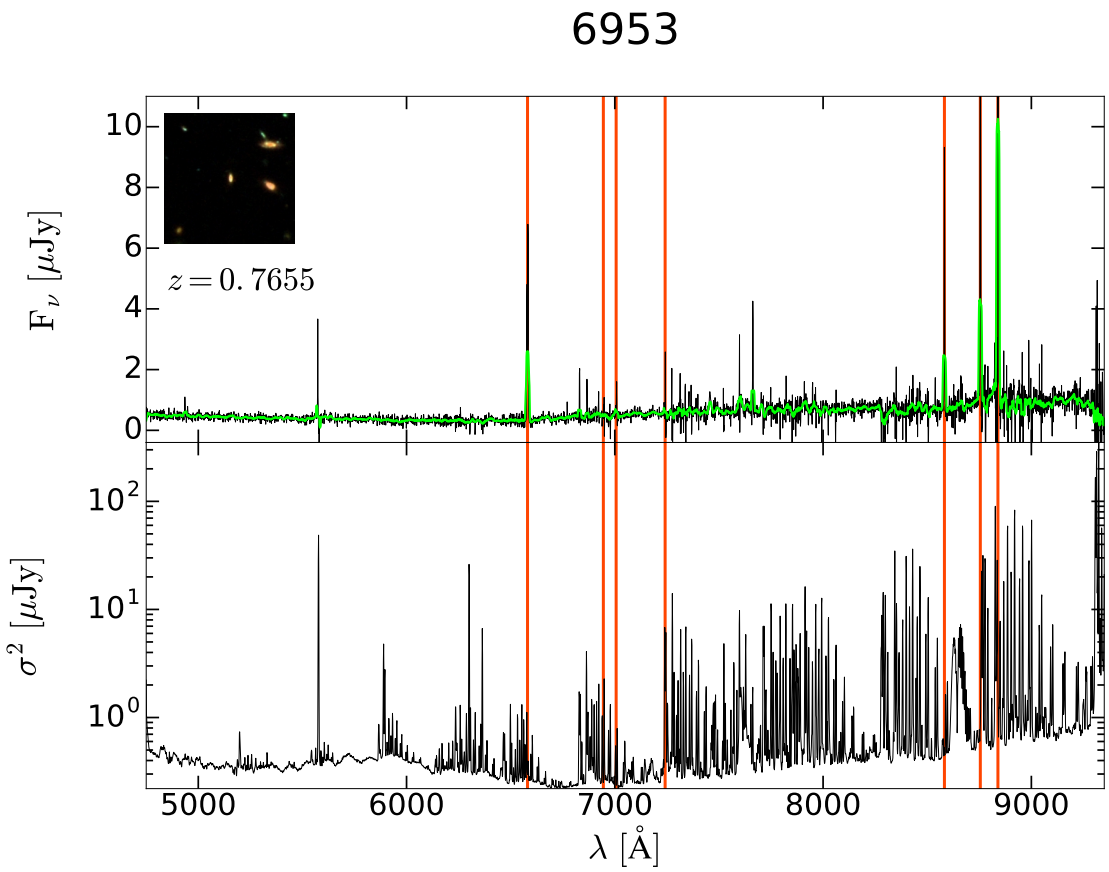

Figure 3.10: continuing Fig. 3.7

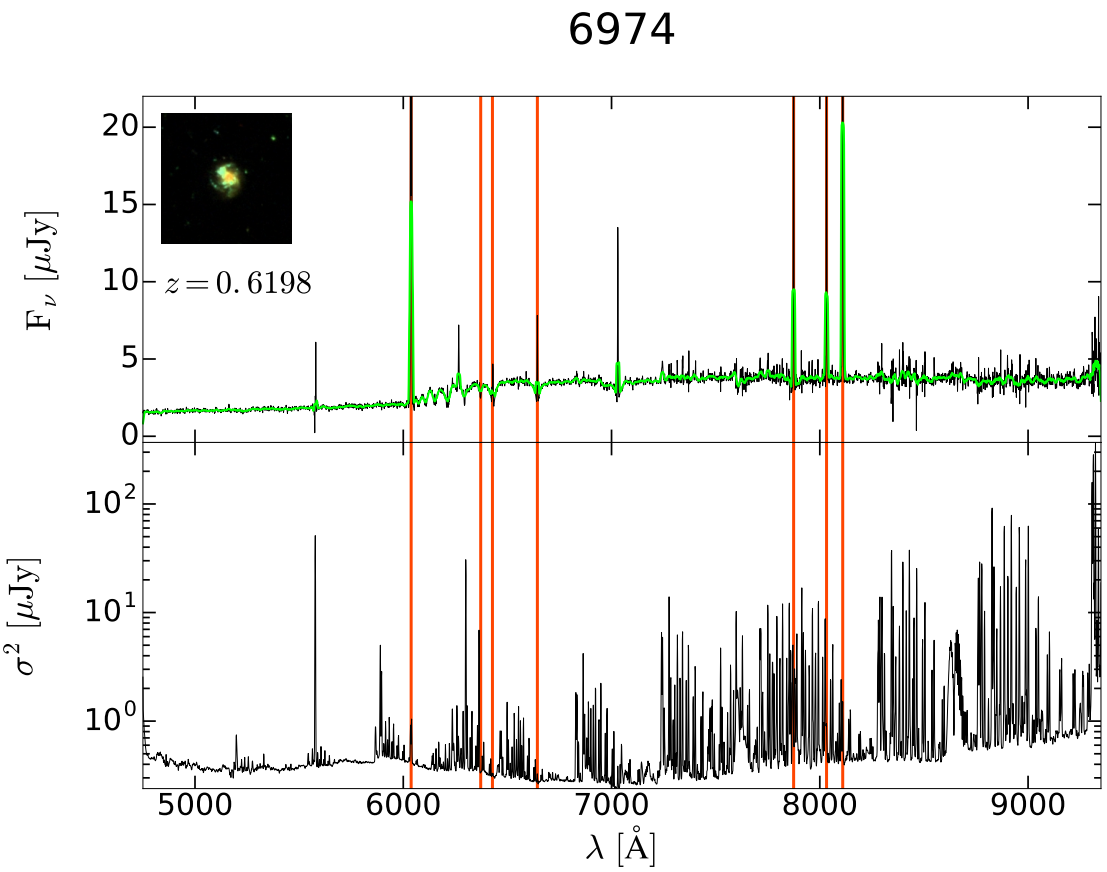

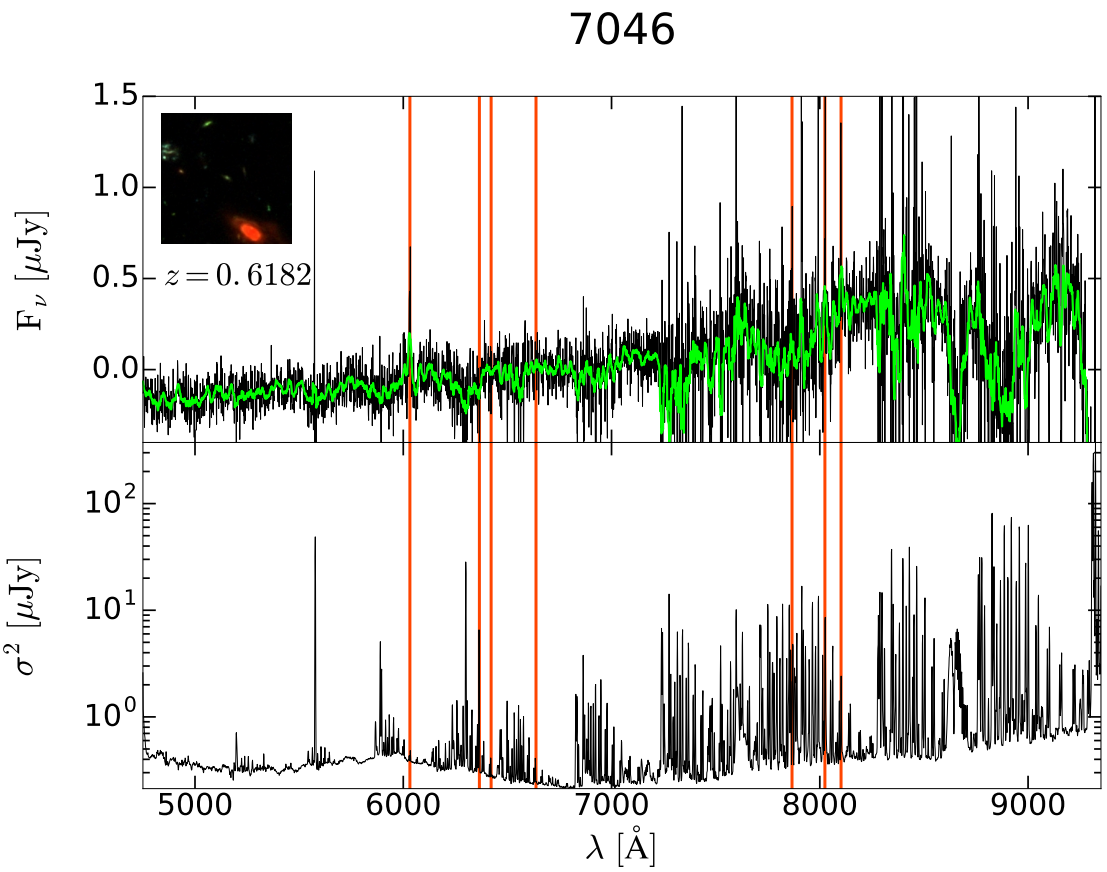

Figure 3.11: continuing Fig. 3.7

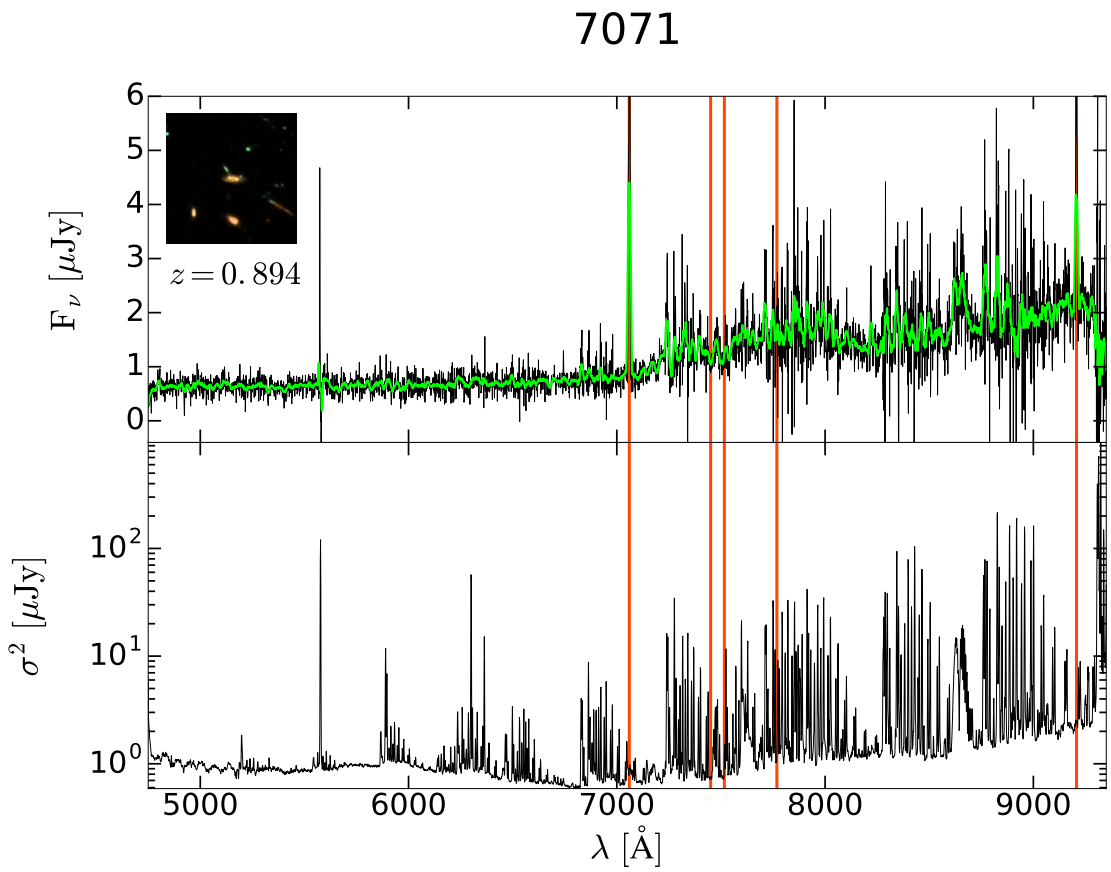

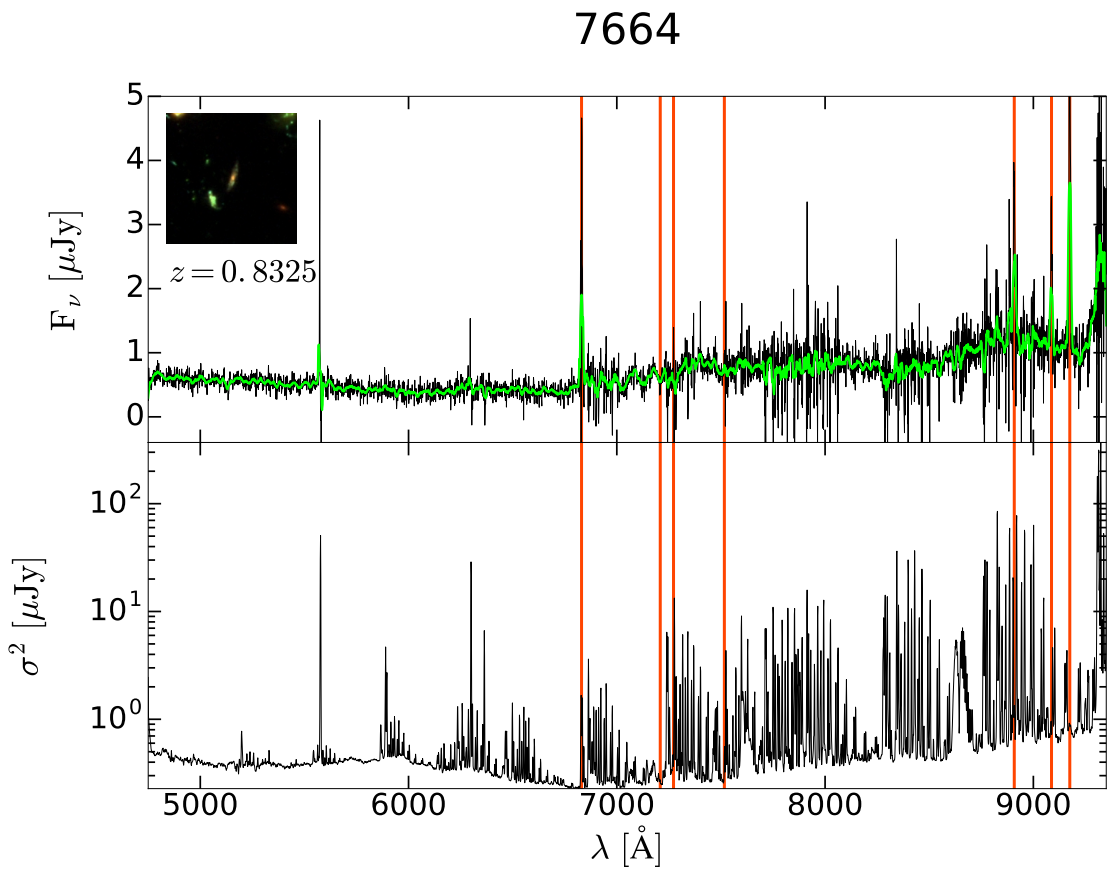

Figure 3.12: continuing Fig. 3.7

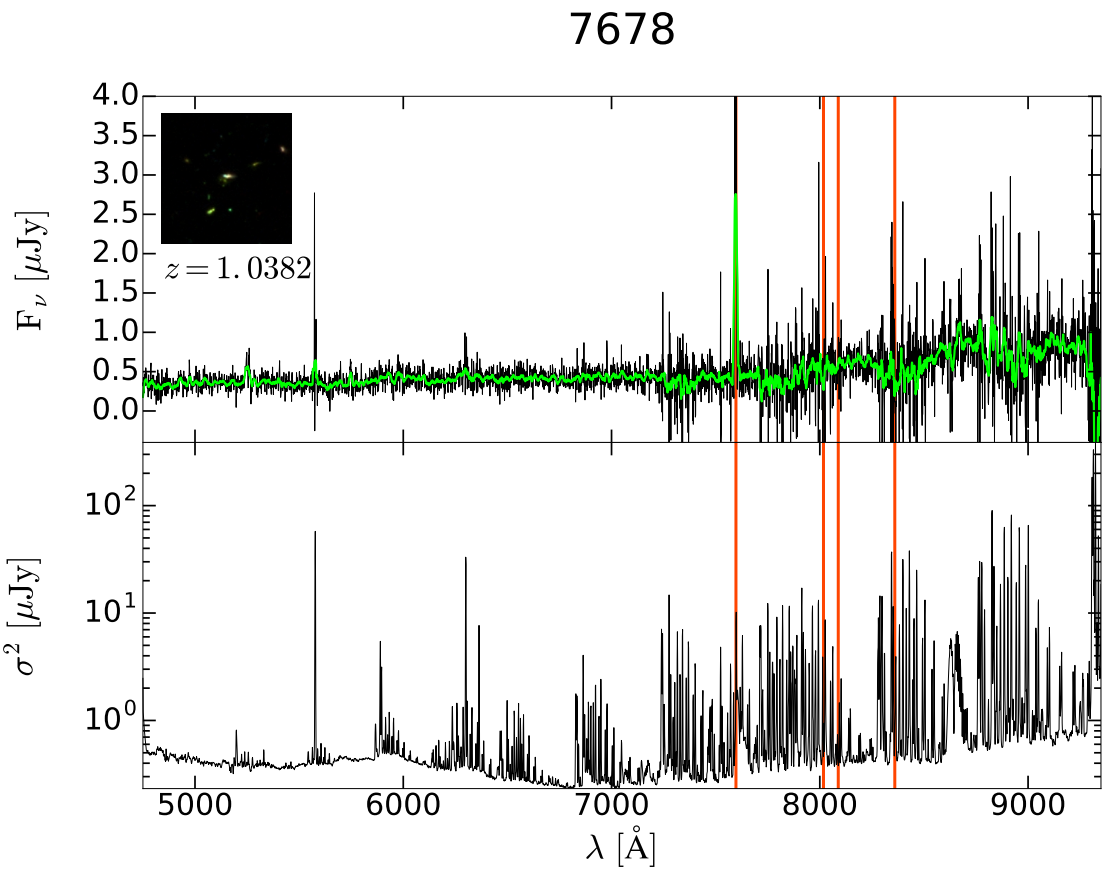

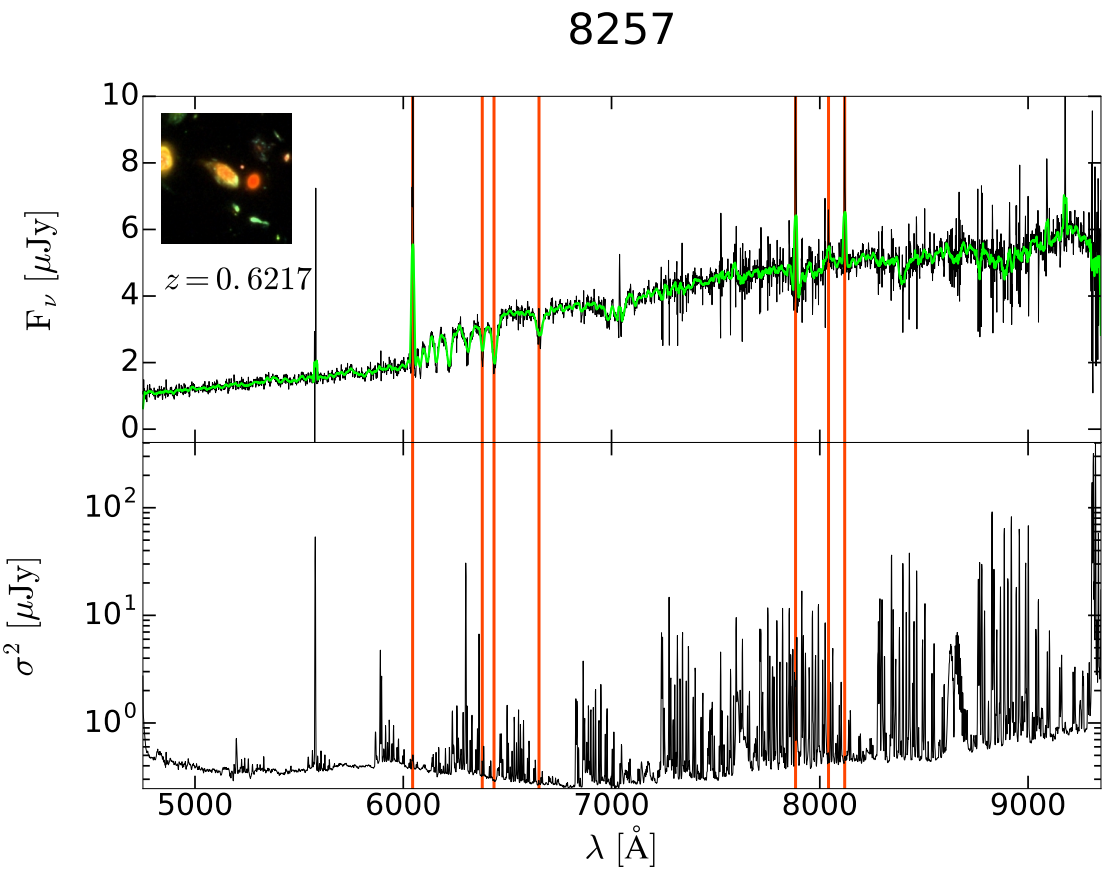

Figure 3.13: continuing Fig. 3.7

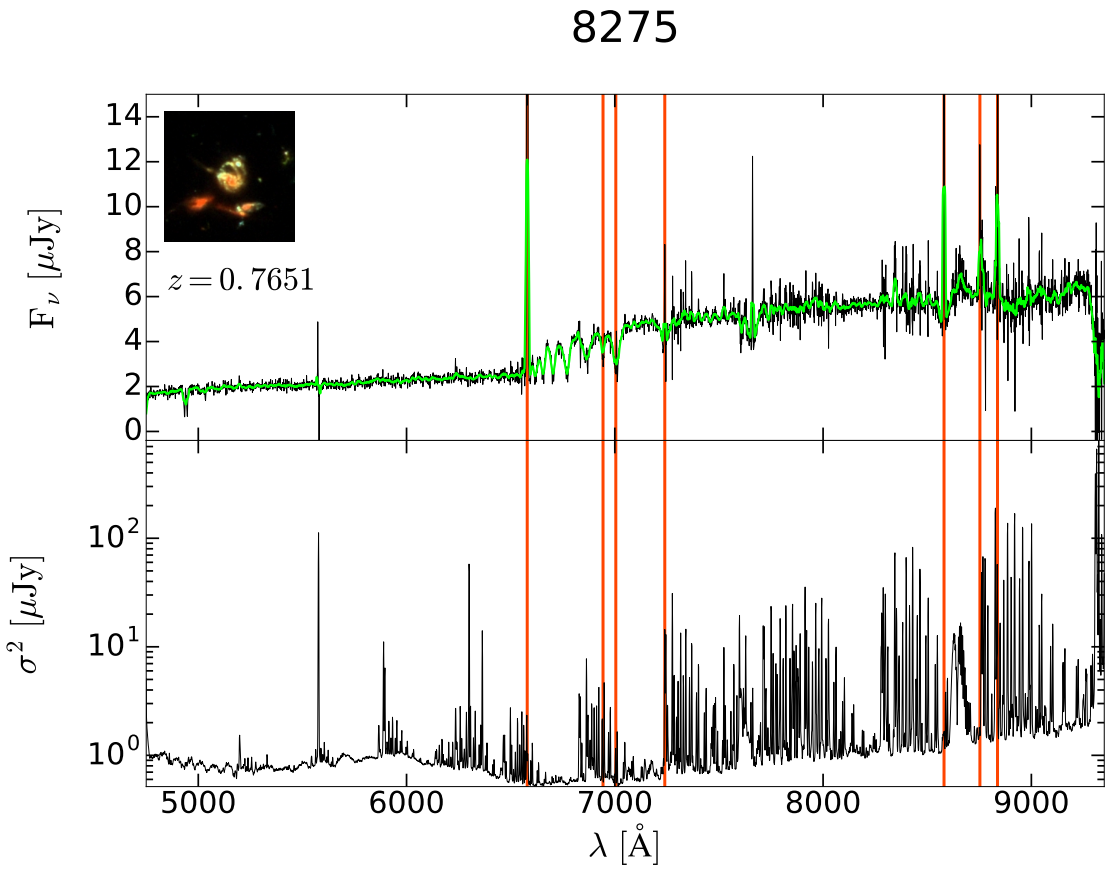

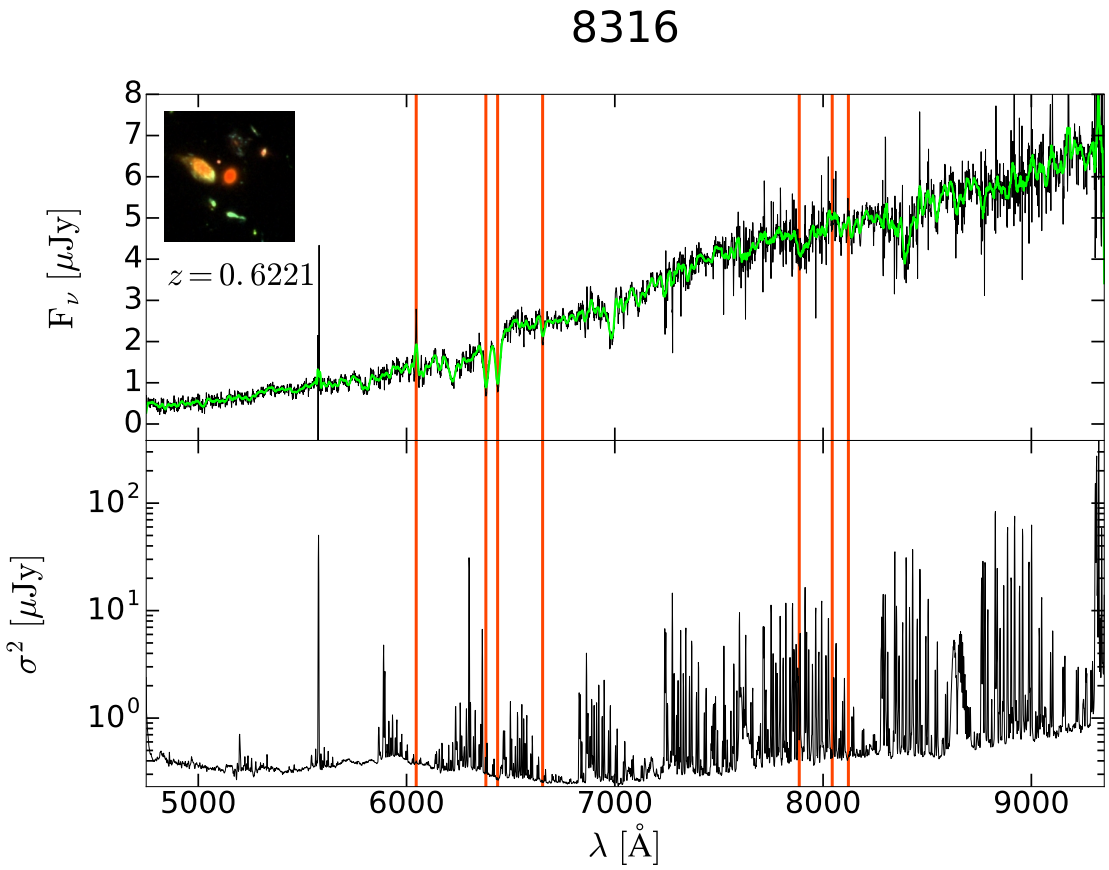

Figure 3.14: continuing Fig. 3.7

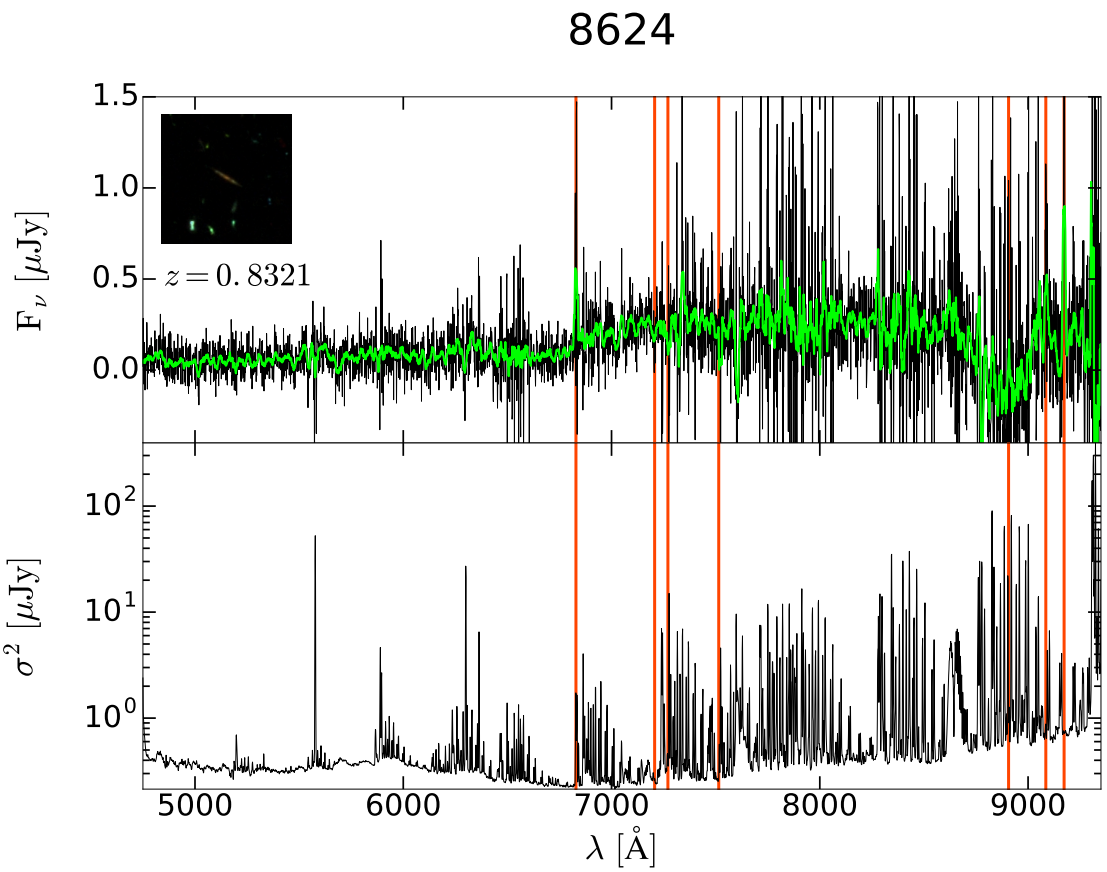

Chapter 4

Physical properties of the sample from an analysis of the Spectral Energy Distributions

In this chapter we present a complete analysis of the physical properties of the sources presented in Chapter 3, derived from the combination of MUSE spectra and their broad-band photometry.
We used two different SED fitting tools: SINOPSIS (see Sec. 4.1.1 and for futher details Appendix B) and *HyperZmass* (see Sec. 4.1.2). For each one of the SED fitting codes we present the results on the stellar mass content and SFR of the considered galaxies. A comparison between the results obtained from the two different softwares will be presented as well along with future perspectives of our work.

4.1 SED fitting procedures

4.1.1 SINOPSIS

The first SED fitting code that we adopted is SINOPSIS (see Appendix B). SINOPSIS is a spectro-photometric fitting code (Fritz et al. 2007; Fritz et al. 2011; Fritz et al. 2014) which enables to retrieve fundamental quantities of galaxies (i.e. star formation rates, extinction, stellar masses, etc.) through the use of Simple Stellar Population models.
Since SINOPSIS allows to combine both spectral and photometric data for a more robust evaluation of the above-mentioned parameters, we decided to improve the MUSE data with the photometric informations presented in the updated version of the multicolour GOODS-MUSIC catalog (GOODS MUlitcolour Southern Infrared Catalog, Grazian et al. 2006) by Santini et al. (2009). [1]
The catalog, which consists of roughly 15000 sources, presents a 15-bands multiwavelength

[1]The multicolour GOODS-MUSIC catalog (Grazian et al., 2006) was extracted from the public data of the GOODS-South survey (GOODS-S, Giavalisco et al. 2004).

Figure 4.1: The spectroscopic redshift distribution of the 16 galaxies in our sample (see Chap. 3, Sec. 3.1.1 and Sec. 3.2): 2 from Dunlop et al. (2016) (*green solid line*) and 14 from Coe et al. (2006) (*grey solid line*). The red dashed line shows the redshift distributions of all the 14 sources (2 from Dunlop et al. 2016; 12 from Coe et al. 2006) runned by SINOPSIS.

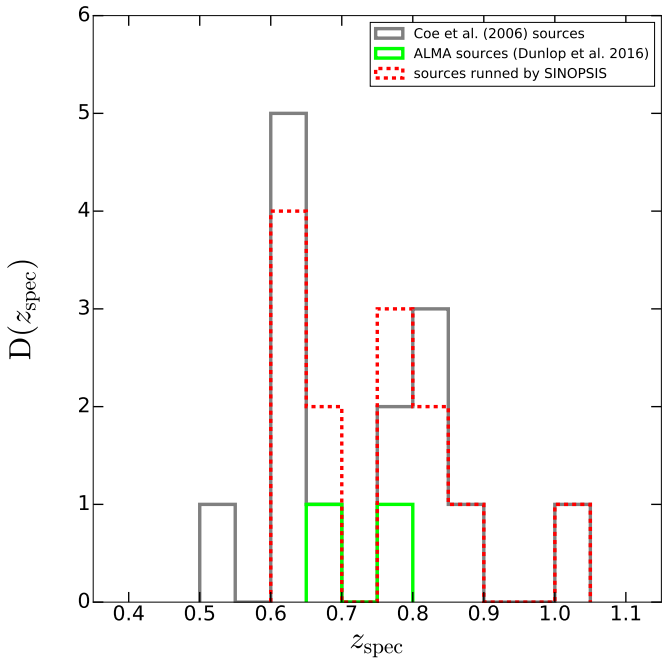

coverage from 0.35 to 24 μm of a $\sim$ 143.2 arcmin^2 area in the CDF-S (Chandra Deep Field South). The multiwavelength coverage is the result of the combination of images from different instruments, i.e. from the data retrieved by the 2.2 m telescope at ESO, VLT-VIMOS, *HST*-ACS, VLT-ISAAC, Spitzer-IRAC and Spitzer-MIPS facilities.

In order to run SINOPSIS it was necessary to create a catalog file, containing the details on the spectra and on the photometric data. Therefore, for each of the 22 sources in our sample (both from Coe et al. 2006 and Dunlop et al. 2016), we associated the photometric data from Santini et al. (2009) to the respective MUSE spectra, matching the sky-coordinates of the two different catalogs (i.e. Coe et al. 2006, Santini et al. 2009) by means of the TOPCAT software. Out of the 22 sources in our list, it was possible to associate photometric data only to 16 objects, thus reducing our sample.

As a result of an initial test on the quality of the SINOPSIS outputs (for further details see Appendix B, Sec. B.5), we decided to shape the structure of the SINOPSIS input catalog in order to compel the code to assume a pre-determined value for the observed Equivalent Width (EW) of the [OII] doublet ($\lambda_0 = 3727.0$ Å), a secondary calibrator for the SFR widely used for sources at high-redshifts ($0.3 < z < 1.5$, e.g. Talia et al. 2015). As a matter of fact, since the [OII]3727 forbidden-line doublet is one of the strongest line in the blue part of the spectrum and hence easily observable even in low S/N spectra, for our sources this emission line doublet represented one of the best SFR estimator

to relay on. For this reason, we decided to measure the EWs of the [OII] within the IRAF software (Tody, 1986). The IRAF procedure required a deblending fit on the two components of the doublet, performed with Gaussian functions, to retrieve their EW. The sum of these EWs allowed us to determine the total EW of the [OII] emission line (a detailed description of the procedure is presented in Appendix B, Sec. B.5.1), a value which we inserted as a constraint in SINOPSIS input catalog.
Therefore, after the creation of the spectro-photometric catalog[2], we run the software (for more details on the setting options used, see Appendix B, Sec. B.4). Nevertheless, before the code run, since SINOPSIS requires the overlap between the photometric data and the spectrum for at least one band to run properly, we had to correct the MUSE spectrum of all the sources for the spaxel aperture. To this aim, we started considering that the MUSE spectral range is covered by three photometric bands in Santini et al. (2009), i.e. the V (F606W), i (F775W) and z (F850LP) bands from ACS-*HST*. Therefore, after defining three wavelength ranges centered in the effective wavelength (λ_c) of the filters (see Table B.4.1) and with a total width of 400 Å, i.e. $5740 \leq \lambda_V \leq 6140$, $7510 \leq \lambda_i \leq 7910$ and $8660 \leq \lambda_z \leq 9060$, for every source we computed the median value of the flux in each λ-range. We chose to adopt the statistic median for its major solidity to fluctuations. The median of the flux over the entire wavelength range allows to avoid a wrong estimate of the continuum emission due to the possible presence of intense emission and/or absorption lines. So, after the extraction of the mean value from the three medians obtained, for each spectrum we multiplied the flux for the retrieved mean, thus obtaining the input spectra for SINOPSIS (see Fig. 4.2, bottom panels) corresponding to the total flux emitted by the sources.
At the end of the run, SINOPSIS succeeded in extracting informations from the spectra of only 14 sources out of 16. Indeed, the 7046 and 8624 objects were rejected from the code with the disclaimer: '`The spectrum will be skipped as its average flux is too low`'. In SINOPSIS, this happens whenever more than 40% of the flux in the input spectrum has negative values ($F_\lambda < 0$), as in the 7046 and 8624 cases.
In Fig. 4.2 (and below) we present the results of the SED-fitting performed by SINOPSIS on the aperture corrected MUSE spectrum (*solid blue line*) and photometric data (Santini et al. 2009; *black filled circles and squares*) for each one of the 16 sources in our sample. The synthetic models presented (*solid orange line*) derives from the Charlot and Bruzual A. (2017) templates with the Chabrier IMF (Chabrier, 2003) and Calzetti attenuation law (Calzetti et al., 1994).
As it appears clear from the plots, in most cases the theoretical models well reproduce the observed data, either spectroscopic and photometric. Nonetheless, the worst SED-fit obtained is for the 6008 galaxy. The origin of this anomaly in the spectrum shape can probably be adressed to a flux contamination due to close-by sources. At this regard, an attentive analysis of the source cut-outs proved to be fundamental thus showing the

[2]Since SINOPSIS cannot use as a constraints to the SSP models the photometric upperlimits, in the catalog we created all the upperlimit values in Santini et al. (2009) were replaced with a 99.0 flag. As a matter of fact, Fritz et al. code reads the 99.0 flag as a sign for the absence of both magnitudes and error measurements.

presence of at least two nearby galaxies. Therefore, in the 1″ radius aperture within which we extracted the spectra, a good amount of the observed flux results to come from these two sources. In addition, after a look at the position of the galaxy in the MUSE image, we realized that the source was really close to one of the edges of the frame. Nonetheless, after the investigation of the output models obtained for the remaining sources, we spotted no more low quality fits but for the 6008 galaxy.

4.1.2 *HyperZmass*

The second SED-fitting code we adopted was *HyperZmass* (Pozzetti et al., 2007), a modified version of the public photometric redshift code HyperZ (Bolzonella et al., 2000). Given the galaxy redshift, either spectroscopic or photometric, the code provides an estimate of the galaxy stellar mass through the use of the SED fitting technique, i.e. computing the best fit SED by minimizing the χ^2 between the observed spectra and the synthetic models. We used synthetic spectral templates with SFR exponentially decreasing with time, i.e. templates with a Star Formation History (SFH) following the analytic approximation for the Schmidt's law (Schmidt, 1959) $\psi(t) \propto \exp^{-t/\tau}$, where τ is the timescale over which the star formation needs to remain constant.
In our analysis, we adopted the Bruzual and Charlot (2003) templates, with a Chabrier IMF (Chabrier, 2003) and the τ timescale free to assume different values among (in unit of Gyr): 0.1, 0.3, 1, 2, 3, 5, 10, 15, 30 and ∞ (i.e. a model with SFR constant with time).

In addition, during the SED fitting analysis, the extinction (A_V) was allowed to span the range of values $0 < A_V < 3$, in steps of 0.05; while the galaxy age was set free to vary between 0.1 to 9 Gyr. At this regard, it is important to underline that the code pre-sets the maximum age achievable for each galaxy on the basis of its redshift, i.e. *HyperZmass* prevents the use of ages higher than the age of the Universe at the galaxy redshift.[3] To minimize the total number of free parameters, the fits were limited to solar metallicity (Z=0.02).
For each galaxy in our sample, in Fig. 4.10 we present the comparison between the values of the stellar mass (in $M_\odot$) retrieved by SINOPSIS and *HyperZmass*. While in the top panel the *HyperZmass* estimates derive from Bruzual and Charlot (2003) models without an a-priori determined SFH (i.e. with no preset value for τ), in the bottom panel the stellar population template has $\tau = \infty$ (i.e. a constant SFH). In both cases, the stellar masses retrieved from the two codes are in good agreement with each other even if the errors are less significant for the *HyperZmass* evaluations.
In the same way, in Fig. 4.11 we report the comparison between the values of the SFR (in $M_\odot$ yr^{-1}) for both the codes and the above-described SFH patterns. Even if no dramatic differences between the SINOPSIS and *HyperZmass* estimates can be recorded, the plot with no predetermined SFH seems to reproduce better the data retrieved by the Fritz et al. (2007) spectro-photometric software. This result is not completely surprising since SINOPSIS standard configuration uses the Free-Form (FF) approach, i.e. the code lets free to vary both the SFH and the extinction (see Appedix B, Sec. B.1). We observe

[3]The adopted cosmology for the *HyperZmass* run had $H_0 = 70$ km s^{-1} Mpc^{-1}, $\Omega_\Lambda = 0.7$ and $\Omega_m = 0.3$

Figure 4.2: SINOPSIS SED-fit of the MUSE spectra and photometric data (Santini et al., 2009) of the 16 sources in our sample (see Chap. 3, Sec. 3.1.1 and Sec. 3.2). **Top panel**: Charlot and Bruzual A. (2017) syntethic model (*solid orange line*) retrieved by SINOPSIS and over-plotted onto the MUSE aperture-corrected spectrum of the source (*solid blue line*). For sake of clarity, the MUSE spectrum presented has been smoothed to reduce the noise without losing the fundamental spectral informations. The photometric measurements from Santini et al. (2009) are presented with black filled circles for the filters used by SINOPSIS as constraints to the synthetic models; black filled squares were used to highlight the magnitudes not taken into account during the fitting procedure because too close to the PAH infrared emission bands. The grey shadowed region marks the wavelength range covered by MUSE (i.e. $4750 < \lambda < 9350$) while the red shadowed areas show the wavelength ranges dominated by the firsts PAH infrared bands (i.e. the $3.1 - 3.7$ and $6.0 - 6.9$ μm bands; e.g. Salama 2008). In the top panel, the measured spectroscopic redshift of the source and an *HST* RGB (B_{435}+V_{606}+z_{850}) $10''$ image of the galaxy are reported too. **Central panel**: zoom in of the top panel into the spectral region observed by MUSE. The theoretical model (*solid orange line*) has been over-plotted onto the aperture corrected MUSE spectrum of the source (*solid blue line*). The filled black circles show the values of the photometric data presented in Santini et al. (2009) for the V (F606W), i (F775W) and z (F850LP) bands. **Bottom panel**: the original MUSE spectrum of the source (*solid purple line*), as retrieved from the MUSE datacubes, plotted with the aperture corrected spectrum (*solid blue line*). The filled black circles show the values of the photometric data presented in Santini et al. (2009) for the V (F606W), i (F775W) and z (F850LP) bands while the grey shadowed vertical regions represent the three wavelength ranges (i.e. $5740 \leq \lambda_V \leq 6140$, $7510 \leq \lambda_i \leq 7910$ and $8660 \leq \lambda_z \leq 9060$) within which we measured the median values of the flux. This procedure allowed us to obtain the aperture correction value for each spectrum since the correction value has been retrieved from the avarage of the three median values of the flux (for more details see Sec.4.1.1).

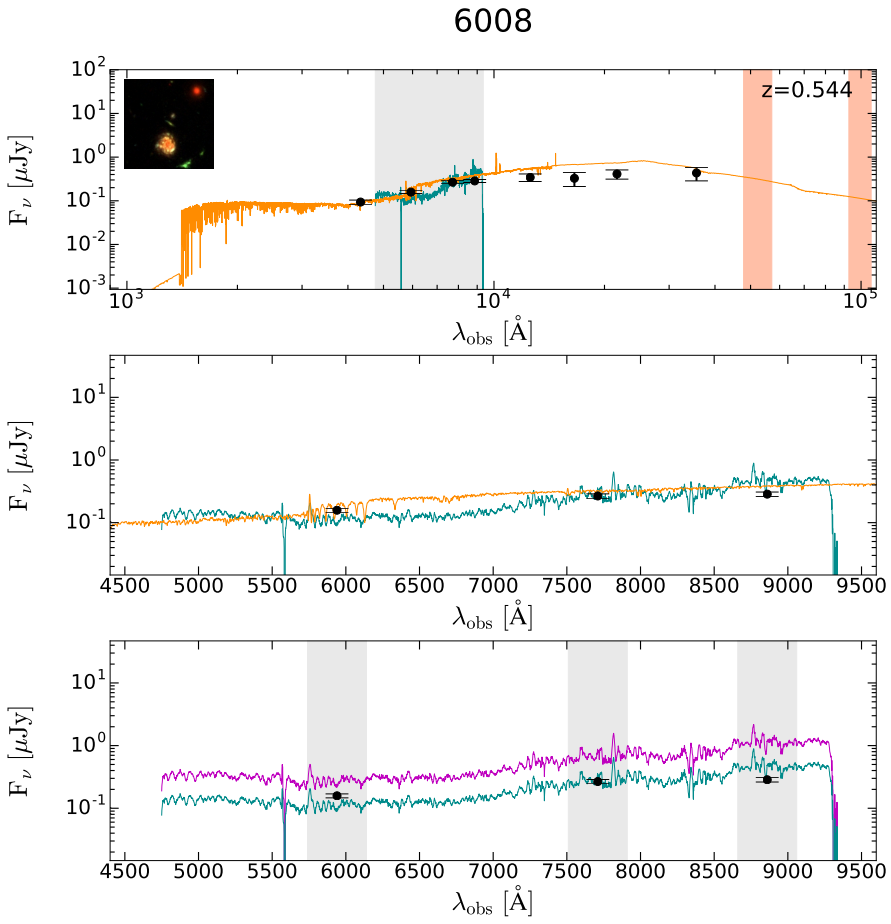

Figure 4.3: continuing Fig. 4.2

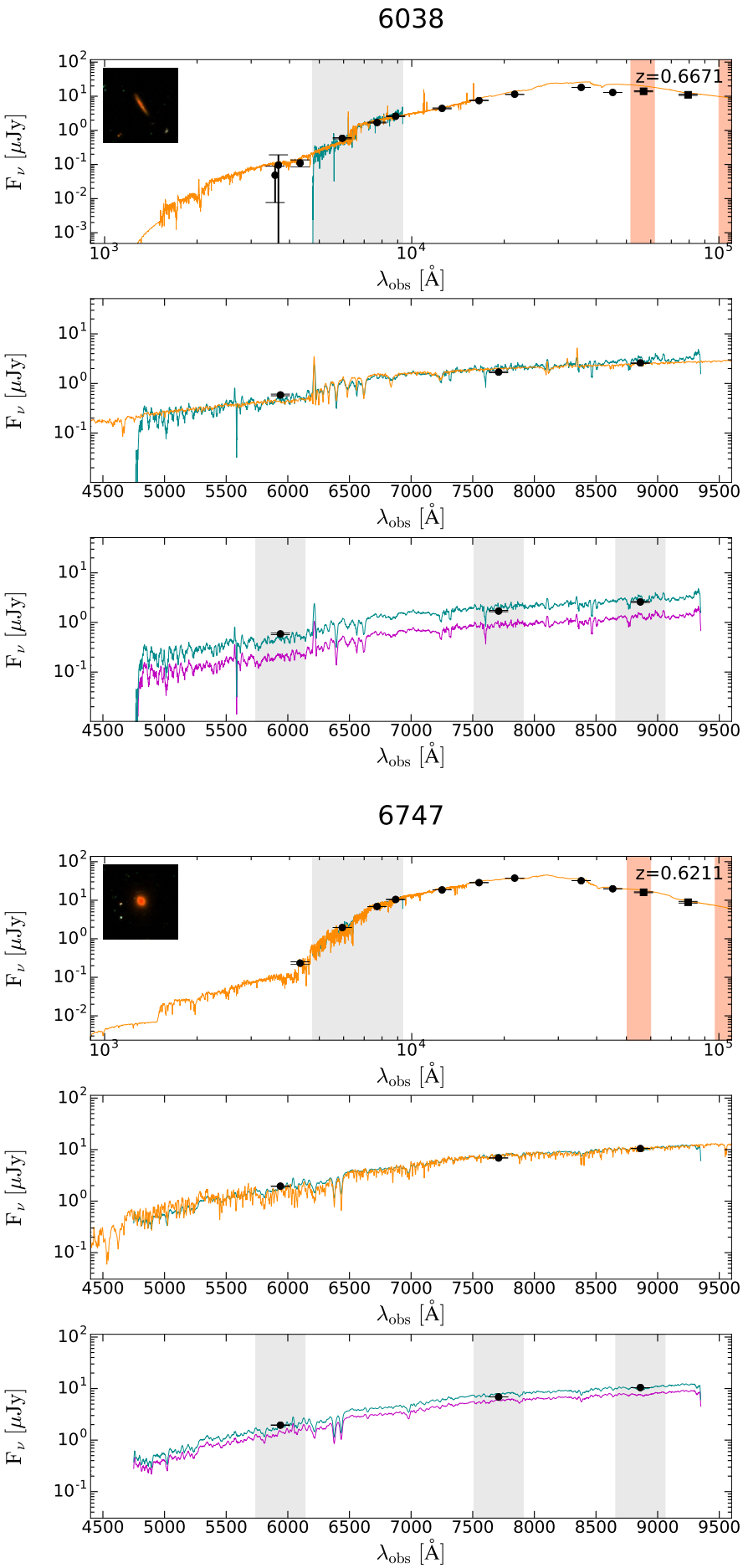

Figure 4.4: continuing Fig. 4.2

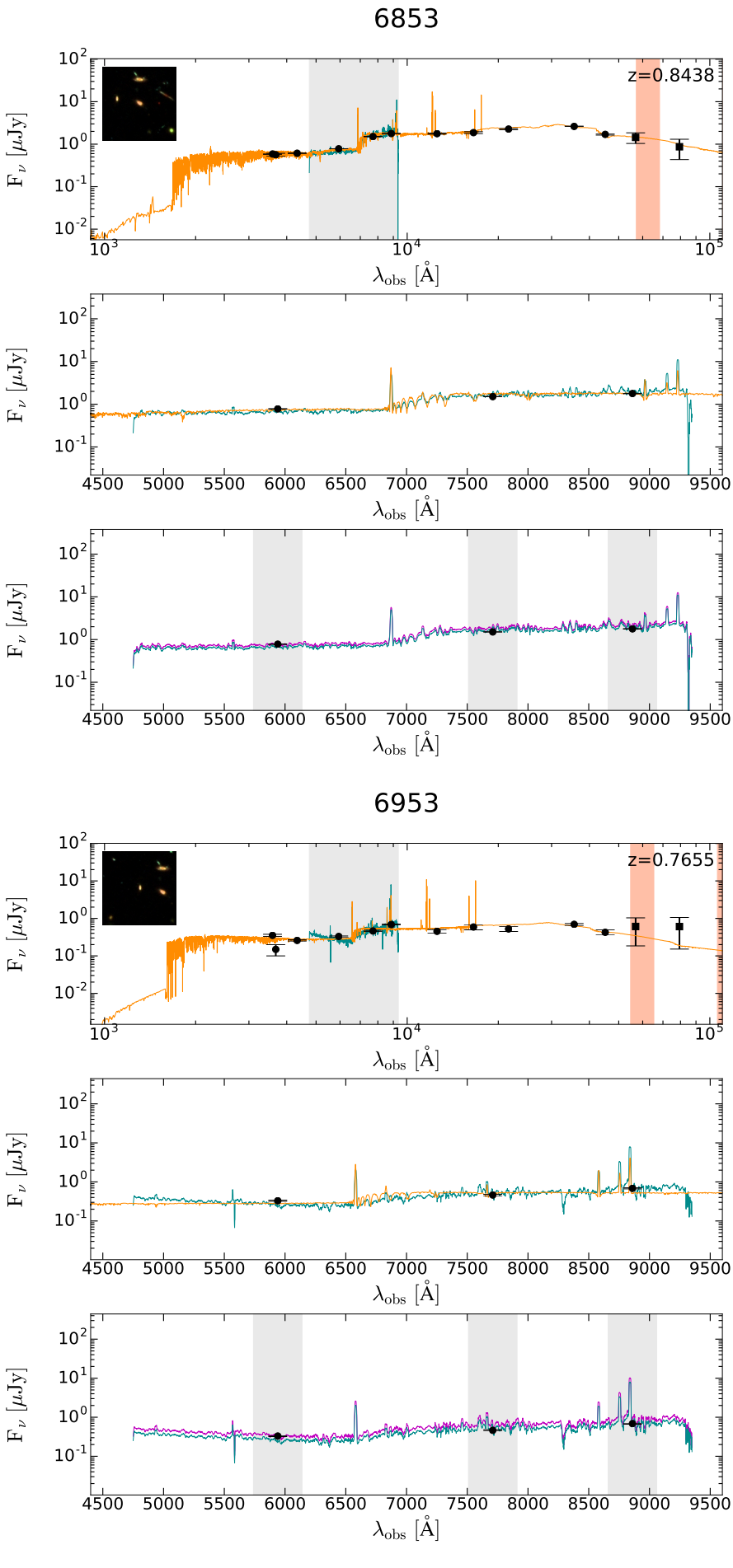

Figure 4.5: continuing Fig. 4.2

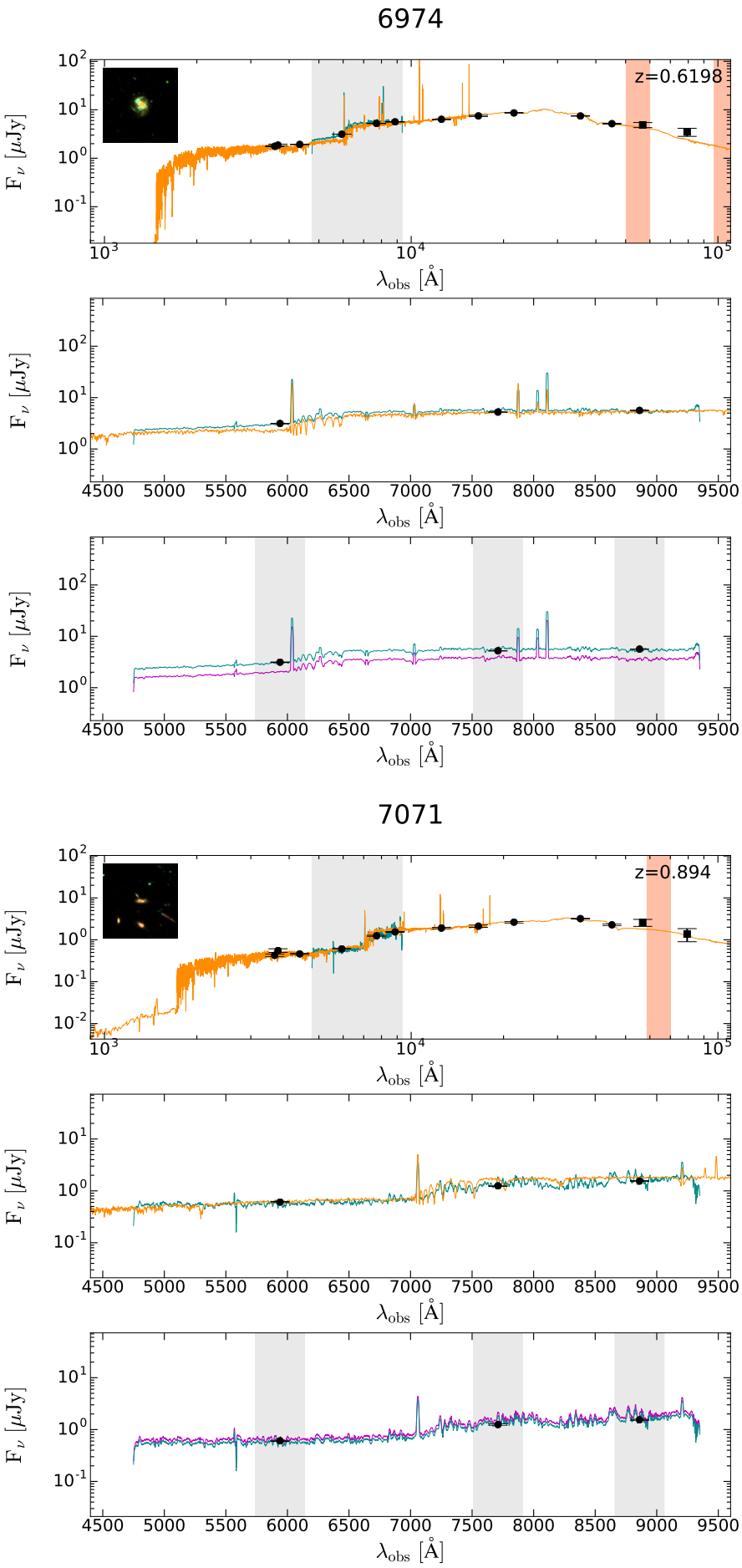

Figure 4.6: continuing Fig. 4.2

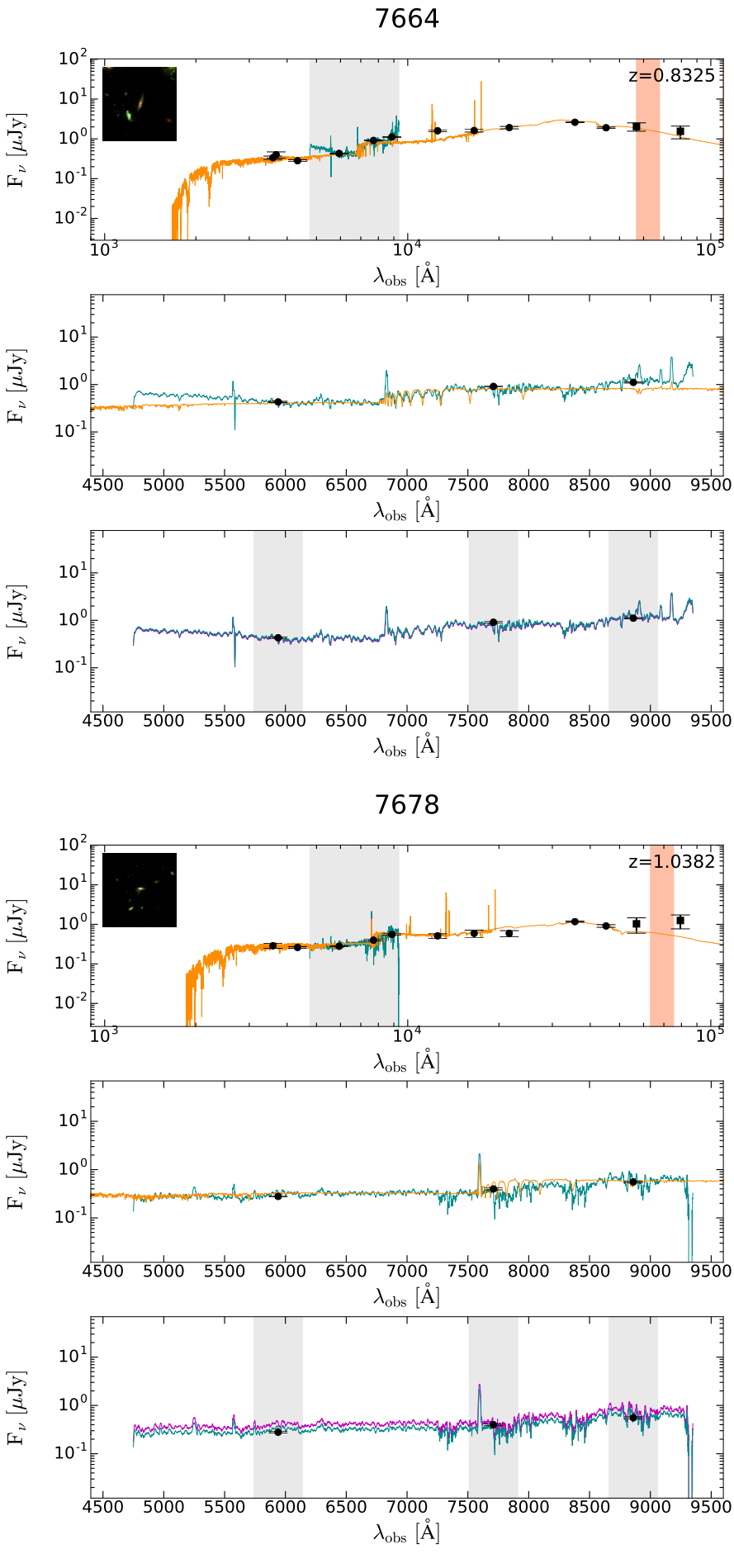

Figure 4.7: continuing Fig. 4.2

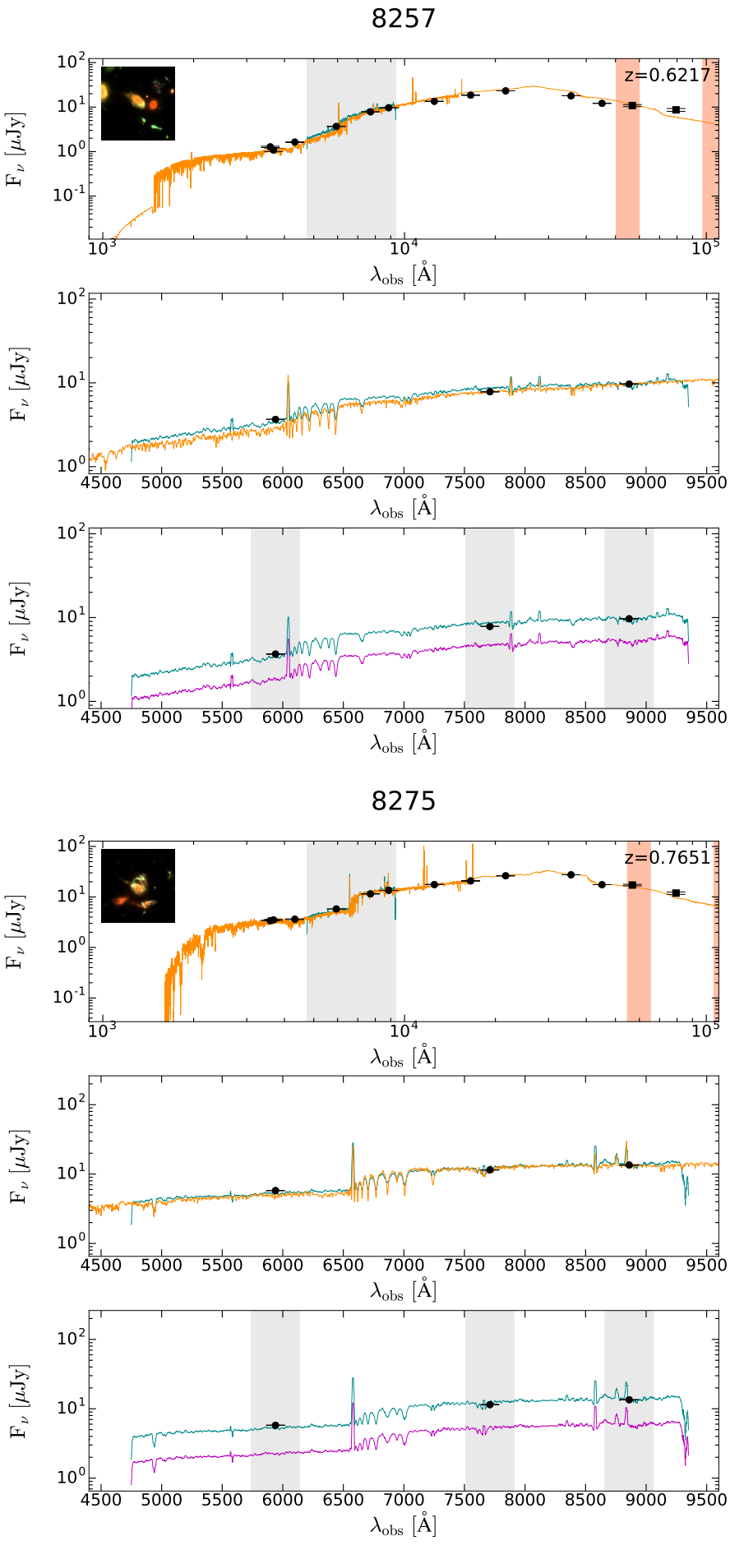

Figure 4.8: continuing Fig. 4.2

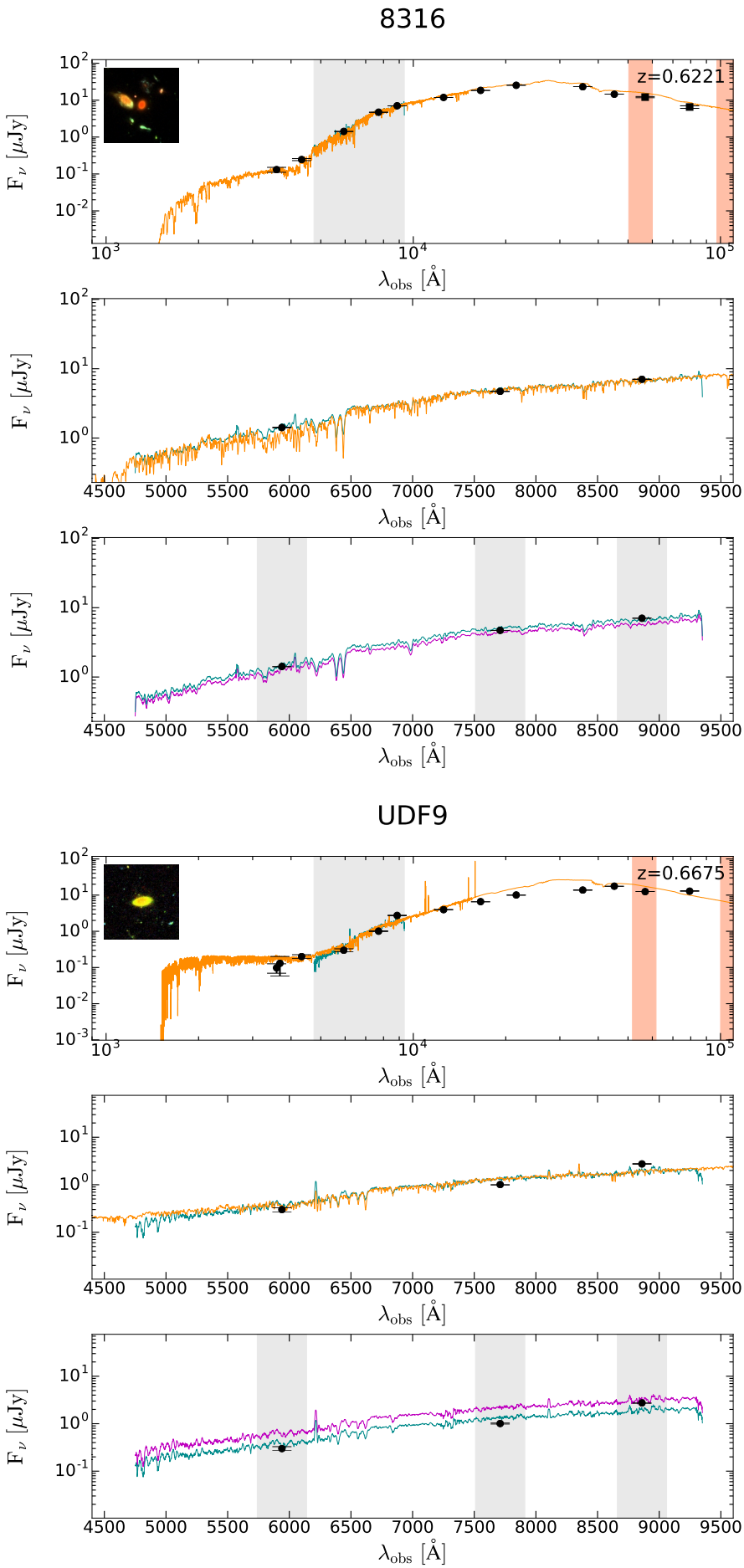

Figure 4.9: continuing Fig. 4.2

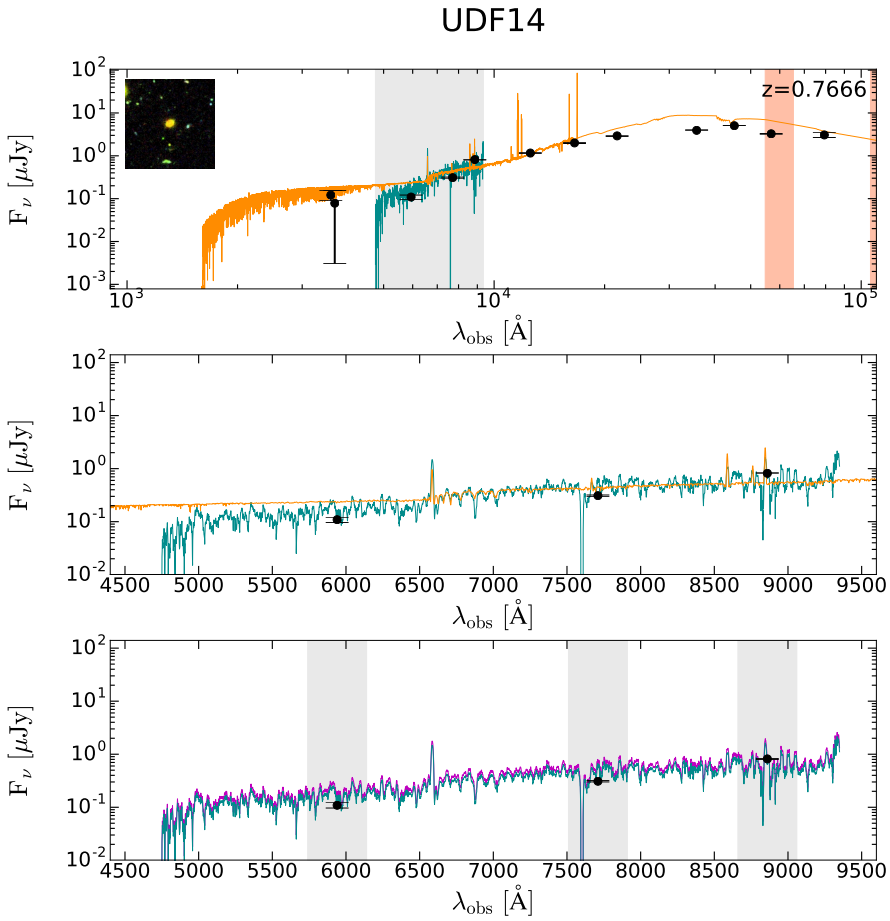

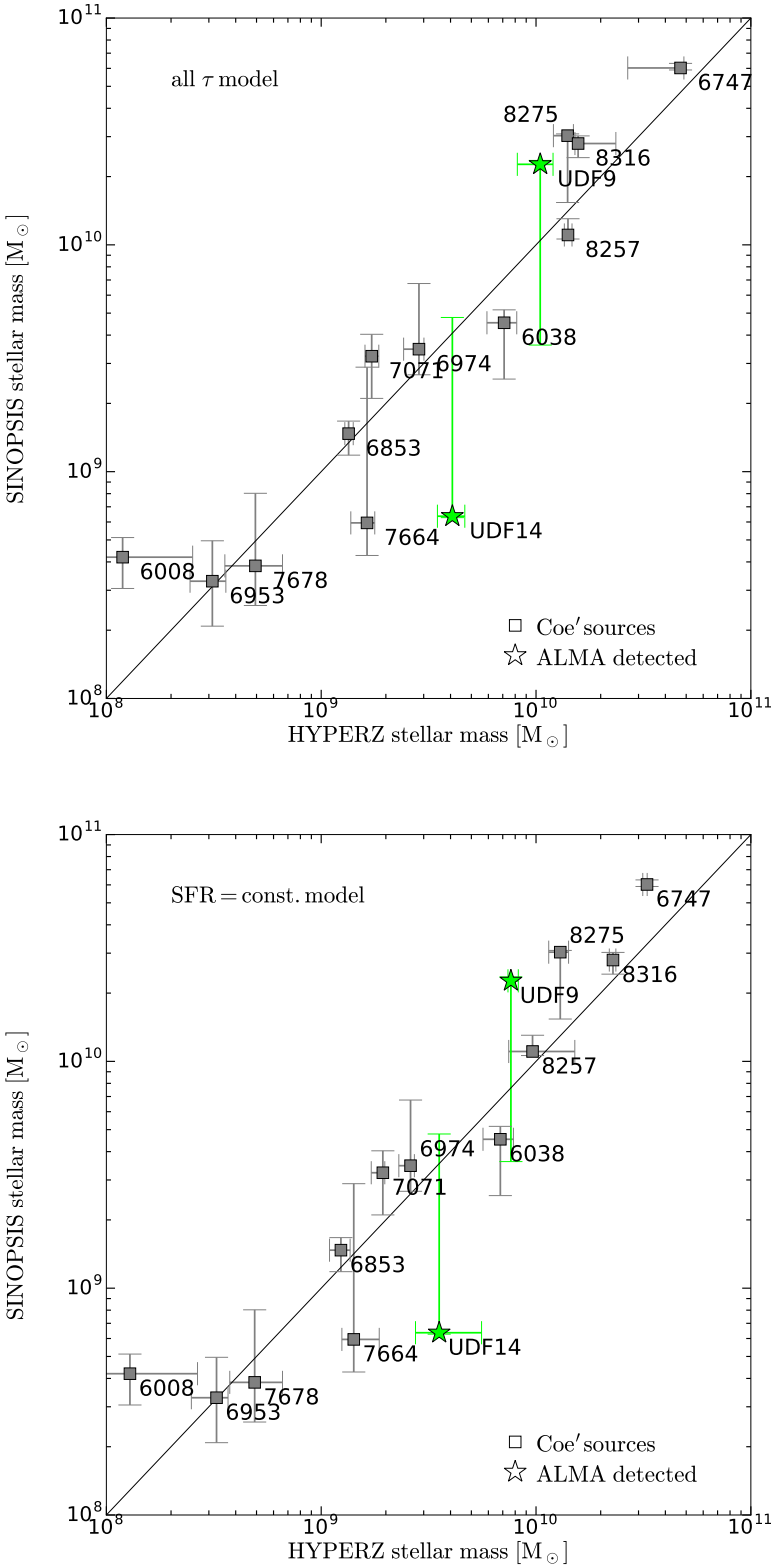

Figure 4.10: SINOPSIS (Fritz et al., 2007) inferred stellar masses vs. *HyperZmass* (Pozzetti et al., 2007) stellar masses for Dunlop et al. (2016) galaxies (*green stars*) and Coe et al. (2006) sources (*grey squares*) in our sample (see Chap. 3, Sec. 3.1.1 and Sec. 3.2). In the **top panel** we report the *HyperZmass* values obtained from a Bruzual and Charlot (2003) syntethic model with Chabrier IMF (Chabrier, 2003) and no predetermined SFH ('all τ model') against the mesurements retrived by SINOPSIS. On the contrary, in the **bottom panel** we present the *HyperZmass* values obtained from a Bruzual and Charlot (2003) syntethic model with Chabrier IMF (Chabrier, 2003) but with a constant SFH ('SFR = const. model').

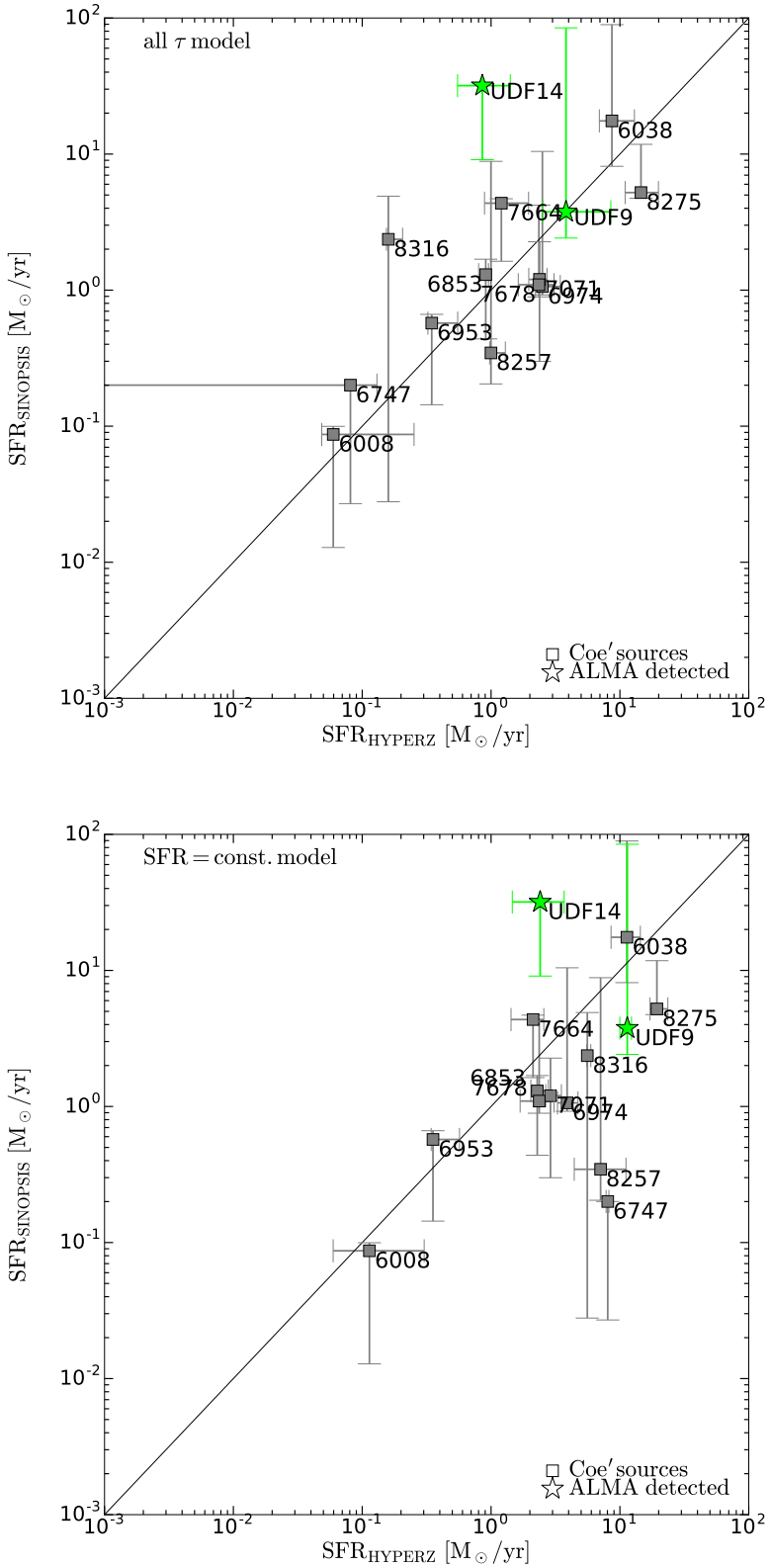

Figure 4.11: SINOPSIS (Fritz et al., 2007) inferred SFRs vs. *HyperZmass* (Pozzetti et al., 2007) SFRs for Dunlop et al. (2016) galaxies (*green stars*) and Coe et al. (2006) sources (*grey squares*) in our sample (see Chap. 3, Sec. 3.1.1 and Sec. 3.2). In the **top panel** we report the *HyperZmass* values obtained from a Bruzual and Charlot (2003) syntethic model with Chabrier IMF (Chabrier, 2003) and no predetermined SFH ('all τ model') against the mesurements retrived by SINOPSIS. On the contrary, in the **bottom panel** we present the *HyperZmass* values obtained always from a Bruzual and Charlot (2003) syntethic model with Chabrier IMF (Chabrier, 2003) but with a constant SFH ('SFR = const. model').

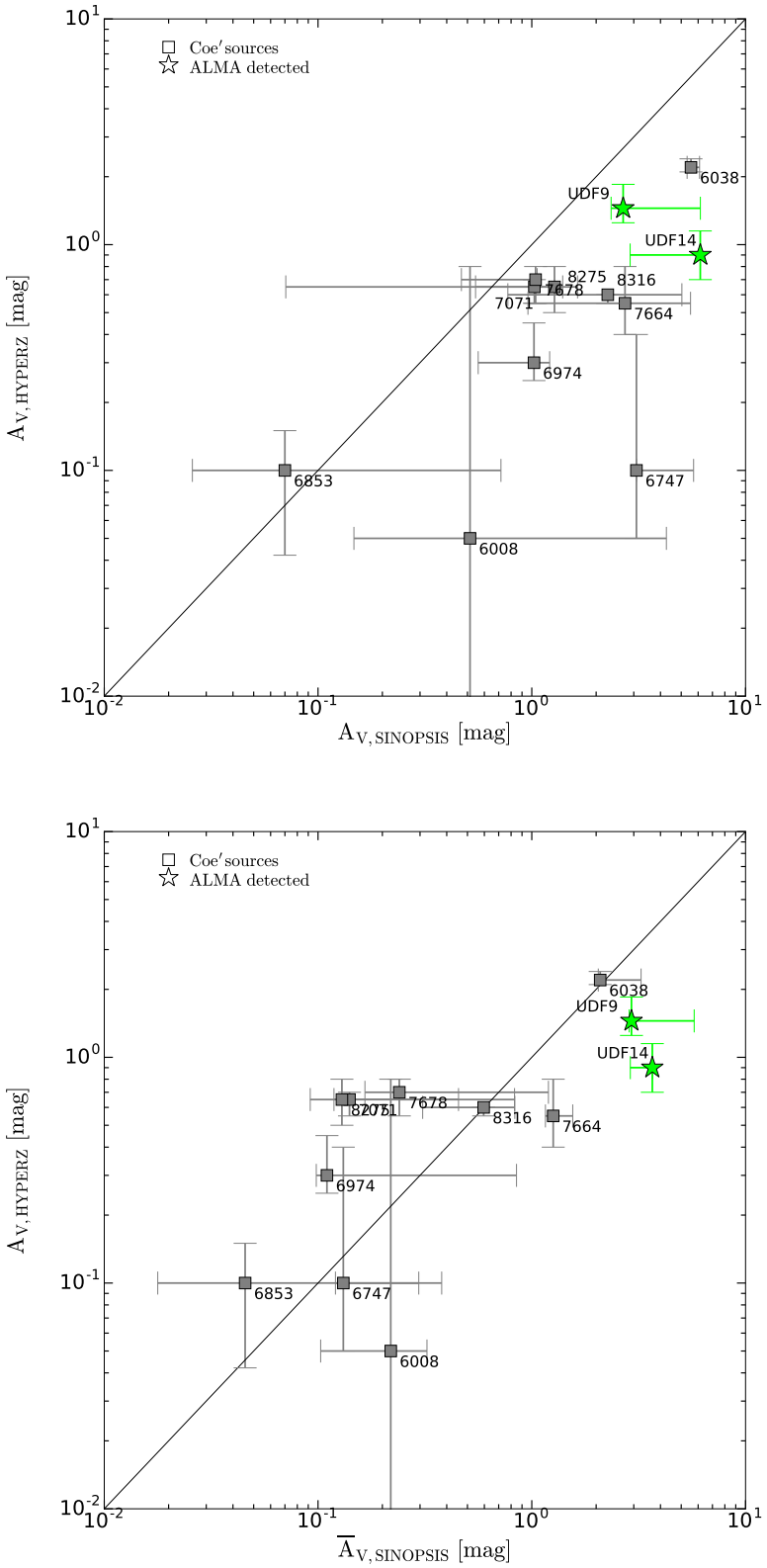

Figure 4.12: *HyperZmass* (Pozzetti et al., 2007) inferred A_V vs. SINOPSIS (Fritz et al., 2007) A_V for Dunlop et al. (2016) galaxies (*green stars*) and Coe et al. (2006) sources (*grey squares*) in our sample (see Chap. 3, Sec. 3.1.1 and Sec. 3.2). In the **top panel** we report the comparison between the *HyperZmass* A_V ($A_{V,HYPERZ}$) and the A_V obtained by SINOPSIS ($A_{V,SINOPSIS}$) for the youngest stellar populations (i.e. populations with age $< 2 \times 10^7$ yr). In the **bottom panel** we present the *HyperZmass* A_V ($A_{V,HYPERZ}$) vs. the A_V obtained by SINOPSIS averaging over all the stellar populations ($\overline{A}_{V,SINOPSIS}$). In both panels, the id of the sources (from Dunlop et al. 2016 and Coe et al. 2006) are reported too.

Figure 4.13: Comparison between SINOPSIS (Fritz et al., 2007) inferred extinction parameter averaged over all the stellar populations ($\overline{A}_{V,SINOPSIS}$) and the A_V obtained by the code for the youngest stellar populations ($A_{V,SINOPSIS}$; i.e. populations with age $< 2 \times 10^7$ yr), for Dunlop et al. (2016) galaxies (*green stars*) and Coe et al. (2006) sources (*grey squares*) in our sample (see Chap. 3, Sec. 3.1.1 and Sec. 3.2). The id of the sources (from Dunlop et al. 2016 and Coe et al. 2006) are reported too.

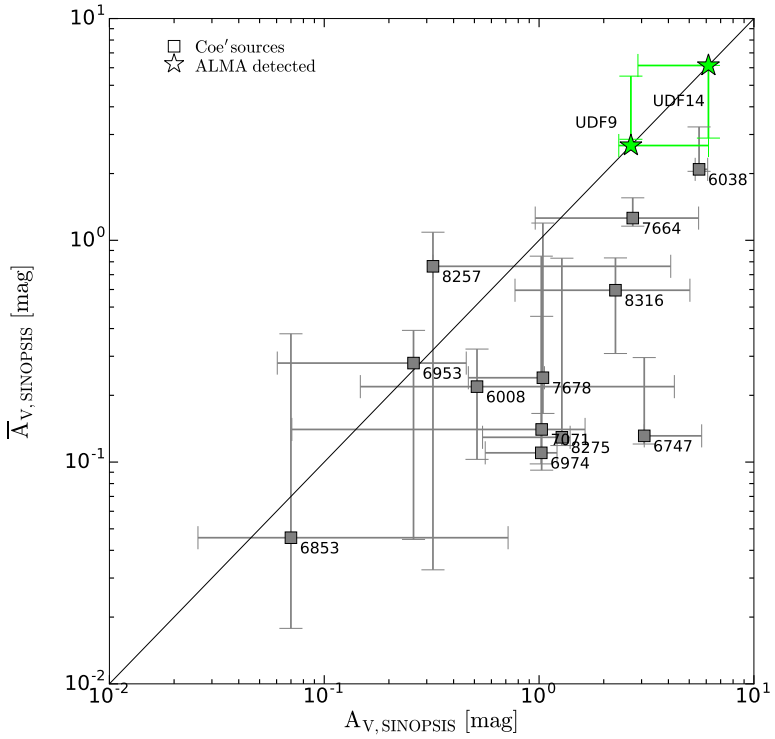

that, in the case of constant SFH, *HyperZmass* retrieves higher values of the SFR than SINOPSIS. As expected, in both cases the scatter between the two dataset is more significant for the SFR measurements than the galaxies stellar mass.
We performed a final comparison between the results obtained from SINOPSIS and *HyperZmass* on the estimates of the extinction parameter A_V. To this aim, in Fig. 4.12 we present two plots: in the top panel the *HyperZmass* extinction values ($A_{V,HYPERZ}$) are set against the SINOPSIS A_V measures ($A_{V,SINOPSIS}$) retrieved for the youngest stellar populations (i.e. populations with age $< 2 \times 10^7$ yr); while in the bottom panel we report the $A_{V,HYPERZ}$ measurements against the SINOPSIS extinction value averaged over all the stellar populations ($\overline{A}_{V,SINOPSIS}$). As expected, the tightest relation between the two codes is obtained in the $A_{V,HYPERZ}$ vs. $\overline{A}_{V,SINOPSIS}$ case (bottom panel). On average, the $A_{V,SINOPSIS}$ values result higher than the ones obtained by $A_{V,HYPERZ}$ accordingly to the 'selective extinction' hypotesis (e.g. Calzetti et al. 1994). The youngest stellar populations are expected to be more extincted than the old stellar populations because of the higher content of dust in the molecular clouds where the new born stars formed. During the evolution history of the stellar populations, stars progressively emerge from the molecular clouds either by means of supernova explosions and/or due to proper motions of the whole star cluster. Therefore, since the stars are no more enshrouded by the dust, the oldest populations result to be less extincted (i.e. present a lower A_V). As a consequence, the average of the A_V over all the galaxy stellar populations is expected to be lower than the A_V of the youngest stellar populations. At this regard we present Fig. 4.13, where the two different A_V measures obtained from SINOPSIS are conmpared. It appears clear that the expected trend deriving from the 'selective extinction' hypotesis is well reproduced.

4.1.3 IR and UV luminosities

We adopted a third and final method for the evaluation of the galaxies SFR and extinction, starting from the measurement of the fluxes at 1500 Å (UV) and at 24 μm (IR). This method, through the use of well-calibrated relations (Kennicutt, 1998) allows to obtain the SFR_{UV+IR} and the infrared extinction excess (A_{IRX}) as functions of the SFR_{UV} and the SFR_{IR} (e.g. Talia et al. 2015). In particular, it results:

$$SFR_{UV+IR} = SFR_{UV} + SFR_{IR} \tag{4.1}$$

$$A_{IRX} = 2.5 \log\left(\frac{SFR_{IR}}{SFR_{UV}} + 1\right) \tag{4.2}$$

To this aim, our first step was the measurement of the SFR_{UV} from the UV flux of the sources (S_{UV}) at 1500 Å, following the Kennicutt's relation (Kennicutt, 1998):

$$SFR_{UV}[M_\odot\ yr^{-1}] = 0.9 \times 10^{-28}\ L_{\nu_e}(1500\ Å)[erg\ s^{-1}\ Hz^{-1}] \tag{4.3}$$

In Eq. 4.3, the rest-frame UV luminosity (L_{ν_e}) can be obtained as a function of the redshift, the luminosity distance (D_L) and the observed flux (S_ν) according to the

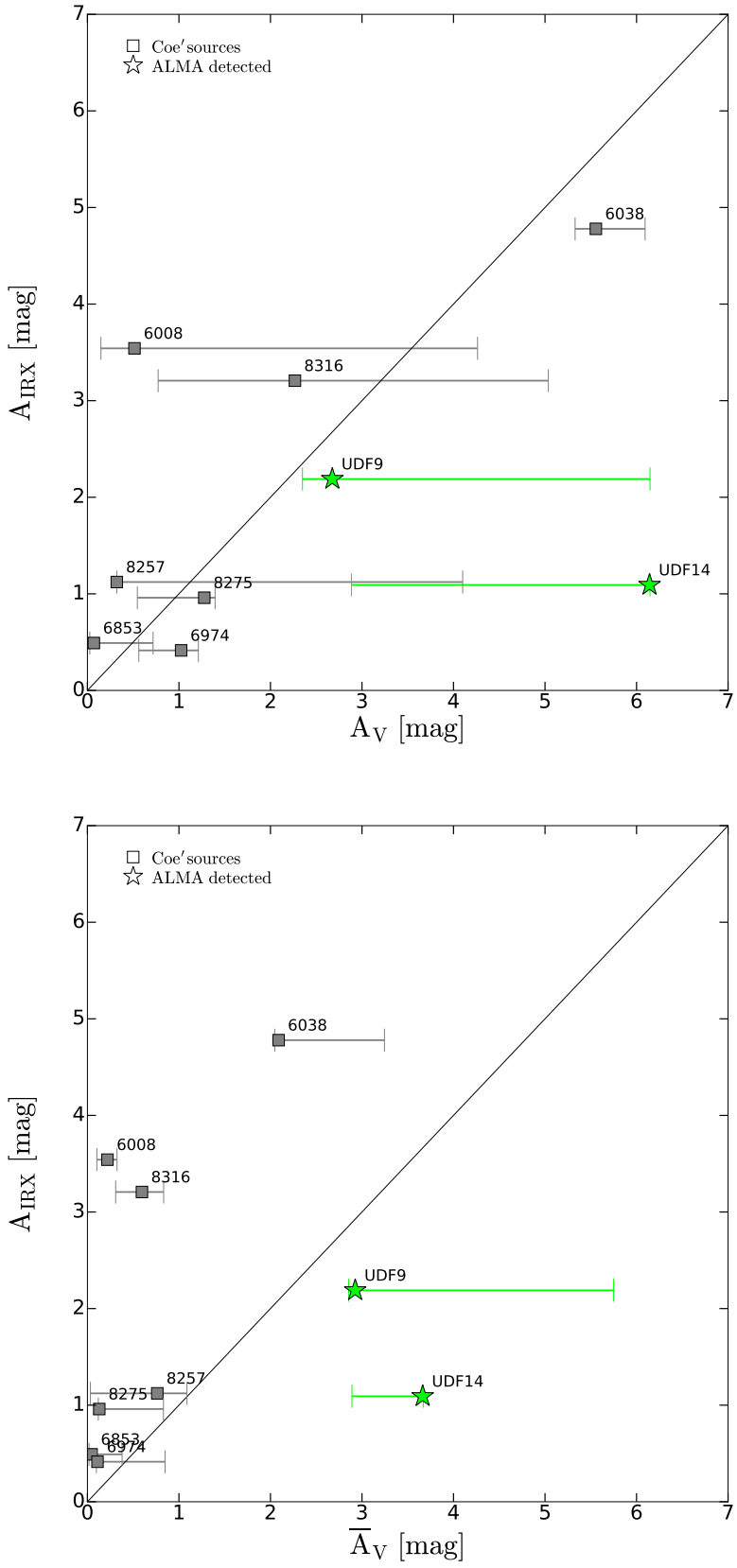

Figure 4.14: The IR extinction excess (A_{IRX}) vs. SINOPSIS (Fritz et al., 2007) optical extinctions for Dunlop et al. (2016) galaxies (*stars*) and Coe et al. (2006) sources (*squares*) in our sample (see Chap. 3, Sec. 3.1.1 and Sec. 3.2). In the **top panel** we present the comparison between the A_{IRX} (obtained from Talia et al. 2015) and SINOPSIS A_V for the youngest population, i.e. age $< 2 \times 10^7$ yr. On the contrary, in the **bottom panel** the A_{IRX} has been compared with SINOPSIS $\overline{A}_V$, i.e. the A_V averaged over all the 11 SSP age bins (for more details see Appendix B Sec. B.4.3). In both panels, the id of the sources (from Dunlop et al. 2016 and Coe et al. 2006) are reported too.

equation:

$$L_{\nu_e} = \frac{4\pi D_L^2}{1+z}\ S_\nu \tag{4.4}$$

While for every source in our sample we obtained the luminosity distance thanks to the internet calculator by Wright (2006), from the SINOPSIS output fitting model we retrieved the measures of the MUSE observed monochromatic flux (in erg cm^{-2} s^{-1} Å^{-1}) at the redshifted wavelength corresponding to the galaxy z. To convert the observed flux from erg cm^{-2} s^{-1} Å^{-1} to erg cm^{-2} s^{-1} Hz^{-1}, as required in the Eq. 4.3, the relation adopted has been:

$$S_\nu = 3.34 \times 10^{-19}\ \lambda^2\ S_\lambda \tag{4.5}$$

thus obtaining:

$$L_{\nu_e} = 3.34 \times 10^{-19}\ \frac{4\pi D_L^2}{1+z}\ \lambda^2\ S_\lambda \tag{4.6}$$

This last equation, inserted in the Eq. 4.3, allowed us to derive the observed SFR_{UV} for all the sources fitted by SINOPSIS (see Table 4.1).

We decided to measure the SFR_{IR} from the 24 μm-MIPS detections in Santini et al. (2009) only after the inspection of the *Herschel* data at 100 and 160 μm from the GOODS-H/PEP catalog (Elbaz et al. 2011, Lutz et al. 2011). For the sources in our sample, we were able to retrieve only one match between the sky-coordinates presented in the photometric catalog by Santini et al. (2009) and the coordinates in the GOODS-H/PEP catalog. We were able to find a convincing FIR counterpart only for the ALMA-detected galaxy UDF14. Therefore, we decided to adopt for our analysis the SFR_{IR} retrieved from the 24 μm luminosities of the sources. At this regard, since the earlier *Herschel* investigations, it was realized that the 24 μm SFR indicator was working very well up to redshift ~ 1, while it starts to fail at higher redshifts by overestimating somewhat the true L_{IR} (Nordon et al. 2010; Nordon et al. 2012; Rodighiero et al. 2010; Elbaz et al. 2011). This is particularly true at $z \sim 2$, where the PAH features enter the observed 24 μm passband. Recently, Magdis et al. (2012) have undertaken a systematic study of the typical SED of normal SF and starburst galaxies at $z \sim 2$, including both PACS and SPIRE data in their analysis. The results obtained by (and subsequently confirmed by Elbaz et al. 2011) pointed out that the mean SED does not evolve along the MS at $z \sim 2$, while it differs for the starbust population (characterized by a warmer dust component). These investigations revamped the use of the 24 μm SFR indicator, ideally allowing the adoption of a universal SED to extrapolate the L_{IR} for MS sources. Therefore, the infrared luminosities was extrapolated from the 24 μm flux densities (presented in Santini et al. 2009) by means of the MS templates of Magdis et al. (2012). Then, to obtain the SFR_{IR}, we applied the Kennicutt's relation (Kennicutt, 1998), properly rescaled for a Chabrier IMF (Chabrier, 2003):

$$SFR_{IR} = 10^{-10}\ L_{IR}\ [L_\odot] \tag{4.7}$$

Table 4.1: Measurements of the SFR and A_{IRX} inferred from the UV and IR luminosities at 1500 Å and 24 μm, respectively. In column 1 we report the source name, while in column 2 and 3 we present the spectroscopic redshift (this work) and the distance luminosity (from the Internet Calculator Wright 2006) of each source. In column 4 we give the luminosity of the source as retrieved from SINOPSIS theoretical models at 1500 Å , while in column 5 the inferred unobscured SFR. In column 6 and 7 we present the logarithm of the luminosity (in [$L_\odot$]) and the inferred SFR we extrapolated from the 24 μm flux densities (presented in Santini et al. 2009) by means of the MS templates of Magdis et al. (2012). In column 8 we report the total SFR (unobscured+obscured) and, finally, in column 9 the IR extinction excess (A_{IRX}) as retrieved from the relation presented in Talia et al. (2015).

id_{Coe}	z	D_L [Gly]	L_{UV}(1500 Å) [10^{-26} erg s^{-1} Hz^{-1}]	SFR_{UV} [$M_\odot$ yr^{-1}]	L_{IR}(24 μm) [$L_\odot$]	SFR_{IR} [$M_\odot$ yr^{-1}]	SFR_{UV+IR} [$M_\odot$ yr^{-1}]	A_{IRX} [mag]
6008	0.5440	10.226	4.89789	0.04408	10.0440	1.10662	1.15070	3.54
6038	0.6671	13.099	5.56266	0.05006	10.6058	4.03460	4.08466	4.78
6747	0.6216	12.007	4.59725	0.04138	-	-	0.04138	-
6853	0.8438	17.475	100.10513	0.99462	9.75461	0.56834	1.56296	0.49
6953	0.7655	15.502	50.07109	0.45640	-	-	0.45640	-
6974	0.6198	11.977	100.61885	1.45697	9.83052	0.67689	2.13386	0.41
7071	0.8940	18.765	60.42521	0.57827	-	-	0.57827	-
7664	0.8325	17.187	50.38431	0.48459	-	-	0.48459	-
7678	1.0382	22.572	80.37848	0.75406	-	-	0.75406	-
8257	0.6217	12.021	80.35206	0.75169	10.1341	1.36176	2.11345	1.12
8275	0.7651	15.492	400.34374	3.90937	10.7446	5.55392	9.46329	0.96
8316	0.6221	12.031	6.73597	0.06062	10.0422	1.10205	1.16267	3.21
UDF9	0.6675	13.109	80.90645	0.80158	10.7175	5.21795	6.01953	2.19
UDF14	0.7666	15.530	60.24925	0.56243	9.98927	0.97560	1.53803	1.09

4.2 The $M_\star$-SFR diagrams

The fundamental results obtained from the above-described three methods (i.e. through the use of SINOPSIS, *HyperZmass* and the UV and IR luminosities) are presented in the form of $M_\star$-SFR diagrams (see Fig. 4.15, Fig. 4.16 and Fig. 4.17, respectively).
In each one of the following $M_\star$-SFR diagrams, we present the inferred SFR of our galaxies against their stellar mass. For sake of clarity, we plotted the ALMA-detected sources (i.e. UDF9 and UDF14) with star-shaped markers, whereas squares refer to the sources from Coe et al. (2006). The black solid line shows the fit of the main-sequence (MS) of star-forming galaxies (from Renzini and Peng 2015) rescaled at the median redshift of our sample, $z = 0.7163$; while the black dashed lines show the starburst and passive limits to the main-sequence (defined as a factor $\times 4$ above and below the MS, Rodighiero et al. 2011). In addition, by means of a colour code we show the information on the extinction parameter, A_V. To make easier for the reader the comparison between the different diagrams, we decided to keep the same range limits for the x and y axes throughout the plots.
On the basis of what has been described above, in Fig. 4.15 we present SINOPSIS results, plotting the value of the SFR (in $M_\odot$ yr^{-1}) retrieved for the youngest stellar populations (i.e. with age $< 2 \times 10^7$ yr) versus the total stellar mass (i.e. the mass locked into stars, both those which are still in the nuclear-burning phase, and remnants; in $M_\odot$). The colour code used refers to the best-fit extinction value of the youngest stellar populations. In the plot, the majority of the sources falls within the limits (*black dashed lines*) of the main-sequence, even though the 6747 and 8257 objects fall in the passive region of the diagram, whereas UDF14, 6038 and 7664 turn to be starburst galaxies. Nonetheless, the most interesting SINOPSIS outcome is strictly related to the values assumed by the extinction parameter. As a matter of fact, the spectro-photometric code from Fritz et al. (2007), without an a-priori hint, identifies the two ALMA-detected sources (i.e. UDF9 and UDF14) as two of the more extincted galaxies in the sample ($A_V > 3$ mag), together with the 6038, 6747 and 7664 objects. This result is in perfect agreement with our expectations. In fact, since ALMA observes in a wavelength range of the e.m. spectrum dominated by the thermal emission of dust, to have significant detections in the ALMA range we expected UDF9 and UDF14 to be, by far, the most extincted galaxies. The expectation is confirmed by SINOPSIS.
In Fig. 4.16 we present *HyperZmass* results for all the 16 sources in our sample since *HyperZmass*, working with only the photometric data of the galaxies, allows to obtain a fit also for 7046 and 8624. In this case, all the sources fall within the MS, with the only exceptions for 6747 and 8316. In fact, while the 6747, 8316 and 8257 sources resulted to be massive ($M_\star > 10^{10}$ $M_\odot$) passive galaxies with low extinction ($0 < A_V < 0.5$ for 6747 and 8257; $0.5 < A_V < 1$ for 8316), the 7678 object appear to be a starburst galaxy.
In this plot it is interesting to underline the narrower range of extinction values assumed by the sources compared to SINOPSIS. As already discussed in Sec. 4.1.2, the reduce range of A_V is the consequence of the different age range adopted by the two codes. In *HyperZmass* the values retrived are measured on stellar populations with age spanning

from 0.1 to 9 Gyr (with the only constraint on the maximum age given by the age of the Universe at the galaxy redshift). Therefore, according to the 'selective extinction' hypotesis (Calzetti et al., 1994), the retrieved extinction values result to be lower than the SINOPSIS ones. In this scenario, it is not surprising if the extinction of the ALMA-detected sources drops to lower values even though the A_V of 6038, UDF9 and UDF14 still assumes the higher values of the entire population sample. Therefore, also from *HyperZmass* outcomes UDF9 and UDF14 turn out to be among the dustiest galaxies in our sample.

Finally, we present in Fig. 4.17 the $M_\star$-SFR diagram for the reduced sample of galaxies (i.e. 9 in all) for which it was possible to measure both the UV and IR SFR. For each source, the plot sets the total SFR, given by the sum of the IR-SFR (from the luminosity at 24 μm) and the UV-SFR (from the observed luminosity at 1500 Å), against the stellar mass retrieved by *HyperZmass*. The colour code adopted for the showed A_V is however based on the SINOPSIS results. Also in this plot the sources lay close to the main-sequence. We note that the IR-SFR accounts for the obscured SFR component that is missed by UV-optical indicators. This implies that UV based SFR, even corrected for dust extinction, could underestimate the total amount of SFR. This is the main explanation of the results presented in Figure 4.17, where we can observe that the less massive galaxy is well above the MS (i.e. a starburst). However, these sources (starburst) represent a very small fraction of star-forming galaxies (on the order of 2%) and they contribute by only 15% to the cosmic SFR density of the Universe (Rodighiero et al., 2011). In conclusions, starbursts are not representative of the normal star-forming galaxies at any redshift, and so UV-optical SFR indicator are appropriate for the bulk of SF galaxies, as in our sample.

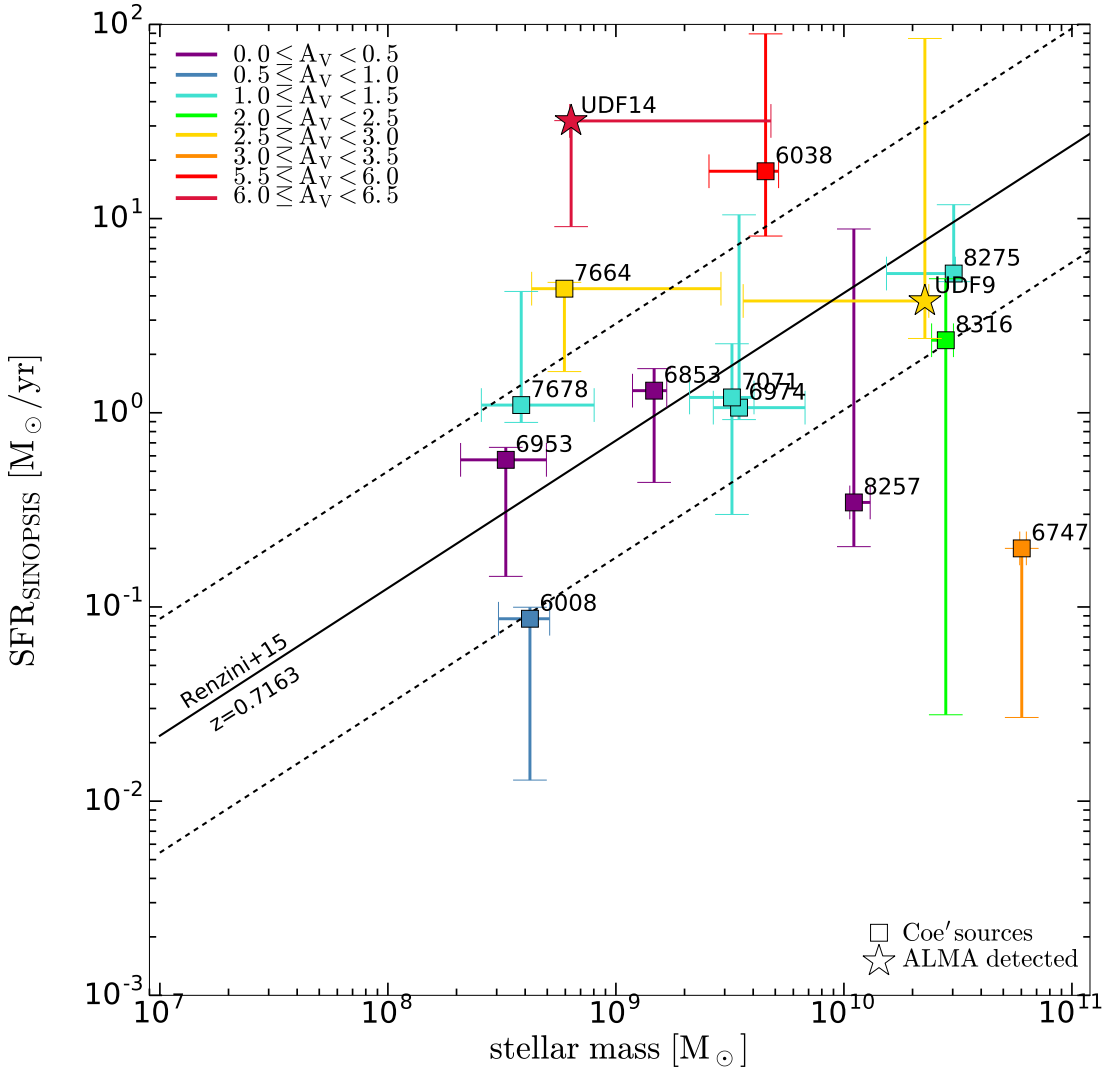

Figure 4.15: SINOPSIS (Fritz et al., 2007) inferred SFR vs. stellar mass for Dunlop et al. (2016) galaxies (*stars*) and Coe et al. (2006) sources (*squares*) in our sample (see Chap. 3, Sec. 3.1.1 and Sec. 3.2). The colour code (i.e. $0.0 < A_V < 0.5$, *purple*; $0.5 < A_V < 1.0$, *blue*; $1.0 < A_V < 1.5$, *cyan*; $2.0 < A_V < 2.5$, *green*; $2.5 < A_V < 3.0$, *yellow*; $3.0 < A_V < 3.5$, *dark orange*; $5.5 < A_V < 6.0$, *red*; $6.0 < A_V < 6.5$, *dark red*) represents the galaxy best-fit extinction value retrieved by SINOPSIS (the A_V for the youngest population, i.e. age $< 2 \times 10^7$ yr). The black solid line shows the fit of the main-sequence of star-forming galaxies (from Renzini and Peng 2015) rescaled at the median redshift of our sample, $z = 0.7163$. The black dashed lines (a factor $\times 4$ above/below the M,SRodighiero et al. 2011) show the starburst and passive limits to the main-sequence of star-forming galaxies. The id of the sources (from Dunlop et al. 2016 and Coe et al. 2006) are also reported. The lack of informations about the 7046 and 8624 sources is due to the rejection of the spectra from the code (for further details see Sec. 4.1.1).

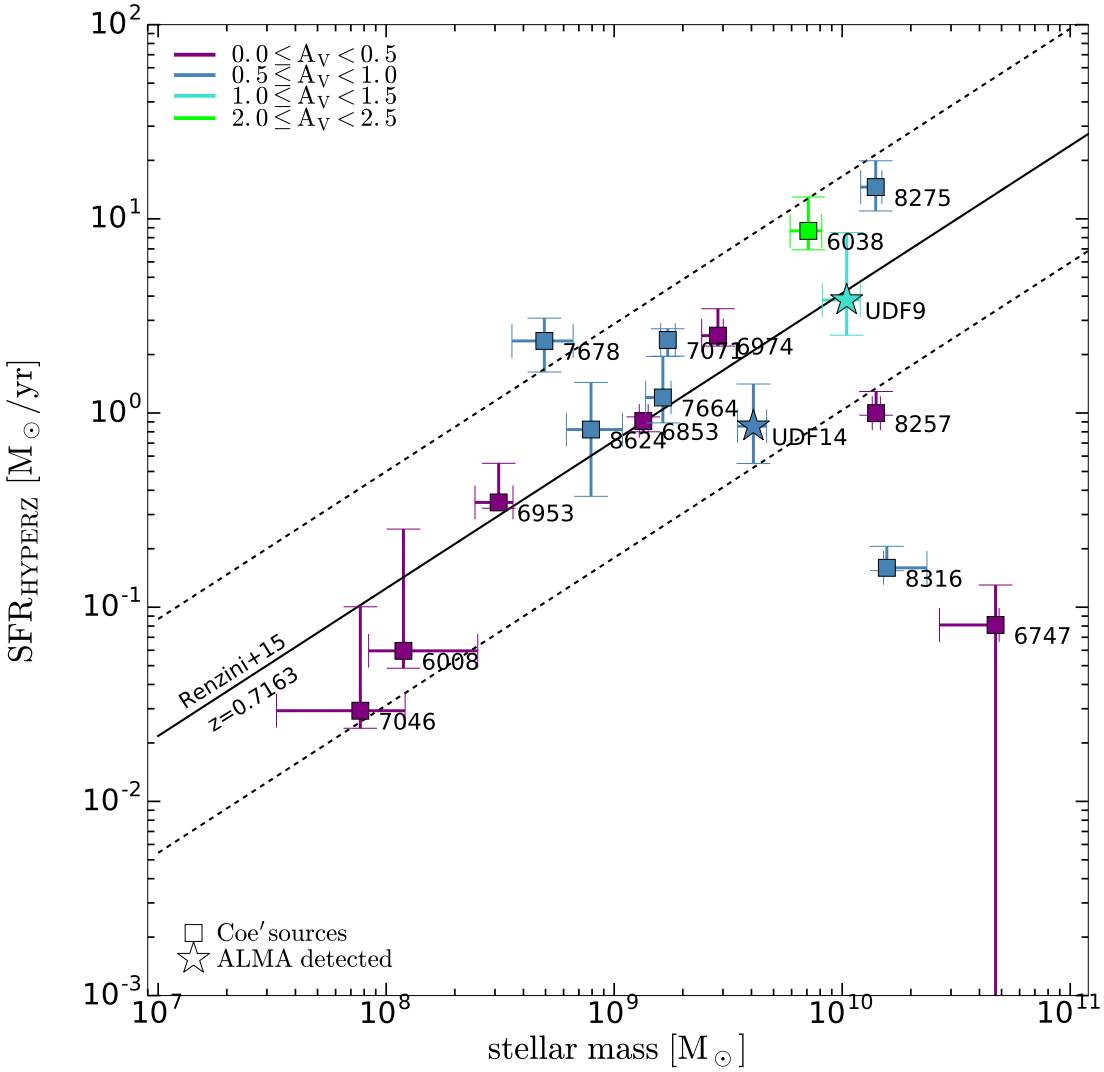

Figure 4.16: *HyperZmass* (Pozzetti et al., 2007) inferred SFR vs. stellar mass for Dunlop et al. (2016) galaxies (*stars*) and Coe et al. (2006) sources (*squares*) in our sample (see Chap. 3, Sec. 3.1.1 and Sec. 3.2). The colour code (i.e. $0.0 < A_V < 0.5$, *purple*; $0.5 < A_V < 1.0$, *blue*; $1.0 < A_V < 1.5$, *cyan*; $2.0 < A_V < 2.5$, *green*) represents the galaxy best-fit extinction value retrieved by *HyperZmass* code with a τ model for the SFH. The black solid line shows the fit of the main-sequence of star-forming galaxies (from Renzini and Peng 2015) rescaled at the median redshift of our sample, $z = 0.7163$. The black dashed lines (a factor $\times 4$ above/below the M,SRodighiero et al. 2011) show the starburst and passive limits to the main-sequence of star-forming galaxies. The id of the sources (from Dunlop et al. 2016 and Coe et al. 2006) are also reported.

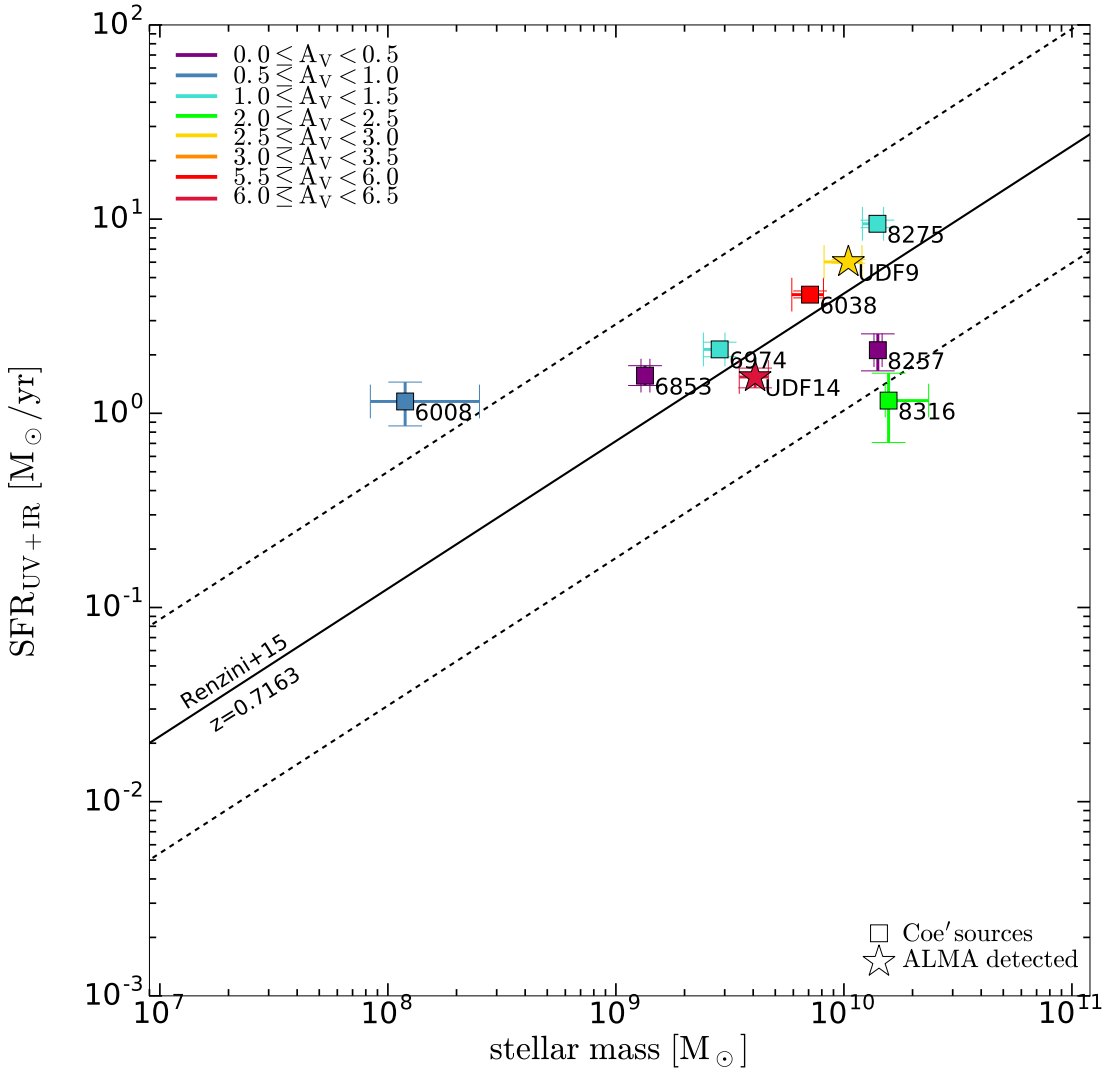

Figure 4.17: Inferred SFR_{UV+IR} vs. stellar mass for Dunlop et al. (2016) galaxies (*stars*) and Coe et al. (2006) sources (*squares*) in our sample (see Chap. 3, Sec. 3.1.1 and Sec. 3.2). The SFR_{UV} has been retrived (see Kennicutt 1998, Talia et al. 2015) from the L_λ(1500Å) of the SINOPSIS output SED-model while the SFR_{IR} has been obtained from the $L_\lambda(24\mu m)$ (Santini et al., 2009), using the Kennicutt (1998) relation with a Chabrier IMF (Chabrier, 2003). The SFR-errorbars presented correspond to the errors in the measurement of the $L_\lambda(24\mu m)$. The galaxies stellar mass reported is the one by the *HyperZmass* code. The colour code (i.e. $0.0 < A_V < 0.5$, *purple*; $0.5 < A_V < 1.0$, *blue*; $1.0 < A_V < 1.5$, *cyan*; $2.0 < A_V < 2.5$, *green*; $2.5 < A_V < 3.0$, *yellow*; $3.0 < A_V < 3.5$, *dark orange*; $5.5 < A_V < 6.0$, *red*; $6.0 < A_V < 6.5$, *dark red*) represents the galaxy best-fit extinction value retrieved by SINOPSIS (the A_V for the youngest population, i.e. age $< 2 \times 10^7$ yr). The black solid line shows the fit of the main-sequence of star-forming galaxies (from Renzini and Peng 2015) rescaled at the median redshift of our sample, $z = 0.7163$. The black dashed lines (a factor $\times 4$ above/below the M,SRodighiero et al. 2011) show the starburst and passive limits to the main-sequence of star-forming galaxies. The id of the sources (from Dunlop et al. 2016 and Coe et al. 2006) are also reported. Sources lacking an IR-detection (i.e. 6747, 6953, 7046, 7071, 7664, 7678 and 8624) are missing in this plot.

4.3 Discussion

We have performed a pilot analysis to understand the potential of including high-resolution spectral information (in particular emission lines) in SED fitting procedures of distant galaxies. We have selected a sample of (intrinsically dusty) ALMA-detected sources at $0.5 < z < 0.8$, where MUSE optical spectra provide a direct measure of [OII] emission lines.
The combination of these two state-of-the-art instruments, working in completely different spectral ranges (millimeter and optical) provides an important test on the potential scientific exploitation of the large data-sets that are becoming publicly available to the community (through the respective data archives). The main aim of this Thesis was to assess the actual statistical impact of combining blank field observations from the two facilities.
We summarize here our main results:

- We found that ALMA-detected sources on small fields are very few (i.e. two ALMA sources in the UDF10 MUSE pointing, UDF3 and UDF14 from Dunlop et al. 2016);

- Their numbers even decrease when searching for meaningful spectral information on MUSE data cubes (i.e. features to determine spectroscopic redshift and provide information on the stellar populations);

- Despite the small numbers in the deepest MUSE pointing in the HUDF (two ALMA sources), we have performed an extensive SED fitting analyses of these objects, comparing different methods;

- We have applied a similar technique to a comparison sample of H-band selected sources in the same region and in the same redshift range;

- Our results show that a spectrophotometric code (SINOPSIS), accounting for the presence of emission lines and combined to broad-band optical/near-IR photometry, returns very high extinctions for the dusty sources selected in the millimeter continuum. One of the two ALMA sources (UDF14) is, indeed, the most obscured and star-forming object of the sample. Such level of obscuration is not recovered by a standard SED fitting approach (e.g. *HyperZmass*), neglecting the presence of emission lines. The A_V derived from SINOPSIS for this starbursting source also exceeds the A_{IRX} computed including *Herschel* photometry, but the large formal uncertainties on this parameter for this source do not provide a conclusive result;

- When looking at the larger comparison sample of normal star-forming galaxies, we found that the two codes provide consistent results, within the range of allowed parameters (in particular the SF histories).

4.4 Future perspectives

The work presented in this Thesis represents a first but fundamental move into a comparative multiwavelength analysis of the HUDF, involving the synergy between ALMA (Dunlop et al., 2016) and MUSE (Bacon et al., paper in prep.) observations.
The glimpse obtained as a result of our work showed us the advantages produced in the scientific analysis of the sources thanks to the use of spectro-photometric fitting codes such as SINOPSIS (Fritz et al., 2007).
In this respect, our future perspectives concern the extension of the adopted procedure to all the MUSE pointings of the HUDF, either publicly-availables or not. From this proceeding, we expect a substantial improvement of the statistical sample presented in our work thus leading to a more exhaustive evaluation of the final results.
We are also interested to investigate possibles outcomes of an ALMA stacking procedure if applied onto the *HST*-detected sources (Coe et al., 2006) in the HUDF. To this aim, a new stacking method has been developed within the ALMA partnership giving the possibility to operate the stacking procedure both on the image and visibility planes. If the employment of this technique is successfull we will have further constraints to give as an input for the theoretical models.
A further temptative we take into account is the possibility to perform a stacking procedure for all the spectra in MUSE datacubes we discarded from our analysis due to the low S/N ratio.

Appendix A

EZ

In this appendix, we will present a concise description of the EZ software (see Garilli et al. 2010), a tool we extensively used to measure the spectroscopic redshifts for all the sources presented in our work. Nonetheless, the employment of a new software always requires an initial training to let the user acquire a good degree of expertise in its use. For this reason, in Sec. A.2 we report the final results obtained on the measurements of the spectroscopic redshifts for a sample of galaxies in the Hubble Frontier Field (HFF) MACS J0416.1-2403. Our data were matched with the z evaluations obtained by Caminha et al. (2016a) to acquire a likelihood estimate of our measures. The results of this match will be describe as well.

A.1 EZ: the software

Developed within the VIMOS-VLT Deep Survey (VVDS) project by Marco Fumana and Bianca Garilli[1] in collaboration with Roberto Scaramella[2] and Stephane Paltani[3], EZ (Easy-Z) is a software for the estimate of spectroscopic redshifts (Garilli et al., 2010). EZ can be used either in unsupervised mode or interactively, with the help of a gtk-based graphical user interface. As a matter of fact, EZ has an user-friendly command window and its use is pretty straightforward even if it is merely an interface to the command-line interpreter.
The program is developed in Python, with the bulk of computations performed in C to increase its computational speed (for the most CPU intensive tasks). Nevertheless, its Python classes can be directly imported in any other Python-based program, thus making it fully embeddable in any application.
The basis of the tool is the *decisional tree*, the very core of the software, which tries to mimic the human decisional process during the redshift measurement.
One of the first step performed by the decisional tree is the emission-line finding: a search

[1]IASF-Milano, INAF, Via Bassini 15, I-20133 Milan, Italy.
[2]INAF, Osservatorio Astronomico di Roma, via Frascati 33, 0040 Monte Porzio Catone (RM), Italy.
[3]ISDC, Observatoire de Genève, CH-1290 Versoix, Switzerland.

algorithm looks for sharp peaks in the spectrum as candidate emission lines and then see whether such peaks can be matched with a single redshift solution. To discard the possible presence of fake peaks due to fringing or noncleaned/badly cleaned cosmic rays, the implemented procedure first builds a *rough peak list* containing the position of all pixels showing a flux above a priori determined significance threshold (values can be user-defined). Then a gaussian is fitted to each of such positions, and only peaks within some default limits are retained. Since the minimum and maximum widths of a line depend on the resolution of the spectrum, limits values are user-configurable. Among the remaining line candidates, a further check is made whether the real peak flux is within a factor of 2 from the peak of the fitting gaussian function. This procedure allows to reject most of the fake peaks which often have an irregular shape.
When no emission lines are found in a spectrum, or when the lines found do not point to one single solution, EZ solve function combines cross-correlation first and a further fitting step to obtain a more robust redshift solution. In fact if m is the number of available spectral templates and so the total number of possible cross-correlations, for the n (user-definable parameter) redshifts corresponding to the retained highest correlation peaks, the fitting procedure allows to discriminate the best solution by the measurement of the lower $\chi^2_{\rm red}$.
If necessary, the sequence of operations performed by EZ can be customized according to user requirements.
When the interactive mode is chosen, the measurement of the spectroscopic redshift can be done automatically (via the decisional tree) or manually (direct recognition in the spectra of distinctive spectral features by user-sight). Nevertheless, if the user have to deal with low S/N spectra the automatic procedure in the majority of cases is not the most reliable. Also the presence of atmospheric emission and/or absorption lines in the spectra can act as an obstacle in obtaining a robust redshift evaluation since there is no provided atmospheric lines catalog to load. For this reason, frequently the search algorithm for emission lines is not able to discard from the rough peak list the presence of an atmospheric emission line, thus making the redshift solution found untrustworthy. It is for these reasons that in our work we had to deal mainly with the manual approach. This method requires quite a good knowledge and ability in recognizing typical features of the spectra. As a consequence, before starting the analysis of HUDF spectra we decided to improve our software skills and spectral features knowledge by determining the spectroscopic redshifts for already known sources.

A.2 MACS J0416.1-2403

Working within the Padua collaboration with the Ferrara CLASH group, made the choice of the training field easy. A paper (Caminha et al., 2016b) on the mass distribution of the Hubble Frontier Field (HFF) MACS J0416.1-2403 (hereafter MACS J0416) has been recently published by some members of the collaboration.
Listed as a MACS cluster (MAssive Cluster Survey, see Ebeling et al. 2010) due to its X-ray brightness ($L_X \approx 10^{45}$ erg s^{-1}), MACS J0416 is a massive ($M_{200} \approx 0.9 \times 10^{15}\ M_\odot$)

galaxy cluster at $z = 0.396$, identified as a merging system (Mann and Ebeling, 2012). Mann and Ebeling classification was based on the observed projected separation (≈ 200 Kpc) of the two brightest cluster galaxies (BCGs) and on the unrelaxed X-ray morphology of the system itself: its double-peaked X-ray structure, where the southern peak is offset by a few arcseconds from the corresponding BCG, it is a well-known expected feature in mergers (e.g. Bradač et al. 2006; Merten et al. 2011). Moreover, on the basis of its predicted Einstein radius, MACS J0416 was designeted as one of the five clusters with high magnification in the CLASH sample.

A.2.1 MUSE pointings

MACS J0416 has been observed with MUSE from two different programs which covered the North-East (NE) and South-West (SW) regions of the cluster.
The NE region was observed within a GTO program (ID 094.A-0115B, PI: J. Richard) in November 2014, for a total of 2 hours splitted in 4 exposures. Deeper observations in the SW region were carried out by the program ID 094.A-0525(A) (PI: F.E. Bauer) obtaining as a result 58 pointings of approximately 11 minutes each, executed over the period October 2014 – February 2015, and leading to a total amount of 11 hours of exposure time[4].
The footprints of these two MUSE pointings are shown in Fig. A.1 (see the white squares), overlaid onto an *HST* color image (V_{606}+i_{775}+z_{850}) of the cluster.
After the use of the MUSE reduction pipeline[5] and the Zurich Atmosphere Purge (ZAP, Soto et al. 2016) tool, the two final data-cubes obtained by Caminha et al. have a spatial pixel scale of $0.2''$, a spectral coverage from 4750 Å to 9350 Å with a dispersion of 1.25 Å/pixel and a fairly constant spectral resolution of ≈ 2.4 Å over the entire spectral range.
Nevertheless, to achieve their goal, Caminha et al. evaluated spectroscopic redshifts for all the AstroDeep Frontier Fields catalog sources[6] (Castellano et al., 2016) in the MUSE field of view. For this reason, 1415 spectra (whereof 716 in the N-E pointing and 699 in the S-W one) have been extracted within circular apertures having a radius[7] of $0.8''$.

A.2.2 EZ $z_{\rm spec}$ measurements

We decided to begin the training starting from Caminha et al. (2016b) sources and choosing randomly a total amount of 63 spectra, whereof 23 in the N-E pointing and 40 in the S-W one.

[4]One of the 58 exposure performed in the MUSE SW region of the cluster had to be discarded because of the presence of a satellite track.

[5]MUSE reduction pipeline version 1.2.1.

[6]The AstroDeep FF catalog reaches a 90% completeness limit at mag F160W ≈ 27.25 for disk-like galaxies. Objects flagged as possible spurious detections in the AstroDeep catalog were not considered in Caminha et al. (2016b).

[7]The dimensions of the spaxel circular aperture has been choosen to provide a good compromise in the effort to maximize the S/N and minimize source confusion.

Figure A.1: Footprints (*in white*) of the two MUSE pointings (ID 094.A-0115B, PI: J.Richard; ID 094.A-0525A, PI: F.E. Bauer) of the HFF MACS J0416 (Ebeling et al., 2010), overlaid onto an *HST* colour image (V_{606}+i_{775}+z_{850}) of the cluster. The empty circles (1′ radius) show the sky-position of the 63 sources (23 in the N-E pointing and 40 in the S-W one) randomly chosen for our training on the measurement of spectroscopic redshifts with EZ (Garilli et al., 2010). The colour of the circles corresponds to the quality flag assigned to our measurement according tothe scheme described in Caminha et al. (2016a) and Balestra et al. (2016), i.e. 3=secure (*green*), 2=likely (*blue*), 1=not-reliable (*red*) and 9=based on a single emission line (*yellow*).

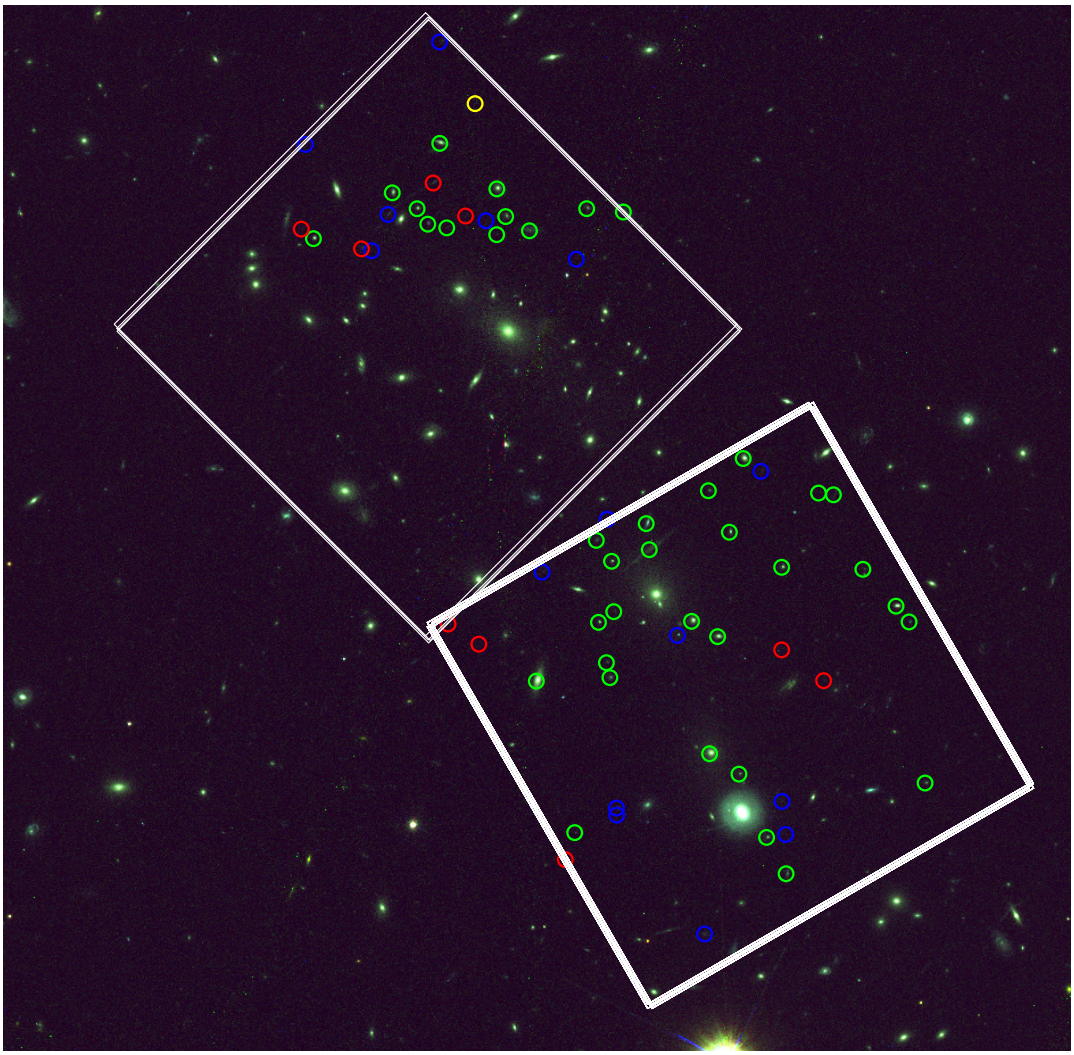

In addition to the spatial area covered by the two MUSE pointings, in Fig. A.1 we show the sky-positions of the 63 sources chosen for the training, the colour code reported corresponds to the values of the quality flags assigned to our measurements (see below). In Table A.1 the spectroscopic redshift measurements from Caminha et al. ($z_{\rm Caminha}$) and this work ($z_{\rm IANI}$) are reported; their quality flags are presented too (respectively $\rm qf_{Caminha}$ and $\rm qf_{IANI}$).

For our measures the quality flags assigned follow the scheme described in Caminha et al. (2016a) and Balestra et al. (2016), i.e. 3=secure, 2=likely, 1=not-reliable and 9=based on a single emission line.

As well-showned in Fig. A.2, about 63% of the total amount of sources show a really good match between our measurements and Caminha et al. ones, since the redshift difference Δz between the two measures is $|\Delta z| \leq 0.01$. However, the leftovers present Δz values up to 2, approximately. A good explanation for this result starts from the consideration of the quality flags. It is immediate to notice that the majority of not-reliable ($\rm qf_{IANI} = 1$, *red*) and some of the likely ($\rm qf_{IANI} = 2$, *blue*) measurements retrieve $|\Delta z|$ values over 0.01. On the contrary, for $|\Delta z| \leq 0.01$ we have almost uniquely secure ($\rm qf_{IANI} = 3$, *green*) and likely measures.

Notwithstanding the whole picture just described, in the $|\Delta z| \geq 0.01$ region there are two sources with a quality flag $\rm qf_{IANI} = 3$. These sources are CLASHVLTJ041609.7-240348 ($z_{\rm Caminha} = 2.0872$, $z_{\rm IANI} = 0.7713$) and IDVLTJ041606.0-240425 ($z_{\rm Caminha} = 3.077$, $z_{\rm IANI} = 0.8467$).

While for CLASHVLTJ041609.7-240348, Caminha et al. spectroscopic redshift is confirmed also by VIMOS measurement (Balestra et al., 2016), for IDVLTJ041606.0-240425 we decided to look at the MUSE data cube and cut-outs since there were no other possible comparisons.

As can be seen Fig. A.3, in the spectrum we observe really intense emission lines for the [OII] ($\lambda_0 = 3272.5$ Å), $\rm H_\beta$ ($\lambda_0 = 4861.3$ Å), [OIII](db−1/3) ($\lambda_0 = 4958.9$ Å) and [OIII](db−1) ($\lambda_0 = 5006.8$ Å) therefore the hypothesized value $z_{\rm IANI} = 0.8467$. Though the presence of these unequivocal lines, Caminha et al. retrieve a redshift value $z_{\rm Caminha} = 3.077$, recognizing as the one and only true emission line in the spectrum a $\rm Ly_\alpha$ ($\lambda_0 = 1215.7$ Å) at $\lambda \approx 4956$ Å. Only after a sight at the cut-out of the source, we realized that the error was in our z-evaluation. The fault was due to the contamination of the spectrum by a close-by source: IDVLTJ041605.9-240425. As a matter of fact, IDVLTJ041605.9-240425 has $z_{\rm Caminha} = 0.8467$ (see Table A.1), value in perfect agreement with our measurement.

Figure A.2: Measured spectroscopic redshift ($z_{\rm IANI}$, this work) vs. spectroscopic redshift ($z_{\rm Caminha}$, Caminha et al. 2016b) for the 63 galaxies (23 from the N-E pointing, 40 from the S-W one) chosen within the HFF MACS J0416 MUSE pointings. The colour code adopted shows the likelihood of our measurements, with the red circles corresponding to $\rm qf_{IANI} = 1$, the blue ones to $\rm qf_{IANI} = 2$, the green ones to $\rm qf_{IANI} = 3$ and finally the yellow ones to $\rm qf_{IANI} = 9$. The quality flag scheme adopted is the one from Caminha et al. (2016a) and (Balestra et al., 2016), i.e. 3=secure, 2=likely, 1=not-reliable and 9=based on a single emission line. Histograms on the redshift distribution of the sources (for $z_{\rm Caminha}$ and $z_{\rm IANI}$) are reported too. In grey the cumulative redshift distributions of the measurements, while in red, blue, green and yellow the sources redshift distributions according to the above-described colour code.

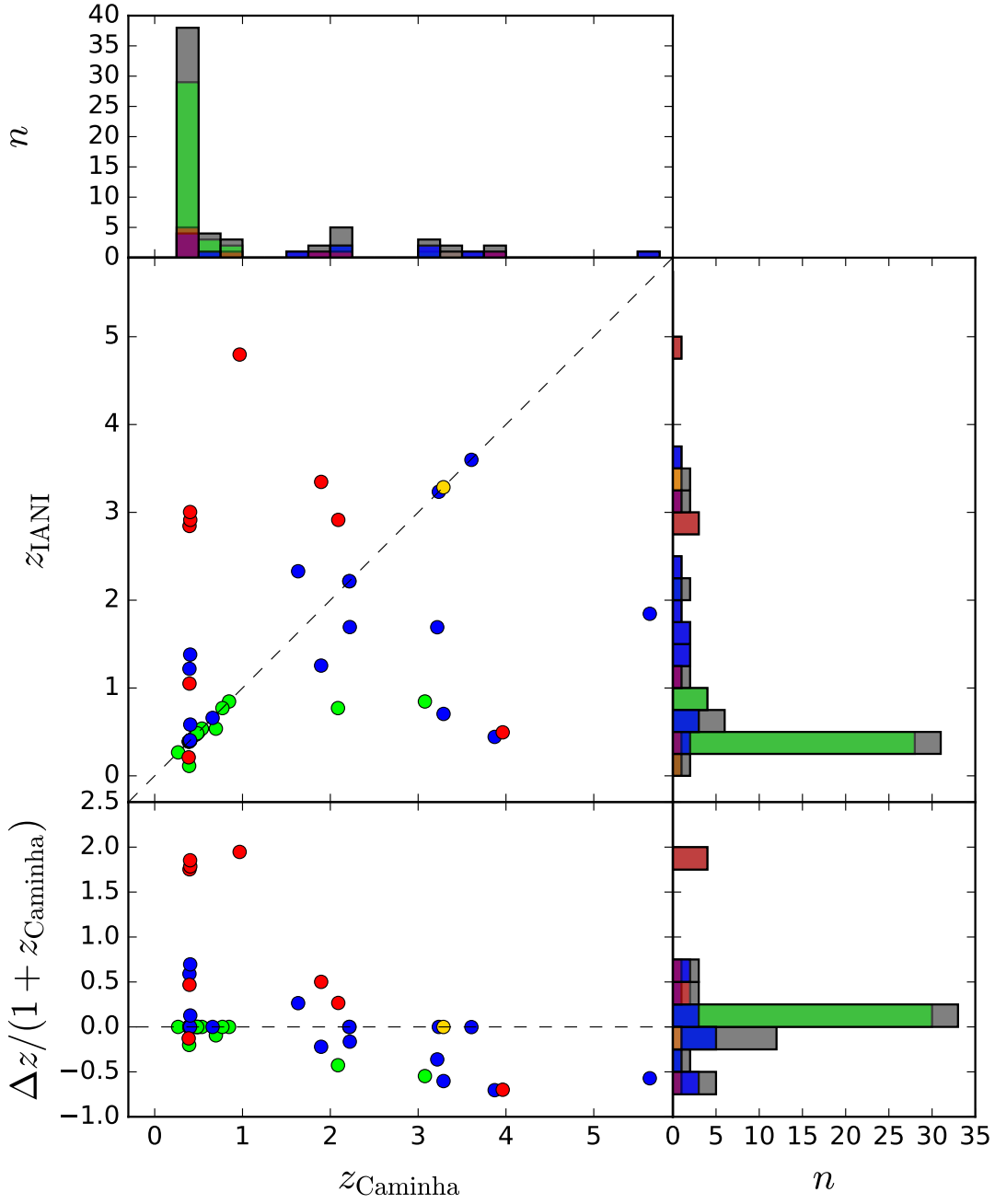

Figure A.3: MUSE spectra of the sources CLASHVLTJ041609.7-240348 (**top panel**) and IDVLTJ041606.0-240425 (**bottom panel**). The spectra presented (black solid line) have been smoothed for sake of clarity. The orange solid lines show the line identification (for the [OII], H_β and [OIII]) at the basis of our spectroscopic redshift measurements whereas with blue solid line are marked the emission lines used for the redshift evaluation in Caminha et al. (2016b). For each source a cut-out colour image is presented too, along with the 0.8″ radius circles (in *magenta*) within which the spectra were extracted from the MUSE data cubes.

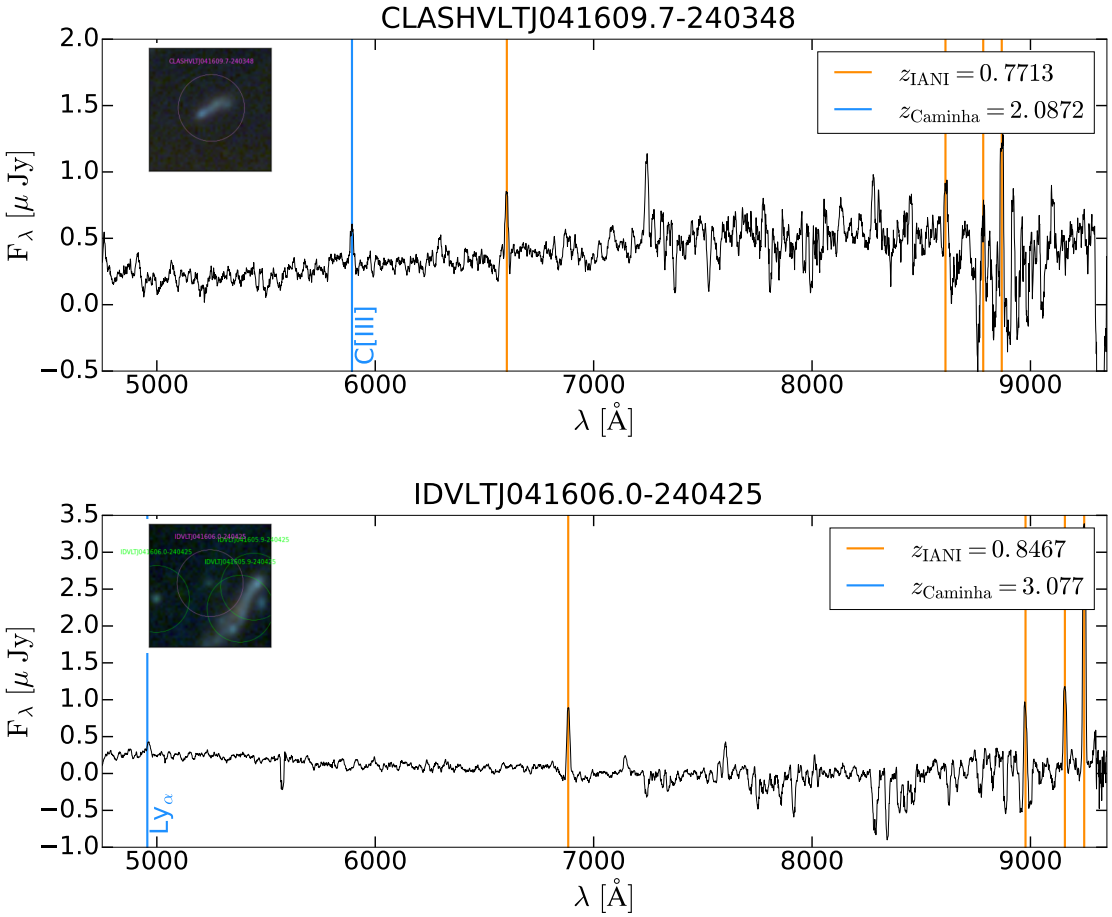

Table A.1: Comparison between the inferred spectroscopic redshifts (this work) and the spectroscopic redshifts retrieved by Caminha et al. (2016b) for the 63 sources in HFF MACS J0416 (Ebeling et al., 2010) within the two MUSE pointings of the cluster (ID 094.A-0115B, PI: J.Richard; ID 094.A-0525A, PI: F.E. Bauer). Column 1 gives the name of the sources as it is presented in Caminha et al. (2016b), while column 2 and 3 give the sky-coordinates of the sources ($\alpha_{\rm J2000.0}$, $\delta_{\rm J2000.0}$). Column 4 and 5 report the estimate of the spectroscopic redshift and respective quality flag of each source in Caminha et al. (2016b), whereas column 6 and 7 present our spectroscopic redshifts and quality flags.

$\rm id_{VLT}$	$\alpha_{\rm J2000.0}$	$\delta_{\rm J2000.0}$	$z_{\rm Caminha}$	$\rm qf_{Caminha}$	$z_{\rm IANI}$	$\rm qf_{IANI}$
CLASHVLTJ041605.1-240442	64.021439	-24.078453	2.2164	3	2.2151	3
CLASHVLTJ041606.4-240434	64.026718	-24.076387	0.3951	3	0.3954	3
CLASHVLTJ041606.6-240422	64.027580	-24.072756	3.2175	3	1.692	2
CLASHVLTJ041606.8-240420	64.028313	-24.072271	0.3924	3	0.3926	3
CLASHVLTJ041606.9-240430	64.028885	-24.075060	0.4001	3	0.4002	3
CLASHVLTJ041607.1-240444	64.029373	-24.079010	0.4017	3	0.4018	3
CLASHVLTJ041607.1-240500	64.029705	-24.083440	0.3969	3	0.3972	3
CLASHVLTJ041607.2-240525	64.029907	-24.090258	2.2173	3	2.2171	2
CLASHVLTJ041607.3-240442	64.030452	-24.078431	0.4036	3	0.4039	3
CLASHVLTJ041607.5-240444	64.031044	-24.078962	1.6333	3	2.3293	2
CLASHVLTJ041607.8-240429	64.032333	-24.074734	0.4678	3	0.4678	3
CLASHVLTJ041608.0-240346	64.033279	-24.062946	0.4846	9	0.4846	3
CLASHVLTJ041608.1-240450	64.033836	-24.080561	0.4014	3	0.4015	3
CLASHVLTJ041608.2-240447	64.033981	-24.079996	0.3901	3	0.3901	3
CLASHVLTJ041608.4-240346	64.034798	-24.062819	0.3887	3	0.3887	3
CLASHVLTJ041608.8-240450	64.036886	-24.080693	0.4032	3	0.4035	3
CLASHVLTJ041608.9-240349	64.037170	-24.063656	0.5376	3	0.5377	3
CLASHVLTJ041609.2-240343	64.038521	-24.062071	0.4053	3	0.4056	3
CLASHVLTJ041609.2-240347	64.038155	-24.063118	0.3973	3	0.3978	3
CLASHVLTJ041609.5-240331	64.039421	-24.058846	3.288	9	3.2858	9
CLASHVLTJ041609.7-240348	64.040596	-24.063545	2.0872	3	0.7713	3
CLASHVLTJ041609.8-240323	64.040894	-24.056511	2.2216	2	1.6939	2
CLASHVLTJ041609.8-240337	64.040886	-24.060349	0.3992	3	0.3995	3
CLASHVLTJ041609.9-240342	64.041161	-24.061848	1.8955	3	3.3469	1
CLASHVLTJ041610.3-240344	64.042854	-24.062220	0.3945	3	0.3948	3
CLASHVLTJ041611.1-240337	64.046455	-24.060392	3.2355	3	3.2346	2
CLASHVLTJ041611.1-240350	64.046120	-24.063953	0.3972	3	0.3977	3
IDVLTJ041605.0-240504	64.020775	-24.084547	0.3978	3	0.398	3
IDVLTJ041605.3-240440	64.021980	-24.077856	0.4051	3	0.4057	3
IDVLTJ041605.6-240435	64.023354	-24.076462	0.3932	3	0.3935	3
IDVLTJ041605.9-240425	64.024574	-24.073643	0.8467	3	0.8468	3
IDVLTJ041606.0-240425	64.025192	-24.073578	3.077	3	0.8467	3
IDVLTJ041606.0-240450	64.024979	-24.080675	0.3872	2	0.2107	1
IDVLTJ041606.4-240446	64.026718	-24.079510	0.3963	2	1.0503	1
IDVLTJ041606.4-240507	64.026703	-24.085243	0.4051	1	0.5837	2
IDVLTJ041606.4-240511	64.026550	-24.086493	0.403	1	0.4043	2
IDVLTJ041606.4-240517	64.026535	-24.087980	0.6967	3	0.5373	3
IDVLTJ041606.6-240512	64.027344	-24.086605	0.3924	3	0.1128	3
IDVLTJ041606.8-240503	64.028488	-24.084211	0.3983	3	0.3984	3
IDVLTJ041607.1-240425	64.029755	-24.073490	0.3953	3	0.3955	3
IDVLTJ041607.7-240433	64.032205	-24.075720	0.5004	3	0.5002	3
IDVLTJ041608.1-240428	64.033947	-24.074569	3.8713	9	0.4435	2
IDVLTJ041608.1-240434	64.033768	-24.076159	0.3968	3	0.3972	3
IDVLTJ041608.1-240441	64.033676	-24.078066	0.3983	2	0.4005	3
IDVLTJ041608.1-240508	64.033562	-24.085497	0.3958	2	1.219	2
IDVLTJ041608.1-240509	64.033554	-24.085762	5.6377	9	1.8451	2
IDVLTJ041608.2-240442	64.034309	-24.078470	0.3966	3	0.3969	3
IDVLTJ041608.3-240431	64.034401	-24.075369	0.3972	3	0.3971	3
IDVLTJ041608.5-240353	64.035225	-24.064732	3.2891	3	0.7049	2
IDVLTJ041608.5-240511	64.035294	-24.086424	0.2669	3	0.2671	3
IDVLTJ041608.6-240515	64.035683	-24.087446	0.9673	3	4.7969	1
IDVLTJ041608.8-240436	64.036644	-24.076569	0.6595	9	0.6596	2
IDVLTJ041609.2-240350	64.038528	-24.063803	0.4841	3	0.4841	3
IDVLTJ041609.4-240348	64.038971	-24.063274	0.404	1	1.3807	2
IDVLTJ041609.4-240445	64.039268	-24.079294	0.3966	1	2.845	1
IDVLTJ041609.6-240347	64.039818	-24.063097	2.0904	9	2.9143	1
IDVLTJ041609.7-240443	64.040543	-24.078533	3.9629	3	0.4952	1
IDVLTJ041609.9-240348	64.041382	-24.063404	0.7712	3	0.7714	3
IDVLTJ041610.0-240346	64.041824	-24.062822	0.3949	3	0.3954	3
IDVLTJ041610.3-240347	64.043030	-24.063036	1.895	3	1.2553	2
IDVLTJ041610.5-240352	64.043709	-24.064411	3.6067	1	3.5981	2
IDVLTJ041610.6-240352	64.044128	-24.064339	0.4052	2	2.9143	1
IDVLTJ041611.2-240349	64.046623	-24.063593	0.403	1	3.0037	1

Appendix B

SINOPSIS

Developed by Jacopo Fritz[1] on the basis of the code in Poggianti et al. (2001) and on the model described in Fritz et al. (2007) and Fritz et al. (2011), **SINOPSIS** (SImulatiNg OPtical Spectra wIth Stellar population models) is a spectro-photometric fitting code[2] with the aim of reproducing the combined spectral and broad-band photometric data of galaxies.
Through the use of Simple Stellar Population models (SSP), the spectral fitting code is able to reproduce the galactic emission from the far UV to the Mid-Infrared, including both the stellar and the nebular emission. Hence, the code enables to derive fundamental quantities that describe the build up of stellar mass and the characteristics of stellar emission in a galaxy (i.e. star formation rates, extinction, age of stellar populations, stellar masses).
In this work, SINOPSIS has been extensively used to mainly obtain the star formation rates (SFRs) and stellar masses for all the sources studied (see Sec. 4.1.1).
In the following pages, the reader will find a concise description of SINOPSIS and its working principles besides the main adjustments to adapt the code to our requirements.

B.1 SINOPSIS: the code

SINOPSIS goal is to reconstruct the Star Formation History (SFH) of galaxies, i.e. the amount of stars formed at each epoch throughout the galaxy evolutionary history, via the SSP models.
An SSP is defined as an assembly of coeval, initially chemically homogenous, single stars. The main physical parameters needed to give a complete description of an SSP are: its age (t), its chemical composition (X, Y) and its Initial Mass Function (IMF). On the basis of this definiton, it appears clear that galaxies are not SSP due to the presence

[1] U.N.A.M., Instituto de Radioastronomía y Astrofísica (IRyA), Morelia, Mexico (`j.fritz@crya.unam.mx`).
[2] SINOPSIS is an open-source software, freely downloadable from `http://www.crya.unam.mx/gente/j.fritz/JFhp/SINOPSIS.html` .

of stars with different age and metallicity. However, a complex population can always be expanded in a series of SSPs. This is the fundamental idea at the basis of many scientific tools, and among them SINOPSIS, for the spectro-photometric analysis of complex systems like galaxies.
So, to achieve its aim, SINOPSIS tries to construct a synthetic model minimizing the differences with the observed features in data, after the measurement of main spectral characteristics.
The measured features that are used to compare the likelihood between the model and the spectra are the avarage flux in significant portions of continuum-dominated spectral regions and the Equivalent Width (EW) of the most important emission and absorpiton lines. The continuum flux is evalueted in specific wavelength ranges to avoid any important spectral line while simultaneously sampling as best as possible the shape of the spectral continuum. Among all the wavelength ranges, particular emphasis is given to the 4000 break and its related parameter D4000 (see Bruzual A. 1983) as it is considered a good indicator of the stellar age. In the matter of the emission lines, SINOPSIS compares the equivalent widths[3] of H_α, H_β, H_δ, H_ϵ + CaII (H), CaII (K), H_η and [OII]. Other lines, even though prominent, are only measured but not used to constrain the model[4].
Therefore, to obtain the synthetic model SINOPSIS combines about 200 theoretical SSP spectra of different ages and common metallicity (Z) with templates of the near (NIR) and mid (MIR) infrared emission assuming no pre-determined star formation history.
The SSP synthetic spectra are built using the Padova evolutionary tracks (i.e. isochrones) from Bressan et al. (2012) (PARSEC) with a Chabrier IMF (see Chabrier 2003), with stellar masses in the range[5] $0.1 \leq M \leq 100\ M_\odot$. The SSP ages span the range from 10^4 yr to 1.4×10^{10} yr.
The optical spectra used in SINOPSIS were obtained from the combination of two different sets of observed stellar atmospheres. The first set uses the new high resolution SSP models by Charlot and Bruzual A. (2017). On the contrary, the second set of SSPs uses the MILES library (see Sánchez-Blázquez et al. 2006). Currently, SINOPSIS[6] allows to use three different Z-values: sub-solar (Z=0.004), solar (Z=0.02) and super-solar (Z=0.04).
The gas emission was computed and included in the theoretical spectra by the use of the photoionization code CLOUDY (Ferland, 1996) while the possible presence in the spectra of forbidden lines (for SSPs younger than $\sim 2 \times 10^7$ yr), i.e. the nebular component, was implemented assuming *case B recombination* (see Osterbrock 1989; for more details see Fritz et al. 2011). Finally, the emission from the circumstellar envelopes of AGB stars was computed and added as described in Bressan et al. (1998).
Because of the high temporal resolution of the integrated optical spectra (from 10^4 yr to

[3]For a complete description of the algorithm for the measument of the EW see Fritz et al. (2014).
[4]For example, the [OIII] line at 5007 Å, beacuse too sensitive to the physical conditions of the gas and of the ionizing source, and the Na and Mg lines at 5890 Å and 5177 Å respectively, because strongly affected by the α-enhancement, a physical process not taken into account by SINOPSIS SSPs.
[5]The isochrones for stars more massive than $25M_\odot$ include also a treatment for the Wolf-Rayet phase.
[6]SINOPSIS version used in this work is 1.6.3 (not yet publicly realesed).

1.4×10^{10} yr), determining the age of stellar populations is beyond the capabilities of any spectral analysis. For this reason, Fritz et al. decided to reduce the stellar age resolution by binning the spectra, thus taking into account both the evolutionary phases of stars and the trends in spectral features as a function of the SSP age (for more details see Fritz et al. 2007). As a matter of fact, the D4000 index and the EW of the CaII (H), CaII (K), [OII], [OIII] and Balmer lines change significantly with the stellar age. Nevertheless, while the spectral line characteristics as a function of age are exploited as the most reliable way to assign an age value to the dominant stellar populations, the shape of the emission in the continuum give constraints both to the total stellar mass and dust attenuation. At the end of this procedure, the number of theoretical spectra retrieved is 12.[7] In the second column of Table B.5 are reported for each age bin the corresponding age interval of the SSPs adopted.

Before being added together, each of the 12 age-binned SSP spectra[8] is weighted with a proper value of the stellar mass and dust extinction by an amount which generally depends on the SSP age itself. For this reason it is important to underline that in SINOPSIS the effect of extinction is treated by assuming that dust is distributed along the line-of-sight between the star and the observer like a slab, an uniform screen as described by Liu et al. (2013). This scenario has been demonstrated a fairly good representation of the dust effect on large scales. Different extinction can be chosen, including the attenuation law from Calzetti et al. (1994) (CAL), the average Milky Way (MW) extinction curve (Cardelli et al., 1989) and the Small Magellanic Cloud (SMC) curve. In Fig. B.1 are shown all the currently implemented extinction curves in SINOPSIS.

The code also includes a treatment of extinction according to the 'selective extinction' hypotesis (e.g. Calzetti et al. 1994), i.e. the extinction is fully dependent on the stellar age[9]. This hypotesis is well-supported since the youngest stellar populations are expected to be found at least partially nested in the dust of molecular clouds where they formed, while as they become older, they progressively emerge from them, either by means of supernova explosions and/or due to proper motions of the star cluster.

Therefore, the model spectrum is constructed as follows:

$$F_{\rm MOD}(\lambda) = \sum_{i=1}^{N_{\rm SSP}} {\rm SFR}(t_i) \cdot \Delta t_i \cdot {\rm F}_i(\lambda) \cdot 10^{-0.4 {\rm R_V} \cdot {\rm E(B-V)}_i \cdot {\rm A}_\lambda / {\rm A_V}} \tag{B.1}$$

where $N_{\rm SSP}$ is the total number of SSP models (each one with a different age but same value in matallicity) and for the i-th SSP: ${\rm F}_i(\lambda)$ is its spectrum, ${\rm SFR}(t_i)$ its star formation rate, Δt_i its time-scale and ${\rm E(B-V)}_i$ its colour excess (i.e. the extinction). ${\rm A}_\lambda/{\rm A_V}$ is the extinction curve normalized in the V-band while ${\rm R_V}$ is the ratio of total to selective absorption in V-band, i.e. ${\rm R_V} = {\rm A_V}/{\rm E(B-V)}$.

[7] This number is always for a fixed metallicity value.

[8] It is important to notice that due to the binning process, the now-on considered spectra are not belonging to Simple Stellar Populations anymore. Nevertheless, for the sake of simplicity, we will continue to use the SSP acronym.

[9] This treatment of dust obscuration allows to well reproduce the intensity of emission lines, the most prominent features of the youngest stars.

The number of free parameters depends on the chosen star formation history. SINOPSIS currently allows only two SFH patterns: the Free-Form (FF) and the Analytic (An) one. If standard settings for the SSP models are used (i.e. the FF approach, see Fritz et al. 2007) SSP averaged spectra up to 12 different ages are used, letting completely free to vary for each one of them both the SFR and the extinction (i.e. $E(B-V)_i$), independently from the age. Hence, in the FF pattern the total number of free parameters amount to 24 (12 values for the SFR and $E(B-V)_i$).
On the contrary the An pattern tries to limit the number of free parameters by assuming an analytical form for both SFR and $E(B-V)_i$ as functions of the cosmic time[10].
The combination which minimizes the differences between the observed and the model spectrum is achieved by the use of an Adaptive Simulated Annealing (ASA) algorithm (for more details see Fritz et al. 2007), a particularly usefull algorithm in solving non-linear problems in a multi-parameters space with several local minima. The algorithm search the best fit by exploring randomly the parameters space and the values retrieved at the end of each iteration depend on the previous trail point.
The use of the ASA method is crucial in obtaining estimates of the uncertainties on physical quantities such as stellar mass, star formation rate, mean ages and so on. As a metter of fact, for each SSP at a given metallicity, several spectral fitting are runned (up to a maximum of 11) each of them starting from a different point in the parameter space. Each fitting run retrieve a best-fit model (with corresponding χ^2) with different final parameters if compared to the others. The χ^2 function is given by:

$$\chi^2 = \sum_{i=1}^{N} \left(\frac{M_i - O_i}{\sigma_i} \right)^2 \tag{B.2}$$

where M_i and O_i denote the quantities measured from the model and the observed spectra respectively while σ_i represents the observed uncertainties and N the total number of observed constraints.
Among the best-fit models, the one which result in the lowest χ^2 is taken as reference (its χ^2 labelled as χ^2_B). As a consequence, for each parameter the uncertainties are calculeted as the minimum and maximum values from all the left over models having a $\chi^2 < \tau_m \chi^2_B$, where τ_m is a threshold coefficient equal to 3 in default setting[11].
The model obtained from SINOPSIS can be considered reliable up to $\sim$ 3 μm due to the onset of the Polycyclic Aromatic Hydrocarbons (PAHs) infrared bands[12]. As a matter of fact, SINOPSIS does not include any treatment of the thermal dust emission component at such long wavelengths, either originated from the interstellar medium or from star forming regions.

[10]For more details about the An SFH pattern please see the user handbook at `http://www.crya.unam.mx/gente/j.fritz/REPOSITORY/SINOPSIS/sinopsis_manual.pdf`

[11]The value of τ_m can be easily customized according to user requirements in the `configuration file`, see Sec. B.2.3.

[12]The infrared bands are observed at 3.29, 6.2, 7.7, 8.7, 11.3, and 12.7 μm and are often accompanied by minor, weaker, bands and underlying broad structures in the 3.1 - 3.7, 6.0 - 6.9, and 11 - 15 μm ranges (Salama, 2008).

Figure B.1: Extinction curves currently implemented in SINOPSIS (v. 1.6.3).

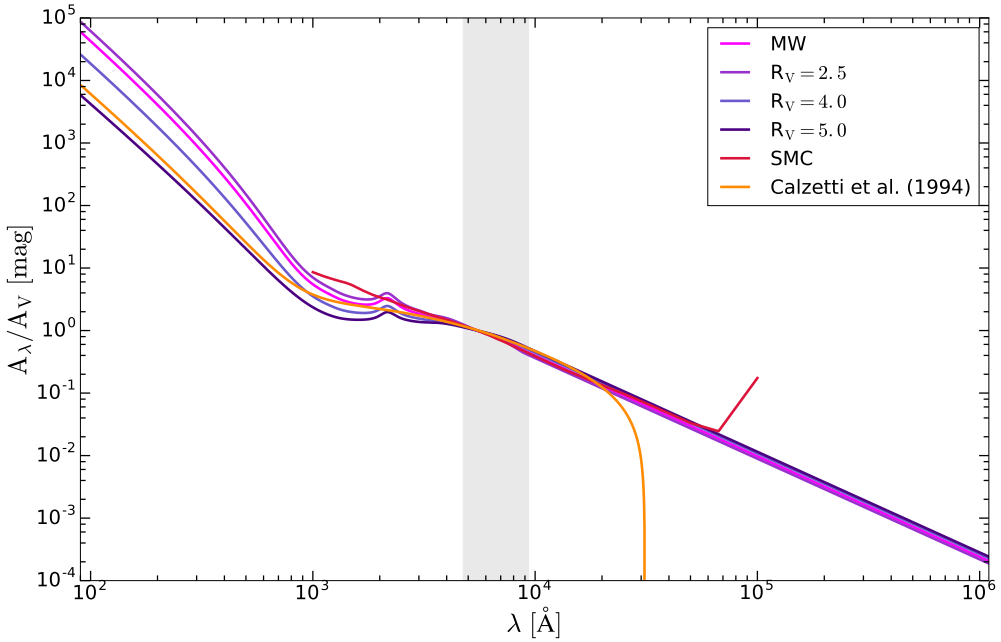

B.2 SINOPSIS: input files

In order to run SINOPSIS, it is necessary to have in a common directory the observed spectra, a catalog and a configuration file.
In the following pages the reader will find usefull informations for a practical use of SINOPSIS; an explaination of the main features of the above mantioned input files will be presented as well with particular attention to the format used to obtain the data presented in this work[13].

B.2.1 The observed spectra

SINOPSIS can acquire the observed spectra in different formats: single ascii files, single fits files, 2-D fits files and 3-D fits files (data-cubes).
If the single ascii file format is chosen, it is important[14] that the wavelength array is given in Å units while the observed flux in erg cm^{-2} s^{-1} $Å^{-1}$. Only if photometric data are not used, the absolute normalization of the flux can be arbitrary. By contrast, in the presence of photometry, the overlap between photometric data and the spectrum is required by SINOPSIS to run properly.

[13]For more details about all the possible structures of the input files not explained in this brief report, please see the user handbook of SINOPSIS by Jacopo Fritz at `http://www.crya.unam.mx/gente/j.fritz/REPOSITORY/SINOPSIS/sinopsis_manual.pdf`

[14]Both the wavelengths and the flux array can be optionally given in logarithmic units.

Table B.1: Example for one of the adotable structures of SINOPSIS input catalog.

3 AB U38eso Bf435w Vf606w

# specname	z_iani	U38_mag	U38_err	B_mag	B_err	V_mag	V_err
spec_6008.txt	0.544	99.0	99.0	26.4721	11.5835052	25.9035	7.5474209
spec_6038.txt	0.6671	26.44382	171.0291481	26.2958	26.8118972	24.4778	3.8484455
spec_6747.txt	0.6211	99.0	99.0	25.4795	8.4126599	23.1732	0.9810774
spec_6853.txt	0.8438	24.52325	8.5775406	24.4328	1.4752196	24.1722	1.1113712
spec_6953.txt	0.7655	25.96451	39.1592245	25.3675	3.9058501	25.1046	3.0955690
spec_6974.txt	0.6198	23.22068	4.3883421	23.1850	1.4471849	22.6586	0.7673877
spec_7046.txt	0.6182	99.0	99.0	27.3507	12.0675816	27.2934	9.4561076
spec_7071.txt	0.894	24.53897	10.5992037	24.7407	3.3141959	24.4413	2.5368567
spec_7121.txt	0.7669	26.6649	161.5218622	26.3059	11.9334784	25.1735	2.9153132
spec_7664.txt	0.8325	24.89333	18.9739827	25.2717	5.1961874	24.8182	3.1810635
spec_7678.txt	1.0382	99.0	99.0	25.3577	4.6453657	25.2856	3.2000719
spec_8257.txt	0.6217	23.81601	8.3028786	23.3667	2.1409752	22.4898	0.8695306
spec_8275.txt	0.7651	22.53704	2.7372650	22.5020	1.5593704	21.9948	0.8695306
spec_8316.txt	0.6221	99.0	99.0	25.4242	6.5319803	23.5204	1.0648184
spec_8624.txt	0.8321	26.40582	104.3845203	26.4069	14.9952760	25.9247	7.6663524

A header, with an arbitrary number of lines, is allowed too, as long as each line begins with a '#' character.

B.2.2 The catalog file

The catalog file contains the details of the spectra and, if required, also the photometric data. The essential informations to provide in the catalog are the spectra filenames and the redshifts.
If photometric data are used too, it is necessary to add: the number of photometric bands to be used as constraints for the model, the magnitude type (currently only Johnson-Vega and AB magnitudes are supported), the bands name, the magnitudes values for each source and band (in Å) and the related errorbars (in flux percentage). If data are not available for one or more of the bands, they must be replaced with a 99.0 flag[15].
As an example, in Table B.1 is reported a catalog file with part of the data used in our work of thesis.
Nevertheless, depending on the format of the observed spectra, the characteristics of this file might change.

B.2.3 The configuration file

In the configuration file, whose name needs to be `config.sin`, are setted up all the remaining parameters required by SINOPSIS to run properly.

[15] All magnitudes values (and errors) above 99.0 are considered by the code as flags.

The configuration file format is quite free since there is no specified order for the parameters; any comment can be added, provided it begins with a '#'. The only one mandatory parameter is the main catalog file name whereas all the others can be omitted, as their values are taken by a default set.
On the basis of the user requirements, the structure of the configuration file changes. To show an example of the `config.sin` file, in Table B.2 we report one of the configuration files used for this work.

B.3 SINOPSIS: output files

SINOPSIS output files are numerous and can be very different in type and format depending on the code version. As a matter of fact, on the basis of the `config.sin` file format (i.e. number of defined entries and corresponding keyword values), SINOPSIS creates a variable number of files, some of which are used as log/record files, some contain results whereas others contain models or modelled quantities.
In the following pages we will briefly describe SINOPSIS essential outputs, always stressing on the outputs used to obtain the results presented in this Thesis. On the contrary, we will not take into account all the output files not produced by SINOPSIS at the end of our runs.

B.3.1 The log file

One of the first output files retrieved by SINOPSIS at the conclusion of each run is a log file. In this file, easily recognizable among all due to the `.log` extension, are contained essential informations on the run and its settings. As a matter of fact, a short summary of the simulation is stored as well as the code version, the date and the starting and ending time of the run, the cosmological parameters used, the input catalog filename, the extinction curve and the SFH pattern chose besides the theoretical dataset used for the SSPs.

B.3.2 The main catalog

The fundamental product of SINOPSIS is the main catalog, a file with a `.out` extension. This catalog contains for each galaxy listed in the input catalog file, the derived properties from the reference model. As a matter of fact, in this file are stored more than 70 values of different physical parameters and characteristics of the best-fit model.
Among all the measures reported in the main catalog, SINOPSIS retrieves the luminosity distance, the best-fit metallicity, the number of measured EWs, the run identification of the reference model and its χ^2, the extinction of the youngest stellar populations, the avarage extinction value for all the stellar populations, a measurement of the SFR

Table B.2: Example for one of the adotable structures of the SINOPSIS configuration file `config.sin`.

```
##############################################################
###                Configuration file for SINOPSIS         ###
###                        version 1.6.3                   ###
###   If a keyword is not defined here, a default value will be assumed, when possible.  ###
##############################################################
##############################################################
### INPUT CATALOG
Name of the input catalog := input.cat
# Allowed keywords: basic, advanced, EW.
Type of input catalog := basic
##############################################################
### OBSERVED SPECTRA CHARACTERISTICS and OPTIONS
# Allowed keywords: ascii, fits, mfits, cube
Format of the observed spectrum or spectra:= ascii
Spectral resolution of the data (FWHM in Angstroem) := 2.5
# Allowed keywords: linear, logarithmic
Wavelength array in linear or logarithmic units := linear
# Allowed keywords: linear, logarithmic
Flux array in linear or logarithmic units := linear
Number of lines to be skipped in the observed spectra (ascii format only) := 0
Cut the observed spectra in the blue part by this amount (in Angstroem) := 0
Cut the observed spectra in the red part by this amount (in Angstroem) := 0
Smooth the observed spectra resolution to match the SSP resolution := no
Smooth the observed spectra to a custom resolution := no
Resolution of the smoothed observed spectra (FWHM in Angstroem) := 6.0
Write the smoothed observed spectra := yes
##############################################################
### NORMALIZATION OF THE MODEL SPECTRUM & OBSERVED CONSTRAINTS (CONTINUUM)
# Allowed keywords: phot, spec, none, norm
Normalize the model spectrum to := norm
Normalisation factor := 1.0e-20
# Allowed keywords: default, custom
Continuum bands definition := default
##############################################################
### EXTINCTION
# Allowed keywords: MW, SMC, CAL, 2.5, 4.0, 5.0
Extinction curve to be adopted := CAL
##############################################################
### CHARACTERISTICS OF THE MODELLING
# Allowed keywords: jm, cb16
SSP set := cb16
# Allowed keywords: ff, dexp, logn
Star formation history pattern := ff
Number of different metallicity values := 3
Metallicity values to be used := 0.004 0.02 0.04
Smooth SSP spectra to the observed spectra resolution := no
##############################################################
### UNCERTAINTIES DETERMINATION
Number of separate runs for each metallicity value := 11
Chi2 threshold value to calculate uncertainties := 3.0
##############################################################
### VARIOUS
Create a model magnitudes catalog := yes
# Allowed keywords: Jon, AB
Magnitudes type for the model catalog := AB
Catalog of redshift-independent distances to be used := mydistances.dat
Redshift value below which a redshift-independent distance is used := 0.00
Output all the best fits for all runs and metallicities := no
Write output file for each reference model := yes
Write out the model spectra without emission lines := yes
Minimize memory usage := y
##############################################################
### DUSTY SSP AND IR CONSTRAINTS
Include dusty SSPs := n
##############################################################
```

for four different age-bin [16] , the total stellar mass of the galaxies for the four different age-bin and for three diverse mass definitions [17] and lots more.

B.3.3 The model spectra

In addition to the already described output files, SINOPSIS produce for each spectrum a file, with the extension `.spec`, into which the panchromatic model calculated from the reference model is stored (see the description of the ASA algorithm in Sec. B.1; for more details see Fritz et al. 2007).
SINOPSIS model spectrum is an array containing for each wavelength (in Å) the related theoretical flux (in erg cm^{-2} s^{-1} $Å^{-1}$). It is on the basis of these very fluxes that if required by the user, the code is also able to construct a catalog containing the model magnitudes (see B.3.5).
These files had been extensively used in this work to plot the best-fit model over the observed spectra thus evaluating the goodness of the fits.

B.3.4 The EW catalog

The EW catalog, one of the main products of SINOPSIS, is a list of measurements for each spectra in the input catalog of the equivalent widths for the most promi-

[16] Notwithstanding the use of 12 SSPs of different ages (see Sec. B.1) to obtain the best-fit model, it has been verified that the relatively high temporal resolution provided by the 12 SSPs does not allowed the recover of the SFH as a function of stellar age. This is due to a intrinsic degeneracy in the typical features of spectra of similar age and different dust attenuation (see Fritz et al. 2007). To surmount this degeneracy, Fritz et al. considered as menaingful for the reconstruction of the SFH only the estimates of the stellar mass in four age bins, defined as follows:

1. $0 - 2 \times 10^7$ yr: stellar populations characterized by lines in emission and the strongest ultraviolet emission;
2. $2 \times 10^7 - 6 \times 10^8$ yr: stellar populations with the Balmer lines at their maximum of intensity in absorption, while the Ca(K) line is almost non detectable;
3. $6 \times 10^8 - 5.6 \times 10^9$ yr: stellar populations with less intense Balmer lines, while the Ca(K) line reaches its maximum intensity in absorption;
4. $5.6 \times 10^9 - 1.4 \times 10^{10}$ yr: stellar populations in which the main spectral features reach an asymptoptic value.

[17] When stellar masses are derived by means of spectro-photometric techniques, it is important to clearly state which definition of mass is used. Actually, the use of spectral synthesis techniques leads to three different definitions of the stellar mass (e.g. Longhetti and Saracco 2009, Renzini 2006), namely:

1. the initial mass of the SSP, at age zero; this is nothing but the mass of gas turned into stars;
2. the mass locked into stars, both those which are still in the nuclear-burning phase, and remnants (i.e. white dwarfs, neutron stars and stellar black holes);
3. the mass of stars that are still shining (i.e. only stars in the nuclear-burning phase)

Note that the difference between the three definitions is a function of the stellar age. As a consequence, SINOPSIS returnes for each of the aformentioned mass defintions the corresponding values. In our work (see Sec. 4) we considered only mass values calculated according to definition n. 2. For more details on SINOPSIS algorithm for the computation of the stellar mass see Fritz et al. (2011).

nent spectral lines. All the lines considered by default from the code are stored in the `spec_lines_param.dat` file, located in the SINOPSIS subdirectory `data`.[18] It is important to underline that the EW measurements reported (in Å) refer to the observed values[19], i.e. not rest-frame. In addition to the EW of the spectral lines, in `spec_lines_param.dat` are also retrieved the values of the D4000 and D_n4000 indexes (for the defintions see Bruzual A. 1983 and Balogh et al. 1999, respectively), the uncertainties on the measurements for each lines and the S/N ratio calculated over the entire spectrum. The EW catalog has a `.EW` extension.

B.3.5 The model magnitudes catalog

Since SINOPSIS uses SSP datasets which span the whole electromagnetic spectrum (from the far-UV to radio wavelengths), the code also allows to calculate the galaxies predicted magnitudes in different photometric bands. To this aim, the model magnitudes, both observed and absolute, are computed by convolving the filters response curve with the spectrum. The filters used in this procedure are all the filters implemented in SINOPSIS.
If the user needs to change the number and/or type of filters used by the code, it is necessary to add in the SINOPSIS subdirectory `data/filters` an ascii file containing for each wavelength of the filter[20] the respective transmission coefficient. The name of the new filter must be shorter or at most six letters long and with a `.dat` extension. It is also necessary to add the complete name ofthe filter in the `filter_list.dat` file, always stored in the SINOPSIS subdirectory `data/filters`.
This catalog is created by the code only if explicitly required by the user in the configuration file (see Sec. B.2.3), with the keyword `yes` at the `Create a model magnitudes catalog` entry. If generated, the model magnitudes file has the `.mag` extension.

B.4 SINOPSIS: our settings

In this section we will present the main considerations and adjustments applied in SINOPSIS to adapt the code to our requirements.

B.4.1 Filters

Since we decided to use Santini's catalog (see Santini et al. 2009) for the photometric data (see Sec. 4.1.1), it has been made necessary to load in SINOPSIS the filters used by Santini et al., i.e. filters for U35 and U38 bands from 2.2ESO; U-VIMOS band from VLT-VIMOS; B (F435W), V (F606W), i (F775W) and z (F850LP) bands from ACS-HST;

[18] The 14 lines measured by the code in default settings are: [OII], H_θ, H_η, H_ζ, Ca(K), Ca(H), H_δ, GCO, H_γ, H_β, [OIII], Mg, NaD and H_α (see Fritz et al. 2014 for more details). An arbitrary number of lines to be measured can be added since the user list follows the same exact format of the original one.

[19] Before making any analysis, these values must be necessarily divided for a $(1 + z)$ factor.

[20] Due to the convolution procedure, it is made necessary to add at the begining and at the end of the filter file a short list of wavelengths for which the transmission coefficient is 0.

Figure B.2: Spectral response (transmission) for 14 filters (U35, U38, U-VIMOS, B, V, i, z, J, H, Ks and the Spitzer-IRAC bands at 3.6μm, 4.5μm, 5.8μm and 8.0μm) presented in the photometric catalog by Santini et al. (2009). The grey shadowed region marks the wavelength range covered by MUSE instrumentation (i.e. $4750 < \lambda < 9350$ Å). We do not report the spectral response for the 24μm Spitzer-MIPS band since not employed in SINOPSIS runs.

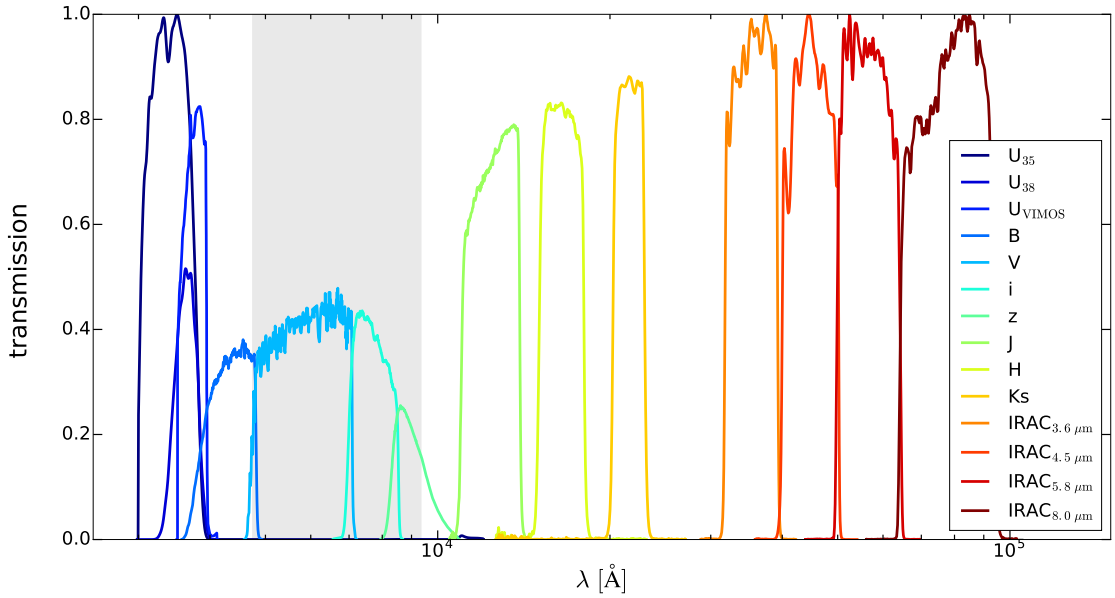

J, H and Ks bands from VLT-ISAAC; bands at 3.6μm, 4.5μm, 5.8μm and 8.0μm from Spitzer-IRAC and the 24 μm band from Spitzer-MIPS. The procedure adopted to add Santini et al. filters in SINOPSIS has been already described in Sec. B.3.5.
Although the presence of a total of 15 filters, for our purposes we decided to discard all possible data from the 24 μm MIPS band since SINOPSIS does not include any treatment of the thermal dust emission component at such long wavelengths, either from the interstellar medium or from star forming regions. As a matter of fact, for the z-range we were interested in ($0.5 < z_{spec} < 1.1$), we had also to consider the presence of the PAH bands.
The spectral response of all filters used in this work is presented in Fig. B.2 while values for the effective wavelength (λ_c) and the passband half-width ($\Delta\lambda$) for each filter are reported in Table B.3 (from Santini et al. 2009).

B.4.2 The extinction law

SINOPSIS allows to use different extinction laws according to the user requirements. In Fig. B.1, we have already shown all the attenuation curves currently implemented in SINOPSIS. The use of a precise extinction curve can be done by using the appropriate keyword in the `config.sin` file at the entry `Extinction curve to be adopted`. In

Table B.3: Filter name, effective wavelength (in μm) and passband half-width (in μm) for the 15 filters in Santini et al. (2009).

Filter name	λ_c [μm]	$\Delta\lambda$ [μm]
U35	0.3590	0.0222
U38	0.3680	0.0170
U-VIMOS	0.3780	0.0197
B (F435W)	0.4330	0.0508
V (F606W)	0.5940	0.1168
i (F775W)	0.7710	0.0710
z (F850LP)	0.8860	0.0554
J (ISAAC)	1.2550	0.1499
H (ISAAC)	1.6560	0.1479
Ks(ISAAC)	2.1630	0.1383
3.6 band	3.5620	0.3797
4.5 band	4.5120	0.5043
5.8 band	5.6860	0.6846
8.0 band	7.9360	1.4797

Table B.4 we list all the available attenuation laws, their keywords and the filename of the curve in SINOPSIS subdirectory `data`.
In our work we decided to take into account the MW extinction curve by Cardelli et al. (1989) and the CAL attenuation law, derived by Calzetti et al. (1994) for local starburst. To operate a choice between these two different extinction curves, we run SINOPSIS twice for all the galaxies in our sample. Maintaining the very same data, the difference between the first and the second run, was all about the changing of the keyword for the adopted attenuation law.
From the analysis, for each galaxy, of the two different output model spectra retrieved by the code (each for a diverse law), we concluded that the best-fit were obtained by means of Calzetti's extinction law (Calzetti et al., 1994). Indeed, the Calzetti's attenuation curve not only fits better Santini's photometric data in the U bands (U35, U38 and when available also U-VIMOS) but also the shape of the bluer part of MUSE spectra continuum. To this regard, in Fig. B.3 we present one of the most meaningful fit obtained.

B.4.3 SSPs ages

Since our sample of galaxies (see Sec.3.2) shows spectroscopic redshifts in the range $0.5 < z_{\rm IANI} < 1.1$, not all the 12 age-binned SSP spectra turned out to be essential for our analysis. In fact, by reason of the use in SINOPSIS of a Friedmann-Robertson-Walker cosmology with $\Omega = 0.3$, $\Lambda = 0.7$ and $\rm H_0 = 70$ km s^{-1} Mpc^{-1}, the older age-bin, i.e. from 10 to 14 Gyr (see Table B.5), has no relevance since at $z = 0.5$ the age of the

Figure B.3: SINOPSIS SED-fit of the MUSE spectra and photometric data (Santini et al., 2009) of one source (6038) out of the 16 in our sample (see Chap. 3, Sec. 3.1.1 and Sec. 3.2). **Top panel**: Charlot and Bruzual A. (2017) syntethic models (*solid orange line*, *solid green line*) retrieved by SINOPSIS with Calzetti's attenuation law (Calzetti et al., 1994) and Cardelli's extinction law (Cardelli et al., 1989), respectively. The theoretical models are over-plotted onto the MUSE aperture-corrected spectrum of the source (*solid black line*). For sake of clarity, the MUSE spectrum presented has been smoothed to reduce the noise without losing the fundamental spectral informations. The photometric measurements from Santini et al. (2009) are presented with black filled circles for the filters used by SINOPSIS as constraints to the synthetic models; black filled diamonds were used to highlight the magnitudes not taken into account during the fitting procedure because too close to the PAH infrared emission bands. The grey shadowed region marks the wavelength range covered by MUSE (i.e. $4750 < \lambda < 9350$) while the red shadowed areas show the wavelength ranges dominated by the firsts PAH infrared bands (i.e. the $3.1 - 3.7$ and $6.0 - 6.9$ μm bands; e.g. Salama 2008). In the top panel, the measured spectroscopic redshift of the source and an *HST* RGB (B_{435}+V_{606}+z_{850}) $10''$ image of the galaxy are reported too. **Bottom panel**: zoom in of the top panel into the spectral region observed by MUSE. The theoretical models (*solid orange line*, *solid green line*) have been over-plotted onto the aperture corrected MUSE spectrum of the source (*solid black line*). The filled black circles show the values of the photometric data presented in Santini et al. (2009) for the V (F606W), i (F775W) and z (F850LP) bands.

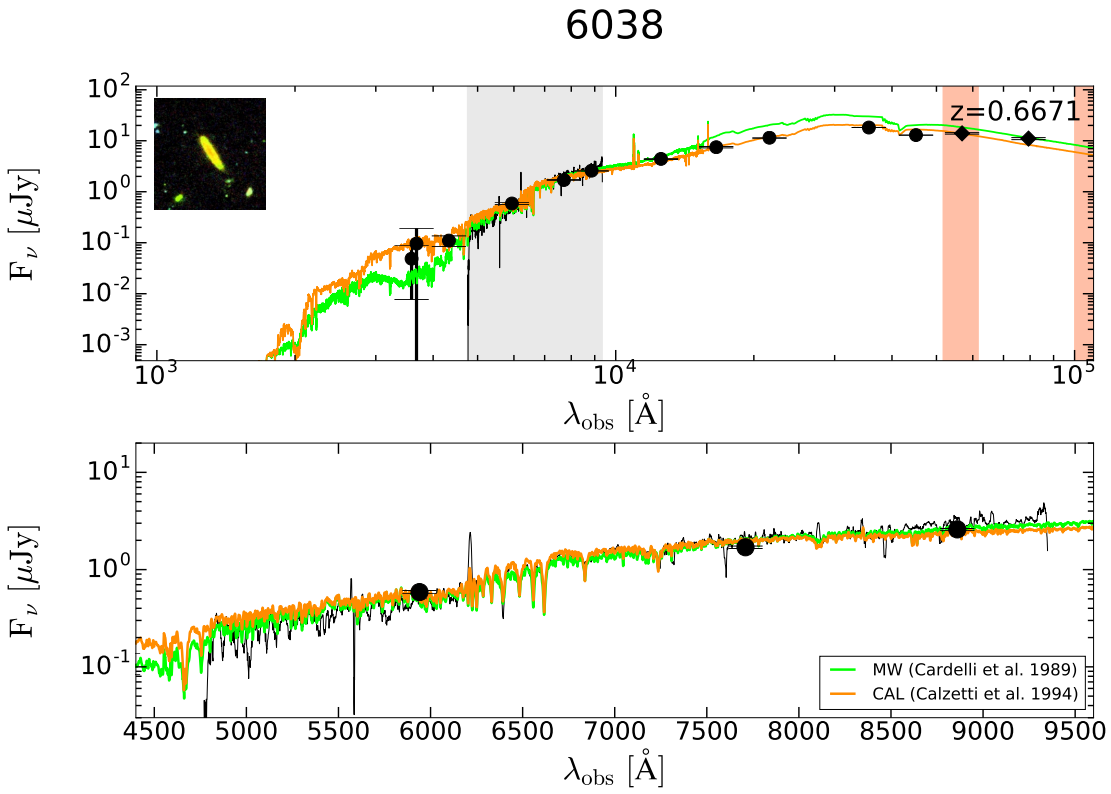

Table B.4: List of the extinction curves currently availables in SINOPSIS (v.1.6.3).

Law	Keyword	Filename
Cardelli et al. (1989)	`MW`	`al_av.dat`
Extinction curve with $R_V = 2.5$	`2.5`	`al_av2_5.dat`
Extinction curve with $R_V = 4.0$	`4.0`	`al_av4.dat`
Extinction curve with $R_V = 5.0$	`5.0`	`al_av5.dat`
Small Magellanic Cloud	`SMC`	`al_av_smc.dat`
Calzetti et al. (1994)	`CAL`	`al_avcalz.dat`

Universe is 8.422 Gyr.[21] Hence, we decided to inhibit the use of the oldest age-bin not only beacuse it refers to stellar populations too old for our sources, but also to avoid a possible overestimate of the total stellar mass of the galaxies. In fact, as already mentioned, the total stellar mass of galaxies is mainly due to older populations, thus the possibility of conspicuos overestimates for this physical parameters. To do so, in the file `ssp_setup_ff_cb16.dat`[22] we modified the values of both the mean extinction and SFR weights for the 12-th SSP population. The values were shrinked from 12 and 24, respectively, to 0 both.
Even though we decided to take into account such a precaution, from a direct analysis of the fitting models retrieved by SINOPSIS we did not record significant differences between the results obtained with or without the 12-th SSP. At this regard, for some of the galaxies in our sample we present in Fig. B.4 the models obtained by the code in the presence of the complete set of 12 SSP (in red) and in the case of only 11 SSP (in green). To make easier the comparison between SINOPSIS models, in Fig. B.4 we decided to plot the fit obtained with all the 12 SSP age bins after multiplying its flux at any wavelength for a 2.5 factor.

B.5 SINOPSIS: results of the first run

After the setting of the above-described initial options (see Sec. B.4) and the creation of the necessary input files (see Sec. B.2), we started a first run of SINOPSIS.
The code succeded in obtaining a fit of the input MUSE observed spectra for all the sources in our sample, with the only exception of the 7046 and 8624 galaxies. The 7046 and 8624 sources were rejected from the code since more than 40% of their flux had negative values. Therefore, the total number of sources for which SINOPSIS retrieved a measurement of the galaxy fundamental parameters was 14 out of which 2 were the ALMA-detcted sources UDF9 and UDF14 (Dunlop et al., 2016).
Nonetheless, a close analysis of the fits obtained showed a not-convincing fitting of the [OII] emission line ($\lambda_0 = 3727.5$ Å). At this regard, in Fig. B.6 we show for each galaxy

[21] The evaluations of the age of the Universe at different redshift here presented has been retrieved from the calculator at `http://www.astro.ucla.edu/~wright/CosmoCalc.html` (Wright, 2006).
[22] This file is placed in SINOPSIS subdirectory `data`.

Figure B.4: SINOPSIS SED-fit of the MUSE spectra and photometric data (Santini et al., 2009) of three sources (6747, 6853, 6953) out of the 16 in our sample (see Chap. 3, Sec. 3.1.1 and Sec. 3.2). **Top panel**: Charlot and Bruzual A. (2017) syntethic models (*solid red line*, *solid green line*) retrieved by SINOPSIS with or without the use of the 12-th SSP age-bin, respectively. The theoretical models are over-plotted onto the MUSE aperture-corrected spectrum of the source (*solid black line*). For sake of clarity, the flux of the theoretical model obtained with all the 12 SSP age-bins has been multiplied by a factor of 1.5, whereas the MUSE spectrum presented has been smoothed to reduce the noise without losing the fundamental spectral informations. The photometric measurements from Santini et al. (2009) are presented with black filled circles for the filters used by SINOPSIS as constraints to the synthetic models; black filled diamonds were used to highlight the magnitudes not taken into account during the fitting procedure because too close to the PAH infrared emission bands. The grey shadowed region marks the wavelength range covered by MUSE (i.e. $4750 < \lambda < 9350$) while the red shadowed areas show the wavelength ranges dominated by the firsts PAH infrared bands (i.e. the $3.1 - 3.7$ and $6.0 - 6.9$ μm bands; e.g. Salama 2008). In the top panel, the measured spectroscopic redshift of the source and an *HST* RGB (B_{435}+V_{606}+z_{850}) $10''$ image of the galaxy are reported too. **Bottom panel**: zoom in of the top panel into the spectral region observed by MUSE. The theoretical models (*solid red line*, *solid green line*) have been over-plotted onto the aperture corrected MUSE spectrum of the source (*solid black line*). The filled black circles show the values of the photometric data presented in Santini et al. (2009) for the V (F606W), i (F775W) and z (F850LP) bands.

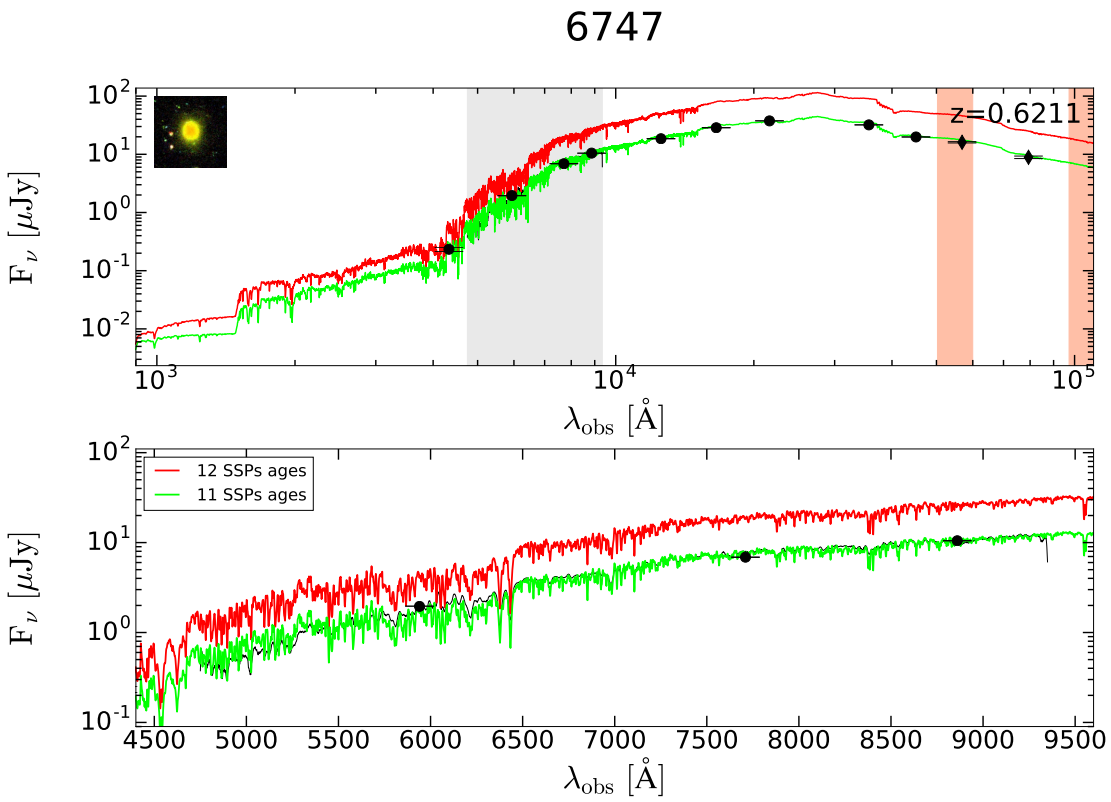

in our sample the SINOPSIS initial fits (*red solid line*) of the [OII] doublet plotted onto the aperture-corrected MUSE spectrum (*black solid line*).

Figure B.5: continuing Fig. B.4

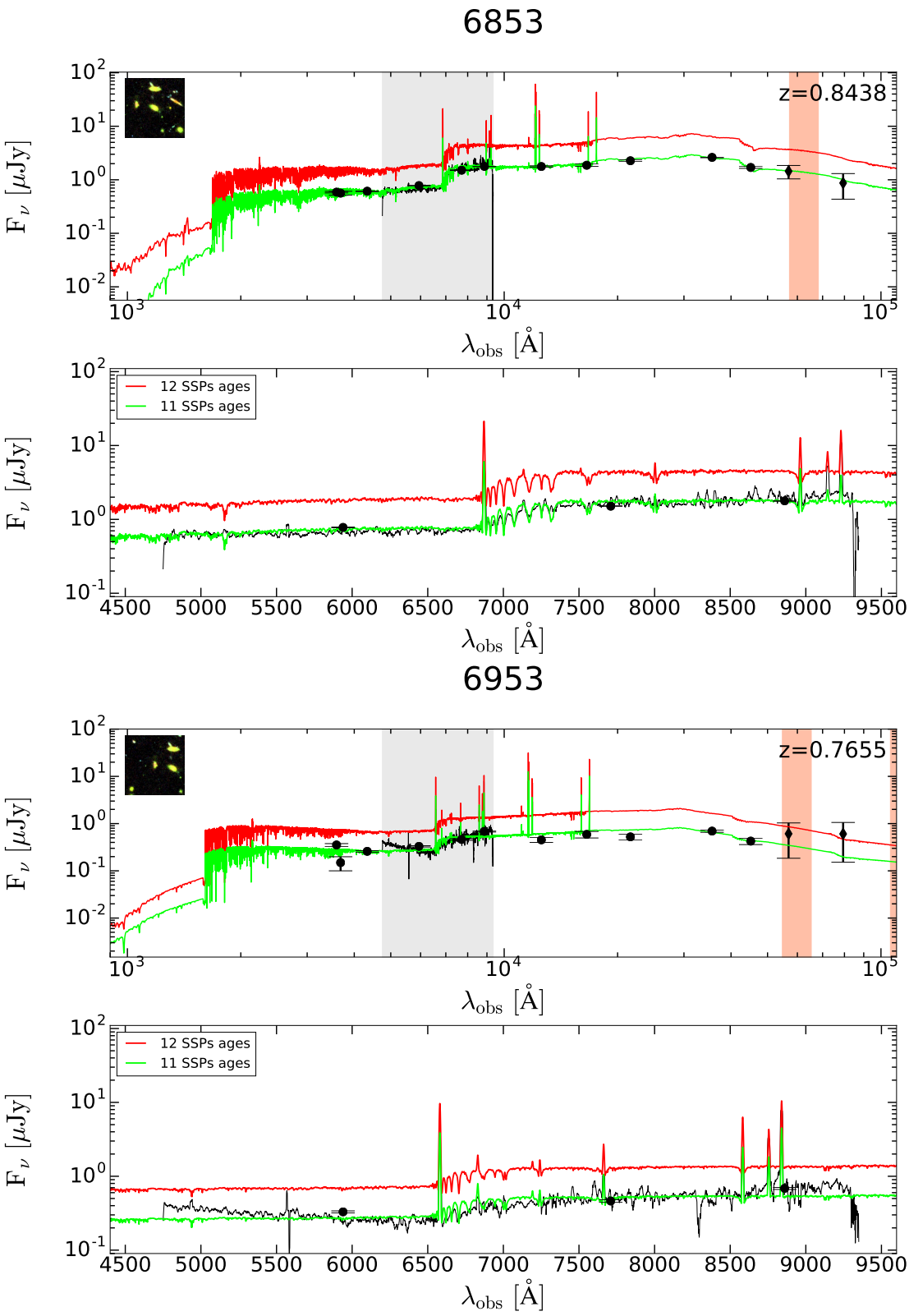

Table B.5: Age interval (in yr), initial E(B-V) color excess and SFR (in $M_\odot$ yr^{-1}) for each of the 12 age-binned SSPs (Charlot and Bruzual A., 2017) used by SINOPSIS. For each value of the E(B-V) and SFR the respective minimum ($E(B-V)_{min}$; SFR_{min}) and maximum values ($E(B-V)_{max}$; SFR_{max}) adoptables by SINOPSIS are reported too. The presented table is retrieved from the setting file `ssp_setup_ff_cb16.dat` in the SINOPSIS subdirectory `data`.

i-th age bin	age interval [yr]	E(B-V)	$E(B-V)_{min}$	$E(B-V)_{max}$	SFR [$M_\odot$ yr^{-1}]	SFR_{min} [$M_\odot$ yr^{-1}]	SFR_{max} [$M_\odot$ yr^{-1}]
1	$(0 \div 1.995) \times 10^6$	0.0	0.0	1.50	10.0	0.0	4000.
2	$(1.995 \div 3.981) \times 10^6$	0.0	0.0	1.50	10.0	0.0	4000.
3	$(3.981 \div 6.918) \times 10^6$	0.0	0.0	1.50	10.0	0.0	4000.
4	$(6.918 \div 19.95) \times 10^6$	0.0	0.0	1.00	100.0	0.0	4000.
5	$(1.995 \div 5.715) \times 10^7$	0.0	0.0	0.80	10.0	0.0	3000.
6	$(5.715 \div 20.28) \times 10^7$	0.0	0.0	0.40	10.0	0.0	3000.
7	$(2.028 \div 5.715) \times 10^8$	0.0	0.0	0.40	10.0	0.0	3000.
8	$(5.715 \div 10.14) \times 10^8$	0.0	0.0	0.40	10.0	0.0	2800.
9	$(1.014 \div 2.999) \times 10^9$	0.0	0.0	0.20	100.0	0.0	2800.
10	$(2.999 \div 5.754) \times 10^9$	0.0	0.0	0.20	200.0	0.0	2800.
11	$(5.754 \div 10.00) \times 10^9$	0.02	0.0	0.20	500.0	0.0	2800.
12	$(1.000 \div 1.400) \times 10^{10}$	0.02	0.0	0.08	0.0	0.0	2800.

The [OII] bad fitting is ascribable to the fact that SINOPSIS has not been developed to work with high-resolution spectra such as the ones obtained by MUSE.[23] As a matter of fact, even though the synthetic templates used by SINOPSIS (Charlot and Bruzual A., 2017) and the MUSE spectra have approximately the same spectral resolution in the wavelength range covered by MUSE, that is ≈ 2.51 Å for the theoretical templates and ≈ 2.4 Å for the spectra, the SSPs do not present any emission line but the only presence of some nebular emissions expected from the models of stellar atmospheres. Nonetheless, for a user-defined collection of emission lines, the synergy between the SSP models and the photoionization code CLOUDY (Ferland, 1996) allowed to obtain a set of SSPs complete in nebular emissions. At this regard, giving as an input in CLOUDY the adopted SSP and some physical parameters essential to describe the gas emission[24], such as the geometry of the emitting region, its metallicity, its electronic density, etc. (for more details see Charlot and Longhetti 2001), the photoionization code retrieves as an output the luminosity of each line. Therefore, from the EW associated to the luminosity of the line, a set of SSPs enriched in Gaussian emission lines were created. As a direct consequence, it is not surprising if the output synthetic model retrieved by SINOPSIS do not reproduce the doublet shape of the [OII]3727 forbidden emission line even if the SSPs spectral resolution is comparable to the one of the MUSE spectra.

[23] We remind the reader that the final data cubes have a spatial pixel scale of $0.2''$, a spectral coverage from 4750 Å to 9350 Å with a dispersion of 1.25 Å/pixel and a fairly constant spectral resolution of ≈ 2.4 Å over the entire spectral range.

[24] The parameters used are those typical of a HII region: hydrohenaverage desnity f 10^2 atoms cm^{-2}, a gas cloud with a inner radius of 10^{-2} pc and a metal abundance corresponding to the metallicity of the relative SSP.

Figure B.6: SINOPSIS fits of the [OII] doublet for each galaxy runned by the code. Overplotted onto the aperture-corrected MUSE spectrum (*black solid line*) of each galaxy, are shown the theoretical models (Charlot and Bruzual A., 2017) retrieved from the first (*red solid line*) and second (*green solid line*) run of SINOPSIS.

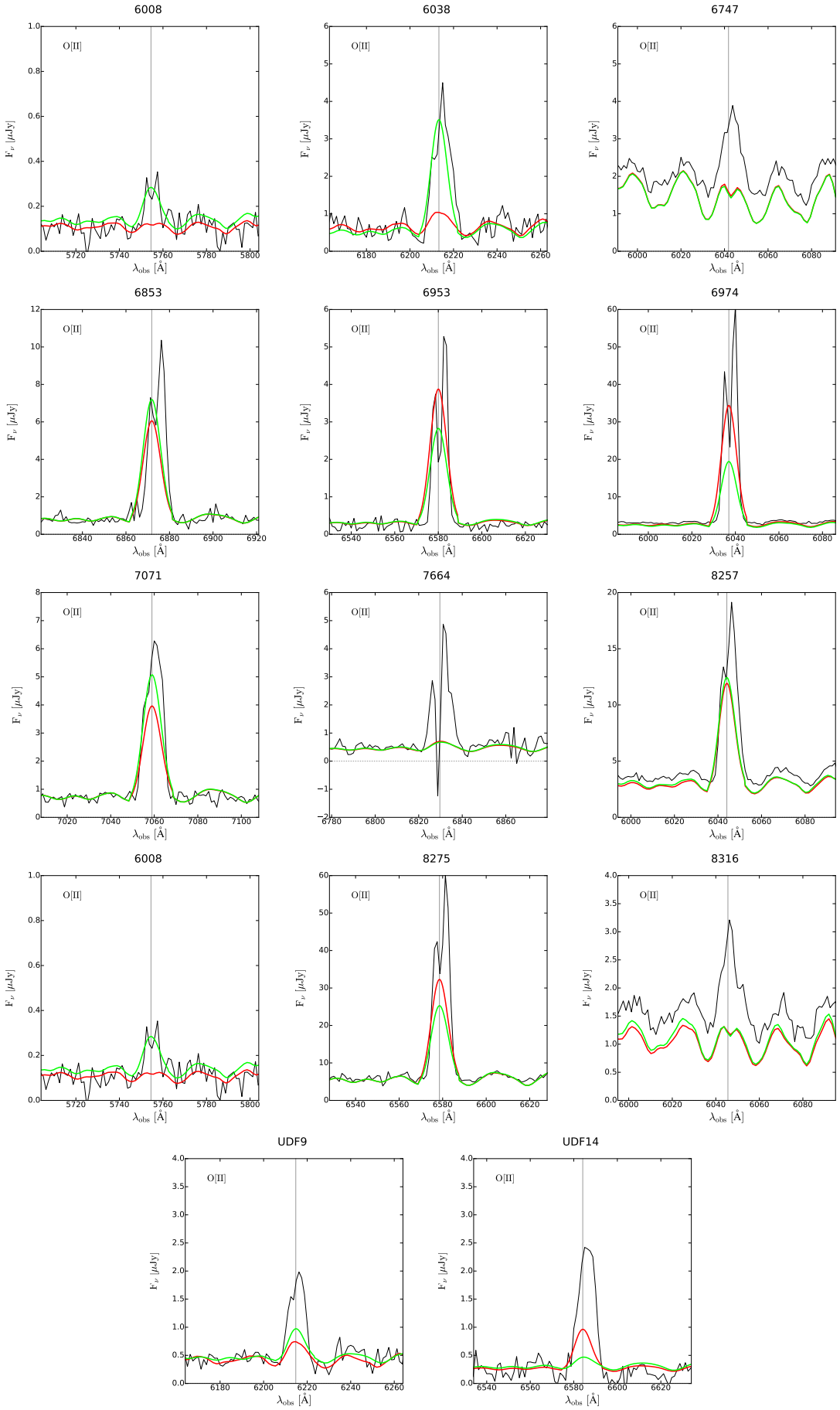

Figure B.7: Comparison between the [OII] EW inferred by IRAF (Tody, 1986) and from SINOPSIS (Fritz et al., 2007) first run, for Dunlop et al. (2016) galaxies (green stars) and Coe et al. (2006) sources (grey squares) in our sample (see Chap. 3, Sec. 3.1.1 and Sec. 3.2). The id of the sources (from Dunlop et al. 2016 and Coe et al. 2006) are reported too.

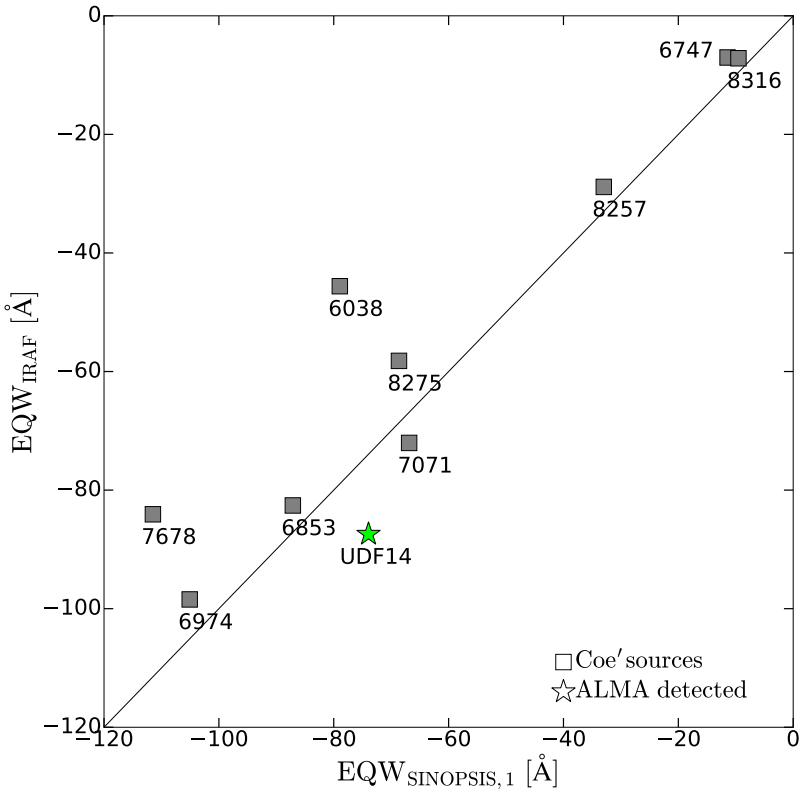

B.5.1 IRAF EW measurements

Since for our high-redshift spectra a correct EW measurement of the [OII] is fundamental to retrieve a robust value of the SFR, we decided to verify the EWs obtained from SINOPSIS first run by means of the IRAF software (Tody, 1986). In particular, after the conversion of our *ascii* spectra in *.fits* format thanks to the IRAF task `rspectext`, we operated a deblending fit (with Gaussian functions) on the two components of the [OII] doublet by means of the key-command `d` implemented within the IRAF `splot` procedure. As a result for the deblended fit of the [OII], IRAF returned for each one of the two components of the doublet the central wavelength, the flux, the EW and the FWHM of the fitted Gaussian functions.

Since the [OII] total EW is given by the sum of the EWs of the single components of the doublet, we easily obtained the [OII] equivalent width to compare with SINOPSIS

first run results. We would like to highlight the fact that since SINOPSIS retrieves the observed values for the lines EW, it was not necessary to de-redshift the spectra in IRAF before the deblending fit. In fact, the IRAF results obtained from the previous described procedure can be directly compared with the ones obtained by SINOPSIS.
As it appears evident from Fig. B.7, the results obtained from IRAF are in good-agreement with what was retrieved from SINOPSIS first run, with the only exception for 7071 and UDF14 which show a clear off-set towards lower values of the [OII] EW.

B.5.2 SINOPSIS: second run

On the basis of the EW obtained with IRAF, we decided to run SINOPSIS a second time but only after having changed the structure of the input files. We decided to adopt a particular shape for the input spectro-photometric catalog in order to compel the code to assume for each spectrum the [OII] EW measured with IRAF. Nonetheless, in the new reshaped input catalog it was necessary to specify for each source not only the redshift, the spectrum filename, the photometric data (magnitudes and errors) and the observed [OII] EW but also the wavelength ranges within which the code had to calculate the continuum and the [OII] width at zero-intensity.
While an estimate of the [OII] width at zero-intensity was easy to obtained from IRAF, to define the λ-ranges for the continuum definition, we resorted to the use of the default continuum intervals utilized by SINOPSIS during the first run and stored in the code setting file `default_cont_bands.dat`. For each source, the adopted wavelength ranges were conveniently redshifted to the respective galaxy z.
Therefore, after the creation of the new input catalog we run SINOPSIS again. A comparison between the SFR obtained from the first and second run of SINOPSIS are presented in Fig. B.8. For most of the objects we do not mark any significative difference between the SFR values obtained from the two runs of the code but for the UDF9 and UDF14 sources.
As a matter of fact, in the case of UDF14 the difference is about a factor 10^2 while for the UDF9 it shrinks to less than a factor 10. The significative difference of values for UDF14 is easy explainable if we consider the fact that in the first run of SINOPSIS, the code was not able to obtain any value for the [OII] EW while in the second run the code was compelled to consider the IRAF measurement.

Figure B.8: Comparison between the SFR inferred by SINOPSIS (Fritz et al., 2007) second run and first run, for Dunlop et al. (2016) galaxies (green stars) and Coe et al. (2006) sources (grey squares) in our sample (see Chap. 3, Sec. 3.1.1 and Sec. 3.2). The id of the sources (from Dunlop et al. 2016 and Coe et al. 2006) are reported too.

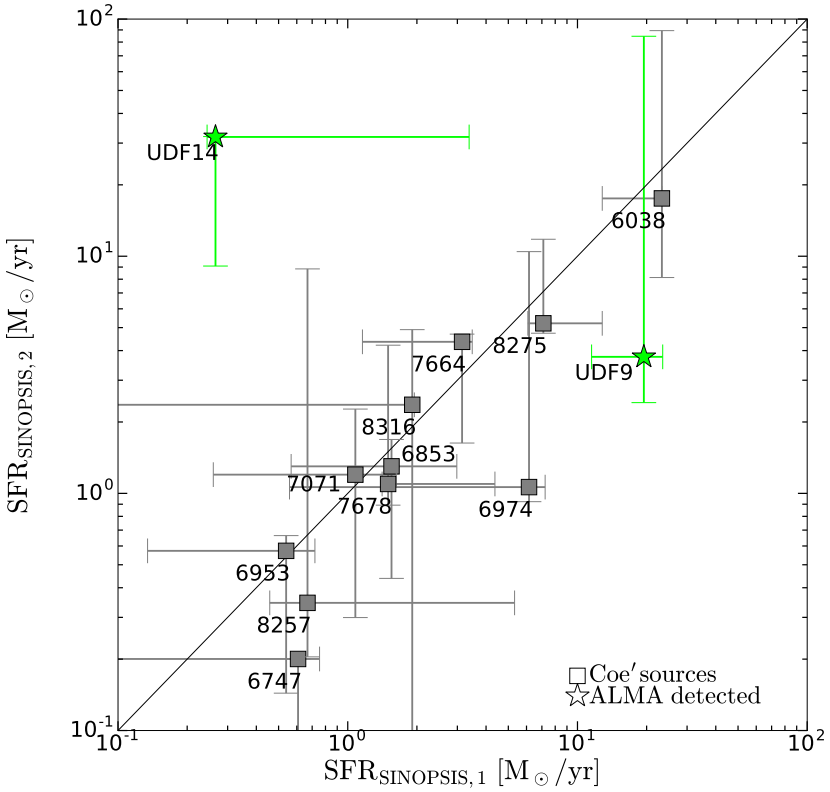

Appendix C

Sources parameters and UV-FIR images

In this Appendix, for each galaxy in our sample (see Chap. 3, Sec. 3.2) we provide their fundamental data (in tables) and postage-stamp of the VIMOS (U band), 2.2 m telescope at ESO (U35 band), *HST*-ACS (F435W, F606W, F775W and F850LP filters), *HST*-WFC3 (F160W filter), ISAAC (J, H, Ks bands), Spitzer MIPS (24 μm), *Herschel* PACS (100 and 160 μm) and *Herschel* SPIRE (250, 350 and 500 μm) images, centered on the sky-coordinates of each source. Two *HST* colour images (B_{435}+V_{606}+z_{850}) of each source with different size, i.e. $10'' \times 10''$ and $30'' \times 30''$, are presented as well. In the postage-stamp images, the green circles, centered in the sky-coordinates of each source (from Coe et al. 2006 and Dunlop et al. 2016), mark the $1''$ radius region within which the spectra were extracted (see Fig. 3.2 and Fig. 3.7) while the red line represents the $5''$ size scale.
For each source, the parameters reported in the table are: the sky-coordinates of the object ($\alpha_{\rm J2000.0}$, $\delta_{\rm J2000.0}$), the Bayesian photometric redshift (z_b) from Coe et al. (2006) along with the spectroscopic redshift ($z_{\rm IANI}$) retrieved from our analysis of the MUSE spectrum, the H-band magnitude of the galaxy (H_{160}) as reported in Coe et al. (2006) (if it is present), the luminosity distance (D_L) as obtained from the Internet Calculator by Wright (2006), the values of the total EW of the [OII] emission line as measured from the first and second run of SINOPSIS ($EW_{\rm SINOPSIS,1}$ and $EW_{\rm SINOPSIS}$, respectively), the logarithm of the stellar mass content of the galaxy as retrieved by SINOPSIS second run ($M_{\star,\rm SINOPSIS}$) and *HyperZmass* ($M_{\star,HyperZmass}$), the SFR from SINOPSIS first run ($SFR_{\rm SINOPSIS,1}$), from SINOPSIS second run ($SFR_{\rm SINOPSIS}$), from *HyperZmass* ($SFR_{\rm HyperZmass}$), from the UV luminosity at 1500 Å ($SFR_{\rm UV}$) and the IR luminosity at 24 μm ($SFR_{\rm IR}$), the extinction values obtained from SINOPSIS second run ($A_{\rm V,SINOPSIS}$ and $\overline{A}_{\rm V,SINOPSIS}$) and *HyperZmass* ($A_{V,HyperZmass}$) and, finally, the IR extinction excess ($A_{\rm IRX}$) from the UV and IR SFRs.

6008

$\alpha_{\rm J2000.0}$ [deg]	53.16608047	$\rm SFR_{SINOPSIS,1}$ [$\rm M_\odot\ yr^{-1}$]	-
$\delta_{\rm J2000.0}$ [deg]	-27.78686714	$\rm SFR_{SINOPSIS}$ [$\rm M_\odot\ yr^{-1}$]	$0.087^{+0.013}_{-0.074}$
z_b	0.502±0.177	$\rm SFR_{HyperZmass}$ [$\rm M_\odot\ yr^{-1}$]	$0.060^{+0.193}_{-0.011}$
$z_{\rm IANI}$	0.5440	$\rm SFR_{UV}$ [$\rm M_\odot\ yr^{-1}$]	0.044
$\rm H_{160}$ [mag]	24.980±0.105	$\rm SFR_{IR}$ [$\rm M_\odot\ yr^{-1}$]	1.107
D_L [Gly]	10.226	$\rm SFR_{UV+IR}$ [$\rm M_\odot\ yr^{-1}$]	1.151
$\rm EW_{SINOPSIS,1}$ [Å]	-	$\rm A_{V,SINOPSIS}$ [mag]	$0.51^{+3.75}_{-0.37}$
$\rm EW_{SINOPSIS}$ [Å]	-13.180	$\rm \overline{A}_{V,SINOPSIS}$ [mag]	$0.22^{+0.10}_{-0.12}$
$\rm M_{\star,SINOPSIS}$ [$\rm M_\odot$]	$8.6230^{+0.0865}_{-0.1380}$	$\rm A_{V,}$*HyperZmass* [mag]	$0.05^{+0.75}_{-0.05}$
$\rm M_{\star,}$*HyperZmass* [$\rm M_\odot$]	$8.0757^{+0.3260}_{-0.1526}$	$\rm A_{IRX}$ [mag]	3.54

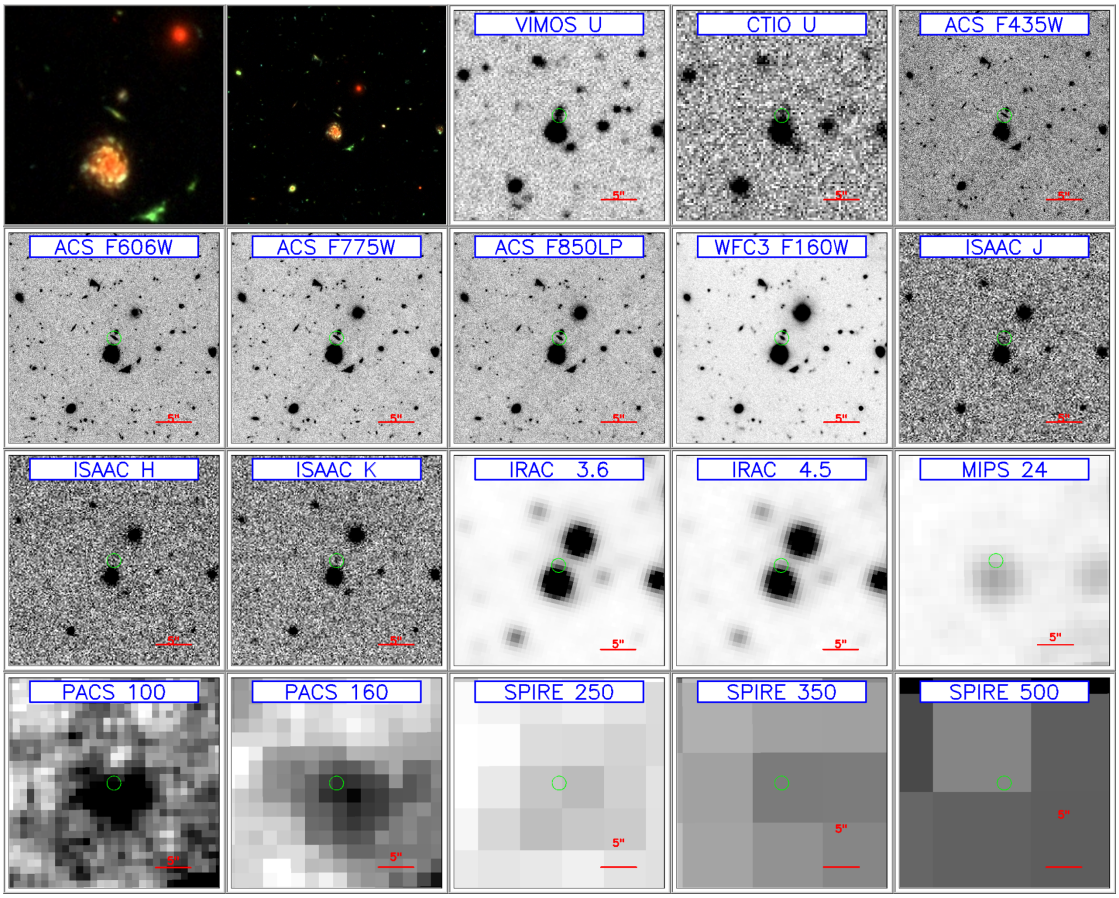

6038

$\alpha_{\rm J2000.0}$ [deg]	53.15722656	$\rm SFR_{SINOPSIS,1}$ [$\rm M_\odot$ $\rm yr^{-1}$]	$23.306^{+0.000}_{-10.486}$
$\delta_{\rm J2000.0}$ [deg]	-27.78526688	$\rm SFR_{SINOPSIS}$ [$\rm M_\odot$ $\rm yr^{-1}$]	$17.530^{+71.856}_{-9.399}$
z_b	0.644±0.193	$\rm SFR_{HyperZmass}$ [$\rm M_\odot$ $\rm yr^{-1}$]	$8.668^{+4.290}_{-1.472}$
$z_{\rm IANI}$	0.6671	$\rm SFR_{UV}$ [$\rm M_\odot$ $\rm yr^{-1}$]	0.050
$\rm H_{160}$ [mag]	21.712±0.070	$\rm SFR_{IR}$ [$\rm M_\odot$ $\rm yr^{-1}$]	4.035
D_L [Gly]	13.099	$\rm SFR_{UV+IR}$ [$\rm M_\odot$ $\rm yr^{-1}$]	4.085
$\rm EW_{SINOPSIS,1}$ [Å]	-78.943	$\rm A_{V,SINOPSIS}$ [mag]	$5.56^{+0.54}_{-0.23}$
$\rm EW_{SINOPSIS}$ [Å]	-45.610	$\rm \overline{A}_{V,SINOPSIS}$ [mag]	$2.089^{+1.156}_{-0.042}$
$\rm M_{\star,SINOPSIS}$ [$\rm M_\odot$]	$9.6565^{+0.0570}_{-0.2483}$	$\rm A_{V,}$*HyperZmass* [mag]	$2.20^{+0.20}_{-0.10}$
$\rm M_{\star,}$*HyperZmass* [$\rm M_\odot$]	$9.8515^{+0.0587}_{-0.0800}$	$\rm A_{IRX}$ [mag]	4.78

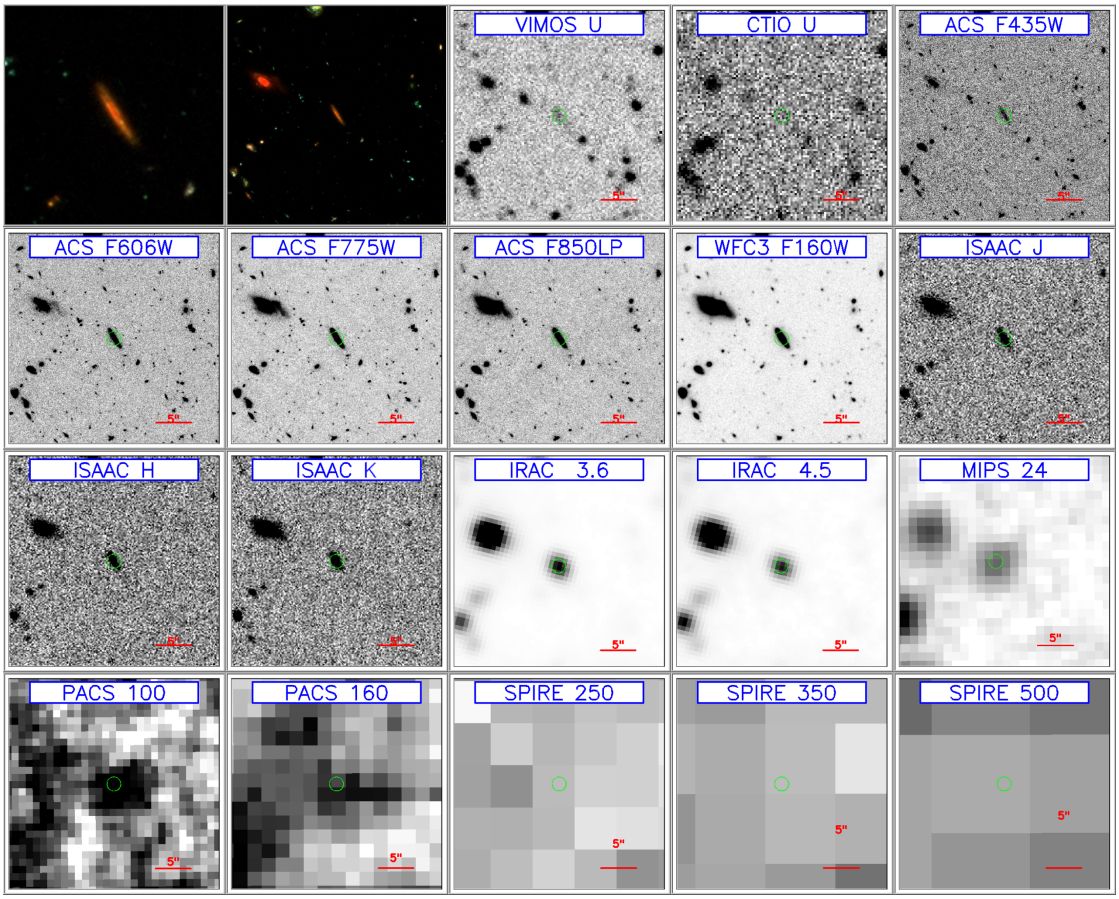

6747

$\alpha_{\rm J2000.0}$ [deg]	53.16163254	$\rm SFR_{SINOPSIS,1}$ [$\rm M_\odot\ yr^{-1}$]	$0.608^{+0.146}_{-0.585}$
$\delta_{\rm J2000.0}$ [deg]	-27.78025436	$\rm SFR_{SINOPSIS}$ [$\rm M_\odot\ yr^{-1}$]	$0.200^{+0.000}_{-0.173}$
z_b	0.560±0.183	$\rm SFR_{HyperZmass}$ [$\rm M_\odot\ yr^{-1}$]	$0.081^{+0.049}_{-0.081}$
$z_{\rm IANI}$	0.6211	$\rm SFR_{UV}$ [$\rm M_\odot\ yr^{-1}$]	0.041
$\rm H_{160}$ [mag]	20.206±0.064	$\rm SFR_{IR}$ [$\rm M_\odot\ yr^{-1}$]	-
D_L [Gly]	12.007	$\rm SFR_{UV+IR}$ [$\rm M_\odot\ yr^{-1}$]	0.041
$\rm EW_{SINOPSIS,1}$ [Å]	-11.427	$\rm A_{V,SINOPSIS}$ [mag]	$3.09^{+2.63}_{-0.00}$
$\rm EW_{SINOPSIS}$ [Å]	-7.030	$\rm \overline{A}_{V,SINOPSIS}$ [mag]	$0.13^{+0.16}_{-0.01}$
$\rm M_{\star,SINOPSIS}$ [$\rm M_\odot$]	$10.7799^{+0.0202}_{-0.0088}$	$\rm A_{V,}$*HyperZmass* [mag]	$0.10^{+0.30}_{-0.05}$
$\rm M_{\star,}$*HyperZmass* [$\rm M_\odot$]	$10.6726^{+0.0157}_{-0.2458}$	$\rm A_{IRX}$ [mag]	-

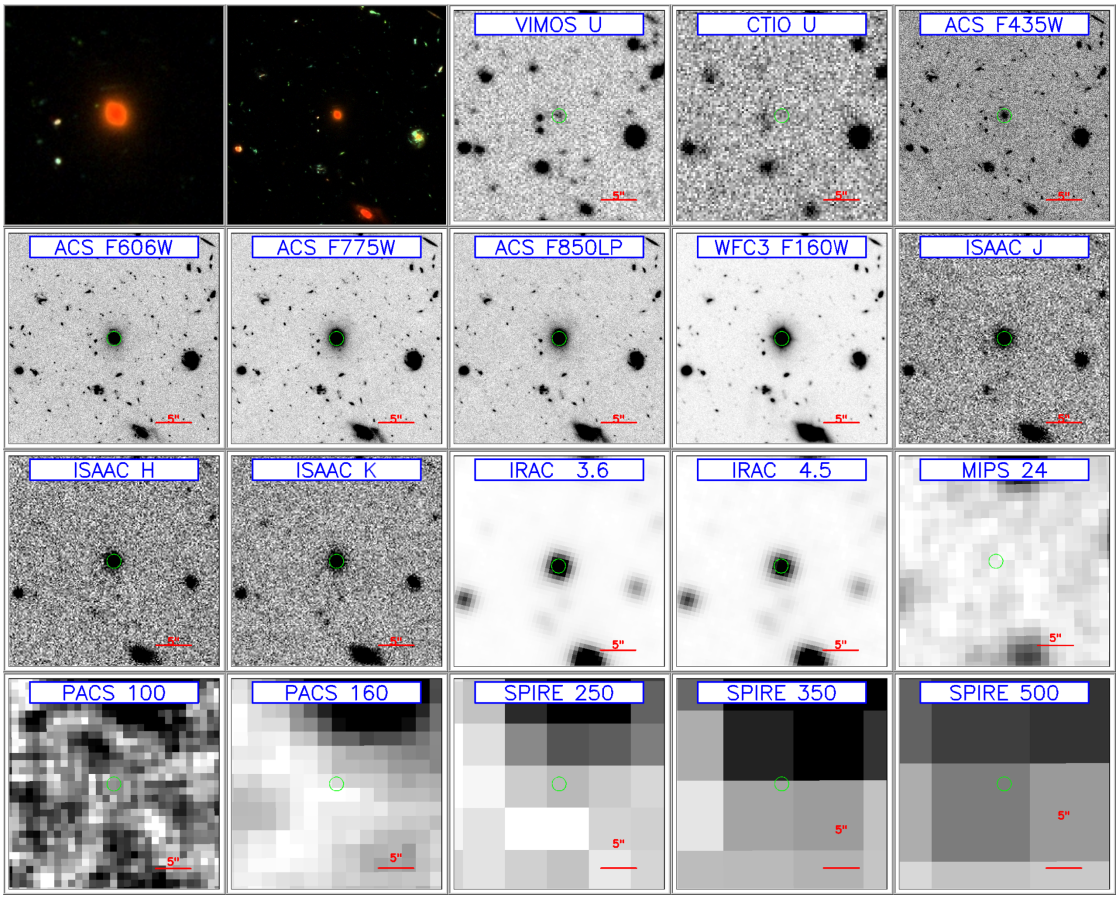

6853

$\alpha_{\rm J2000.0}$ [deg]	53.15183640	$\rm SFR_{SINOPSIS,1}$ [$\rm M_\odot$ $\rm yr^{-1}$]	$1.551^{+1.434}_{-0.984}$
$\delta_{\rm J2000.0}$ [deg]	-27.78286362	$\rm SFR_{SINOPSIS}$ [$\rm M_\odot$ $\rm yr^{-1}$]	$1.300^{+0.388}_{-0.862}$
z_b	0.703±0.200	$\rm SFR_{HyperZmass}$ [$\rm M_\odot$ $\rm yr^{-1}$]	$0.909^{+0.046}_{-0.109}$
$z_{\rm IANI}$	0.8438	$\rm SFR_{UV}$ [$\rm M_\odot$ $\rm yr^{-1}$]	0.995
$\rm H_{160}$ [mag]	23.012±0.083	$\rm SFR_{IR}$ [$\rm M_\odot$ $\rm yr^{-1}$]	0.568
D_L [Gly]	17.475	$\rm SFR_{UV+IR}$ [$\rm M_\odot$ $\rm yr^{-1}$]	1.563
$\rm EW_{SINOPSIS,1}$ [Å]	-87.123	$\rm A_{V,SINOPSIS}$ [mag]	$0.07^{+0.65}_{-0.04}$
$\rm EW_{SINOPSIS}$ [Å]	-82.590	$\rm \overline{A}_{V,SINOPSIS}$ [mag]	$0.05^{+0.33}_{-0.03}$
$\rm M_{\star,SINOPSIS}$ [$\rm M_\odot$]	$9.1676^{+0.0553}_{-0.0948}$	$\rm A_{V,}$*HyperZmass* [mag]	$0.10^{+0.05}_{-0.06}$
$\rm M_{\star,}$*HyperZmass* [$\rm M_\odot$]	$9.1276^{+0.0215}_{-0.0176}$	$\rm A_{IRX}$ [mag]	0.49

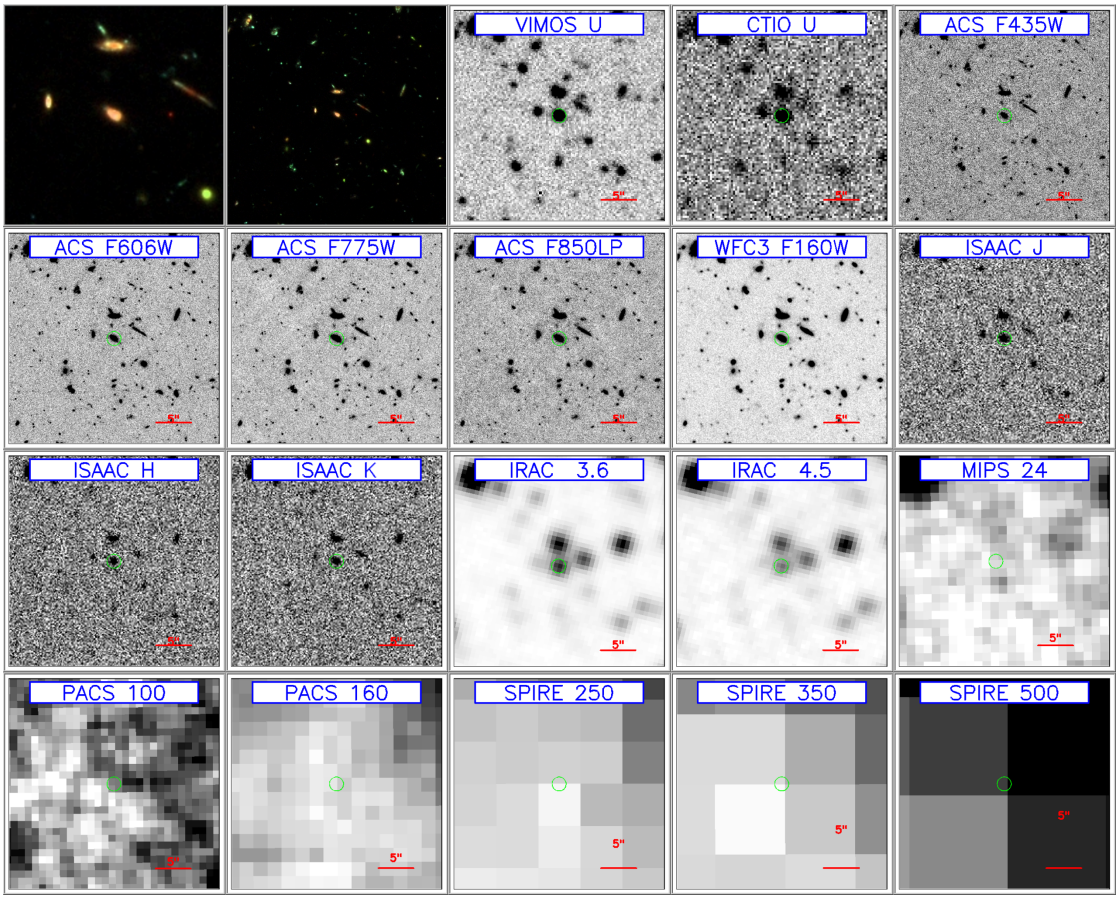

6953

$\alpha_{\rm J2000.0}$ [deg]	53.15278625	$\rm SFR_{SINOPSIS,1}$ [$\rm M_\odot\ yr^{-1}$]	$0.539^{+0.180}_{-0.405}$
$\delta_{\rm J2000.0}$ [deg]	-27.78269577	$\rm SFR_{SINOPSIS}$ [$\rm M_\odot\ yr^{-1}$]	$0.572^{+0.091}_{-0.429}$
z_b	0.744±0.205	$\rm SFR_{HyperZmass}$ [$\rm M_\odot\ yr^{-1}$]	$0.346^{+0.205}_{-0.023}$
$z_{\rm IANI}$	0.7655	$\rm SFR_{UV}$ [$\rm M_\odot\ yr^{-1}$]	0.456
$\rm H_{160}$ [mag]	24.457±0.098	$\rm SFR_{IR}$ [$\rm M_\odot\ yr^{-1}$]	-
D_L [Gly]	15.502	$\rm SFR_{UV+IR}$ [$\rm M_\odot\ yr^{-1}$]	0.456
$\rm EW_{SINOPSIS,1}$ [Å]	-130.708	$\rm A_{V,SINOPSIS}$ [mag]	$0.26^{+0.20}_{-0.20}$
$\rm EW_{SINOPSIS}$ [Å]	-110.190	$\rm \overline{A}_{V,SINOPSIS}$ [mag]	$0.28^{+0.11}_{-0.23}$
$\rm M_{\star,SINOPSIS}$ [$\rm M_\odot$]	$8.5170^{+0.1782}_{-0.1982}$	$\rm A_{V,}$*HyperZmass* [mag]	$0^{+0.25}_{-0.00}$
$\rm M_{\star,}$*HyperZmass* [$\rm M_\odot$]	$8.4933^{+0.0628}_{-0.1038}$	$\rm A_{IRX}$ [mag]	-

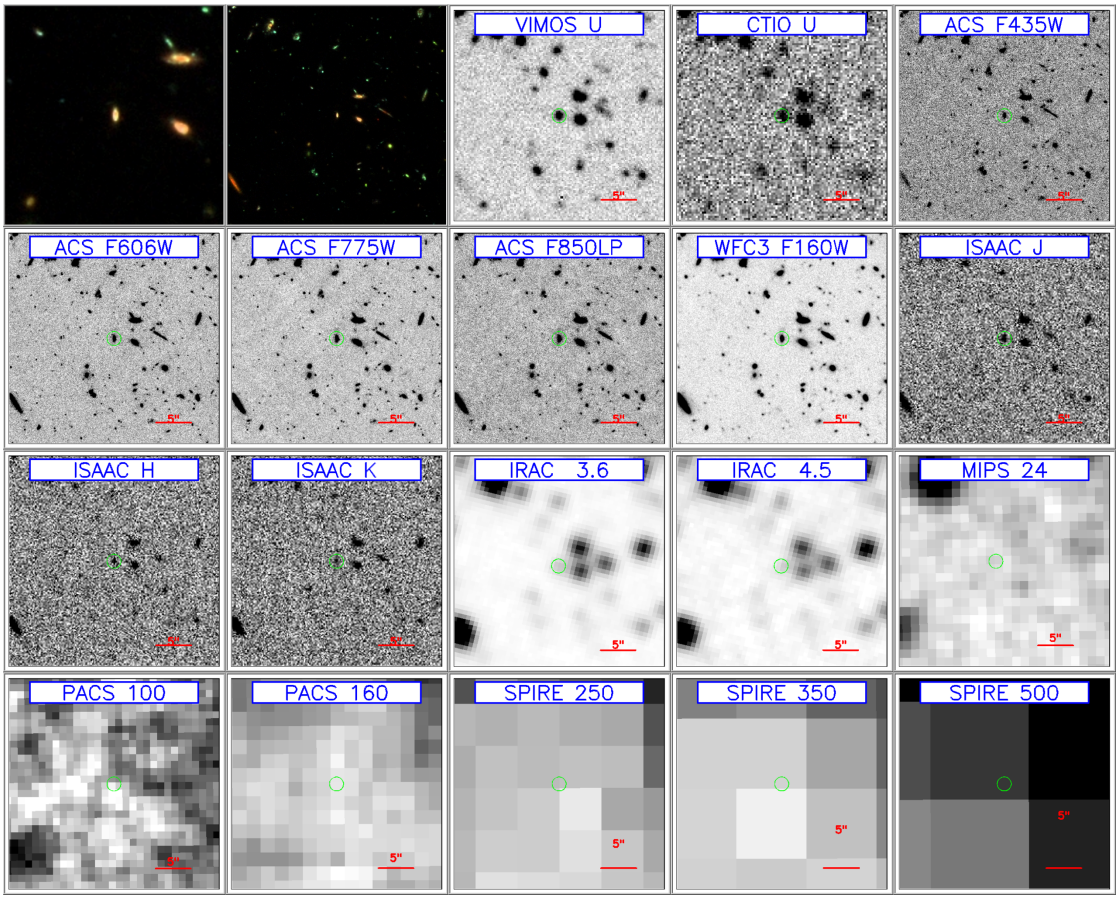

6974

$\alpha_{\rm J2000.0}$ [deg]	53.15818787	$\rm SFR_{SINOPSIS,1}$ [$\rm M_\odot$ $\rm yr^{-1}$]	$6.153^{+1.078}_{-5.596}$
$\delta_{\rm J2000.0}$ [deg]	-27.78109169	$\rm SFR_{SINOPSIS}$ [$\rm M_\odot$ $\rm yr^{-1}$]	$1.063^{+9.394}_{-0.140}$
z_b	0.660±0.195	$\rm SFR_{HyperZmass}$ [$\rm M_\odot$ $\rm yr^{-1}$]	$2.503^{+0.942}_{-0.291}$
$z_{\rm IANI}$	0.6198	$\rm SFR_{UV}$ [$\rm M_\odot$ $\rm yr^{-1}$]	1.457
$\rm H_{160}$ [mag]	21.613±0.064	$\rm SFR_{IR}$ [$\rm M_\odot$ $\rm yr^{-1}$]	0.677
D_L [Gly]	11.977	$\rm SFR_{UV+IR}$ [$\rm M_\odot$ $\rm yr^{-1}$]	2.134
$\rm EW_{SINOPSIS,1}$ [Å]	-105.082	$\rm A_{V,SINOPSIS}$ [mag]	$1.02^{+0.19}_{-0.46}$
$\rm EW_{SINOPSIS}$ [Å]	-98.440	$\rm \overline{A}_{V,SINOPSIS}$ [mag]	$0.11^{+0.74}_{-0.01}$
$\rm M_{\star,SINOPSIS}$ [$\rm M_\odot$]	$9.5401^{+0.2894}_{-0.1129}$	$\rm A_{V,}$*HyperZmass* [mag]	$0.30^{+0.15}_{-0.05}$
$\rm M_{\star,}$*HyperZmass* [$\rm M_\odot$]	$9.4551^{+0.0232}_{-0.0714}$	$\rm A_{IRX}$ [mag]	0.41

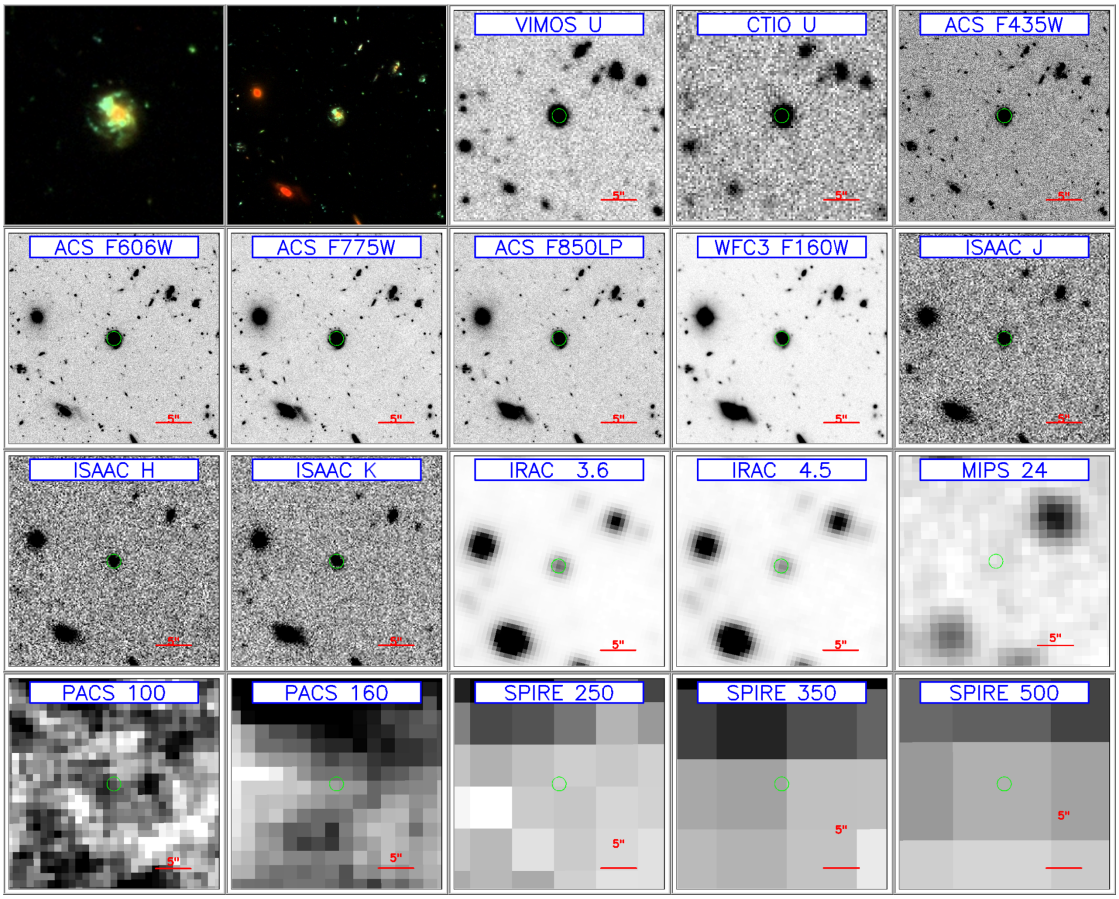

7046

$\alpha_{\mathrm{J2000.0}}$ [deg]	53.16096115	$\mathrm{SFR_{SINOPSIS,1}}$ [$\mathrm{M_\odot\ yr^{-1}}$]	-
$\delta_{\mathrm{J2000.0}}$ [deg]	-27.78285217	$\mathrm{SFR_{SINOPSIS}}$ [$\mathrm{M_\odot\ yr^{-1}}$]	-
z_b	0.558±0.183	$\mathrm{SFR_{HyperZmass}}$ [$\mathrm{M_\odot\ yr^{-1}}$]	$0.029^{+0.071}_{-0.006}$
z_{IANI}	0.6182	$\mathrm{SFR_{UV}}$ [$\mathrm{M_\odot\ yr^{-1}}$]	-
$\mathrm{H_{160}}$ [mag]	25.758±0.121	$\mathrm{SFR_{IR}}$ [$\mathrm{M_\odot\ yr^{-1}}$]	-
D_L [Gly]	11.939	$\mathrm{SFR_{UV+IR}}$ [$\mathrm{M_\odot\ yr^{-1}}$]	-
$\mathrm{EW_{SINOPSIS,1}}$ [Å]	-	$\mathrm{A_{V,SINOPSIS}}$ [mag]	-
$\mathrm{EW_{SINOPSIS}}$ [Å]	-	$\overline{\mathrm{A}}_{\mathrm{V,SINOPSIS}}$ [mag]	-
$\mathrm{M_{\star,SINOPSIS}}$ [$\mathrm{M_\odot}$]	-	$\mathrm{A_{V,}}_{HyperZmass}$ [mag]	$0^{+0.70}_{-0.00}$
$\mathrm{M_{\star,}}_{HyperZmass}$ [$\mathrm{M_\odot}$]	$7.8866^{+0.1963}_{-0.3677}$	$\mathrm{A_{IRX}}$ [mag]	-

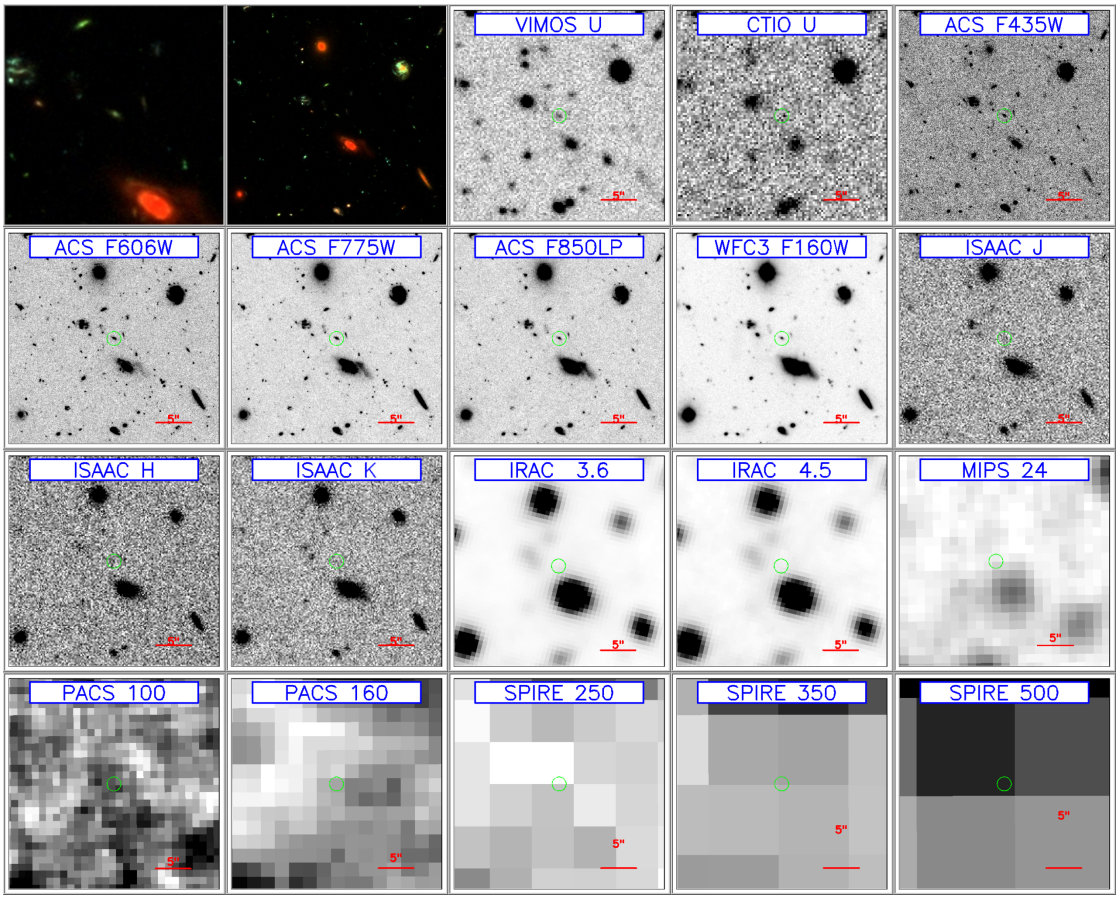

7071

$\alpha_{\rm J2000.0}$ [deg]	53.15186310	$\rm SFR_{SINOPSIS,1}$ [$\rm M_\odot$ $\rm yr^{-1}$]	$1.079^{+0.547}_{-0.819}$
$\delta_{\rm J2000.0}$ [deg]	-27.78195763	$\rm SFR_{SINOPSIS}$ [$\rm M_\odot$ $\rm yr^{-1}$]	$1.200^{+1.068}_{-0.900}$
z_b	0.731±0.204	$\rm SFR_{HyperZmass}$ [$\rm M_\odot$ $\rm yr^{-1}$]	$2.377^{+0.340}_{-0.415}$
$z_{\rm IANI}$	0.8940	$\rm SFR_{UV}$ [$\rm M_\odot$ $\rm yr^{-1}$]	0.578
$\rm H_{160}$ [mag]	22.878±0.082	$\rm SFR_{IR}$ [$\rm M_\odot$ $\rm yr^{-1}$]	-
D_L [Gly]	18.765	$\rm SFR_{UV+IR}$ [$\rm M_\odot$ $\rm yr^{-1}$]	0.578
$\rm EW_{SINOPSIS,1}$ [Å]	-66.873	$\rm A_{V,SINOPSIS}$ [mag]	$1.03^{+0.61}_{-0.96}$
$\rm EW_{SINOPSIS}$ [Å]	-72.040	$\rm \overline{A}_{V,SINOPSIS}$ [mag]	$0.14^{+0.31}_{-0.05}$
$\rm M_{\star,SINOPSIS}$ [$\rm M_\odot$]	$9.5090^{+0.0967}_{-0.1860}$	$\rm A_{V,}$*HyperZmass* [mag]	$0.65^{+0.05}_{-0.10}$
$\rm M_{\star,}$*HyperZmass* [$\rm M_\odot$]	$9.2351^{+0.0330}_{-0.0312}$	$\rm A_{IRX}$ [mag]	-

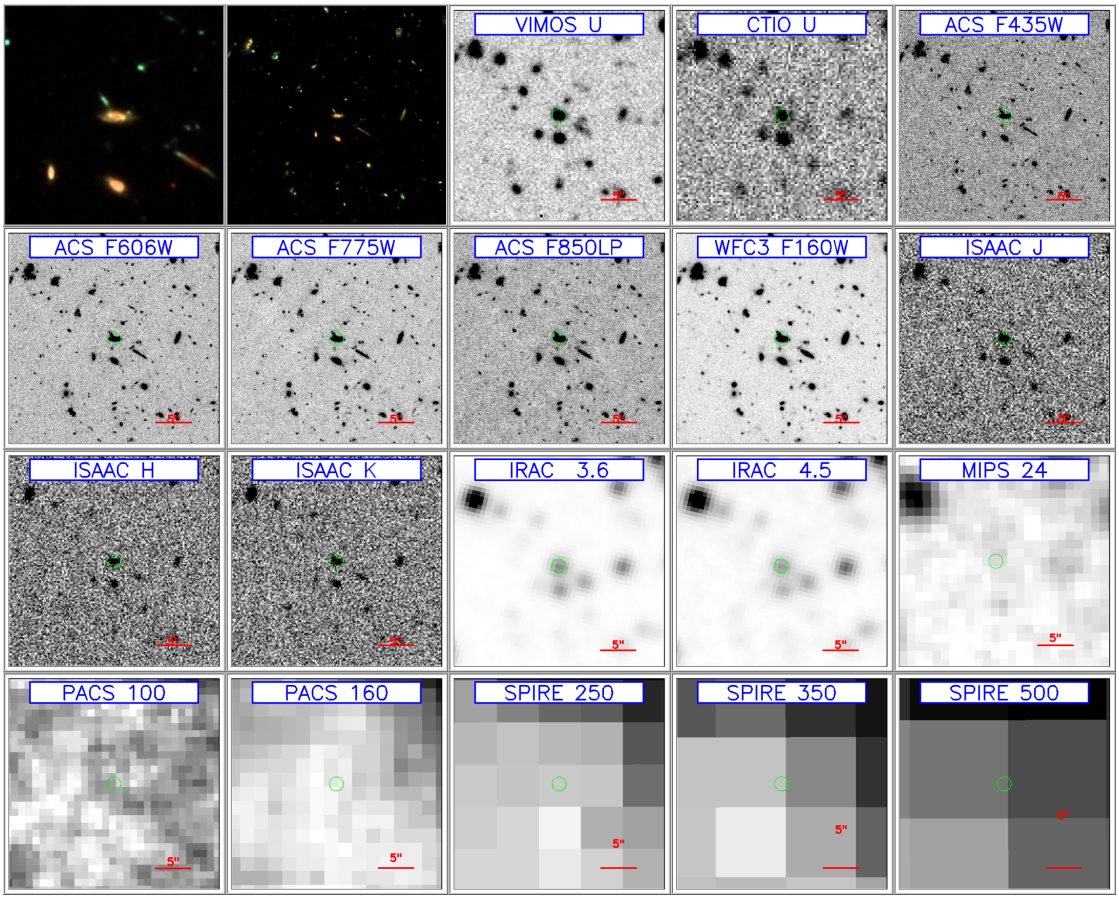

7664

$\alpha_{\rm J2000.0}$ [deg]	53.15398026	$\rm SFR_{SINOPSIS,1}$ [$\rm M_\odot\ yr^{-1}$]	$3.146^{+0.337}_{-1.987}$
$\delta_{\rm J2000.0}$ [deg]	-27.77099228	$\rm SFR_{SINOPSIS}$ [$\rm M_\odot\ yr^{-1}$]	$4.356^{+0.338}_{-2.726}$
z_b	0.761±0.207	$\rm SFR_{HyperZmass}$ [$\rm M_\odot\ yr^{-1}$]	$1.202^{+0.753}_{-0.312}$
$z_{\rm IANI}$	0.8325	$\rm SFR_{UV}$ [$\rm M_\odot\ yr^{-1}$]	0.485
$\rm H_{160}$ [mag]	23.314±0.084	$\rm SFR_{IR}$ [$\rm M_\odot\ yr^{-1}$]	-
D_L [Gly]	17.187	$\rm SFR_{UV+IR}$ [$\rm M_\odot\ yr^{-1}$]	0.485
$\rm EW_{SINOPSIS,1}$ [Å]	NaN	$\rm A_{V,SINOPSIS}$ [mag]	$2.73^{+2.80}_{-1.77}$
$\rm EW_{SINOPSIS}$ [Å]	-41.270	$\rm \overline{A}_{V,SINOPSIS}$ [mag]	$1.26^{+0.29}_{-0.10}$
$\rm M_{\star,SINOPSIS}$ [$\rm M_\odot$]	$8.7742^{+0.6866}_{-0.1437}$	$\rm A_{V,}$*HyperZmass* [mag]	$0.55^{+0.25}_{-0.15}$
$\rm M_{\star,}$*HyperZmass* [$\rm M_\odot$]	$9.2135^{+0.0358}_{-0.0757}$	$\rm A_{IRX}$ [mag]	-

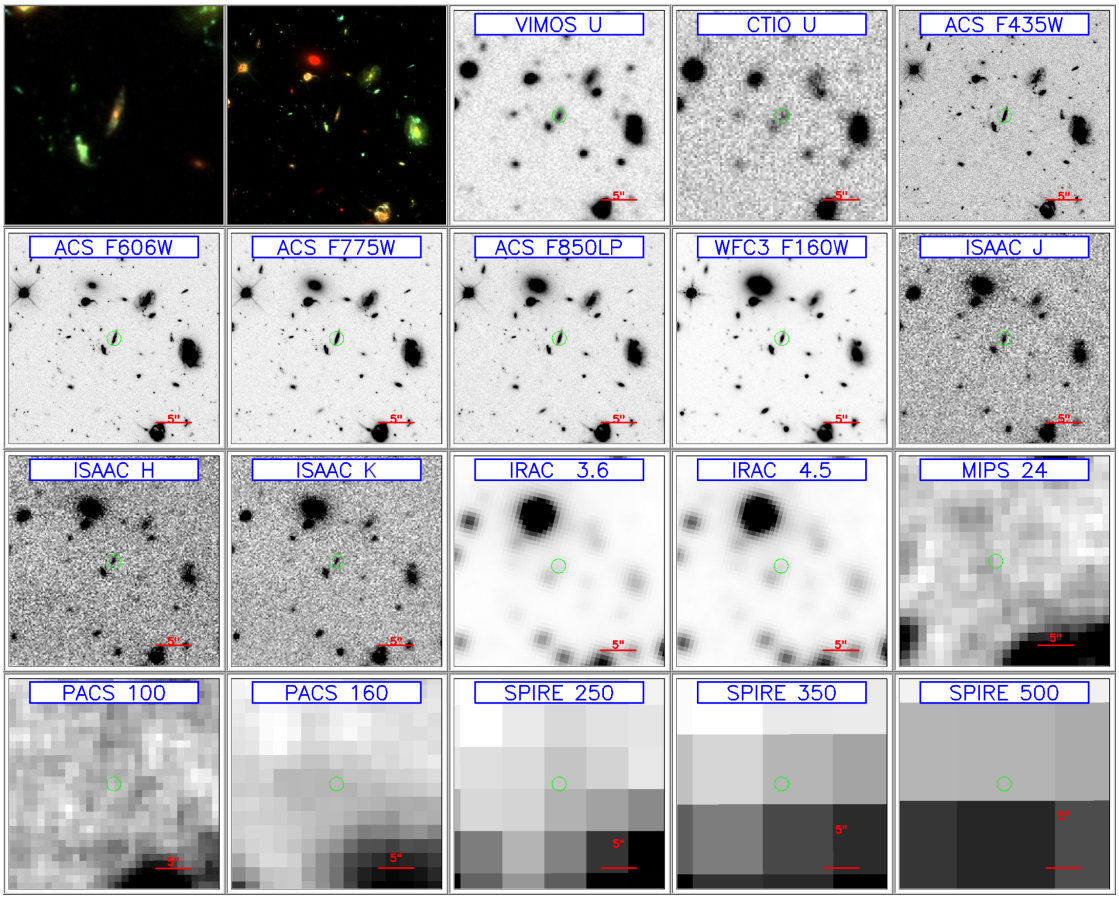

7678

$\alpha_{\rm J2000.0}$ [deg]	53.16246414	$\rm SFR_{SINOPSIS,1}$ [$\rm M_\odot$ $\rm yr^{-1}$]	$1.499^{+2.873}_{-0.088}$
$\delta_{\rm J2000.0}$ [deg]	-27.77091789	$\rm SFR_{SINOPSIS}$ [$\rm M_\odot$ $\rm yr^{-1}$]	$1.096^{+3.119}_{-0.204}$
z_b	0.707±0.201	$\rm SFR_{HyperZmass}$ [$\rm M_\odot$ $\rm yr^{-1}$]	$2.350^{+0.730}_{-0.724}$
$z_{\rm IANI}$	1.0382	$\rm SFR_{UV}$ [$\rm M_\odot$ $\rm yr^{-1}$]	0.754
$\rm H_{160}$ [mag]	24.192±0.094	$\rm SFR_{IR}$ [$\rm M_\odot$ $\rm yr^{-1}$]	-
D_L [Gly]	22.572	$\rm SFR_{UV+IR}$ [$\rm M_\odot$ $\rm yr^{-1}$]	0.754
$\rm EW_{SINOPSIS,1}$ [Å]	-111.490	$\rm A_{V,SINOPSIS}$ [mag]	$1.04^{+0.02}_{-0.57}$
$\rm EW_{SINOPSIS}$ [Å]	-84.080	$\rm \overline{A}_{V,SINOPSIS}$ [mag]	$0.24^{+0.96}_{-0.07}$
$\rm M_{\star,SINOPSIS}$ [$\rm M_\odot$]	$8.5847^{+0.3199}_{-0.1748}$	$\rm A_{V,}$*HyperZmass* [mag]	$0.70^{+0.10}_{-0.15}$
$\rm M_{\star,}$*HyperZmass* [$\rm M_\odot$]	$8.6937^{+0.1262}_{-0.1422}$	$\rm A_{IRX}$ [mag]	-

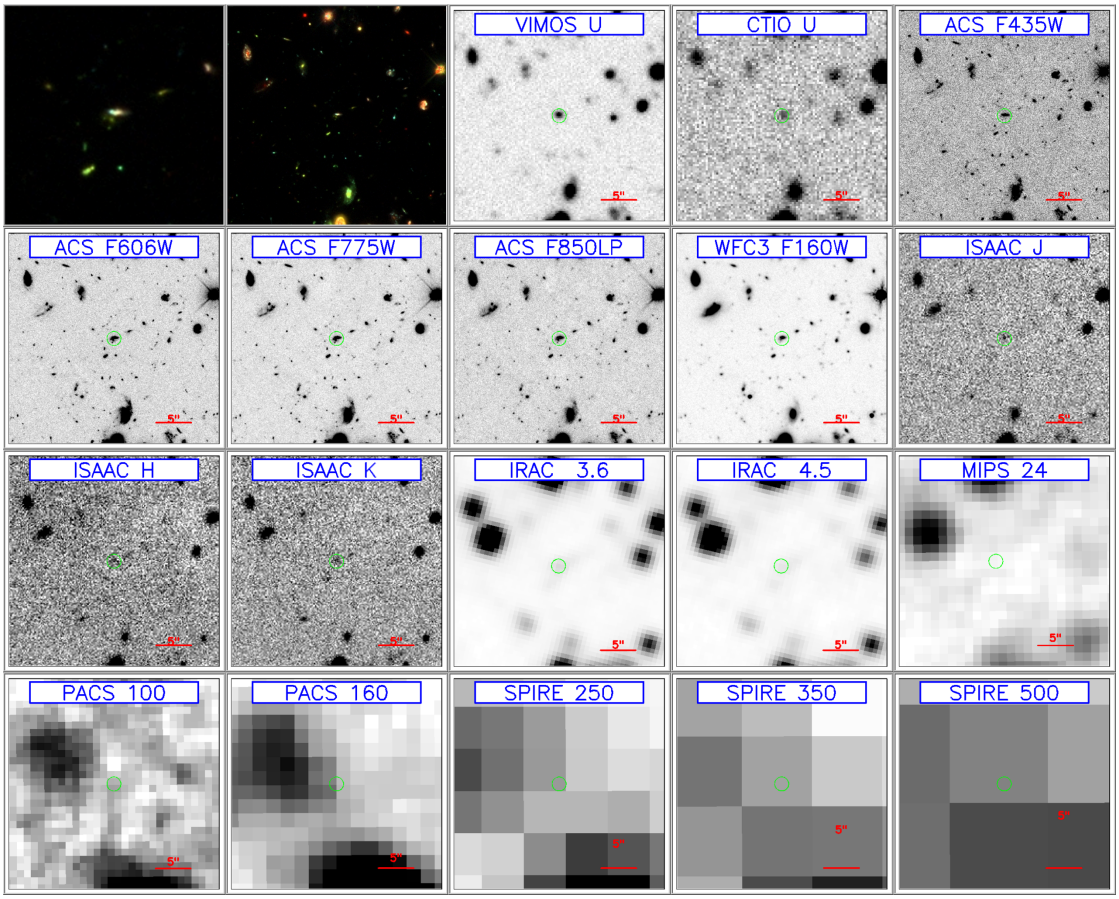

8257

$\alpha_{\rm J2000.0}$ [deg]	53.16078568	$\rm SFR_{SINOPSIS,1}$ [$\rm M_\odot\ yr^{-1}$]	$0.668^{+4.656}_{-0.210}$
$\delta_{\rm J2000.0}$ [deg]	-27.77544975	$\rm SFR_{SINOPSIS}$ [$\rm M_\odot\ yr^{-1}$]	$0.345^{+8.496}_{-0.141}$
z_b	0.621±0.191	$\rm SFR_{HyperZmass}$ [$\rm M_\odot\ yr^{-1}$]	$0.998^{+0.293}_{-0.024}$
$z_{\rm IANI}$	0.6217	$\rm SFR_{UV}$ [$\rm M_\odot\ yr^{-1}$]	0.752
$\rm H_{160}$ [mag]	20.591±0.064	$\rm SFR_{IR}$ [$\rm M_\odot\ yr^{-1}$]	1.362
D_L [Gly]	12.021	$\rm SFR_{UV+IR}$ [$\rm M_\odot\ yr^{-1}$]	2.114
$\rm EW_{SINOPSIS,1}$ [Å]	-32.980	$\rm A_{V,SINOPSIS}$ [mag]	$0.32^{+3.78}_{-0.00}$
$\rm EW_{SINOPSIS}$ [Å]	-28.860	$\rm \overline{A}_{V,SINOPSIS}$ [mag]	$0.76^{+0.32}_{-0.73}$
$\rm M_{\star,SINOPSIS}$ [$\rm M_\odot$]	$10.0436^{+0.0716}_{-0.0178}$	$\rm A_{V,}$*HyperZmass* [mag]	$0^{+0.15}_{-0.00}$
$\rm M_{\star,}$*HyperZmass* [$\rm M_\odot$]	$10.1487^{+0.0188}_{-0.0169}$	$\rm A_{IRX}$ [mag]	1.12

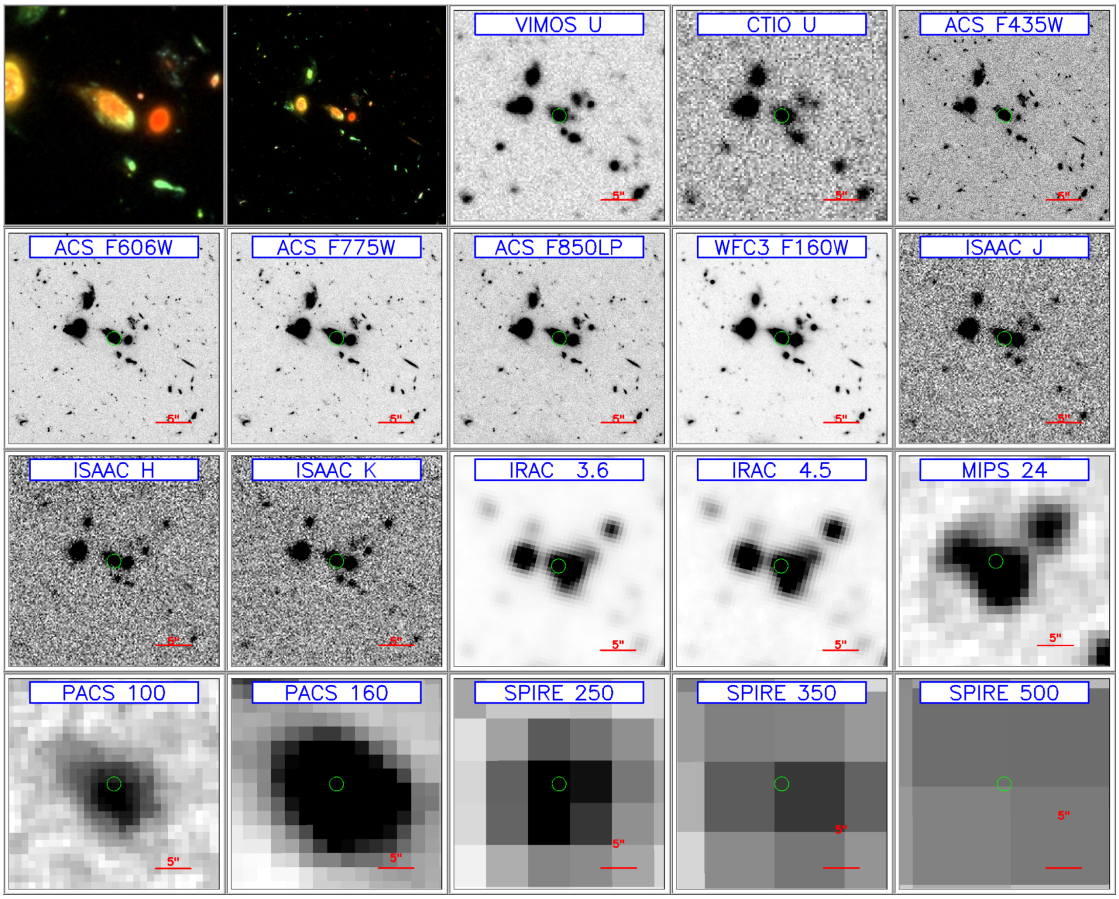

8275

$\alpha_{\rm J2000.0}$ [deg]	53.15205765	$\rm SFR_{SINOPSIS,1}$ [$\rm M_\odot$ $\rm yr^{-1}$]	$7.103^{+5.715}_{-1.022}$
$\delta_{\rm J2000.0}$ [deg]	-27.77471733	$\rm SFR_{SINOPSIS}$ [$\rm M_\odot$ $\rm yr^{-1}$]	$5.212^{+6.579}_{-0.477}$
z_b	0.705±0.201	$\rm SFR_{HyperZmass}$ [$\rm M_\odot$ $\rm yr^{-1}$]	$14.572^{+5.334}_{-3.595}$
$z_{\rm IANI}$	0.7651	$\rm SFR_{UV}$ [$\rm M_\odot$ $\rm yr^{-1}$]	3.909
$\rm H_{160}$ [mag]	20.751±0.064	$\rm SFR_{IR}$ [$\rm M_\odot$ $\rm yr^{-1}$]	5.554
D_L [Gly]	15.492	$\rm SFR_{UV+IR}$ [$\rm M_\odot$ $\rm yr^{-1}$]	9.463
$\rm EW_{SINOPSIS,1}$ [Å]	-68.642	$\rm A_{V,SINOPSIS}$ [mag]	$1.28^{+0.12}_{-0.73}$
$\rm EW_{SINOPSIS}$ [Å]	-58.200	$\rm \overline{A}_{V,SINOPSIS}$ [mag]	$0.13^{+0.70}_{-0.01}$
$\rm M_{\star,SINOPSIS}$ [$\rm M_\odot$]	$10.4815^{+0.0077}_{-0.2948}$	$\rm A_{V,}$*HyperZmass* [mag]	$0.65^{+0.15}_{-0.15}$
$\rm M_{\star,}$*HyperZmass* [$\rm M_\odot$]	$10.1471^{+0.0270}_{-0.0661}$	$\rm A_{IRX}$ [mag]	0.96

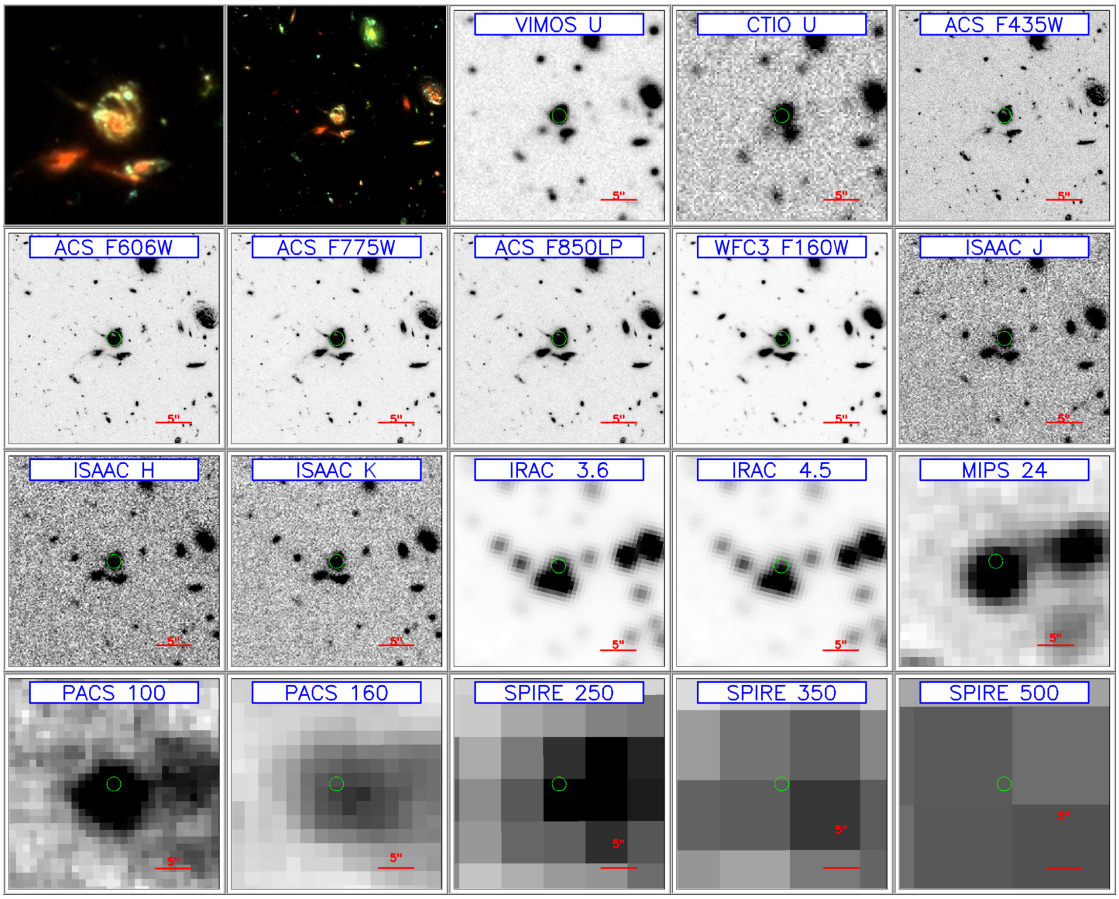

8316

$\alpha_{\rm J2000.0}$ [deg]	53.16015244	$\rm SFR_{SINOPSIS,1}$ [$\rm M_\odot$ $\rm yr^{-1}$]	$1.909^{+0.041}_{-1.903}$
$\delta_{\rm J2000.0}$ [deg]	-27.77552986	$\rm SFR_{SINOPSIS}$ [$\rm M_\odot$ $\rm yr^{-1}$]	$2.364^{+2.539}_{-2.336}$
z_b	0.675±0.197	$\rm SFR_{HyperZmass}$ [$\rm M_\odot$ $\rm yr^{-1}$]	$0.160^{+0.046}_{-0.005}$
$z_{\rm IANI}$	0.6221	$\rm SFR_{UV}$ [$\rm M_\odot$ $\rm yr^{-1}$]	0.061
$\rm H_{160}$ [mag]	20.689±0.064	$\rm SFR_{IR}$ [$\rm M_\odot$ $\rm yr^{-1}$]	1.102
D_L [Gly]	12.031	$\rm SFR_{UV+IR}$ [$\rm M_\odot$ $\rm yr^{-1}$]	1.163
$\rm EW_{SINOPSIS,1}$ [Å]	-9.534	$\rm A_{V,SINOPSIS}$ [mag]	$2.27^{+2.77}_{-1.49}$
$\rm EW_{SINOPSIS}$ [Å]	-7.160	$\rm \overline{A}_{V,SINOPSIS}$ [mag]	$0.60^{+0.24}_{-0.29}$
$\rm M_{\star,SINOPSIS}$ [$\rm M_\odot$]	$10.4468^{+0.0336}_{-0.0622}$	$\rm A_{V,}$*HyperZmass* [mag]	$0.60^{+0.00}_{-0.05}$
$\rm M_{\star,}$*HyperZmass* [$\rm M_\odot$]	$10.1959^{+0.1757}_{-0.0148}$	$\rm A_{IRX}$ [mag]	3.21

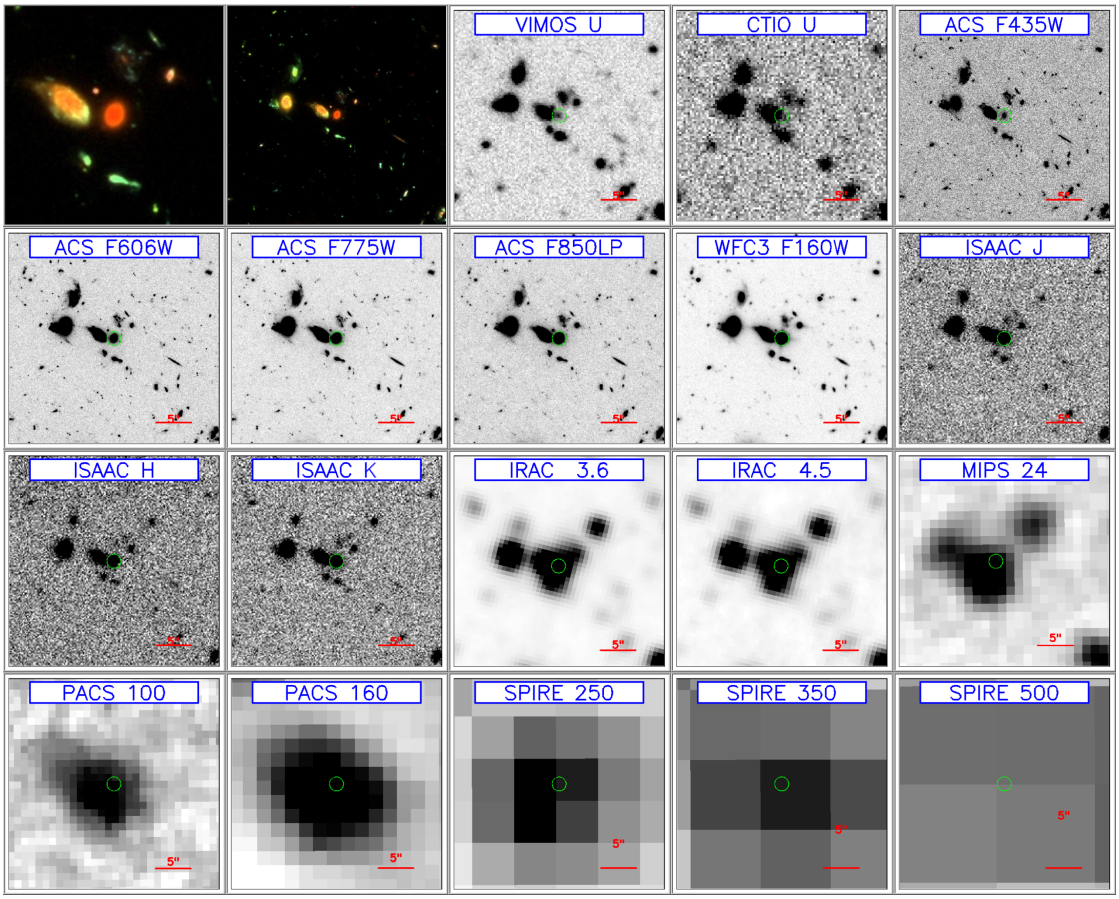

8624

$\alpha_{\rm J2000.0}$ [deg]	53.15746307	$\rm SFR_{SINOPSIS,1}$ [$\rm M_\odot$ $\rm yr^{-1}$]	-
$\delta_{\rm J2000.0}$ [deg]	-27.77644920	$\rm SFR_{SINOPSIS}$ [$\rm M_\odot$ $\rm yr^{-1}$]	-
z_b	0.780±0.209	$\rm SFR_{HyperZmass}$ [$\rm M_\odot$ $\rm yr^{-1}$]	$0.822^{+0.615}_{-0.450}$
$z_{\rm IANI}$	0.8321	$\rm SFR_{UV}$ [$\rm M_\odot$ $\rm yr^{-1}$]	-
$\rm H_{160}$ [mag]	24.233±0.095	$\rm SFR_{IR}$ [$\rm M_\odot$ $\rm yr^{-1}$]	-
D_L [Gly]	17.177	$\rm SFR_{UV+IR}$ [$\rm M_\odot$ $\rm yr^{-1}$]	-
$\rm EW_{SINOPSIS,1}$ [Å]	-	$\rm A_{V,SINOPSIS}$ [mag]	-
$\rm EW_{SINOPSIS}$ [Å]	-	$\overline{\rm A}_{\rm V,SINOPSIS}$ [mag]	-
$\rm M_{\star,SINOPSIS}$ [$\rm M_\odot$]	-	$\rm A_{V,}$*HyperZmass* [mag]	$0.90^{+0.25}_{-0.40}$
$\rm M_{\star,}$*HyperZmass* [$\rm M_\odot$]	$8.8984^{+0.1379}_{-0.1080}$	$\rm A_{IRX}$ [mag]	-

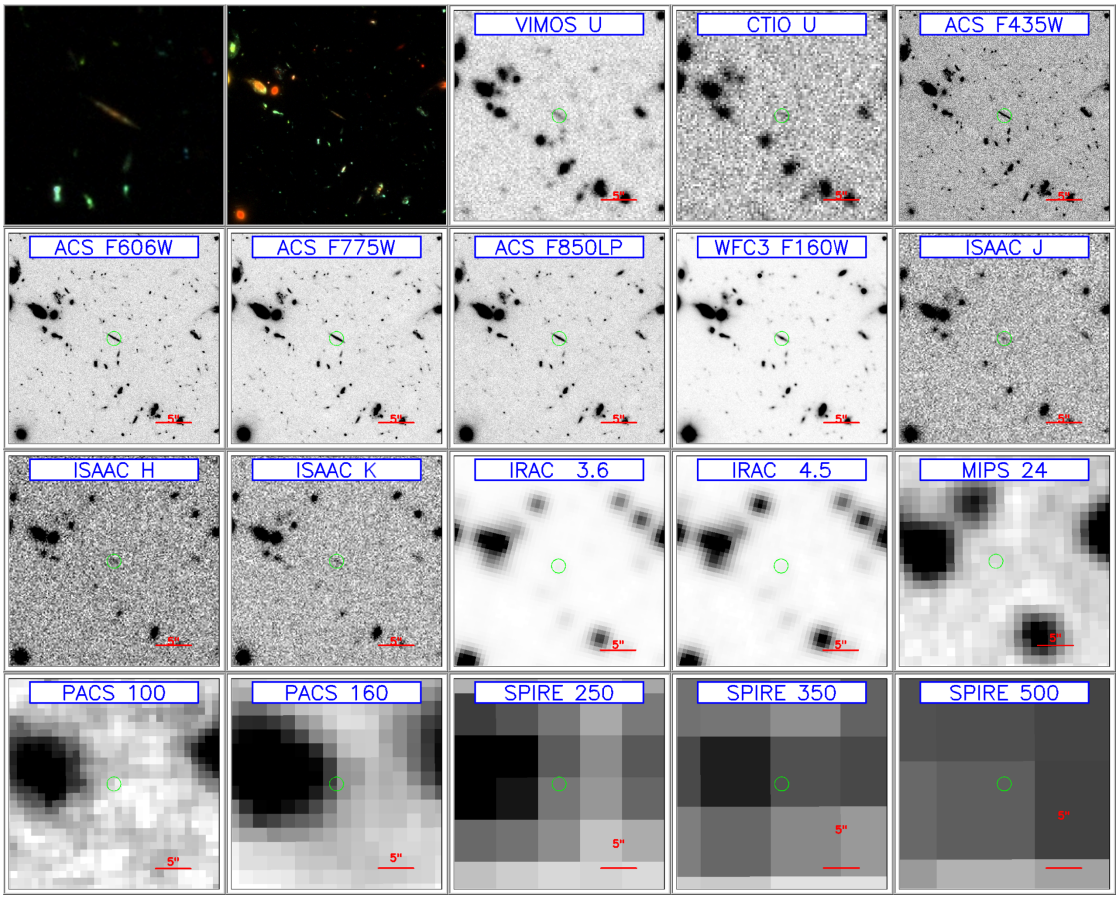

UDF9

$\alpha_{\rm J2000.0}$ [deg]	53.18092	$\rm SFR_{SINOPSIS,1}$ [$\rm M_\odot$ $\rm yr^{-1}$]	$19.451^{+4.049}_{-7.930}$
$\delta_{\rm J2000.0}$ [deg]	-27.77624	$\rm SFR_{SINOPSIS}$ [$\rm M_\odot$ $\rm yr^{-1}$]	$3.765^{+80.869}_{-1.351}$
z_b	-	$\rm SFR_{HyperZmass}$ [$\rm M_\odot$ $\rm yr^{-1}$]	$3.817^{+4.683}_{-1.301}$
$z_{\rm IANI}$	0.6675	$\rm SFR_{UV}$ [$\rm M_\odot$ $\rm yr^{-1}$]	0.802
$\rm H_{160}$ [mag]	21.41	$\rm SFR_{IR}$ [$\rm M_\odot$ $\rm yr^{-1}$]	5.218
D_L [Gly]	13.109	$\rm SFR_{UV+IR}$ [$\rm M_\odot$ $\rm yr^{-1}$]	6.020
$\rm EW_{SINOPSIS,1}$ [Å]	-	$\rm A_{V,SINOPSIS}$ [mag]	$2.68^{+3.47}_{-0.33}$
$\rm EW_{SINOPSIS}$ [Å]	-27.920	$\overline{\rm A}_{\rm V,SINOPSIS}$ [mag]	$2.93^{+2.82}_{-0.07}$
$\rm M_{\star,SINOPSIS}$ [$\rm M_\odot$]	$10.3551^{+0.0172}_{-0.7969}$	$\rm A_{V,}$*HyperZmass* [mag]	$1.45^{+0.40}_{-0.20}$
$\rm M_{\star,}$*HyperZmass* [$\rm M_\odot$]	$10.0195^{+0.0597}_{-0.1065}$	$\rm A_{IRX}$ [mag]	2.19

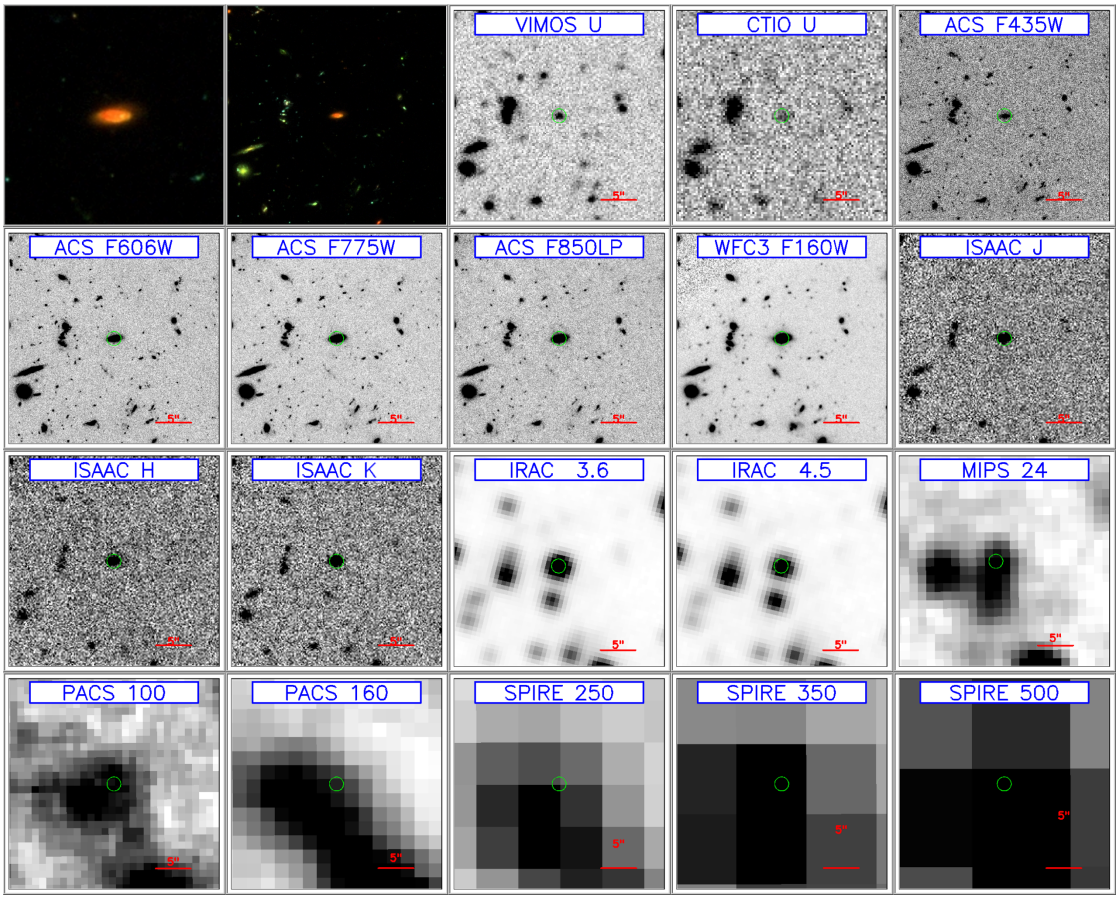

UDF14

$\alpha_{\mathrm{J2000.0}}$ [deg]	53.17069244	$\mathrm{SFR_{SINOPSIS,1}}$ [$\mathrm{M_\odot\ yr^{-1}}$]	$0.266^{+3.110}_{-0.021}$
$\delta_{\mathrm{J2000.0}}$ [deg]	-27.78197289	$\mathrm{SFR_{SINOPSIS}}$ [$\mathrm{M_\odot\ yr^{-1}}$]	$31.839^{+0.117}_{-22.748}$
z_b	0.775±0.209	$\mathrm{SFR_{HyperZmass}}$ [$\mathrm{M_\odot\ yr^{-1}}$]	$0.855^{+0.555}_{-0.306}$
z_{IANI}	0.7666	$\mathrm{SFR_{UV}}$ [$\mathrm{M_\odot\ yr^{-1}}$]	0.562
$\mathrm{H_{160}}$ [mag]	22.76	$\mathrm{SFR_{IR}}$ [$\mathrm{M_\odot\ yr^{-1}}$]	0.976
D_L [Gly]	15.530	$\mathrm{SFR_{UV+IR}}$ [$\mathrm{M_\odot\ yr^{-1}}$]	1.538
$\mathrm{EW_{SINOPSIS,1}}$ [Å]	-73.949	$\mathrm{A_{V,SINOPSIS}}$ [mag]	$6.14^{+0.00}_{-3.26}$
$\mathrm{EW_{SINOPSIS}}$ [Å]	-87.430	$\overline{\mathrm{A}}_{\mathrm{V,SINOPSIS}}$ [mag]	$3.66^{+0.00}_{-0.77}$
$\mathrm{M_{\star,SINOPSIS}}$ [$\mathrm{M_\odot}$]	$8.8036^{+0.8763}_{-0.0063}$	$\mathrm{A_{V,}}_{HyperZmass}$ [mag]	$0.90^{+0.25}_{-0.20}$
$\mathrm{M_{\star,}}_{HyperZmass}$ [$\mathrm{M_\odot}$]	$9.6105^{+0.0580}_{-0.0696}$	$\mathrm{A_{IRX}}$ [mag]	1.09

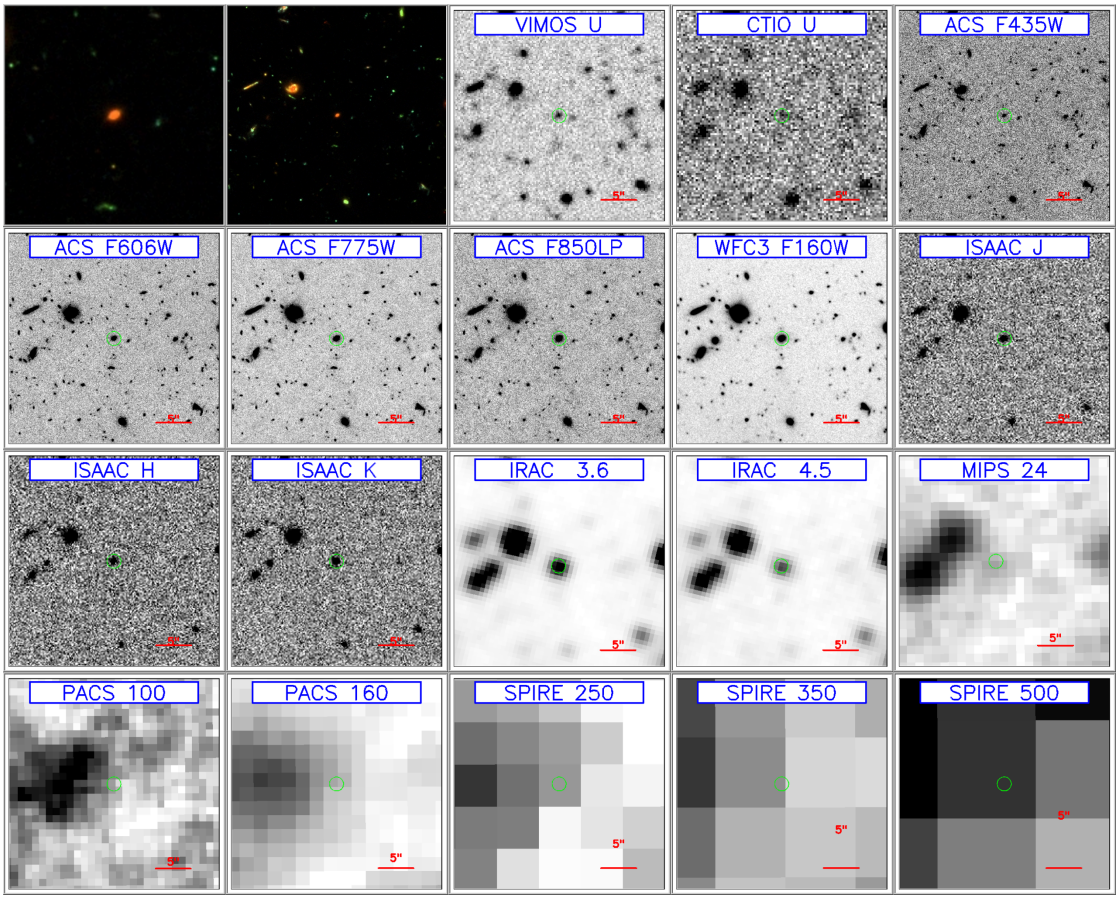

Bibliography

Bacon, R., Accardo, M., Adjali, L., Anwand, H., Bauer, S., Biswas, I., Blaizot, J., Boudon, D., Brau-Nogue, S., Brinchmann, J., Caillier, P., Capoani, L., Carollo, C. M., Contini, T., Couderc, P., Daguisé, E., Deiries, S., Delabre, B., Dreizler, S., Dubois, J., Dupieux, M., Dupuy, C., Emsellem, E., Fechner, T., Fleischmann, A., François, M., Gallou, G., Gharsa, T., Glindemann, A., Gojak, D., Guiderdoni, B., Hansali, G., Hahn, T., Jarno, A., Kelz, A., Koehler, C., Kosmalski, J., Laurent, F., Le Floch, M., Lilly, S. J., Lizon, J.-L., Loupias, M., Manescau, A., Monstein, C., Nicklas, H., Olaya, J.-C., Pares, L., Pasquini, L., Pécontal-Rousset, A., Pelló, R., Petit, C., Popow, E., Reiss, R., Remillieux, A., Renault, E., Roth, M., Rupprecht, G., Serre, D., Schaye, J., Soucail, G., Steinmetz, M., Streicher, O., Stuik, R., Valentin, H., Vernet, J., Weilbacher, P., Wisotzki, L., and Yerle, N. (2010). The MUSE second-generation VLT instrument. In *Ground-based and Airborne Instrumentation for Astronomy III*, volume 7735 of Proc. SPIE, page 773508.

Bacon, R., Accardo, M., Adjali, L., Anwand, H., Bauer, S.-M., Blaizot, J., Boudon, D., Brinchmann, J., Brotons, L., Caillier, P., Capoani, L., Carollo, M., Comin, M., Contini, T., Cumani, C., Daguis, E., Deiries, S., Delabre, B., Dreizler, S., Dubois, J.-P., Dupieux, M., Dupuy, C., Emsellem, E., Fleischmann, A., François, M., Gallou, G., Gharsa, T., Girard, N., Glindemann, A., Guiderdoni, B., Hahn, T., Hansali, G., Hofmann, D., Jarno, A., Kelz, A., Kiekebusch, M., Knudstrup, J., Koehler, C., Kollatschny, W., Kosmalski, J., Laurent, F., Le Floch, M., Lilly, S., Lizon à L'Allemand, J.-L., Loupias, M., Manescau, A., Monstein, C., Nicklas, H., Niemeyer, J., Olaya, J.-C., Palsa, R., Parès, L., Pasquini, L., Pécontal-Rousset, A., Pello, R., Petit, C., Piqueras, L., Popow, E., Reiss, R., Remillieux, A., Renault, E., Rhode, P., Richard, J., Roth, J., Rupprecht, G., Schaye, J., Slezak, E., Soucail, G., Steinmetz, M., Streicher, O., Stuik, R., Valentin, H., Vernet, J., Weilbacher, P., Wisotzki, L., Yerle, N., and Zins, G. (2012). News of the MUSE. *The Messenger*, 147:4–6.

Balestra, I., Mercurio, A., Sartoris, B., Girardi, M., Grillo, C., Nonino, M., Rosati, P., Biviano, A., Ettori, S., Forman, W., Jones, C., Koekemoer, A., Medezinski, E., Merten, J., Ogrean, G. A., Tozzi, P., Umetsu, K., Vanzella, E., van Weeren, R. J., Zitrin, A., Annunziatella, M., Caminha, G. B., Broadhurst, T., Coe, D., Donahue, M., Fritz, A., Frye, B., Kelson, D., Lombardi, M., Maier, C., Meneghetti, M., Monna, A., Postman, M., Scodeggio, M., Seitz, S., and Ziegler, B. (2016). VizieR Online Data Catalog:

CLASH-VLT: the FF cluster MACS J0416.1-2403 (Balestra+, 2016). *VizieR Online Data Catalog*, 222.

Balogh, M. L., Morris, S. L., Yee, H. K. C., Carlberg, R. G., and Ellingson, E. (1999). Differential Galaxy Evolution in Cluster and Field Galaxies at z˜0.3. ApJ, 527:54–79.

Beckwith, S. V. W., Caldwell, J., Clampin, M., de Marchi, G., Dickinson, M., Ferguson, H., Fruchter, A., Hook, R., Jogee, S., Koekemoer, A., Lucas, R., Malhotra, S., Giavalisco, M., Panagia, N., Rhoads, J., Soderblom, D. R., Royle, T., Stiavelli, M., Somerville, R., Casertano, S., Margon, B., and Blades, J. C. (2003). The Hubble Ultra Deep Field. In *American Astronomical Society Meeting Abstracts #202*, volume 35 of *Bulletin of the American Astronomical Society*, page 723.

Benítez, N., Ford, H., Bouwens, R., Menanteau, F., Blakeslee, J., Gronwall, C., Illingworth, G., Meurer, G., Broadhurst, T. J., Clampin, M., Franx, M., Hartig, G. F., Magee, D., Sirianni, M., Ardila, D. R., Bartko, F., Brown, R. A., Burrows, C. J., Cheng, E. S., Cross, N. J. G., Feldman, P. D., Golimowski, D. A., Infante, L., Kimble, R. A., Krist, J. E., Lesser, M. P., Levay, Z., Martel, A. R., Miley, G. K., Postman, M., Rosati, P., Sparks, W. B., Tran, H. D., Tsvetanov, Z. I., White, R. L., and Zheng, W. (2004). Faint Galaxies in Deep Advanced Camera for Surveys Observations. ApJS, 150:1–18.

Bertin, E. and Arnouts, S. (1996). SExtractor: Software for source extraction. A&AS, 117:393–404.

Bolzonella, M., Miralles, J.-M., and Pelló, R. (2000). Photometric redshifts based on standard SED fitting procedures. A&A, 363:476–492.

Bouwens, R. J., Illingworth, G. D., Oesch, P. A., Labbé, I., Trenti, M., van Dokkum, P., Franx, M., Stiavelli, M., Carollo, C. M., Magee, D., and Gonzalez, V. (2011). Ultraviolet Luminosity Functions from 132 z ˜ 7 and z ˜ 8 Lyman-break Galaxies in the Ultra-deep HUDF09 and Wide-area Early Release Science WFC3/IR Observations. ApJ, 737:90.

Bradač, M., Clowe, D., Gonzalez, A. H., Marshall, P., Forman, W., Jones, C., Markevitch, M., Randall, S., Schrabback, T., and Zaritsky, D. (2006). Strong and Weak Lensing United. III. Measuring the Mass Distribution of the Merging Galaxy Cluster 1ES 0657-558. ApJ, 652:937–947.

Bressan, A., Granato, G. L., and Silva, L. (1998). Modelling intermediate age and old stellar populations in the Infrared. A&A, 332:135–148.

Bressan, A., Marigo, P., Girardi, L., Salasnich, B., Dal Cero, C., Rubele, S., and Nanni, A. (2012). PARSEC: stellar tracks and isochrones with the PAdova and TRieste Stellar Evolution Code. MNRAS, 427:127–145.

Brinchmann, J., Charlot, S., White, S. D. M., Tremonti, C., Kauffmann, G., Heckman, T., and Brinkmann, J. (2004). The physical properties of star-forming galaxies in the low-redshift Universe. MNRAS, 351:1151–1179.

Bromm, V., Yoshida, N., Hernquist, L., and McKee, C. F. (2009). The formation of the first stars and galaxies. Nature, 459:49–54.

Bruzual, G. and Charlot, S. (2003). Stellar population synthesis at the resolution of 2003. MNRAS, 344:1000–1028.

Bruzual A., G. (1983). Spectral evolution of galaxies. I - Early-type systems. ApJ, 273:105–127.

Calzetti, D. (2001). The Dust Opacity of Star-forming Galaxies. PASP, 113:1449–1485.

Calzetti, D., Armus, L., Bohlin, R. C., Kinney, A. L., Koornneef, J., and Storchi-Bergmann, T. (2000). The Dust Content and Opacity of Actively Star-forming Galaxies. ApJ, 533:682–695.

Calzetti, D., Kinney, A. L., and Storchi-Bergmann, T. (1994). Dust extinction of the stellar continua in starburst galaxies: The ultraviolet and optical extinction law. ApJ, 429:582–601.

Caminha, G. B., Grillo, C., Rosati, P., Balestra, I., Karman, W., Lombardi, M., Mercurio, A., Nonino, M., Tozzi, P., Zitrin, A., Biviano, A., Girardi, M., Koekemoer, A. M., Melchior, P., Meneghetti, M., Munari, E., Suyu, S. H., Umetsu, K., Annunziatella, M., Borgani, S., Broadhurst, T., Caputi, K. I., Coe, D., Delgado-Correal, C., Ettori, S., Fritz, A., Frye, B., Gobat, R., Maier, C., Monna, A., Postman, M., Sartoris, B., Seitz, S., Vanzella, E., and Ziegler, B. (2016a). CLASH-VLT: A highly precise strong lensing model of the galaxy cluster RXC J2248.7-4431 (Abell S1063) and prospects for cosmography. A&A, 587:A80.

Caminha, G. B., Grillo, C., Rosati, P., Balestra, I., Mercurio, A., Vanzella, E., Biviano, A., Caputi, K. I., Delgado-Correal, C., Karman, W., Lombardi, M., Meneghetti, M., Sartoris, B., and Tozz, P. (2016b). A refined mass distribution of the cluster MACS J0416.1−2403 from a new large set of spectroscopic multiply lensed sources. *ArXiv e-prints*.

Capak, P. L., Riechers, D., Scoville, N. Z., Carilli, C., Cox, P., Neri, R., Robertson, B., Salvato, M., Schinnerer, E., Yan, L., Wilson, G. W., Yun, M., Civano, F., Elvis, M., Karim, A., Mobasher, B., and Staguhn, J. G. (2011). A massive protocluster of galaxies at a redshift of z˜5.3. Nature, 470:233–235.

Cardelli, J. A., Clayton, G. C., and Mathis, J. S. (1989). The relationship between infrared, optical, and ultraviolet extinction. ApJ, 345:245–256.

Castellano, M., Amorín, R., Merlin, E., Fontana, A., McLure, R. J., Mármol-Queraltó, E., Mortlock, A., Parsa, S., Dunlop, J. S., Elbaz, D., Balestra, I., Boucaud, A., Bourne, N., Boutsia, K., Brammer, G., Bruce, V. A., Buitrago, F., Capak, P., Cappelluti, N., Ciesla, L., Comastri, A., Cullen, F., Derriere, S., Faber, S. M., Giallongo, E., Grazian, A., Grillo, C., Mercurio, A., Michałowski, M. J., Nonino, M., Paris, D., Pentericci,

L., Pilo, S., Rosati, P., Santini, P., Schreiber, C., Shu, X., and Wang, T. (2016). The ASTRODEEP Frontier Fields catalogues. II. Photometric redshifts and rest frame properties in Abell-2744 and MACS-J0416. A&A, 590:A31.

Chabrier, G. (2003). Galactic Stellar and Substellar Initial Mass Function. PASP, 115:763–795.

Charlot, S. and Bruzual A., G. (2017). in prep.

Charlot, S. and Longhetti, M. (2001). Nebular emission from star-forming galaxies. MNRAS, 323:887–903.

Coe, D., Benítez, N., Sánchez, S. F., Jee, M., Bouwens, R., and Ford, H. (2006). Galaxies in the Hubble Ultra Deep Field. I. Detection, Multiband Photometry, Photometric Redshifts, and Morphology. AJ, 132:926–959.

Combes, F., García-Burillo, S., Braine, J., Schinnerer, E., Walter, F., and Colina, L. (2013). Gas fraction and star formation efficiency at z $\leq$ 1.0. A&A, 550:A41.

Daddi, E., Dickinson, M., Morrison, G., Chary, R., Cimatti, A., Elbaz, D., Frayer, D., Renzini, A., Pope, A., Alexander, D. M., Bauer, F. E., Giavalisco, M., Huynh, M., Kurk, J., and Mignoli, M. (2007). Multiwavelength Study of Massive Galaxies at z˜2. I. Star Formation and Galaxy Growth. ApJ, 670:156–172.

Driver, S. P., Windhorst, R. A., and Griffiths, R. E. (1995). The Contribution of Late-Type/Irregulars to the Faint Galaxy Counts from Hubble Space Telescope Medium-Deep Survey Images. ApJ, 453:48.

Dunlop, J. S., McLure, R. J., Biggs, A. D., Geach, J. E., Michalowski, M. J., Ivison, R. J., Rujopakarn, W., van Kampen, E., Kirkpatrick, A., Pope, A., Scott, D., Swinbank, A. M., Targett, T. A., Aretxaga, I., Austermann, J. E., Best, P. N., Bruce, V. A., Chapin, E. L., Charlot, S., Cirasuolo, M., Coppin, K. E. K., Ellis, R. S., Finkelstein, S. L., Hayward, C. C., Hughes, D. H., Ibar, E., Khochfar, S., Koprowski, M. P., Narayanan, D., Papovich, C., Peacock, J. A., Robertson, B., Vernstrom, T., van der Werf, P. P., Wilson, G. W., and Yun, M. (2016). A deep ALMA image of the Hubble Ultra Deep Field. *ArXiv e-prints*.

Ebeling, H., Edge, A. C., Mantz, A., Barrett, E., Henry, J. P., Ma, C. J., and van Speybroeck, L. (2010). The X-ray brightest clusters of galaxies from the Massive Cluster Survey. MNRAS, 407:83–93.

Elbaz, D., Dickinson, M., Hwang, H. S., Díaz-Santos, T., Magdis, G., Magnelli, B., Le Borgne, D., Galliano, F., Pannella, M., Chanial, P., Armus, L., Charmandaris, V., Daddi, E., Aussel, H., Popesso, P., Kartaltepe, J., Altieri, B., Valtchanov, I., Coia, D., Dannerbauer, H., Dasyra, K., Leiton, R., Mazzarella, J., Alexander, D. M., Buat, V., Burgarella, D., Chary, R.-R., Gilli, R., Ivison, R. J., Juneau, S., Le Floc'h, E., Lutz, D., Morrison, G. E., Mullaney, J. R., Murphy, E., Pope, A., Scott, D., Brodwin,

M., Calzetti, D., Cesarsky, C., Charlot, S., Dole, H., Eisenhardt, P., Ferguson, H. C., Förster Schreiber, N., Frayer, D., Giavalisco, M., Huynh, M., Koekemoer, A. M., Papovich, C., Reddy, N., Surace, C., Teplitz, H., Yun, M. S., and Wilson, G. (2011). GOODS-Herschel: an infrared main sequence for star-forming galaxies. A&A, 533:A119.

Ellis, R. S., McLure, R. J., Dunlop, J. S., Robertson, B. E., Ono, Y., Schenker, M. A., Koekemoer, A., Bowler, R. A. A., Ouchi, M., Rogers, A. B., Curtis-Lake, E., Schneider, E., Charlot, S., Stark, D. P., Furlanetto, S. R., and Cirasuolo, M. (2013). The Abundance of Star-forming Galaxies in the Redshift Range 8.5-12: New Results from the 2012 Hubble Ultra Deep Field Campaign. ApJ, 763:L7.

Ferland, G. J. (1996). *Hazy, A Brief Introduction to Cloudy 90*.

Fritz, J., Poggianti, B. M., Bettoni, D., Cava, A., Couch, W. J., D'Onofrio, M., Dressler, A., Fasano, G., Kjærgaard, P., Moles, M., and Varela, J. (2007). A spectrophotometric model applied to cluster galaxies: the WINGS dataset. A&A, 470:137–152.

Fritz, J., Poggianti, B. M., Cava, A., Moretti, A., Varela, J., Bettoni, D., Couch, W. J., D'Onofrio D'Onofrio, M., Dressler, A., Fasano, G., Kjærgaard, P., Marziani, P., Moles, M., and Omizzolo, A. (2014). WINGS-SPE. III. Equivalent width measurements, spectral properties, and evolution of local cluster galaxies. A&A, 566:A32.

Fritz, J., Poggianti, B. M., Cava, A., Moretti, A., and WINGS Collaboration (2011). Equivalent Width Measurements in Optical Spectra of Galaxies in Local Clusters: Hints on the Star Formation History in Clusters. *Baltic Astronomy*, 20:435–441.

Garilli, B., Fumana, M., Franzetti, P., Paioro, L., Scodeggio, M., Le Fèvre, O., Paltani, S., and Scaramella, R. (2010). EZ: A Tool For Automatic Redshift Measurement. PASP, 122:827–838.

Giacconi, R., Rosati, P., Tozzi, P., Borgani, S., Hasinger, G., Bergeron, J., Gilmozzi, R., Nonino, M., Gilli, R., Zirm, A., Wang, J. X., Zheng, W., Kellermann, K. I., Shaver, P., Schreier, E., Koekemoer, A., Grogin, N., and Norman, C. (2000). The Chandra Deep Field South. In *American Astronomical Society Meeting Abstracts*, volume 32 of *Bulletin of the American Astronomical Society*, page 1562.

Giavalisco, M., Ferguson, H. C., Koekemoer, A. M., Dickinson, M., Alexander, D. M., Bauer, F. E., Bergeron, J., Biagetti, C., Brandt, W. N., Casertano, S., Cesarsky, C., Chatzichristou, E., Conselice, C., Cristiani, S., Da Costa, L., Dahlen, T., de Mello, D., Eisenhardt, P., Erben, T., Fall, S. M., Fassnacht, C., Fosbury, R., Fruchter, A., Gardner, J. P., Grogin, N., Hook, R. N., Hornschemeier, A. E., Idzi, R., Jogee, S., Kretchmer, C., Laidler, V., Lee, K. S., Livio, M., Lucas, R., Madau, P., Mobasher, B., Moustakas, L. A., Nonino, M., Padovani, P., Papovich, C., Park, Y., Ravindranath, S., Renzini, A., Richardson, M., Riess, A., Rosati, P., Schirmer, M., Schreier, E., Somerville, R. S., Spinrad, H., Stern, D., Stiavelli, M., Strolger, L., Urry, C. M., Vandame, B., Williams, R., and Wolf, C. (2004). The Great Observatories Origins Deep Survey: Initial Results from Optical and Near-Infrared Imaging. ApJ, 600:L93–L98.

Grazian, A., Fontana, A., de Santis, C., Nonino, M., Salimbeni, S., Giallongo, E., Cristiani, S., Gallozzi, S., and Vanzella, E. (2006). The GOODS-MUSIC sample: a multicolour catalog of near-IR selected galaxies in the GOODS-South field. A&A, 449:951–968.

Grogin, N. A., Kocevski, D. D., Faber, S. M., Ferguson, H. C., Koekemoer, A. M., Riess, A. G., Acquaviva, V., Alexander, D. M., Almaini, O., Ashby, M. L. N., Barden, M., Bell, E. F., Bournaud, F., Brown, T. M., Caputi, K. I., Casertano, S., Cassata, P., Castellano, M., Challis, P., Chary, R.-R., Cheung, E., Cirasuolo, M., Conselice, C. J., Roshan Cooray, A., Croton, D. J., Daddi, E., Dahlen, T., Davé, R., de Mello, D. F., Dekel, A., Dickinson, M., Dolch, T., Donley, J. L., Dunlop, J. S., Dutton, A. A., Elbaz, D., Fazio, G. G., Filippenko, A. V., Finkelstein, S. L., Fontana, A., Gardner, J. P., Garnavich, P. M., Gawiser, E., Giavalisco, M., Grazian, A., Guo, Y., Hathi, N. P., Häussler, B., Hopkins, P. F., Huang, J.-S., Huang, K.-H., Jha, S. W., Kartaltepe, J. S., Kirshner, R. P., Koo, D. C., Lai, K., Lee, K.-S., Li, W., Lotz, J. M., Lucas, R. A., Madau, P., McCarthy, P. J., McGrath, E. J., McIntosh, D. H., McLure, R. J., Mobasher, B., Moustakas, L. A., Mozena, M., Nandra, K., Newman, J. A., Niemi, S.-M., Noeske, K. G., Papovich, C. J., Pentericci, L., Pope, A., Primack, J. R., Rajan, A., Ravindranath, S., Reddy, N. A., Renzini, A., Rix, H.-W., Robaina, A. R., Rodney, S. A., Rosario, D. J., Rosati, P., Salimbeni, S., Scarlata, C., Siana, B., Simard, L., Smidt, J., Somerville, R. S., Spinrad, H., Straughn, A. N., Strolger, L.-G., Telford, O., Teplitz, H. I., Trump, J. R., van der Wel, A., Villforth, C., Wechsler, R. H., Weiner, B. J., Wiklind, T., Wild, V., Wilson, G., Wuyts, S., Yan, H.-J., and Yun, M. S. (2011). CANDELS: The Cosmic Assembly Near-infrared Deep Extragalactic Legacy Survey. ApJS, 197:35.

Illingworth, G. D., Magee, D., Oesch, P. A., Bouwens, R. J., Labbé, I., Stiavelli, M., van Dokkum, P. G., Franx, M., Trenti, M., Carollo, C. M., and Gonzalez, V. (2013). The HST eXtreme Deep Field (XDF): Combining All ACS and WFC3/IR Data on the HUDF Region into the Deepest Field Ever. ApJS, 209:6.

Kellermann, K. I., Sramek, R., Schmidt, M., Shaffer, D. B., and Green, R. (1995). VLA observations of objects in the Palomar Bright Quasar Survey. *Astronomy Data Image Library.*

Kennicutt, R. C. and Evans, N. J. (2012). Star Formation in the Milky Way and Nearby Galaxies. ARA&A, 50:531–608.

Kennicutt, Jr., R. C. (1998). Star Formation in Galaxies Along the Hubble Sequence. ARA&A, 36:189–232.

Kirkpatrick, A., Pope, A., Sajina, A., Roebuck, E., Yan, L., Armus, L., Díaz-Santos, T., and Stierwalt, S. (2015). The Role of Star Formation and an AGN in Dust Heating of z = 0.3-2.8 Galaxies. I. Evolution with Redshift and Luminosity. ApJ, 814:9.

Koekemoer, A. M., Faber, S. M., Ferguson, H. C., Grogin, N. A., Kocevski, D. D., Koo, D. C., Lai, K., Lotz, J. M., Lucas, R. A., McGrath, E. J., Ogaz, S., Rajan, A., Riess,

A. G., Rodney, S. A., Strolger, L., Casertano, S., Castellano, M., Dahlen, T., Dickinson, M., Dolch, T., Fontana, A., Giavalisco, M., Grazian, A., Guo, Y., Hathi, N. P., Huang, K.-H., van der Wel, A., Yan, H.-J., Acquaviva, V., Alexander, D. M., Almaini, O., Ashby, M. L. N., Barden, M., Bell, E. F., Bournaud, F., Brown, T. M., Caputi, K. I., Cassata, P., Challis, P. J., Chary, R.-R., Cheung, E., Cirasuolo, M., Conselice, C. J., Roshan Cooray, A., Croton, D. J., Daddi, E., Davé, R., de Mello, D. F., de Ravel, L., Dekel, A., Donley, J. L., Dunlop, J. S., Dutton, A. A., Elbaz, D., Fazio, G. G., Filippenko, A. V., Finkelstein, S. L., Frazer, C., Gardner, J. P., Garnavich, P. M., Gawiser, E., Gruetzbauch, R., Hartley, W. G., Häussler, B., Herrington, J., Hopkins, P. F., Huang, J.-S., Jha, S. W., Johnson, A., Kartaltepe, J. S., Khostovan, A. A., Kirshner, R. P., Lani, C., Lee, K.-S., Li, W., Madau, P., McCarthy, P. J., McIntosh, D. H., McLure, R. J., McPartland, C., Mobasher, B., Moreira, H., Mortlock, A., Moustakas, L. A., Mozena, M., Nandra, K., Newman, J. A., Nielsen, J. L., Niemi, S., Noeske, K. G., Papovich, C. J., Pentericci, L., Pope, A., Primack, J. R., Ravindranath, S., Reddy, N. A., Renzini, A., Rix, H.-W., Robaina, A. R., Rosario, D. J., Rosati, P., Salimbeni, S., Scarlata, C., Siana, B., Simard, L., Smidt, J., Snyder, D., Somerville, R. S., Spinrad, H., Straughn, A. N., Telford, O., Teplitz, H. I., Trump, J. R., Vargas, C., Villforth, C., Wagner, C. R., Wandro, P., Wechsler, R. H., Weiner, B. J., Wiklind, T., Wild, V., Wilson, G., Wuyts, S., and Yun, M. S. (2011). CANDELS: The Cosmic Assembly Near-infrared Deep Extragalactic Legacy Survey-The Hubble Space Telescope Observations, Imaging Data Products, and Mosaics. ApJS, 197:36.

Kroupa, P. (2001). On the variation of the initial mass function. MNRAS, 322:231–246.

Lilly, S. J., Le Fevre, O., Hammer, F., and Crampton, D. (1996). The Canada-France Redshift Survey: The Luminosity Density and Star Formation History of the Universe to Z approximately 1. ApJ, 460:L1.

Liu, G., Calzetti, D., Hong, S., Whitmore, B., Chandar, R., O'Connell, R. W., Blair, W. P., Cohen, S. H., Frogel, J. A., and Kim, H. (2013). Extinction and Dust Geometry in M83 H II Regions: An Hubble Space Telescope/WFC3 Study. ApJ, 778:L41.

Longhetti, M. and Saracco, P. (2009). Stellar mass estimates in early-type galaxies: procedures, uncertainties and models dependence. MNRAS, 394:774–794.

Lutz, D., Poglitsch, A., Altieri, B., Andreani, P., Aussel, H., Berta, S., Bongiovanni, A., Brisbin, D., Cava, A., Cepa, J., Cimatti, A., Daddi, E., Dominguez-Sanchez, H., Elbaz, D., Förster Schreiber, N. M., Genzel, R., Grazian, A., Gruppioni, C., Harwit, M., Le Floc'h, E., Magdis, G., Magnelli, B., Maiolino, R., Nordon, R., Pérez García, A. M., Popesso, P., Pozzi, F., Riguccini, L., Rodighiero, G., Saintonge, A., Sanchez Portal, M., Santini, P., Shao, L., Sturm, E., Tacconi, L. J., Valtchanov, I., Wetzstein, M., and Wieprecht, E. (2011). PACS Evolutionary Probe (PEP) - A Herschel key program. A&A, 532:A90.

Madau, P. (1995). Radiative transfer in a clumpy universe: The colors of high-redshift galaxies. ApJ, 441:18–27.

Madau, P. and Dickinson, M. (2014). Cosmic Star-Formation History. ARA&A, 52:415–486.

Madau, P., Ferguson, H. C., Dickinson, M. E., Giavalisco, M., Steidel, C. C., and Fruchter, A. (1996). High-redshift galaxies in the Hubble Deep Field: colour selection and star formation history to z˜4. MNRAS, 283:1388–1404.

Magdis, G. E., Daddi, E., Béthermin, M., Sargent, M., Elbaz, D., Pannella, M., Dickinson, M., Dannerbauer, H., da Cunha, E., Walter, F., Rigopoulou, D., Charmandaris, V., Hwang, H. S., and Kartaltepe, J. (2012). The Evolving Interstellar Medium of Star-forming Galaxies since z = 2 as Probed by Their Infrared Spectral Energy Distributions. ApJ, 760:6.

Mann, A. W. and Ebeling, H. (2012). X-ray-optical classification of cluster mergers and the evolution of the cluster merger fraction. MNRAS, 420:2120–2138.

McMullin, J. P., Waters, B., Schiebel, D., Young, W., and Golap, K. (2007). CASA Architecture and Applications. In Shaw, R. A., Hill, F., and Bell, D. J., editors, *Astronomical Data Analysis Software and Systems XVI*, volume 376 of *Astronomical Society of the Pacific Conference Series*, page 127.

Merten, J., Coe, D., Dupke, R., Massey, R., Zitrin, A., Cypriano, E. S., Okabe, N., Frye, B., Braglia, F. G., Jiménez-Teja, Y., Benítez, N., Broadhurst, T., Rhodes, J., Meneghetti, M., Moustakas, L. A., Sodré, Jr., L., Krick, J., and Bregman, J. N. (2011). Creation of cosmic structure in the complex galaxy cluster merger Abell 2744. MNRAS, 417:333–347.

Noeske, K. G., Weiner, B. J., Faber, S. M., Papovich, C., Koo, D. C., Somerville, R. S., Bundy, K., Conselice, C. J., Newman, J. A., Schiminovich, D., Le Floc'h, E., Coil, A. L., Rieke, G. H., Lotz, J. M., Primack, J. R., Barmby, P., Cooper, M. C., Davis, M., Ellis, R. S., Fazio, G. G., Guhathakurta, P., Huang, J., Kassin, S. A., Martin, D. C., Phillips, A. C., Rich, R. M., Small, T. A., Willmer, C. N. A., and Wilson, G. (2007). Star Formation in AEGIS Field Galaxies since z=1.1: The Dominance of Gradually Declining Star Formation, and the Main Sequence of Star-forming Galaxies. ApJ, 660:L43–L46.

Nordon, R., Lutz, D., Genzel, R., Berta, S., Wuyts, S., Magnelli, B., Altieri, B., Andreani, P., Aussel, H., Bongiovanni, A., Cepa, J., Cimatti, A., Daddi, E., Fadda, D., Förster Schreiber, N. M., Lagache, G., Maiolino, R., Pérez García, A. M., Poglitsch, A., Popesso, P., Pozzi, F., Rodighiero, G., Rosario, D., Saintonge, A., Sanchez-Portal, M., Santini, P., Sturm, E., Tacconi, L. J., Valtchanov, I., and Yan, L. (2012). The Impact of Evolving Infrared Spectral Energy Distributions of Galaxies on Star Formation Rate Estimates. ApJ, 745:182.

Nordon, R., Lutz, D., Shao, L., Magnelli, B., Berta, S., Altieri, B., Andreani, P., Aussel, H., Bongiovanni, A., Cava, A., Cepa, J., Cimatti, A., Daddi, E., Dominguez, H., Elbaz,

D., Förster Schreiber, N. M., Genzel, R., Grazian, A., Magdis, G., Maiolino, R., Pérez García, A. M., Poglitsch, A., Popesso, P., Pozzi, F., Riguccini, L., Rodighiero, G., Saintonge, A., Sanchez-Portal, M., Santini, P., Sturm, E., Tacconi, L., Valtchanov, I., Wetzstein, M., and Wieprecht, E. (2010). The star-formation rates of $1.5 \leq z \leq 2.5$ massive galaxies. A&A, 518:L24.

Osterbrock, D. E. (1989). *Astrophysics of gaseous nebulae and active galactic nuclei*.

Peng, Y.-j., Lilly, S. J., Kovač, K., Bolzonella, M., Pozzetti, L., Renzini, A., Zamorani, G., Ilbert, O., Knobel, C., Iovino, A., Maier, C., Cucciati, O., Tasca, L., Carollo, C. M., Silverman, J., Kampczyk, P., de Ravel, L., Sanders, D., Scoville, N., Contini, T., Mainieri, V., Scodeggio, M., Kneib, J.-P., Le Fèvre, O., Bardelli, S., Bongiorno, A., Caputi, K., Coppa, G., de la Torre, S., Franzetti, P., Garilli, B., Lamareille, F., Le Borgne, J.-F., Le Brun, V., Mignoli, M., Perez Montero, E., Pello, R., Ricciardelli, E., Tanaka, M., Tresse, L., Vergani, D., Welikala, N., Zucca, E., Oesch, P., Abbas, U., Barnes, L., Bordoloi, R., Bottini, D., Cappi, A., Cassata, P., Cimatti, A., Fumana, M., Hasinger, G., Koekemoer, A., Leauthaud, A., Maccagni, D., Marinoni, C., McCracken, H., Memeo, P., Meneux, B., Nair, P., Porciani, C., Presotto, V., and Scaramella, R. (2010). Mass and Environment as Drivers of Galaxy Evolution in SDSS and zCOSMOS and the Origin of the Schechter Function. ApJ, 721:193–221.

Peng, Y.-j., Lilly, S. J., Renzini, A., and Carollo, M. (2013). The Intriguing Life of Massive Galaxies: The Connections between α_s , β and Merging. In Thomas, D., Pasquali, A., and Ferreras, I., editors, *The Intriguing Life of Massive Galaxies*, volume 295 of *IAU Symposium*, pages 167–170.

Poggianti, B. M., Bressan, A., and Franceschini, A. (2001). Star Formation and Selective Dust Extinction in Luminous Starburst Galaxies. ApJ, 550:195–203.

Pozzetti, L., Bolzonella, M., Lamareille, F., Zamorani, G., Franzetti, P., Le Fèvre, O., Iovino, A., Temporin, S., Ilbert, O., Arnouts, S., Charlot, S., Brinchmann, J., Zucca, E., Tresse, L., Scodeggio, M., Guzzo, L., Bottini, D., Garilli, B., Le Brun, V., Maccagni, D., Picat, J. P., Scaramella, R., Vettolani, G., Zanichelli, A., Adami, C., Bardelli, S., Cappi, A., Ciliegi, P., Contini, T., Foucaud, S., Gavignaud, I., McCracken, H. J., Marano, B., Marinoni, C., Mazure, A., Meneux, B., Merighi, R., Paltani, S., Pellò, R., Pollo, A., Radovich, M., Bondi, M., Bongiorno, A., Cucciati, O., de la Torre, S., Gregorini, L., Mellier, Y., Merluzzi, P., Vergani, D., and Walcher, C. J. (2007). The VIMOS VLT Deep Survey. The assembly history of the stellar mass in galaxies: from the young to the old universe. A&A, 474:443–459.

Renzini, A. (2006). Stellar Population Diagnostics of Elliptical Galaxy Formation. ARA&A, 44:141–192.

Renzini, A. (2009). A different approach to galaxy evolution. MNRAS, 398:L58–L62.

Renzini, A. and Peng, Y.-j. (2015). An Objective Definition for the Main Sequence of Star-forming Galaxies. ApJ, 801:L29.

Rodighiero, G., Cimatti, A., Gruppioni, C., Popesso, P., Andreani, P., Altieri, B., Aussel, H., Berta, S., Bongiovanni, A., Brisbin, D., Cava, A., Cepa, J., Daddi, E., Dominguez-Sanchez, H., Elbaz, D., Fontana, A., Förster Schreiber, N., Franceschini, A., Genzel, R., Grazian, A., Lutz, D., Magdis, G., Magliocchetti, M., Magnelli, B., Maiolino, R., Mancini, C., Nordon, R., Perez Garcia, A. M., Poglitsch, A., Santini, P., Sanchez-Portal, M., Pozzi, F., Riguccini, L., Saintonge, A., Shao, L., Sturm, E., Tacconi, L., Valtchanov, I., Wetzstein, M., and Wieprecht, E. (2010). The first Herschel view of the mass-SFR link in high-z galaxies. A&A, 518:L25.

Rodighiero, G., Daddi, E., Baronchelli, I., Cimatti, A., Renzini, A., Aussel, H., Popesso, P., Lutz, D., Andreani, P., Berta, S., Cava, A., Elbaz, D., Feltre, A., Fontana, A., Förster Schreiber, N. M., Franceschini, A., Genzel, R., Grazian, A., Gruppioni, C., Ilbert, O., Le Floch, E., Magdis, G., Magliocchetti, M., Magnelli, B., Maiolino, R., McCracken, H., Nordon, R., Poglitsch, A., Santini, P., Pozzi, F., Riguccini, L., Tacconi, L. J., Wuyts, S., and Zamorani, G. (2011). The Lesser Role of Starbursts in Star Formation at z = 2. ApJ, 739:L40.

Rodighiero, G., Renzini, A., Daddi, E., Baronchelli, I., Berta, S., Cresci, G., Franceschini, A., Gruppioni, C., Lutz, D., Mancini, C., Santini, P., Zamorani, G., Silverman, J., Kashino, D., Andreani, P., Cimatti, A., Sánchez, H. D., Le Floch, E., Magnelli, B., Popesso, P., and Pozzi, F. (2014). A multiwavelength consensus on the main sequence of star-forming galaxies at z ˜2. MNRAS, 443:19–30.

Rujopakarn, W., Dunlop, J. S., Rieke, G. H., Ivison, R. J., Cibinel, A., Nyland, K., Jagannathan, P., Silverman, J. D., Alexander, D. M., Biggs, A. D., Bhatnagar, S., Ballantyne, D. R., Dickinson, M., Elbaz, D., Geach, J. E., Hayward, C. C., Kirkpatrick, A., McLure, R. J., Michalowski, M. J., Miller, N. A., Narayanan, D., Owen, F. N., Pannella, M., Papovich, C., Pope, A., Rau, U., Robertson, B. E., Scott, D., Swinbank, A. M., van der Werf, P., van Kampen, E., Weiner, B. J., and Windhorst, R. A. (2016). VLA and ALMA Imaging of Intense, Galaxy-Wide Star Formation in z ˜ 2 Galaxies. *ArXiv e-prints*.

Salama, F. (2008). PAHs in Astronomy - A Review. In Kwok, S. and Sanford, S., editors, *Organic Matter in Space*, volume 251 of *IAU Symposium*, pages 357–366.

Salpeter, E. E. (1955). The Luminosity Function and Stellar Evolution. ApJ, 121:161.

Sánchez-Blázquez, P., Peletier, R. F., Jiménez-Vicente, J., Cardiel, N., Cenarro, A. J., Falcón-Barroso, J., Gorgas, J., Selam, S., and Vazdekis, A. (2006). Medium-resolution Isaac Newton Telescope library of empirical spectra. MNRAS, 371:703–718.

Santini, P., Fontana, A., Grazian, A., Salimbeni, S., Fiore, F., Fontanot, F., Boutsia, K., Castellano, M., Cristiani, S., de Santis, C., Gallozzi, S., Giallongo, E., Menci, N., Nonino, M., Paris, D., Pentericci, L., and Vanzella, E. (2009). Star formation and mass assembly in high redshift galaxies. A&A, 504:751–767.

Santini, P., Maiolino, R., Magnelli, B., Lutz, D., Lamastra, A., Li Causi, G., Eales, S., Andreani, P., Berta, S., Buat, V., Cooray, A., Cresci, G., Daddi, E., Farrah, D., Fontana, A., Franceschini, A., Genzel, R., Granato, G., Grazian, A., Le Floc'h, E., Magdis, G., Magliocchetti, M., Mannucci, F., Menci, N., Nordon, R., Oliver, S., Popesso, P., Pozzi, F., Riguccini, L., Rodighiero, G., Rosario, D. J., Salvato, M., Scott, D., Silva, L., Tacconi, L., Viero, M., Wang, L., Wuyts, S., and Xu, K. (2014). The evolution of the dust and gas content in galaxies. A&A, 562:A30.

Schlegel, D. J., Finkbeiner, D. P., and Davis, M. (1998). Maps of Dust Infrared Emission for Use in Estimation of Reddening and Cosmic Microwave Background Radiation Foregrounds. ApJ, 500:525–553.

Schmidt, M. (1959). The Rate of Star Formation. ApJ, 129:243.

Schreiber, C., Pannella, M., Elbaz, D., Béthermin, M., Inami, H., Dickinson, M., Magnelli, B., Wang, T., Aussel, H., Daddi, E., Juneau, S., Shu, X., Sargent, M. T., Buat, V., Faber, S. M., Ferguson, H. C., Giavalisco, M., Koekemoer, A. M., Magdis, G., Morrison, G. E., Papovich, C., Santini, P., and Scott, D. (2015). The Herschel view of the dominant mode of galaxy growth from z = 4 to the present day. A&A, 575:A74.

Soto, K. T., Lilly, S. J., Bacon, R., Richard, J., and Conseil, S. (2016). ZAP - enhanced PCA sky subtraction for integral field spectroscopy. MNRAS, 458:3210–3220.

Tacconi, L. J., Genzel, R., Neri, R., Cox, P., Cooper, M. C., Shapiro, K., Bolatto, A., Bouché, N., Bournaud, F., Burkert, A., Combes, F., Comerford, J., Davis, M., Schreiber, N. M. F., Garcia-Burillo, S., Gracia-Carpio, J., Lutz, D., Naab, T., Omont, A., Shapley, A., Sternberg, A., and Weiner, B. (2010). High molecular gas fractions in normal massive star-forming galaxies in the young Universe. Nature, 463:781–784.

Talia, M., Cimatti, A., Pozzetti, L., Rodighiero, G., Gruppioni, C., Pozzi, F., Daddi, E., Maraston, C., Mignoli, M., and Kurk, J. (2015). The star formation rate cookbook at $1 < z < 3$: Extinction-corrected relations for UV and [OII]λ3727 luminosities. A&A, 582:A80.

Tody, D. (1986). The IRAF Data Reduction and Analysis System. In Crawford, D. L., editor, *Instrumentation in astronomy VI*, volume 627 of Proc. SPIE, page 733.

Venemans, B. P., Bañados, E., Decarli, R., Farina, E. P., Walter, F., Chambers, K. C., Fan, X., Rix, H.-W., Schlafly, E., McMahon, R. G., Simcoe, R., Stern, D., Burgett, W. S., Draper, P. W., Flewelling, H., Hodapp, K. W., Kaiser, N., Magnier, E. A., Metcalfe, N., Morgan, J. S., Price, P. A., Tonry, J. L., Waters, C., AlSayyad, Y., Banerji, M., Chen, S. S., González-Solares, E. A., Greiner, J., Mazzucchelli, C., McGreer, I., Miller, D. R., Reed, S., and Sullivan, P. W. (2015). The Identification of Z-dropouts in Pan-STARRS1: Three Quasars at $6.5 \leq z \leq 6.7$. ApJ, 801:L11.

Walter, F., Decarli, R., Aravena, M., Carilli, C., Bouwens, R., da Cunha, E., Daddi, E., Ivison, R. J., Riechers, D., Smail, I., Swinbank, M., Weiss, A., Anguita, T., Assef, R.,

Bacon, R., Bauer, F., Bell, E. F., Bertoldi, F., Chapman, S., Colina, L., Cortes, P. C., Cox, P., Dickinson, M., Elbaz, D., Gónzalez-López, J., Ibar, E., Inami, H., Infante, L., Hodge, J., Karim, A., Le Fevre, O., Magnelli, B., Neri, R., Oesch, P., Ota, K., Popping, G., Rix, H.-W., Sargent, M., Sheth, K., van der Wel, A., van der Werf, P., and Wagg, J. (2016). ALMA Spectroscopic Survey in the Hubble Ultra Deep Field: Survey Description. *ArXiv e-prints*.

Williams, R. E., Baum, S., Bergeron, L. E., Bernstein, N., Blacker, B. S., Boyle, B. J., Brown, T. M., Carollo, C. M., Casertano, S., Covarrubias, R., de Mello, D. F., Dickinson, M. E., Espey, B. R., Ferguson, H. C., Fruchter, A., Gardner, J. P., Gonnella, A., Hayes, J., Hewett, P. C., Heyer, I., Hook, R., Irwin, M., Jones, D., Kaiser, M. E., Levay, Z., Lubenow, A., Lucas, R. A., Mack, J., MacKenty, J. W., Madau, P., Makidon, R. B., Martin, C. L., Mazzuca, L., Mutchler, M., Norris, R. P., Perriello, B., Phillips, M. M., Postman, M., Royle, P., Sahu, K., Savaglio, S., Sherwin, A., Smith, T. E., Stiavelli, M., Suntzeff, N. B., Teplitz, H. I., van der Marel, R. P., Walker, A. R., Weymann, R. J., Wiggs, M. S., Williger, G. M., Wilson, J., Zacharias, N., and Zurek, D. R. (2000). The Hubble Deep Field South: Formulation of the Observing Campaign. AJ, 120:2735–2746.

Williams, R. E., Blacker, B., Dickinson, M., Dixon, W. V. D., Ferguson, H. C., Fruchter, A. S., Giavalisco, M., Gilliland, R. L., Heyer, I., Katsanis, R., Levay, Z., Lucas, R. A., McElroy, D. B., Petro, L., Postman, M., Adorf, H.-M., and Hook, R. (1996). The Hubble Deep Field: Observations, Data Reduction, and Galaxy Photometry. AJ, 112:1335.

Wright, E. L. (2006). A Cosmology Calculator for the World Wide Web. PASP, 118:1711–1715.